

**Chemical Vapour Deposition of
Titanium and Vanadium Arsenide
Thin Films**

Tegan Thomas

Supervised by Prof. C. J. Carmalt and Prof. I. P. Parkin

A thesis presented to University College London in partial fulfilment
of the requirements for the degree of Doctor of philosophy

I, Tegan Thomas, confirm that the work presented in this thesis is my own. Where information has been derived from other sources, I confirm that this has been indicated in the thesis.

Abstract

This thesis describes the chemical vapour deposition (CVD) of titanium and vanadium arsenide thin films. The compounds $[\text{TiCl}_4(\text{AsPh}_3)]$, $[\text{TiCl}_4(\text{AsPh}_3)_2]$, $[\text{TiCl}_4(\text{Ph}_2\text{AsCH}_2\text{AsPh}_2)]$, $[\text{TiCl}_4(\text{tBuAsH}_2)_n]$ have been synthesised from the reaction of TiCl_4 with the corresponding arsine, and they have been investigated as potential single-source precursors to TiAs. Additionally, $[\text{TiCl}_3(\text{NMe}_2)(\mu\text{-NMe}_2)_2\text{AsCl}]$ has been synthesised from the reaction of TiCl_4 and $\text{As}(\text{NMe}_2)_3$, and although was thought not to be a suitable single-source precursor to TiAs due to its lack of preformed Ti-As bonds, its use as a potential single-source precursor to TiN has been investigated. All synthesised compounds have been characterised using NMR, mass spectrometry and elemental analysis, and decompositional profiles studied by thermogravimetric analysis (TGA).

Aerosol assisted (AA) and low pressure (LP)CVD have been used to investigate the use of the compounds as single-source precursors, with deposited films analysed by X-ray powder diffraction, wavelength dispersive X-ray (WDX) analysis and scanning electron microscopy (SEM).

Thin films of TiAs have been deposited *via* the dual-source atmospheric pressure (AP)CVD reactions of tBuAsH_2 with both TiCl_4 and $[\text{Ti}(\text{NMe}_2)_4]$. This arsenic precursor has also been investigated within the deposition of VAs films *via* dual-source routes with its reaction with VCl_4 and VOCl_3 . All deposited films have been characterised using X-ray powder diffraction, WDX, X-ray photoelectron spectroscopy (XPS), Raman microscopy, and SEM, with properties such as adherence, hardness, water contact angles and reflectivity measured.

Acknowledgements

Firstly I would like to thank my supervisors Prof. C. J. Carmalt and Prof. I. P. Parkin for their research ideas, knowledge and support over the last three years. I have thoroughly enjoyed my time as a Ph.D. student, and I thank you for having me in your group. Thanks also goes to Dr. C. S. Blackman for his help with APCVD and for showing me that CVD can work. I also thank the EPSRC for funding and SAFC Hitech Ltd. for the supply of $t\text{BuAsH}_2$.

I thank Dr. S. E. Potts, Dr. C. E. Knapp and Dr. D. Pugh for showing me the ropes and for answering my many questions. I also thank Dr. D. Pugh for his help with the single crystal XRD and for the lovely crystal structures. I thank everyone that is and has been a part of lab 308 for providing a friendly research environment, and for the laughs and encouragement along the way.

Thanks goes to G. Maxwell, Dr. A. Aleiv, Dr. S. Firth and Dr. G. Hyett for their help with EA, NMR, TGA/DSC and Raman microscopy, and XRD, respectively. K. Reeves, Dr. E. Smith, and Y. Shin are thanked for their help with SEM and WDX, XPS and AFM, and Dr. R. Binions and C. Crick are thanked for their help with UV-Vis and water contact angle measurements.

Last, and by no means least, I thank my family for their love and support. Thank you for always believing in me, I dedicate this thesis to you.

Contents

Title Page	1
Declaration	2
Abstract	3
Acknowledgements	4
Contents	5
List of Figures and Tables	11
<i>Chapter 1 – Introduction</i>	
1.1 Bulk Transition Metal Arsenides	23
1.1.1 Bulk Material Synthesis	23
1.1.1.1 Alternative Methods for Elemental Combination	24
1.1.1.2 Solid State Metathesis Routes	24
1.1.1.3 Liquid-Mediated Metathesis	25
1.1.1.4 Reductive Routes	26
1.1.1.5 Other Routes	27
1.1.1.6 Nanoparticles	28
1.1.2 General Structural Trends	28
1.1.2.1 The TiP Structure	30
1.1.2.2 The MnP Structure	30
1.1.2.3 The NiAs Structure	30
1.1.3 Phase Transitions Between the MnP and NiAs Structures	31
1.1.4 Potential Applications of Transition Metal Arsenides	31
1.2 The Potential of Transition Metal Arsenide Thin Films	31
1.2.1 III/V Semiconductors	32
1.2.1.1 Spintronics	32

1.2.1.2 Non-volatile Transistors	33
1.3 Thin Film Deposition <i>via</i> CVD	33
1.3.1 Fundamentals of CVD	33
1.3.2 CVD Precursors	34
1.3.2.1 Decomposition of As(NMe ₂) ₃	35
1.3.2.2 Decomposition of ^t BuAsH ₂	35
1.3.3 Types of CVD	36
1.3.3.1 Aerosol Assisted (AA)CVD	36
1.3.3.2 Low Pressure (LP)CVD	37
1.3.3.3 Atmospheric Pressure (AP)CVD	38
1.4 Transition Metal Group 15 Films	38
1.4.1 Transition Metal Nitride Thin Films	38
1.4.2 Transition Metal Phosphide Thin Films	41
1.4.3 Transition Metal Arsenide Thin Films	44
1.4.3.1 Manganese Arsenide	45
1.4.3.2 Iron Arsenide	47
1.4.3.3 Cobalt Arsenide	47
1.4.3.4 Cadmium Arsenide	49
1.4.3.5 A Single-Source Attempt to SnAs	50
1.5 Thesis Aims	51

Chapter 2 - The Synthesis and Characterisation of Titanium(IV) Arsine Complexes

2.1 Experimental	59
2.1.1 General Procedures and Instrumentation	59
2.1.2 Physical Measurements	60
2.1.3 Synthesis of Titanium(IV) Arsine Complexes	60
2.1.3.1 Synthesis of [TiCl ₄ (AsPh ₃)] (2.1)	60
2.1.3.2 Synthesis of [TiCl ₄ (AsPh ₃) ₂] (2.2)	61
2.1.3.3 Reaction of TiCl ₄ and Ph ₂ AsCH ₂ AsPh ₂ (2.3)	61
2.1.3.4 Reaction of TiCl ₄ and ^t BuAsH ₂ (2.4)	62

2.1.3.5 Synthesis of $[\text{TiCl}_3(\text{NMe}_2)(\mu\text{-NMe}_2)_2\text{AsCl}]$ (2.5)	62
2.1.3.6 Reaction of TiCl_4 with 2 $\text{As}(\text{NMe}_2)_3$ (2.6)	63
2.1.3.7 Reaction of $[\text{Ti}(\text{NMe}_2)_4]$ with AsCl_3 (2.7)	63
2.2 Results and Discussion	64
2.2.1 Reactions of TiCl_4 with AsPh_3	64
2.2.2 The Reaction of TiCl_4 with $\text{Ph}_2\text{AsCH}_2\text{AsPh}_2$ (2.3)	68
2.2.3 The Reaction of TiCl_4 with ${}^t\text{BuAsH}_2$ (2.4)	69
2.2.4 Synthesis of $[\text{TiCl}_3(\text{NMe}_2)(\mu\text{-NMe}_2)_2\text{AsCl}]$ (2.5) and Investigation Into the Observed NMe_2 , Cl Exchange via the Synthesis of (2.6) and (2.7).	70
2.2.4.1 The reaction of TiCl_4 and 2 $\text{As}(\text{NMe}_2)_3$ (2.6)	72
2.2.4.2 The reaction of $[\text{Ti}(\text{NMe}_2)_4]$ and AsCl_3 (2.7)	73
2.3 Conclusions	74
<i>Chapter 3 - Single-source CVD Attempts to TiAs</i>	
3.1 Experimental	78
3.1.1 General Procedures, Precursors and Substrate	78
3.1.2 Physical Measurements	78
3.1.3 CVD Equipment and Methods	78
3.1.3.1 Aerosol Assisted (AA)CVD	78
3.1.3.2 Vapour Draw Low Pressure (LP)CVD	80
3.1.4 AACVD Precursor Delivery	80
3.2 Results and Discussion	82
3.2.1 Thermogravimetric Analysis	82
3.2.1.1 $[\text{TiCl}_4(\text{AsPh}_3)]$ (2.1) and $[\text{TiCl}_4(\text{AsPh}_3)_2]$ (2.2)	83
3.2.1.2 $[\text{TiCl}_4(\text{Ph}_2\text{AsCH}_2\text{AsPh}_2)]$ (2.3)	84
3.2.1.3 $[\text{TiCl}_4({}^t\text{BuAsH}_2)_n]$ (2.4)	84
3.2.1.4 $[\text{TiCl}_3(\text{NMe}_2)(\mu\text{-NMe}_2)_2\text{AsCl}]$ (2.5)	85
3.2.2 Aerosol Assisted (AA)CVD	85
3.2.2.1 $[\text{TiCl}_4(\text{AsPh}_3)]$ (2.1) and $[\text{TiCl}_4(\text{AsPh}_3)_2]$ (2.2)	85
3.2.2.2 $[\text{TiCl}_4({}^t\text{BuAsH}_2)_n]$ (2.4)	87

3.2.2.3 [TiCl ₃ (μ-NMe ₂) ₂ (NMe ₂)AsCl] (2.5)	90
3.2.3 Vapour Draw Low Pressure (LP)CVD	90
3.2.3.1 The LPCVD of [TiCl ₄ (AsPh ₃)] (2.1) and [TiCl ₄ (AsPh ₃) ₂] (2.2)	91
3.2.3.2 The LPCVD of [TiCl ₄ (Ph ₂ AsCH ₂ AsPh ₂)] (2.3)	94
3.2.3.3 The LPCVD of [TiCl ₃ (NMe ₂)(μ-NMe ₂) ₂ AsCl] (2.4)	96
3.2.4 Conclusions	97
<i>Chapter 4 - The APCVD of TiAs Thin Films</i>	
4.1 Introduction	100
4.2 Experimental	101
4.2.1 Precursors and Substrate	101
4.2.2 APCVD Equipment and Methods	101
4.2.3 Physical Measurements of Deposited Films	103
4.3 The APCVD of TiCl₄ and ^tBuAsH₂	104
4.3.1 Introduction	104
4.3.2 TiAs Deposition and Visual Appearance	105
4.3.3 TiAs Characterisation	107
4.3.3.1 Powder X-ray Diffraction Analysis (XRD)	107
4.3.3.2 Wavelength Dispersive X-ray (WDX) Analysis	108
4.3.3.3 X-ray Photoelectron Spectroscopy (XPS)	109
4.3.3.4 Raman Microscopy Analysis	112
4.3.4 TiAs Morphology	113
4.3.4.1 Scanning Electron Microscopy Analysis (SEM)	113
4.3.4.2 Atomic Force Microscopy (AFM) Analysis	114
4.3.5 TiAs Film Properties	116
4.3.5.1 Adherence, Hardness and Resistivity	116
4.3.5.2 Optical Properties	116
4.3.5.3 Water Contact Angle Measurements	118
4.3.6 Conclusions	119
4.4 The APCVD of [Ti(NMe₂)₄] and ^tBuAsH₂	120
4.4.1 Introduction	120

4.4.2 TiAs Deposition and Visual Appearance	121
4.4.3 TiAs Characterisation	122
4.4.3.1 X-ray Powder Diffraction (XRD) Analysis	122
4.4.3.2 Wavelength Dispersive X-ray (WDX) Analysis	123
4.4.3.3 X-ray Photoelectron Spectroscopy (XPS)	124
4.4.3.4 Raman Microscopy	125
4.4.4 TiAs Morphology	125
4.4.5 TiAs Film Properties	127
4.4.5.1 Adherence, Hardness and Resistivity	127
4.4.5.2 Optical Properties	127
4.4.5.3 Water Contact Angle Measurements	129
4.4.6 Conclusions	130

Chapter 5 - The APCVD of VAs Thin Films

5.1 Introduction	132
5.2 Experimental	133
5.2.1 Precursors and Substrate	133
5.2.2 APCVD Equipment and Methods	133
5.2.3 Physical Measurements of Deposited Films	134
5.3 APCVD of VCl_4 and $tBuAsH_2$	134
5.3.1 Introduction	134
5.3.2 VAs Deposition and Visual Appearance	135
5.3.3 VAs Characterisation	136
5.3.3.1 Powder X-ray Diffraction (XRD) Analysis	136
5.3.3.2 Wavelength Dispersive X-ray (WDX) Analysis	137
5.3.3.3 X-ray Photoelectron Spectroscopy (XPS)	139
5.3.3.4 Raman Microscopy Analysis	141
5.3.4 VAs Morphology Analysis	142
5.3.5 VAs Properties	144
5.3.5.1 Adherence, Hardness and Resistivity	144
5.3.5.2 Optical Properties	144

5.3.5.3 Water Contact Angle Measurements	145
5.3.6 Conclusions	146
5.4 APCVD of VOCl_3 and ${}^t\text{BuAsH}_2$	147
5.4.1 Introduction	147
5.4.2 VAs Deposition and Visual Appearance	148
5.4.3 VAs Characterisation	149
5.4.3.1 X-ray Powder Diffraction (XRD) Analysis	149
5.4.3.2 Wavelength Dispersive X-ray (WDX) Analysis	150
5.4.3.3 X-ray Photoelectron Spectroscopy (XPS) Analysis	151
5.4.3.4 Raman Microscopy Analysis	152
5.4.4 VAs Morphology	153
5.4.5 VAs Film Properties	155
5.4.5.1 Adherence, Hardness and Resistivity	155
5.4.5.2 Optical Properties	155
5.4.5.3 Water Contact Angle Measurements	157
5.4.6 Conclusions	158
<i>Chapter 6 – Conclusions</i>	
6.1 The Synthesis of potential single-source precursors to TiAs	160
6.2 Single-source CVD Attempts to TiAs	161
6.3 The APCVD of TiAs Thin Films	162
6.4 The APCVD of VAs Thin Films	164
6.5 Summary	165
<i>Chapter 7 – Appendices</i>	
A1 Publications	167
A2 Crystal Data for $[\text{TiCl}_4(\text{AsPh}_3)]$ (2.1)	168
A3 Crystal Data for $[\text{TiCl}_4(\text{AsPh}_3)_2]$ (2.2)	173
A4 Crystal Data for $[\text{TiCl}_3(\text{NMe}_2)(\mu\text{-NMe}_2)_2\text{AsCl}]$ (2.5)	182
A5 Crystal Data for $[\text{TiCl}_2(\mu\text{-Cl})_2(\text{NMe}_2)(\text{NHMe}_2)]_2$ (2.7)	187

List of Figures and Tables

Chapter 1 – Introduction

- Figure 1.1** Synthesis of NiAs using the nickel dithiocarbamate arsenic scavenger. 28
- Figure 1.2** Crystal structures of the TiP (a), MnP (b) and NiAs (c) adopted by the 3d transition metal monoarsenides. 29
- Figure 1.3** Schematic representing the seven steps involved in CVD. 1. Generation of gaseous precursors. 2. Transportation of gaseous reactants into the reaction chamber. 3. Formation of intermediates following the gas phase reaction of the gaseous reactants. 4. Deposition of material onto the substrate as a result of heterogeneous reactions. 5. Diffusion of deposited material across the substrate resulting in the formation of crystallisation centres. 6. Gaseous by-product removal as a result of diffusion/convection. 7. Transportation of gaseous by-products and unreacted precursors away and out of the reaction chamber. 34
- Figure 1.4** Heterogeneous decomposition of $\text{As}(\text{NMe}_2)_3$ via β -hydride elimination. 35
- Figure 1.5** Proposed routes of decomposition of ${}^t\text{BuAsH}_2$. 36
- Figure 1.6** Proposed decomposition pathway of metal dimethylamide and ammonia in the deposition of MN films. 40
- Figure 1.7** Selected examples of single-source precursors to titanium nitride. 41
- Figure 1.8** Selected examples of single-source precursor to transition metal phosphides. 43
- Figure 1.9** Selected examples of phosphine precursors used in the deposition 44

of transition metal phosphides.

Figure 1.10 The structure of the manganese precursor tricarbonylmethylcyclopentadienyl manganese (TCM). 46

Figure 1.11 Schematic representing the different layers and relative compositions formed upon the exposure of a steel substrate to molten lead at 500 °C for 100 hours. 47

Figure 1.12 Successful single-source precursors to CoAs. 49

Figure 1.13 Tin arsenide adduct $[\text{SnCl}_4(\text{AsPh}_3)_2]$ used in an attempt to deposit SnAs *via* AACVD. 50

Table 1.1 Crystal structures exhibited by the 3d transition metal monoarsenides. 29

Table 1.2 Average transition metal-arsenic bond lengths. 30

Table 1.3 Selected data for CoP films deposited *via* the dual-source route of TNC and ${}^t\text{Bu}_2\text{PH}$, compared to that using the single-source precursor $[\text{Co}(\text{CO})_2(\text{P}({}^t\text{Bu})_2\text{H}(\text{NO}))]$. 42

Table 1.4 Selected data for CoAs films deposited *via* the dual-source route of TNC and ${}^t\text{Bu}_2\text{AsH}$, compared to those deposited using the single-source precursors $[\text{Co}_2(\text{CO})_6\text{As}_2]$ and $[\text{Co}(\text{CO})_2(\text{As}({}^t\text{Bu})_2\text{H})(\text{NO})]$. 48

Chapter 2 - The Synthesis and Characterisation of Titanium(IV) Arsine Complexes

Figure 2.1 ORTEP representation of $[\text{TiCl}_4(\text{AsPh}_3)]$ (2.1) with thermal ellipsoids at the 50% probability level. Hydrogen atoms are omitted for clarity. 66

Figure 2.2 ORTEP representation of $[\text{TiCl}_4(\text{AsPh}_3)_2]$ (2.2) showing one of the two orientations of the disordered AsPh_3 group. Thermal ellipsoids are at the 50% probability level, with hydrogen atoms omitted for clarity. Symmetry transformations used to generate equivalent atoms: $1^i -x + 1, -y + 2, -z + 2$. 67

Figure 2.3 Proposed structure of (2.3) synthesised <i>via</i> the 1:1 reaction of TiCl_4 and $\text{Ph}_2\text{AsCH}_2\text{AsPh}_2$.	68
Figure 2.4 Proposed structure of (2.4) synthesised from the reaction of TiCl_4 with ${}^t\text{BuAsH}_2$.	69
Figure 2.5 ORTEP representation of $[\text{TiCl}_3(\text{NMe}_2)(\mu\text{-NMe}_2)_2\text{AsCl}]$ (2.5) with thermal ellipsoids at the 50% probability level. Hydrogen atoms have been omitted for clarity.	71
Figure 2.6 Schematic representing two potential structures adopted by (2.6) .	72
Figure 2.7 ORTEP representation of $[\text{TiCl}_2(\mu\text{-Cl})_2(\text{NMe}_2)(\text{NHMe}_2)]_2$ (2.7) with thermal ellipsoids at the 50% probability level. Hydrogen atoms (excluding the amine NH) have been omitted for clarity.	73
Table 2.1 Selected bond lengths (\AA) and angles ($^\circ$) for $[\text{TiCl}_4(\text{AsPh}_3)]$ (2.1) .	66
Table 2.2 Selected bond lengths (\AA) and angles ($^\circ$) for $[\text{TiCl}_4(\text{AsPh}_3)]$ (2.2) .	67
Table 2.3 Selected bond lengths (\AA) and angles ($^\circ$) for $[\text{TiCl}_3(\text{NMe}_2)(\mu\text{-NMe}_2)_2\text{AsCl}]$ (2.5) .	71
Table 2.4 Selected bond lengths (\AA) and angles ($^\circ$) for $[\text{TiCl}_2(\mu\text{-Cl})_2(\text{NMe}_2)(\text{NHMe}_2)]_2$ (2.7) .	74
 Chapter 3 - Single-source CVD Attempts to TiAs	
Figure 3.1 Schematic illustrating the synthesis of compounds (2.1) – (2.5) <i>via</i> the reaction of TiCl_4 with (i) AsPh_3 , (ii) 2AsPh_3 , (iii) $\text{Ph}_2\text{AsCH}_2\text{AsPh}_2$, (iv) ${}^t\text{BuAsH}_2$ and (v) $\text{As}(\text{NMe}_2)_3$.	77
Figure 3.2 Schematic representing the equipment used within the AACVD of compounds (2.1) , (2.2) , (2.4) and (2.5) .	79
Figure 3.3 Schematic representing the equipment used within the vapour draw LPCVD of compounds (2.1) , (2.2) , (2.3) and (2.5) in an attempt to deposit TiAs.	80
Figure 3.4 TGA plots for compounds (2.1) – (2.5) between 100 and 500 $^\circ\text{C}$.	82

Figure 3.5 Typical X-ray powder diffraction pattern for the rainbow films deposited during the AACVD of [TiCl ₄ (AsPh ₃)] (2.1) and [TiCl ₄ (AsPh ₃) ₂] (2.2) with comparison to a reference TiO ₂ anatase powder diffractogram.	86
Figure 3.6 Typical X-ray powder diffractograms for rainbow films deposited <i>via</i> the AACVD of [TiCl ₄ (^t BuAsH ₂) _{<i>n</i>}] (2.4) using a simultaneous method of precursor delivery at substrate temperatures of 400 and 600 °C, and a sequential precursor delivery method at 400 °C, with comparison to a reference TiO ₂ anatase powder diffractogram.	88
Figure 3.7 Scanning electron micrographs of TiO ₂ anatase films deposited <i>via</i> the AACVD of [TiCl ₄ (^t BuAsH ₂) _{<i>n</i>}] (2.4) using the simultaneous precursor delivery method, at substrate temperatures of 400 °C (a) and 600 °C (b) (x100,000 magnification).	89
Figure 3.8 Typical X-ray powder diffractograms for films deposited <i>via</i> the LPCVD of [TiCl ₄ (AsPh ₃)] (2.1) [TiCl ₄ (AsPh ₃) ₂] (2.2) at 600 °C within regions 1 (black), 2 (dark grey) and 4 (light grey).	92
Figure 3.9 Typical X-ray powder diffractograms for films deposited <i>via</i> the LPCVD of [TiCl ₄ (Ph ₂ AsCH ₂ AsPh ₂)] (2.3) at 600 °C within regions 1 (black), 2 (dark grey).	95
Figure 3.10 Typical X-ray powder diffractograms for films deposited <i>via</i> the LPCVD of [TiCl ₃ (NMe ₂)(μ-NMe) ₂ AsCl] (2.4) at 600 °C within regions 1 (black), 4 (dark grey) and 5 (light grey).	96
Table 3.1 Table summarising the experimental parameters investigated within the AACVD of compounds (2.1) , (2.2) , (2.4) and (2.5) . N.B. Compound (2.3) was not investigated using AACVD due to its insolubility within a range of tested solvents including toluene, dichloromethane (DCM) and hexane.	81
Table 3.2 Residual mass data from the TGA of compounds (2.1) – (2.5) compared to the calculated residual mass for decomposition to TiAs.	82

Table 3.3 Wavelength dispersive X-ray (WDX) analysis showing typical values for the rainbow films deposited <i>via</i> the AACVD of [TiCl ₄ (AsPh ₃)] (2.1) and [TiCl ₄ (AsPh ₃) ₂] (2.2) .	87
Table 3.4 Wavelength dispersive X-ray (WDX) analysis showing typical values for the rainbow films deposited <i>via</i> the AACVD of [TiCl ₄ (<i>t</i> BuAsH ₂) _{<i>n</i>}] (2.4) using a simultaneous and sequential precursor delivery method at substrate temperatures of 400 and 600 °C.	89
Table 3.5 Schematic illustrating the different depositions observed within the LPCVD of compounds (2.1) , (2.2) , (2.3) , and (2.5) , where region 6 represents the substrate closest to the sample vial, and 1, the substrate closet to the vacuum.	91
Table 3.6 Wavelength dispersive X-ray (WDX) analysis showing typical values for the films deposited <i>via</i> the LPCVD of [TiCl ₄ (AsPh ₃)] (2.1) at 600 °C within regions 1, 2 and 4 of the tube furnace.	93
Table 3.7 Wavelength dispersive X-ray (WDX) analysis showing typical values for the films deposited <i>via</i> the LPCVD of [TiCl ₄ (AsPh ₃) ₂] (2.2) at 600 °C within regions 1, and 2 of the tube furnace.	93
Table 3.8 Wavelength dispersive X-ray (WDX) analysis showing typical values for the films deposited <i>via</i> the LPCVD of [TiCl ₄ (Ph ₂ AsCH ₂ AsPh ₂)] (2.3) at 600 °C within regions 1, 2 and 3 of the tube furnace.	95
Table 3.9 Wavelength dispersive X-ray (WDX) analysis showing typical values for the films deposited <i>via</i> the LPCVD of [TiCl ₃ (NMe ₂)(<i>μ</i> -NMe) ₂ AsCl] (2.4) at 600 °C within regions 1, 4 and 5 of the tube furnace.	97

Chapter 4 - The APCVD of TiAs Thin Films

Figure 4.1 The crystal structure of TiP which TiAs is known to adopt.	100
Figure 4.2 Schematic representing the inside of the stainless steel bubblers used in APCVD, and how the redirection of hot N ₂ gas into the bubbler causes movement of precursors out of the bubbler, ultimately resulting in	102

precursor delivery to the mixing chamber.

Figure 4.3 Digital photographs illustrating the difference in visual appearance of the TiAs films deposited *via* the APCVD of TiCl₄ and ^tBuAsH₂ at deposition temperatures of 450 °C and 500 °C (left), and 550 °C (right). **105**

Figure 4.4 The effect of substrate temperature on the deposition rate of TiAs from the APCVD of TiCl₄ and ^tBuAsH₂. **106**

Figure 4.5 Typical X-ray powder diffraction pattern for TiAs films deposited *via* the APCVD of TiCl₄ and ^tBuAsH₂ between the substrate temperatures 450 °C – 550 °C, with comparison to a reference TiAs powder diffractogram of bulk material. **107**

Figure 4.6 Schematic representing how the molar percentage of the titanium species TiAs, TiO₂ and the titanium arsenate species vary with depth within a TiAs film deposited from the APCVD of TiCl₄ and ^tBuAsH₂ at a substrate temperature of 500 °C (total etch time of 27,000 seconds). **110**

Figure 4.7 Schematic representing how the atomic percentage composition varies with depth within a TiAs film deposited from the APCVD of TiCl₄ and ^tBuAsH₂ at a substrate temperature of 500 °C (total etch time of 27,000 seconds). **111**

Figure 4.8 Raman spectra for TiAs films deposited *via* the APCVD of TiCl₄ and ^tBuAsH₂ at substrate temperatures 450 – 550 °C and deposition time lengths of 30, 60 and 120 seconds. **112**

Figure 4.9 Scanning electron micrographs of TiAs film deposited *via* the APCVD of TiCl₄ and ^tBuAsH₂ at 500 °C using deposition times of 30 (a), 60 (b) and 120 seconds (c) (x10,000 magnification). **113**

Figure 4.10 Scanning electron micrographs of TiAs films deposited *via* the APCVD of TiCl₄ and ^tBuAsH₂ using a deposition time of 120 seconds and substrate temperatures of 450 (a), 500 (b) and 550 °C (c) (x10,000 magnification). **114**

Figure 4.11 Scanning electron micrograph of an unnucleated area within a TiAs film deposited <i>via</i> the APCVD of TiCl ₄ and tBuAsH ₂ at 500 °C for 120 seconds (x3,700 magnification).	114
Figure 4.12 Atomic force micrographs representing a 5 μm x 5 μm region of TiAs deposited using a deposition time of 120 seconds and substrate temperatures of 450 °C (a), 500 °C (b) and 550 °C (c).	115
Figure 4.13 Percentage reflectance data for TiAs films deposited <i>via</i> the APCVD of TiCl ₄ and tBuAsH ₂ using a range of substrate temperatures and deposition times.	117
Figure 4.14 Percentage transmittance measurements for TiAs films deposited <i>via</i> the APCVD of TiCl ₄ and tBuAsH ₂ using a range of substrate temperatures and deposition times.	117
Figure 4.15 Photographs of a 10 μl water droplet on the surface of TiAs deposited <i>via</i> the APCVD of TiCl ₄ and tBuAsH ₂ .	118
Figure 4.16 Digital photographs illustrating the high reflectivity (left) and gold appearance on the leading edge (right) of TiAs films deposited <i>via</i> the APCVD of [Ti(NMe ₂) ₄] and tBuAsH ₂ .	121
Figure 4.17 Typical X-ray powder diffraction pattern for TiAs films deposited <i>via</i> the APCVD of [Ti(NMe ₂) ₄] and tBuAsH ₂ between the substrate temperatures 350 °C – 500 °C, with comparison to a reference TiAs diffractogram of bulk material.	122
Figure 4.18 X-ray powder diffraction patterns for TiAs films deposited <i>via</i> the APCVD of [Ti(NMe ₂) ₄] and tBuAsH ₂ in a 1:2 ratio, using a deposition time length of 60 seconds, at substrate temperatures of 450 °C (blue), and 500 °C (black), with comparison to a reference TiAs diffractogram of bulk material.	123
Figure 4.19 Comparison of typical Raman spectra for TiAs films deposited <i>via</i> the APCVD of [Ti(NMe ₂) ₄] and tBuAsH ₂ , and TiCl ₄ and tBuAsH ₂ .	125
Figure 4.20 Scanning electron micrographs of TiAs films deposited <i>via</i> the	126

APCVD of $[\text{Ti}(\text{NMe}_2)_4]$ and ${}^t\text{BuAsH}_2$ using a substrate temperature of 500 °C and deposition times of 60 (left) and 120 (right) seconds (x10,000 magnification).

Figure 4.21 Scanning electron micrographs of TiAs films deposited *via* the APCVD of $[\text{Ti}(\text{NMe}_2)_4]$ and ${}^t\text{BuAsH}_2$ using a deposition time of 60 seconds and substrate temperatures of 350 °C (a.), 400 °C (b.), 450 °C (c.), 500 °C (d.) and 550 °C (e.) (x10,000 magnification). **126**

Figure 4.22 Scanning electron micrograph representing a typical image of the TiAs films deposited *via* the APCVD of $[\text{Ti}(\text{NMe}_2)_4]$ and ${}^t\text{BuAsH}_2$ showing islands of deposit (x40,000 magnification). **127**

Figure 4.23 Percentage reflectance data for TiAs films deposited *via* the APCVD of $[\text{Ti}(\text{NMe}_2)_4]$ and ${}^t\text{BuAsH}_2$ using a range of substrate temperatures and deposition times. **128**

Figure 4.24 Percentage transmittance data for TiAs films deposited *via* the APCVD of $[\text{Ti}(\text{NMe}_2)_4]$ and ${}^t\text{BuAsH}_2$ using a range of substrate temperatures and deposition times. **129**

Figure 4.25 Photographs of an 8 μl water droplet on the surface of TiAs deposited *via* the APCVD of $[\text{Ti}(\text{NMe}_2)_4]$ and ${}^t\text{BuAsH}_2$. **129**

Table 4.1 Experimental conditions for TiAs films deposited from the APCVD of TiCl_4 and ${}^t\text{BuAsH}_2$. **104**

Table 4.2 Wavelength Dispersive X-ray (WDX) analysis of TiAs films deposited *via* the APCVD of TiCl_4 and ${}^t\text{BuAsH}_2$ using a range of substrate temperatures, TiCl_4 to ${}^t\text{BuAsH}_2$ ratios and deposition times. **108**

Table 4.3 Water contact angle measurements ($^\circ$) of TiAs films deposited *via* the APCVD of TiCl_4 and ${}^t\text{BuAsH}_2$. **118**

Table 4.4 Experimental conditions for TiAs films deposited from the APCVD of $[\text{Ti}(\text{NMe}_2)_4]$ and ${}^t\text{BuAsH}_2$. **120**

Table 4.5 Wavelength dispersive X-ray analysis of TiAs films deposited *via* **124**

the APCVD of $[\text{Ti}(\text{NMe}_2)_4]$ and ${}^t\text{BuAsH}_2$ in a 1:2 ratio, using a range of substrate temperatures and deposition times.

Table 4.6 Water contact angle measurements ($^\circ$) of TiAs films deposited *via* the APCVD of $[\text{Ti}(\text{NMe}_2)_4]$ and ${}^t\text{BuAsH}_2$. **130**

Chapter 5 - The APCVD of VAs Thin Films

Figure 5.1 The crystal structure of MnP which VAs is known to adopt. **132**

Figure 5.2 Typical X-ray powder diffraction pattern for VAs films deposited *via* the APCVD of VCl_4 and ${}^t\text{BuAsH}_2$ between the substrate temperatures $550\text{ }^\circ\text{C} - 600\text{ }^\circ\text{C}$, with comparison to a reference VAs diffractogram of bulk material. **136**

Figure 5.3 X-ray powder diffraction patterns for VAs films deposited *via* the APCVD of VCl_4 and ${}^t\text{BuAsH}_2$ in a 1:2 ratio, using a deposition time length of 120 seconds, at substrate temperatures of $550\text{ }^\circ\text{C}$ (blue), and $600\text{ }^\circ\text{C}$ (black), with comparison to a reference VAs diffractogram of bulk material. **137**

Figure 5.4 Schematic representing how the atomic percentage composition varies with depth within a VAs film deposited from the APCVD of VCl_4 and ${}^t\text{BuAsH}_2$ at a substrate temperature of $600\text{ }^\circ\text{C}$ (total etch time of 1860 seconds). **140**

Figure 5.5 Typical Raman spectrum for VAs films deposited *via* the APCVD of VCl_4 and ${}^t\text{BuAsH}_2$ for a deposition time length of 120 seconds. **141**

Figure 5.6 Raman spectrum for a VAs film deposited *via* the APCVD of VCl_4 and ${}^t\text{BuAsH}_2$ at a substrate temperature of $600\text{ }^\circ\text{C}$ for a deposition time length of 60 seconds. **142**

Figure 5.7 Scanning electron micrographs of VAs films deposited *via* the APCVD of VCl_4 and ${}^t\text{BuAsH}_2$ at $600\text{ }^\circ\text{C}$ using deposition times of 60 (a.) and 120 (b.) seconds (x10,000 magnification). **143**

Figure 5.8 Scanning electron micrograph of a VAs film deposited *via* the APCVD of VCl_4 and ${}^t\text{BuAsH}_2$ at $600\text{ }^\circ\text{C}$ using a deposition time of 120 **143**

seconds showing the fractured surface (x1,000 magnification).	
Figure 5.9 Reflectance and transmittance data for a VAs film deposited <i>via</i> the APCVD of VCl ₄ and ^t BuAsH ₂ at a substrate temperature of 600 °C and for a deposition time of 60 seconds.	145
Figure 5.10 Photographs of an 8 μl water droplet on the surface of VAs deposited <i>via</i> the APCVD of VCl ₄ and ^t BuAsH ₂ .	146
Figure 5.11 Digital photograph illustrating the typical appearance of VAs films deposited <i>via</i> the APCVD of VOCl ₃ and ^t BuAsH ₂ .	148
Figure 5.12 Typical X-ray powder diffraction pattern for VAs films deposited <i>via</i> the APCVD of VOCl ₃ and ^t BuAsH ₂ between the substrate temperatures 550 °C – 600 °C, with comparison to a reference VAs diffractogram of bulk material.	149
Figure 5.13 X-ray powder diffraction patterns for VAs films deposited <i>via</i> the APCVD of VOCl ₃ and ^t BuAsH ₂ in a 1:4 ratio, using a deposition time length of 60 seconds, at substrate temperatures of 550 °C (blue), and 600 °C (black), with comparison to a reference VAs diffractogram of bulk material.	150
Figure 5.14 Comparison of typical Raman spectra for VAs films deposited <i>via</i> the APCVD of VOCl ₃ and ^t BuAsH ₂ and VCl ₄ and ^t BuAsH ₂ .	152
Figure 5.15 Scanning electron micrographs of VAs films deposited <i>via</i> the APCVD of VOCl ₃ and ^t BuAsH ₂ at 550 °C using a VOCl ₃ to ^t BuAsH ₂ ratio of 1:4 and deposition times of 60 (a) and 120 seconds (b) (x10,000 magnification).	153
Figure 5.16 Scanning electron micrographs of VAs films deposited <i>via</i> the APCVD of VOCl ₃ and ^t BuAsH ₂ using a VOCl ₃ to ^t BuAsH ₂ ratio of 1:4, a deposition time of 60 seconds, and substrate temperatures of 550 °C (a) and 600 °C (b) (x10,000 magnification).	154
Figure 5.17 Scanning electron micrographs of VAs films deposited <i>via</i> the APCVD of VOCl ₃ and ^t BuAsH ₂ at 550 °C and deposition times of 2 minutes, using VOCl ₃ to ^t BuAsH ₂ ratios of (a) 1:2 and (b) 1:4 (x10,000	154

magnification).	
Figure 5.18 Typical scanning electron micrograph of VAs films deposited <i>via</i> the APCVD of VOCl_3 and ${}^t\text{BuAsH}_2$. Specific image is of a VAs film deposited at 550 °C for 2 minutes using a VOCl_3 to ${}^t\text{BuAsH}_2$ ratio of 1:4 (x40,000 magnification).	154
Figure 5.19 Percentage reflectance data for VAs films deposited <i>via</i> the APCVD of VOCl_3 and ${}^t\text{BuAsH}_2$ using a range of substrate temperatures, deposition times, and VOCl_3 to ${}^t\text{BuAsH}_2$ ratios.	156
Figure 5.20 Percentage transmittance data for VAs films deposited <i>via</i> the APCVD of VOCl_3 and ${}^t\text{BuAsH}_2$ using a range of substrate temperatures, deposition times, and VOCl_3 to ${}^t\text{BuAsH}_2$ ratios.	156
Figure 5.21 Photographs of an 8 μl water droplet on the surface of VAs deposited <i>via</i> the APCVD of VOCl_3 and ${}^t\text{BuAsH}_2$.	157
Table 5.1 Experimental conditions used to deposit VAs films from the APCVD of VCl_4 and ${}^t\text{BuAsH}_2$.	135
Table 5.2 WDX analysis for VAs films deposited <i>via</i> the APCVD of VCl_4 and ${}^t\text{BuAsH}_2$ using substrate temperatures of 550 and 600 °C, and deposition time lengths of 60 and 120 seconds.	138
Table 5.3 Comparison of at.% contribution within a VAs film deposited <i>via</i> the APCVD of VCl_4 and ${}^t\text{BuAsH}_2$ at 600 °C and a TiAs film deposited <i>via</i> the APCVD of TiCl_4 and ${}^t\text{BuAsH}_2$ at 500 °C after etching for 1800 seconds.	140
Table 5.4 Water contact angle measurements (°) of VAs films deposited <i>via</i> the APCVD of VCl_4 and ${}^t\text{BuAsH}_2$.	146
Table 5.5 Experimental conditions for VAs films deposited <i>via</i> the APCVD of VCl_4 and ${}^t\text{BuAsH}_2$. Experiments highlighted in grey represent the VAs films on which analysis was conducted.	147
Table 5.6 WDX analysis for VAs films deposited <i>via</i> the APCVD of VOCl_3 and ${}^t\text{BuAsH}_2$ using a range of substrate temperatures, deposition time lengths	151

and VOCl_3 to ${}^t\text{BuAsH}_2$ ratios.

Table 5.7 Water contact angle measurements ($^\circ$) of VAs films deposited *via* the APCVD of VOCl_3 and ${}^t\text{BuAsH}_2$. **157**

Chapter 1

Introduction

Arsenic is the 20th most abundant of the elements within the earth's crust, 14th in seawater and 12th in the human body. Commercially, it has been used within agriculture, and more surprising medicine, however recent interest has concerned its potential within electronics.¹

Bulk transition metal arsenides are well studied, and although transition metal nitride and phosphide thin films are well researched and find important commercial applications, knowledge regarding transition metal arsenide thin films remains limited. Research into the transition metal arsenides, has until recently, been limited by the availability of suitably volatile precursors. However, with recent advances within precursor availability and deposition methods (for example aerosol assisted chemical vapour deposition (AACVD)), research into this area has now been facilitated.

This thesis describes the research into the deposition of titanium and vanadium arsenide thin films *via* aerosol assisted (AA), low pressure (LP) and atmospheric pressure (AP) chemical vapour deposition (CVD). The synthesis of new molecular precursors to TiAs films will be described, along with the full characterisation and functional testing of the deposited TiAs and VAs films. The introduction chapter will set the scene with regards to metal arsenide research, with bulk transition metal arsenide synthesis and deposition of transition metal arsenide thin films discussed.

1.1 Bulk Transition Metal Arsenides

1.1.1 Bulk Material Synthesis

Metal arsenides are known to exhibit compositions which range from M_9As to M_3As_7 , and have traditionally been synthesised *via* the direct combination of elemental arsenic

and transition metals at high temperatures.² Typically these reactions are conducted over several days or weeks to ensure that a homogenous single phase reaction product is achieved, however, due to the associated costs concerning both the high temperatures and time required for such reactions, alternative synthetic routes were sought; these alternate routes are described below.

1.1.1.1 Alternative Methods for Elemental Combination

Mechanical alloying provides an alternative route for the combination of elemental precursors without the need for high temperatures. During mechanical alloying intense deformation of the particles occurs, eliminating the need for component melting and thus high temperatures.^{3,4} However, similarly to the high temperature route, the number of accessible material phases is limited, with only mono- and di-arsenide synthesis possible.

A wider range of transition metal arsenide phases have successfully been synthesised using vapour transport,^{5,6} whereby single crystals of a compound are grown from its elements *via* a concentration gradient achieved by temperature differences.⁷ Additionally, transition metal rich arsenide phases have been synthesised *via* the arc-melting of monoarsenides, with the intentional loss of arsenic within a sealed system causing alteration of the compound stoichiometry, enabling the synthesis of phases unobtainable by traditional high temperature synthesis alone.⁸

1.1.1.2 Solid State Metathesis Routes

In addition to synthetic methods involving the direct combination of elements, transition metal arsenides have successfully been synthesised using Na_3As and metal halide *via* solid state metathesis (SSM) routes. SSM reactions are a variant on self propagating high temperature synthesis (SHS), and involve the reaction of an alkali metal or alkaline earth metal pnictide, chalcogenide, silicide or boride with a metal halide (*Eq. 1*). Similarly to SHS reactions, the reactions are rapid and external energy is required for reaction initiation only.⁹



M = Li, Na, K, Mg, Ca, Sr, Ba

E = B, Si, N, P, As, Sb, Bi, O, S, Se, Te

M' = Transition/main group/actinide metal

X = Halogen

The driving force of SSM reactions is the large lattice energy of the salt co-product produced, with the specific temperature reached during the exothermic reaction critical in determining which material phase is produced. SSM reactions are thought to occur by either total reduction to the elements followed by recombination, or a metathetical exchange of ions within a molten flux; the actual mechanism is believed to lie between the two.¹⁰

SSM reactions have been used for the synthesis of a variety of transition metal arsenides including TiAs, CrAs, Cu₃As, NbAs₂ and Zn₃As₂ at temperatures between 25 – 550 °C.¹¹ It is believed that the low temperature initiation of the reactions is a result of the low boiling point of the metal halides used, in addition to efficient reagent contact.¹² Advancement within the SSM method supports this, with reactions occurring spontaneously without the need for initiation when liquid metal precursors are used. It is believed that by employing the liquid metal halide, the high temperatures required for overcoming solid-state diffusion barriers are avoided. However, it was noted that spontaneous initiation was highly dependent upon the scale of the reaction.¹³

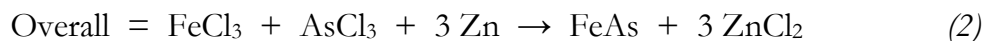
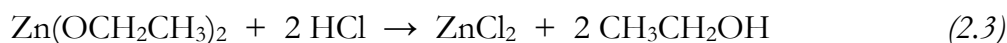
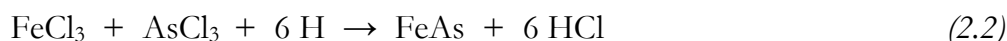
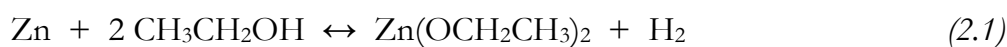
1.1.1.3 Liquid-Mediated Metathesis

Lower temperature synthetic routes to transition metal arsenides have additionally been achieved by liquid-mediated metathetical synthesis. Upon combining nickel and cobalt dihalides with sodium arsenide and refluxing in toluene for 48 hours, amorphous transition metal arsenides are produced. Refluxing in toluene has a similar effect to that of using liquid metal halides, whereby the surface area of interaction and hence reaction is increased, resulting in reactions at significantly lower temperatures.¹⁴

Liquid-mediated metathesis reactions have also proven successful in the synthesis of amorphous transition metal arsenides at room temperature *via* the reaction of metal halides and Na₃As in ammonia for 36 hours. Similarly to when using liquid metal halides, the reactions did not require initiation. It is believed that the liquid ammonia creates a change in the state of the precursors, with the reaction proceeding in both a solid state and in solution. The liquid ammonia acts as a heat sink and as such absorbs the reaction enthalpy, with the result being the formation of spherical nanocrystallites rather than material with sharp angles and faces as typically observed for SSM reactions.¹⁵

1.1.1.4 Reductive Routes

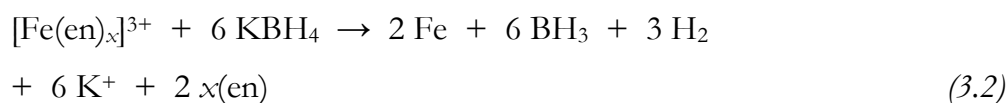
Iron arsenide (FeAs) has been synthesised *via* a recombination pathway reaction of FeCl₃ or FeCl₂·4H₂O, and AsCl₃ in the presence of Zn and ethanol at 150 – 180 °C for 12 hours. It is believed that during the process the reagents are reduced to their elements, with the following reaction pathway proposed (*Eq. 2.1 – 2.3*).¹⁶ In addition to FeAs, CoAs has also been successfully synthesised *via* this route.¹⁷



Employing this recombination reaction with ultrasound, transition metal arsenide synthesis can be conducted at room temperature. The ultrasonic waves cause cavitation resulting in bubble formation, which oscillate and grow until they eventually collapse *via* implosion. It is this implosion which causes shockwaves to dissipate through the solution, providing the energy for reaction and thus enabling reactions to occur at room temperature. Additionally, the ultrasonic waves remove unreactive

coatings from the reagents and cause large particles to break up, increasing the surface area for reaction.¹⁸

Reductive routes involving metal halides, arsenic, and KBH_4 in ethylenediamine at 100 °C have also proven successful. These reactions occur at temperatures as low as 100 °C, and result in crystalline transition metal arsenides after four hours. The role of the solvent is important here, with the following reaction mechanism proposed (using FeAs synthesis as an example) (*Eq. 3.1 – 3.3*).¹⁹ Additionally, other reduction routes have included the direct reduction of arsenates in hydrogen at relatively low temperatures (400 – 1050 °C).²⁰



1.1.1.5 Other Routes

Bulk transition metal arsenides have additionally been synthesised using the reactive-flux technique. Low melting caesium arsenide (Cs_3As_7) was used as the flux which when combined with Ti, Cr, Hf, Ta and Re in a 1:1 ratio within a quartz tube and heated to 900 – 950 °C under vacuum for 5 – 7 days, resulted in the formation of single crystals of TiAs_2 , CrAs , HfAs_2 , TaAs_2 and Re_3As_7 .²¹

Transition metal arsenides have also been synthesised as by-products during investigations involving arsenic scavengers for the removal of arsenic within shale oil. Nickel dithiocarbamate (DTC) was found to be an effective scavenger for a variety of arsenic species upon its thermal decomposition to produce the active catalyst NiS. Reaction of NiS with a variety of arsenic species typically found within shale oil, resulted in NiAsS formation, which on further reaction with H_2 , resulted in NiAs (**Figure 1.1**).²²

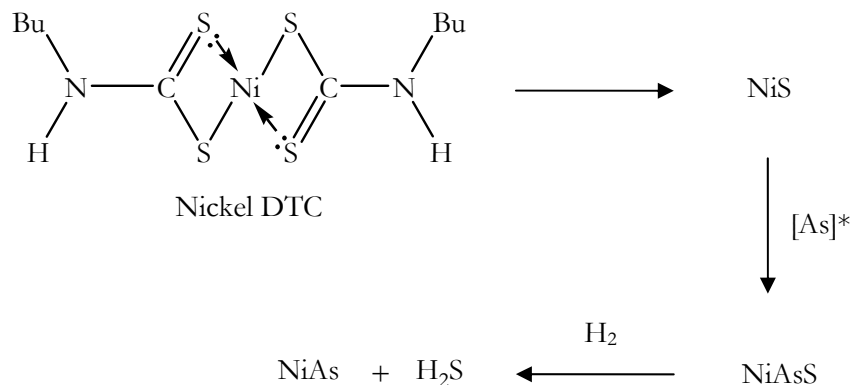


Figure 1.1 Synthesis of NiAs using the nickel dithiocarbamate arsenic scavenger.²²

1.1.1.6 Nanoparticles

In addition to bulk material, interest surrounds the formation of transition metal arsenide nanoparticles due to their exhibited size dependant physical properties, which may prove beneficial in applications such as sensing and data storage. Transition metal arsenide nanoparticles have been synthesised from the reduction of metal phosphate in a H₂/Ar atmosphere at high temperatures,²³ and additionally at lower temperatures *via* the reaction of triphenylarsine oxide and dimanganesedecacarbonyl in the presence of trioctylphosphine oxide.²⁴

1.1.2 General Structural Trends

Consideration of the structure of the 3d transition metal monoarsenides shows a competition between two crystal structures. Excluding ScAs which adopts the NaCl rock salt structure, both the hexagonal B8₁ (NiAs) and the orthorhombic B31 (MnP) structure exist; the B8₁ phase (or the closely related TiP) at the start and the end of the series, and the B31 phase (or the closely related structures of FeAs and CoAs) in between (**Figure 1.2 and Table 1.1**). Interestingly, MnAs exhibits both the NiAs and MnP structure depending upon the temperature, indicative that the two structures lie energetically close together.²⁵

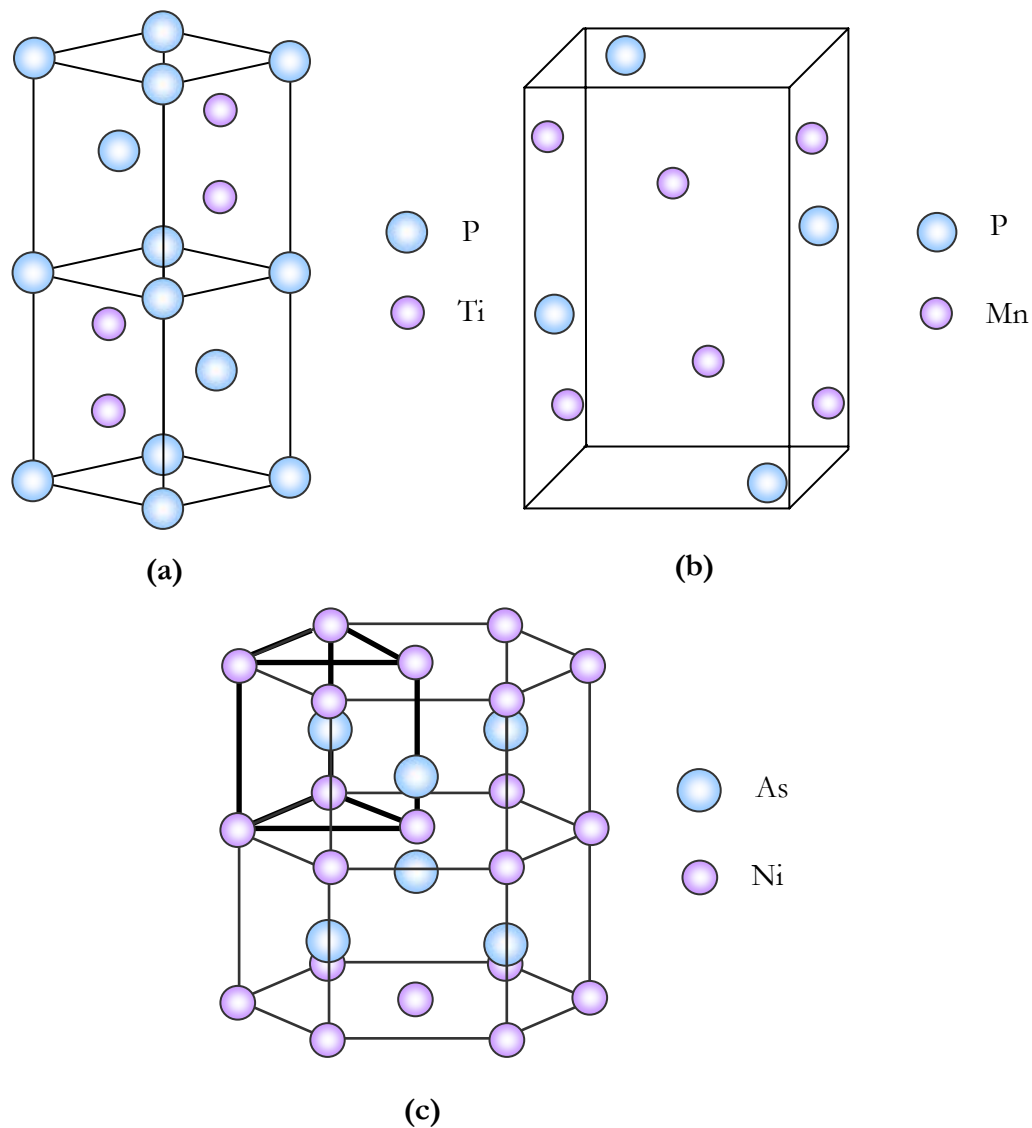


Figure 1.2 Crystal structures of the TiP (a), MnP (b) and NiAs (c) adopted by the 3d transition metal monoarsenides.

Table 1.1 Crystal structures exhibited by the 3d transition metal monoarsenides.

ScAs	TiAs	VAs	CrAs	MnAs	FeAs	CoAs	NiAs
NaCl	TiP	MnP		Both MnP and NiAs exhibited	MnP type		NiAs

Table 1.2 Average transition metal-arsenic bond lengths.

Transition metal arsenide	Average M-As bond length (Å)	Reference
TiAs	2.60	26
VAs	2.54	27
CrAs	2.51	28
MnAs	2.57	29
FeAs	2.44	30
CoAs	2.42	31
NiAs	2.44	32

1.1.2.1 The TiP Structure

TiAs is known to adopt the orthorhombic TiP crystal system, whereby two non-equivalent phosphorus atoms occupy octahedral and trigonal prismatic holes, with a difference of 0.11 Å between the two Ti-P bond lengths.^{26,33}

1.1.2.2 The MnP Structure

Similarly to TiP, MnP exhibits an orthorhombic unit cell. In MnP the phosphorus atoms are surrounded by six manganese atoms occupying the corners of a highly distorted triangular prism, with zigzag chains of phosphorus atoms extending in the *b*-direction.³⁴ As the MnP is considered to be a distorted NiAs structure, the two structures are energetically very similar.³⁵ This structure is adopted by the majority of the 3d transition metal arsenides, with VAs, CrAs, MnAs, FeAs and CoAs adopting this structure.

1.1.2.3 The NiAs Structure

NiAs exhibits a primitive hexagonal unit cell, whereby nickel atoms occupy octahedral sites between two layers of closely packed arsenic atoms.³²

1.1.3 Phase Transitions Between the MnP and NiAs Structures

MnAs adopts either the NiAs or MnP structure depending upon temperature. At approximately 313 K MnAs transforms from the ferromagnetic hexagonal NiAs structure, to the paramagnetic orthorhombic MnP structure.³⁶ Interestingly, although bulk MnAs demonstrates this structural phase transition, no equivalent structural phase transition was observed within synthesised MnAs nanocrystals; however, the ferromagnetic transition associated with this structure change was still observed, indicating that the magnetic properties are not sensitive to substantial structural changes.²⁴

In addition to MnAs, CrAs and CoAs also exhibit this MnP to NiAs phase transition, however the structural transitions occur at the significantly higher temperatures of approximately 1180 K and 1250 K respectively.³⁷

1.1.4 Potential Applications of Transition Metal Arsenides

There have been several studies concerning the use of transition metal arsenide materials within a variety of applications. They have been involved within investigations as a potential negative electrode material for use within Li-ion batteries,³⁸ superconductors,³⁹⁻⁴² and half-metallic materials, which could find application within the field of spintronics (**Section 1.2.1.1**).⁴³

1.2 The Potential of Transition Metal Arsenide Thin Films

As described above, bulk transition metal arsenides exhibit a range of potential industrially important properties. In particular, bulk manganese arsenide has received a great deal of interest due to its magnetic properties, and more recent interest in the material has concerned the effect of manganese doping of GaAs within III/V semiconductors.

1.2.1 III/V Semiconductors

As the name suggests, III/V semiconductors are semiconductors which consist of elements from both group three and five of the periodic table (also referred to as groups 13 and 15). Due to their exhibited band gaps and high electron mobility, they find use within a variety of applications including lasers, photovoltaics and LEDs, and as such are an industrially valuable group of compounds.



Traditionally, III/V semiconductors have been synthesised *via* the combination of GaMe₃, InMe₃ or AlMe₃ with the group V hydride gas (NH₃, PH₃ or AsH₃) (Eq. 4), however due to problems associated with use of the group V hydride gas, alternative precursors have been used as safer and more manageable alternatives (e.g. ^tBuAsH₂ and As(NMe₂)₃).⁴⁴⁻⁴⁷ In addition, single-source precursor routes to III/V semiconductors have also been investigated, which have involved precursors with either Lewis acid-base dative bonds,^{48,49} or direct σ -bonds between the group III and V elements.⁵⁰

Recent interest has sparked within the area of III/V semiconductors on the observation of ferromagnetism when heavily doped with manganese.⁵¹⁻⁵³ Initially it was believed that the ferromagnetism arose due to MnAs nanoparticles, however studies involving (In, Mn)As later indicated that the ferromagnetism was as a result of near neighbour Mn pairs.⁵⁴ Such ferromagnetic semiconductors hold potential within the field of spintronics and non-volatile transistors.

1.2.1.1 Spintronics

Spintronics is an emerging field which combines both information storage and information processing by exploiting both the quantum spin and charge of an electron. The magnetic phase of a ferromagnetic semiconductor can be controlled using an

electric field, with the material being either ferromagnetic or paramagnetic depending on whether a negative or positive voltage is applied.⁵²

1.2.1.2 Non-volatile Transistors

To enable computers to run for long periods of time without encountering heat generation problems, non-volatile transistors are required. Non-volatile transistors would be capable of retaining their logical state even when their power supply is rapidly switched on and off, circumventing problems associated with heat generation. Although synthesised ferromagnetic semiconductors have demonstrated the desired properties, their Curie temperatures are much lower than room temperature. As such, active research into raising the Curie temperature is underway.⁵³

1.3 Thin Film Deposition *via* CVD

Thin films often demonstrate properties which vary greatly from those associated with the bulk material, and as such, advances within thin film depositions are opening up a variety of research avenues, particularly within the design and development of novel materials such as the previously described III/V semiconductors. CVD is one of the main techniques used for the deposition of thin films.

1.3.1 Fundamentals of CVD

CVD can be defined in a number of ways, but in general, describes the deposition of a solid coating *via* a chemical transformation of gaseous precursors. Due to its non-line-of-sight deposition capabilities, low cost, and high throughput, CVD finds its greatest application within the electronics industry. Additionally, CVD enables high levels of control over uniformity, thickness and structure, whilst also maintaining highly pure deposits; as such, it is often the technique of choice for the deposition of thin films.

There are a great number of variants within the technique that is CVD, however it is generally considered that all CVD deposition processes undergo the following seven steps (**Figure 1.3**):

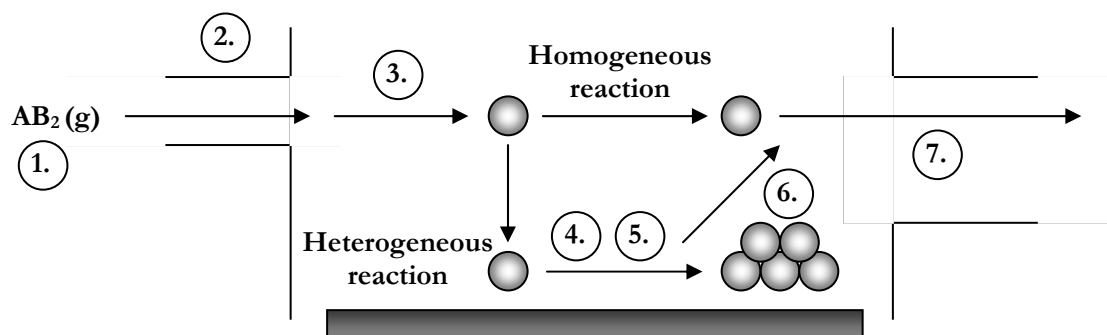


Figure 1.3 Schematic representing the seven steps involved in CVD. **1.** Generation of gaseous precursors. **2.** Transportation of gaseous reactants into the reaction chamber. **3.** Formation of intermediates following the gas phase reaction of the gaseous reactants. **4.** Deposition of material onto the substrate as a result of heterogeneous reactions. **5.** Diffusion of deposited material across the substrate resulting in the formation of crystallisation centres. **6.** Gaseous by-product removal as a result of diffusion/convection. **7.** Transportation of gaseous by-products and unreacted precursors away and out of the reaction chamber.

1.3.2 CVD Precursors

Typically within CVD, metals, metal hydrides and halides, and metalorganic compounds are employed as precursors. The choice of precursor will ultimately dictate what material is deposited, and the specific conditions required to achieve it. CVD can either be conducted using multiple precursors (dual-source) or a single precursor which contains all necessary components with desired bonds already preformed (single-source). Dual-source routes typically employ commercially available precursors and generally result in low film impurities, however, inconsistencies between vaporisation rates and deposition temperatures of multiple precursors typically results in non-stoichiometric films. Single-source precursors enable high control over film stoichiometries and generally decompose at lower substrate temperatures, however, films are typically deposited with a lower crystallinity content.

Early examples of CVD were limited due to the lack of commercially available precursors, and due to an increase in demand for CVD technology, along with an

increase in understanding of the processes involved, more complex precursors are now readily commercially available. To be suitable for use within CVD the precursor must:⁵⁵

- Be cost effective and readily available at a high purity.
- Exhibit low toxicity, flammability and explosivity.
- Exhibit a vapour which is stable at room temperature.
- Deposit at a suitable deposition rate and substrate temperature.
- Undergo thermal decomposition/chemical reaction at temperatures lower than its melting point.

Although gaseous precursors require only simple CVD reactors and their use can be readily metered, due to handling and storage problems associated with such precursors, the development of volatile liquid or solid precursors was necessary; within the deposition of metal arsenide films, $\text{As}(\text{NMe}_2)_3$ and ${}^t\text{BuAsH}_2$ have been two successful alternatives to the traditionally used AsH_3 .

1.3.2.1 Decomposition of $\text{As}(\text{NMe}_2)_3$

The arsenic precursor $\text{As}(\text{NMe}_2)_3$ decomposes at low temperature (*ca.* 300 °C) *via* β -hydride elimination to deposit films with low carbon contamination (**Figure 1.4**).⁵⁶

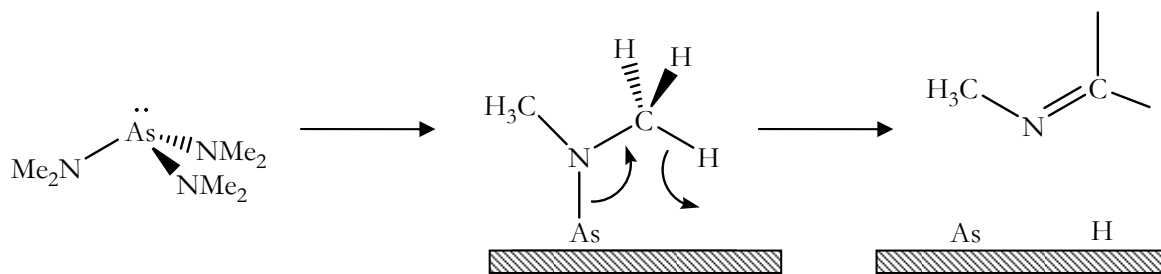


Figure 1.4 Heterogeneous decomposition of $\text{As}(\text{NMe}_2)_3$ *via* β -hydride elimination.⁵⁶

1.3.2.2 Decomposition of ${}^t\text{BuAsH}_2$

${}^t\text{BuAsH}_2$ remains the most successful liquid arsenic precursor to date, due to its convenient vapour pressure, and pyrolysis at lower temperatures than AsH_3 . Similarly

to $\text{As}(\text{NMe}_2)_3$, its decomposition is also thought to occur *via* β -hydride elimination, however for ${}^t\text{BuAsH}_2$ many other decomposition routes are proposed, including radical disproportionation and recombination reactions (**Figure 1.5**).⁵⁷⁻⁶⁰

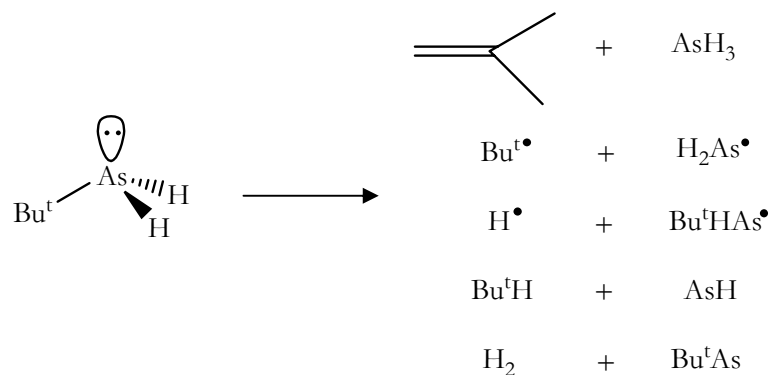


Figure 1.5 Proposed routes of decomposition of ${}^t\text{BuAsH}_2$.⁵⁷⁻⁶⁰

1.3.3 Types of CVD

In addition to the development of precursors, CVD methods have also advanced. A variety of CVD methods now exist, with all techniques demonstrating both weaknesses and strengths, with specific strengths being advantageous for specific applications. Although a range of CVD techniques are available, discussion will be limited here to aerosol assisted (AA), low pressure (LP) and atmospheric pressure (AP)CVD, which are the techniques which have been used within this thesis.

1.3.3.1 Aerosol Assisted (AA)CVD

Improvements within precursor delivery away from conventional CVD methods have widened the scope of materials achievable *via* CVD. AACVD is a variant of CVD which utilises aerosol formation of a precursor in solvent, to circumvent problems associated with low precursor volatility. The involatile precursor is dissolved in a suitable solvent/solvents, so as to enable precursor aerosol droplet formation when subjected to ultrasound, typically producing droplet sizes of 1 – 10 μm . With sufficient ultrasonic intensity, ejection of aerosol droplets from the liquid-gas interface results, which when introduced to a carrier gas flow, enables precursor movement within a

CVD system. Through control of ultrasound intensity and the rate of carrier gas flow, aerosol size and the amount of aerosol produced can be controlled respectively.⁶¹

Although AACVD involves a more complicated mechanism of deposition compared to conventional CVD methods due to solvent and precursor atomisation, evaporation and vapourisation considerations, it demonstrates the following advantages:⁶²

- It is a relatively low cost process.
- Typically involves the use of single-source precursors which allow for high control over specific material stoichiometries.
- Due to the formation of the aerosol droplets, precursor delivery is relatively simple.
- It can be conducted using a variety of CVD environments including low pressure (LP) and atmospheric pressure (AP)CVD, making the method extremely versatile.
- Enables high deposition rates.

When conducting AACVD, due to the nature in which the precursor delivery is facilitated by the specific solvent used, choice of solvent is vital. The solvent must:

- Exhibit a low viscosity.
- Exhibit a low vapour pressure.
- Allow for high solubility of the precursor.

1.3.3.2 Low Pressure (LP)CVD

As the name suggests LPCVD involves the deposition of materials at low pressures. LPCVD is typically employed when using hazardous or toxic vapour phases due to its reduced pressure safety aspect. LPCVD is the most commonly employed CVD method, and typically involves the heating of suitably volatile single- or dual-source precursors so as to cause sublimation/evaporation, thereby facilitating the movement

of precursor to the reaction chamber. LPCVD is capable of producing high quality epitaxial films at low deposition temperatures, and although more expensive equipment is required, these advantages often outweigh employing other CVD techniques.⁶²

1.3.3.3 Atmospheric Pressure (AP)CVD

APCVD involves the deposition of materials at atmospheric pressure and typically involves the use of commercially available precursors. Although single-source precursors can be used, due to volatility and contamination issues, dual-source precursors dominate within this technique. Unlike LPCVD, expensive equipment is not required, which in addition to its ease of incorporation within a continuous process system, makes APCVD an attractive industrial deposition technique.

1.4 Transition Metal Group 15 Films

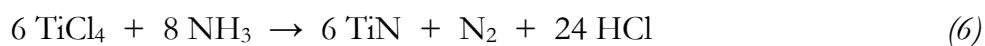
When considering the level of research conducted on transition metal group 15 films, great variation can be observed upon moving down the group. Whilst transition metal nitride films deposited *via* CVD, particularly that of titanium nitride, have been extensively studied, limited information concerning transition metal arsenide thin films is known. To illustrate this and to highlight the similar research pathways for group 15 transition metal films, films of the nitrides, phosphides and arsenides will be discussed.

1.4.1 Transition Metal Nitride Thin Films

Metal nitride thin films are known to exhibit a variety of interesting and commercially applicable chemical and physical properties. Traditionally these films have been prepared by the reactions of metal halides/hydrides with nitrogen and hydrogen (*Eq. 5*),⁶³ however due to the high temperatures required for these depositions, alternative routes were sought.

Upon substitution of N_2/H_2 with ammonia, it was discovered that metal nitride deposition could be conducted at significantly lower temperatures (550 °C) (*Eq. 6*). This discovery was not only beneficial with regards to the cost associated with the

deposition process, but also would allow for the deposition of metal nitrides onto a larger range of substrates (i.e. glass, plastics, silicon chips), thus enabling investigation into the use of metal nitrides within a wider variety of applications.⁶⁴



As less toxic and pyrophoric organometallic alternatives to the traditionally used metal halides and hydrides became available, other precursors for the deposition of metal nitrides were investigated. Metal dimethylamide precursors were of particular interest due to their direct metal-nitrogen σ -bonds, and upon investigation, amides of titanium, zirconium, niobium and tantalum were found to decompose in N_2/H_2 to their respective metal nitrides at temperatures as low as 300 – 500 °C; much lower than conventionally used routes.⁶⁵ It was later discovered that the introduction of ammonia to these systems allowed decompositions to be conducted at lower temperatures (200 – 400 °C), with depositions carried out successfully on a wide variety of substrates including silicon, vitreous carbon and boron.^{66,67} It was originally thought that these metal dimethylamido decompositions occurred *via* a single-source route, however, labelling studies later showed that the nitrogen incorporation was as a result of the NH_3 rather than the precursor (**Figure 1.6**).^{68,69} Single-source routes have however been successfully used in the deposition of transition metal nitride films, and have included silylamines such as $[\text{MCl}_4\{\text{NH}(\text{R})(\text{SiR}'_3)\}]$ which have proven to provide successful low temperature deposition routes.⁷⁰

In addition to conventional thermally activated (TA)CVD, transition metal nitride thin films have also been deposited *via* atomic layer deposition (ALD). ALD is a type of CVD in which depositions can occur at lower temperatures, and due to the alternate precursor introduction onto the substrate, greater control over film thickness

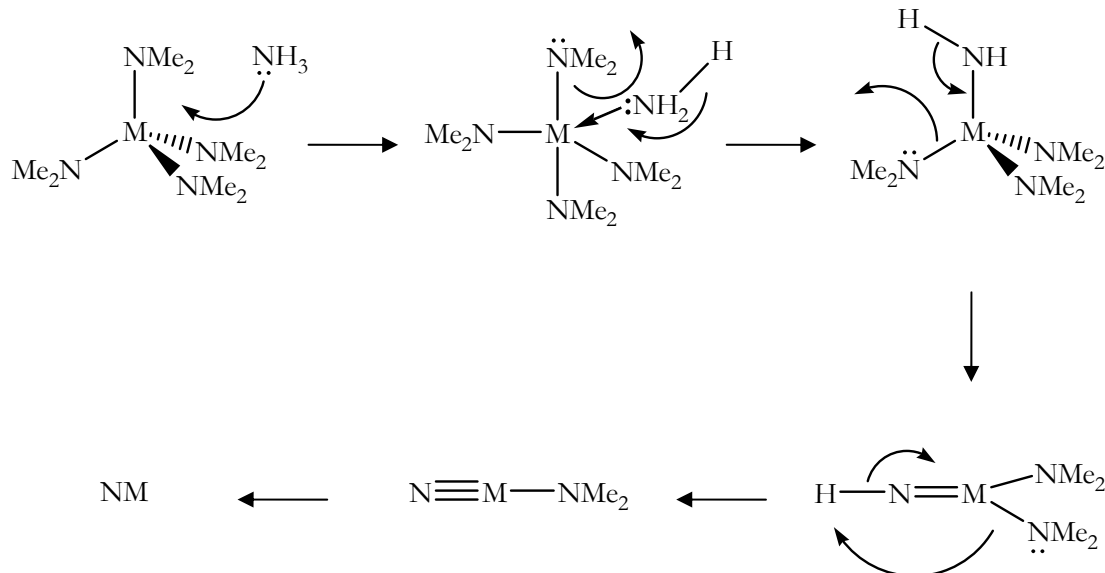


Figure 1.6 Proposed decomposition pathway of metal dimethylamide and ammonia in the deposition of MN films.⁶⁹

is possible. Similarly to TACVD, the ALD of metal chlorides and ammonia results in the deposition of metal nitrides, and on substitution of ammonia with 1,1-dimethylhydrazine within the ALD of metal halides, depositions can occur at temperatures as low as 200 °C.⁷¹

Although CVD provides the advantage of being a non-line of sight deposition method, physical vapour deposition (PVD) routes to transition metal nitrides have also been successful. Zirconium, niobium and molybdenum nitrides have successfully been deposited *via* reactive d.c. magnetron sputtering in an N₂/Ar atmosphere, with resultant films exhibiting similar hardness to films deposited *via* CVD.⁷²

Ion beam assisted deposition has also proven a successful deposition technique,⁷³ with lower deposition temperatures required when the pressure of the gas is reduced using a compact microwave ion source.⁷⁴

Out of all the transition metal nitrides, titanium nitride films are the most intensively studied, and have been successfully deposited *via* APCVD routes including the use of amido and imido titanium(IV) precursors (**1.1**),⁷⁵ and silylamines,⁷⁶ in addition to single-source LPCVD routes including use of titanium imido (**1.2**),^{77,78} and

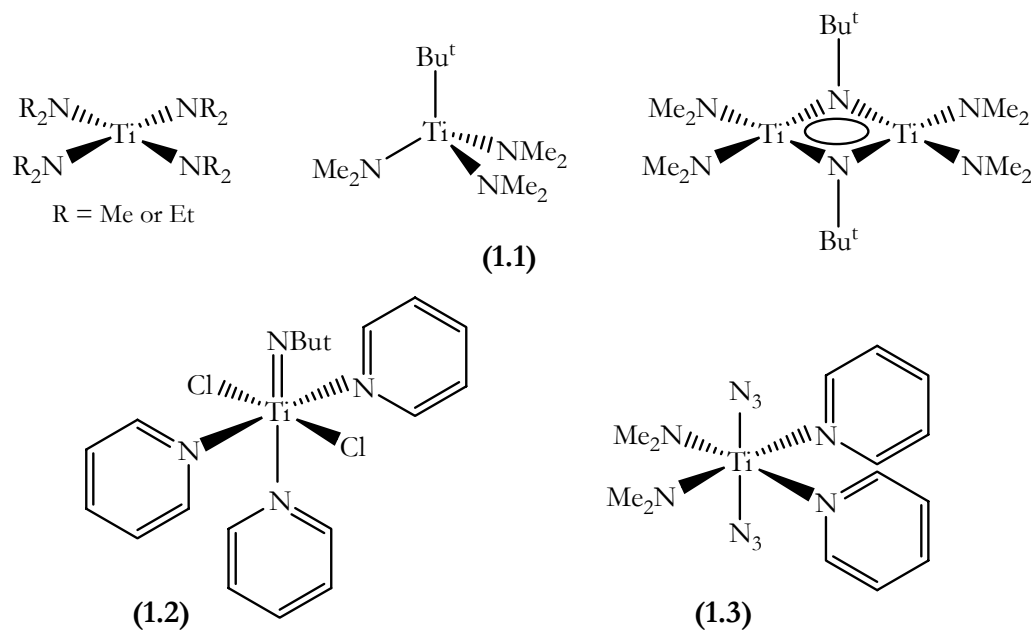


Figure 1.7 Selected examples of single-source precursors to titanium nitride.

titanium azide precursors **(1.3)**.^{79,80} Due to its high chemical resistivity, hardness and attractive gold appearance,^{81,82} TiN thin films are extremely industrially important, and as such, a great amount of research is conducted in this area.

1.4.2 Transition Metal Phosphide Thin Films

Like transition metal nitrides, transition metal phosphide films also exhibit useful properties such as high hardness and metallic conductivity, and consequently also find commercial applications. Resembling that of the transition metal nitride films, initial routes to transition metal phosphide films also involved the use of hydride and halide precursors, with high temperatures required for deposition. In addition, use of the highly hazardous PH_3 and PCl_3 were unfavoured, and as such, less toxic and more ‘user friendly’ precursors were desired.⁸³

Isobutylphosphine and tertiarybutylphosphine were the first reported organometallic phosphorus sources within the deposition of films *via* metal organic vapour phase epitaxy (MOVPE). Both precursors were used as liquids contained within atmospheric pressure bubblers, instantly identifying themselves as safer and more

manageable alternatives to traditionally used PH_3 and PCl_3 . Their use within MOVPE with trimethylindium allowed high quality InP films to be deposited. Although the films were not as pure as those obtained when using PH_3 , the potential for organometallic compounds to replace the traditionally used hazardous precursors was identified.⁸⁴

Preliminary research into organometallic precursors to transition metal phosphide films included the investigation of $[\text{Co}(\text{CO})_3(\text{PEt}_3)_2]$ as a potential single-source precursor to CoP films. The precursor was chosen for its 1:1 ratio of Co to P, and its decomposition in H_2 resulted in Co and Co_2P phases.⁸⁵ As research into potential organometallic single-source routes to transition metal phosphides proceeded, single-source routes became ever more successful. The precursor $[\text{Co}(\text{CO})_2\{\text{P}(\text{tBu})_2\text{H}\}(\text{NO})]$ (**1.4**) was found to not only be an excellent single-source precursor to CoP, but also demonstrated films comparable to those deposited *via* the dual-source MOCVD of tricarbonylnitrosylcobalt (TNC) and di-tertiarybutylphosphine. Although the dual-source route remained superior due to the faster associated deposition times, the potential for single-source routes to replace dual-source techniques was demonstrated (**Table 1.3**).⁸⁶

In addition to MOCVD, single-source precursors to transition metal phosphide films have also been successful *via* LP and AACVD methods.⁸⁷ Successful LPCVD has included the deposition of titanium phosphide thin films from $[\text{TiCl}_4(\text{Cy}^{\text{hex}}\text{PH}_2)_2]$,^{88,89} $[\text{TiCl}_4(\text{dppm})]$ (**1.5**) and $[\text{TiCl}_4(\text{dppe})]$ (where $\text{dppm} = \text{Ph}_2\text{PCH}_2\text{PPh}_2$ and $\text{dppe} = \text{Ph}_2\text{PCH}_2\text{CH}_2\text{PPh}_2$),⁹⁰ and AACVD, the deposition of GeP films using $[\text{Cy}^{\text{Hex}}\text{PGeCl}_3]$.⁹¹

Table 1.3 Selected data for CoP films deposited *via* the dual-source route of TNC and tBu_2PH , compared to that using the single-source precursor $[\text{Co}(\text{CO})_2\{\text{P}(\text{tBu})_2\text{H}\}(\text{NO})]$.⁸⁶

Precursor(s)	Deposition temp (°C)	Co/P	Growth rate (Å min ⁻¹)
TNC + $(\text{tBu})_2\text{PH}$	500	1.3	150
$[\text{Co}(\text{CO})_2\{\text{P}(\text{tBu})_2\text{H}\}(\text{NO})]$	500	1.2	6

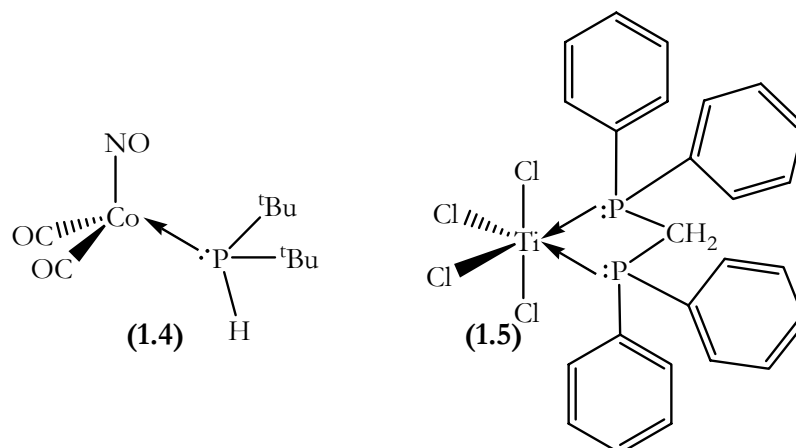


Figure 1.8 Selected examples of single-source precursor to transition metal phosphides.

Although single-source precursor routes to transition metal phosphide thin films have been successful, dual-source CVD routes are most commonly used. Following its initial success replacing PH_3 in the deposition of InP , tertiarybutylphosphine **(1.6)** has proven successful in the deposition of transition metal phosphides. The first dual-source route to TiP thin films was achieved *via* the dual-source APCVD of TiCl_4 and ${}^t\text{BuPH}_2$. It was proposed that the decomposition proceeded *via* the formation of a $[\text{TiCl}_4({}^t\text{BuPH}_2)_2]$ gas phase adduct, with the loss of HCl and ${}^t\text{BuCl}$. The deposition was rapid and resulted in high quality TiP films.⁹²

Following this, TiP films were later deposited *via* the dual-source APCVD of TiCl_4 and $\text{Cy}^{\text{hex}}\text{PH}_2$ **(1.7)**. Although similar in quality to TiP films deposited using ${}^t\text{BuPH}_2$, ${}^t\text{BuPH}_2$ was reported to be the superior phosphine precursor due to the shorter deposition times and lower bubbler temperatures associated with its use.⁹³ $\text{Cy}^{\text{hex}}\text{PH}_2$ has also been shown to be a successful phosphine precursor for the deposition of other metal phosphides including CrP films deposited *via* APCVD with $\text{Cr}(\text{CO})_6$,⁹⁴ and GeP ,⁹⁵ NbP , VP ,⁹⁶ TaP ,⁹⁷ and MoP ,⁹⁸ *via* APCVD with the corresponding metal halide.

In addition to the primary organometallic phosphorus precursors ${}^t\text{BuPH}_2$ and $\text{Cy}^{\text{hex}}\text{PH}_2$, PhPH_2 **(1.8)** has also been used in the deposition of both transition and main group metal phosphides. PhPH_2 has successfully been used to deposit TiP and SnP *via* APCVD with TiCl_4 and SnCl_4 respectively.^{93,99}

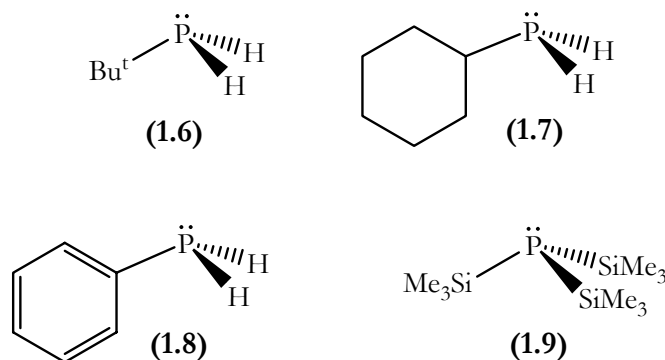


Figure 1.9 Selected examples of phosphine precursors used in the deposition of transition metal phosphides.

Tertiary phosphine precursors have also proven successful in the deposition of transition metal phosphides, with TiP deposited *via* the APCVD of TiCl₄ and P(SiMe₃)₃ (1.9).¹⁰⁰

An alternative route to the deposition of transition metal phosphides has involved adaptation of the transition metal precursor. As was the case for the metal nitrides, substitution of metal halides for dimethylamido equivalents resulted in the deposition of transition metal phosphide at lower deposition temperatures. Transition metal dimethylamido equivalents have been used in the deposition of VP,¹⁰¹ and additionally, TiP, ZrP and HfP thin films.¹⁰² In addition to dimethylamido precursors, VP has also been deposited using the vanadium precursor VOCl₃.⁹⁶

1.4.3 Transition Metal Arsenide Thin Films

Thin layers of transition metal arsenides have been reported as early as the 1950's,¹⁰³ with early deposition methods including vacuum evaporation. Although such techniques allowed for the deposition of transition metal arsenide thin films at low temperatures, a lack of suitable volatile arsenide precursors meant that research was limited.

With the increasing interest concerning the potential for III/V materials within future high speed electronic and optoelectronic devices, alternatives to the group V hydrides were sought so as to enable commercialisation of the materials. Similarly to

PH₃, AsH₃ also has problems associated with its toxicity, handling and storage, and as such, studies to find alternatives to AsH₃ were conducted. Trimethyl- and triethyl-arsine were two proposed candidates, however upon investigation, GaAs films deposited using these precursors exhibited poor morphology.¹⁰⁴

Following the successful substitution of PH₃ with ^tBuPH₂ and ⁱBuPH₂ within the deposition of InP,⁸⁴ analogous studies were conducted for GaAs. GaAs films deposited *via* the MOCVD of GaMe₃ and ^tBuAsH₂ were found to exhibit similar quality and surface morphology to those previously achieved using AsH₃, in addition to lower carbon incorporation and deposition temperatures.^{44,45}

With an increase in available organometallic alternatives to AsH₃, such as ^tBuAsH₂, and developments within CVD techniques, research into transition metal arsenide thin films was facilitated. However, even with these advancements, transition metal arsenide thin film knowledge still remains extremely limited, with only a few select examples reported in the literature.

1.4.3.1 Manganese Arsenide

Due to its first order transition from the hexagonal NiAs ferromagnetic structure to the orthorhombic MnP structure at 313 K,¹⁰⁵ MnAs is an important material due to its potential magnetic applications.¹⁰⁶ It was first deposited as a thin film in 1994 *via* the MOCVD of tricarbonylmethylcyclopentadienyl manganese and arsine, with depositions investigated over substrate temperatures 300 – 700 °C and conducted on GaAs (100) and sapphire substrates. MnAs was found to deposit between substrate temperatures of 350 – 650 °C to yield strongly adherent, polycrystalline films, with all deposits being identified as the 1:1 MnAs phase. Although deposition temperature affected the exhibited polycrystalline morphology of the films, all films were found to exhibit the abrupt magnetic change at the Curie temperature of 315 K, similar to that exhibited by the bulk material.¹⁰⁷

Further magnetic and electrical investigations of the deposited MnAs films indicated that the specific Curie temperature as exhibited by the films was highly dependent on film thickness, with a lower Curie temperature observed for thinner

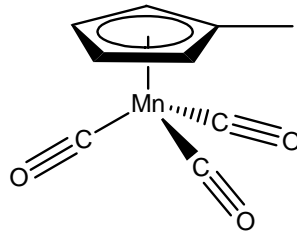


Figure 1.10 The structure of the manganese precursor tricarbonylmethylcyclopentadienyl manganese.

films. On heating through the phase transition, the MnAs film resistance was found to increase, however the increase in resistance was smaller than that observed for bulk material, which can be attributed to the lack of micro- and macro-cracks as found within the bulk material.¹⁰⁸

To determine the role of the substrate on the exhibited MnAs film properties, MnAs has also been deposited on GaAs (001), silicon and oxidised silicon. Observation of films deposited on the different substrates showed that MnAs grown on GaAs (001) exhibited grains parallel to GaAs, whilst those films grown on silicon and oxidised silicon exhibited randomly orientated grains. The Curie temperatures were found to alter with substrate, with higher Curie temperatures (340 K) reported for depositions of MnAs on GaAs (001), much higher than that exhibited by the bulk.¹⁰⁹

Following the observation that the Curie temperature of bulk MnAs material could be made closer to room temperature upon the partial atomic substitution of antimony for arsenic, deposition of the ternary compound $\text{MnAs}_{1-x}\text{Sb}_x$ was attempted. $\text{MnAs}_{1-x}\text{Sb}_x$ ($0 < x < 0.08$) was successfully deposited *via* the MOCVD of tricarbonylmethylcyclopentadienyl manganese, arsine and trimethylantimony, and as predicted, the Curie temperature of the film was found to decrease with an increase in antimony. The incorporation of approximately 4% antimony, resulted in a Curie temperature close to room temperature.¹¹⁰ In addition, it has also been reported that upon substituting a nonmagnetic atom (titanium) for manganese within $\text{Mn}_{1-x}\text{Ti}_x\text{As}$, a decrease in T_C is observed with an increase in titanium, approaching a T_C of 0 K when $x = 1$.¹¹¹

1.4.3.2 Iron Arsenide

At room temperature iron arsenide can exist in two phases, FeAs or Fe₂As.¹¹² Mono iron arsenide is a semiconducting material which adopts an orthorhombic structure, and when found as a nano-crystalline impurity within GaAs thin films, has been linked to light-enhanced magnetism.¹¹³ In addition, Fe-As based superconductors exhibit high T_c's (critical-temperatures), a property which had previously only been observed within the cuprates.¹¹⁴

FeAs thin films have been created *via* non-conventional deposition routes on steel substrates from their exposure to molten lead (2 wt. % antimony and 0.2 wt. % arsenic) at 500 °C for 100 hours. The FeAs films demonstrated thicknesses of approximately 40 μm, and were composed of two layers: an outer layer exhibiting an approximate 1:1 ratio of Fe:As, and an inner layer made up of Fe-As-Sb-Pb (**Figure 1.11**). It was proposed that the FeAs films were created as a result of steel corrosion within the molten lead bath under a highly reducing environment, resulting in migration of metals between the steel and the molten Pb-Sb-As. The FeAs films created were reported to be of similar quality to those deposited *via* liquid phase epitaxy methods.¹¹⁵

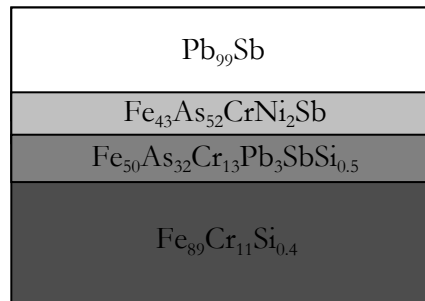


Figure 1.11 Schematic representing the different layers and relative compositions formed upon the exposure of a steel substrate to molten lead at 500 °C for 100 hours.¹¹⁵

1.4.3.3 Cobalt Arsenide

Cobalt arsenide is known to exist in several phases, including CoAs, Co₂As, Co₃As₂ and CoAs₃.^{6,112,116} The room temperature stable cobalt rich phases CoAs and Co₂As exhibit metallic behaviour, and have demonstrated themselves as potential Schottky or Ohmic

contact layers for III/V substrates.¹¹⁷ Initial studies concerning the deposition of CoAs thin films *via* organometallic routes involved investigation of the single-source precursor $[\text{Co}(\text{CO})_3(\text{AsEt}_2)_2]$. Similarly to the phosphine analogue, the precursor was chosen for its 1:1 ratio of Co to As and its zero valency cobalt centres, which were hoped to eliminate the need for a reducing agent. Unlike the phosphorus equivalent, the decomposition of $[\text{Co}(\text{CO})_3(\text{AsEt}_2)_2]$ between 70 °C and 300 °C resulted in decomposition to Co and Co_2As in both H_2 and N_2 atmospheres. From this, it was proposed that the Co-As bond was stronger than that of the Co-P, and focus for improvement of single-source routes should concern strengthening the Co-X bond.⁸⁵

Table 1.4 Selected data for CoAs films deposited *via* the dual-source route of TNC and $(^t\text{Bu})_2\text{AsH}$, compared to those deposited using the single-source precursors $[\text{Co}_2(\text{CO})_6\text{As}_2]$ and $[\text{Co}(\text{CO})_2\{\text{As}^t\text{Bu}_2\text{H}\}(\text{NO})]$.⁸⁶

Precursor(s)	Deposition temp (°C)	Co/As	Growth rate (\AA min^{-1})
TNC + $(^t\text{Bu})_2\text{AsH}$	400	1.1	330
$[\text{Co}_2(\text{CO})_6\text{As}_2]$	500	1.1	30
$[\text{Co}(\text{CO})_2\{\text{As}^t\text{Bu}_2\text{H}\}(\text{NO})]$	400	0.9	4
$[\text{Co}(\text{CO})_2\{\text{As}^t\text{Bu}_2\text{H}\}(\text{NO})]$	500	0.7	5

Studies involving single-source precursors to CoAs were later used to highlight the consistency between films deposited *via* single- and dual-source routes. The MOCVD of tricarbonylnitrosylcobalt (TNC) and di-tertiarybutyl arsine was compared to that of the use of the single-source precursors $[\text{Co}_2(\text{CO})_6\text{As}_2]$ **(1.10)** and $[\text{Co}(\text{CO})_2\{\text{As}^t\text{Bu}_2\text{H}\}(\text{NO})]$ **(1.11)** at deposition temperatures between 400 °C and 500 °C. All routes resulted in the successful deposition of polycrystalline CoAs, exhibiting material compositions Co_xAs_y ($x/y = 0.7 - 1.1$). Precursor routes containing nitrogen did not result in nitrogen contamination within the deposited CoAs films, however chlorine incorporation (0.4%) was noted within films deposited using $[\text{Co}_2(\text{CO})_6\text{As}_2]$,

arising as a result of its preparation. Overall, the CoAs films deposited *via* all routes demonstrated consistency, with the only notable major difference between the routes being the associated deposition time length. Whilst the dual-source route to CoAs remained the superior route due to its higher associated film growth rate, the potential for single-source precursors was established (**Table 1.4**).⁸⁶

Further investigation into potential single-source routes to CoAs (**Figure 1.12**), has included the single-source precursor $[\text{Co}(\text{CO})_4\{\text{AsN}(\text{tBu})\text{CH}_2\text{CH}_2\text{N}(\text{tBu})\}]$ (**1.12**), which successfully deposited CoAs films at substrate temperatures as low as 210 °C. All deposited CoAs films were polycrystalline and exhibited the stoichiometric 1:1 phase. In comparison to previously reported CoAs depositions, the conditions required were mild, which were thought to be as a result of both the increased dissociation energy of the Co-As σ -bond, and the clean removal of the chelating amine ligand.¹¹⁸

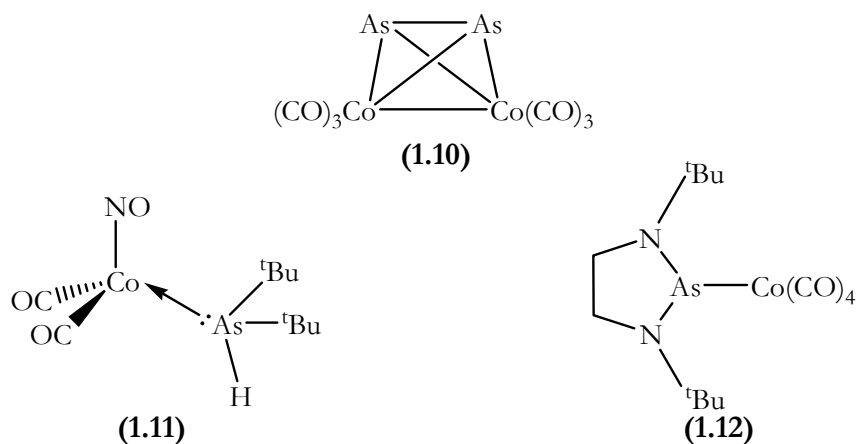


Figure 1.12 Successful single-source precursors to CoAs.

1.4.3.4 Cadmium Arsenide

Cadmium arsenide (Cd_3As_2) is an *n*-type narrow band gap semiconductor and its films have traditionally been deposited *via* vapour evaporation techniques (i.e. sublimation).¹¹⁹ Amorphous thin films of cadmium arsenide have been reported to condense onto mica, NaCl and KCl substrates below 400 K at 10^{-3} Pa, with the observation of an amorphous-crystalline transition upon film exposure to heat, or electron-beam treatment.¹²⁰ Upon increasing the vacuum to 6×10^{-5} Pa and employing

pulsed laser evaporation, crystalline cadmium arsenide thin films were successfully deposited at temperatures as low as 298 K.¹²¹

Structure and growth analysis of thin amorphous cadmium arsenide films indicated an island growth mechanism of deposition. It was reported that the observed morphology of the CdAs films was highly dependent on both the rate of deposition and the substrate temperature. The CdAs films were observed to alter from conical agglomerates, columnar structures, low density columnar structures and to a uniform film upon an increase in film deposition. Additionally, an increase in the substrate temperature also resulted in the disappearance of the columnar structure to give a more uniform film.¹²²

1.4.3.5 A Single-Source Attempt to SnAs

The tin arsenide complex $[\text{SnCl}_4(\text{AsPh}_3)_2]$ (**1.13**) was synthesised and used within AACVD in an attempt to deposit SnAs thin films. AACVD of the proposed single-source precursor using a substrate temperature of 430 °C, resulted in only SnO_2 and SnCl_2 being deposited. Due to the lack of arsenic within the deposited films, it was proposed that the decomposition route of (**1.13**) did not involve the loss of PhCl , but rather the sequential loss of Ph_3AsCl_2 and/or AsPh_3 .¹²³

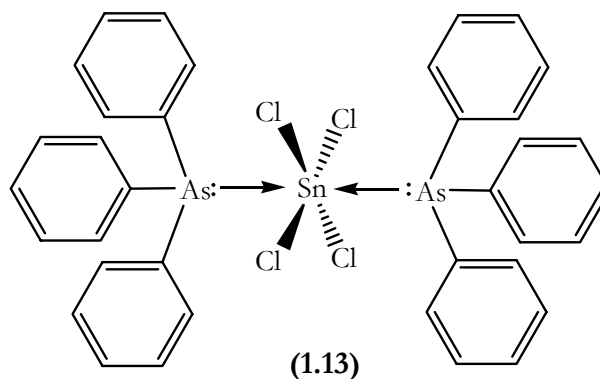


Figure 1.13 Tin arsenide adduct $[\text{SnCl}_4(\text{AsPh}_3)_2]$ used in an attempt to deposit SnAs *via* AACVD.¹²³

1.5 Thesis Aims

Apart from the key III/V materials and MnAs, FeAs, CoAs, CdAs as discussed, limited information concerning metal arsenides as thin films is known, particularly concerning the transition metal arsenides; which is surprising due to their attractive bulk material properties. Due to the limited research into the properties of early transition metal arsenides and lack of research into their deposition as thin films, research into the deposition of titanium and vanadium arsenide thin films *via* CVD will be discussed. Both single- and dual-source routes to titanium arsenide thin films have been attempted, whilst vanadium arsenide thin film research has solely involved dual-source APCVD. A range of both single- and dual-source precursors have been investigated where appropriate, with all successfully deposited films investigated for their physical properties. This thesis consists of the following chapters:

Chapter 2 – The Synthesis and Characterisation of Titanium(IV) Arsine Complexes – The synthesis and characterisation of titanium arsine adducts synthesised from the reaction of TiCl_4 with n equivalents of AsPh_3 (where $n = 1, 2$), $\text{Ph}_2\text{AsCH}_2\text{AsPh}_2$, ${}^t\text{BuAsH}_2$ and $\text{As}(\text{NMe}_2)_3$ in an attempt to synthesise single-source precursors to TiAs will be discussed.

Chapter 3 – Single-source CVD Attempts to TiAs – The titanium arsine adducts, as synthesised within chapter 2, were used within AA and LPCVD in an attempt to deposit TiAs thin films. The results of these attempted depositions will be discussed, in addition to thermal decomposition studies of the complexes.

Chapter 4 – The APCVD of TiAs Thin Films – The dual-source APCVD reactions of the titanium precursors TiCl_4 and $\text{Ti}(\text{NMe}_2)_4$, with ${}^t\text{BuAsH}_2$ will be described, with characterisation of the resultant films discussed.

Chapter 5 – The APCVD of VAs Thin Films – The dual-source APCVD reactions of the vanadium precursors VCl_4 and VOCl_3 , with ${}^t\text{BuAsH}_2$ will be described, with characterisation of the resultant films discussed.

Chapter 6 – Conclusions – The overall conclusions of the work described within this thesis will be discussed.

References

- 1 B. K. Mandal and K. T. Suzuki, *Talanta*, 2002, **58**, 201.
- 2 J. C. Bailor, H. J. Emelius, R. Nyholm and A. F. Trotman-Dickenson, *Comprehensive Inorganic Chemistry*, Pergamon Press, 1973.
- 3 L. Wee, P. G. McCormick and R. Street, *Scr. Mater.*, 1999, **40**, 1205.
- 4 Y. K. Kim and Y. W. Cho, *J. Alloys Compd.*, 2005, **393**, 211.
- 5 G. S. Saini, L. D. Calvert and J. B. Taylor, *Can. J. Chem.*, 1964, **42**, 630.
- 6 J. Ackermann and A. Wold, *J. Phys. Chem. Solids*, 1977, **38**, 1013.
- 7 H. Schafer, H. Jacob and K. Etzel, *Z. Anorg. Allg. Chem.*, 1956, **286**, 27.
- 8 S. Rundquist, B. Carlsson and C. O. Pontchour, *Acta Chem. Scand.*, 1969, **23**, 2188.
- 9 I. P. Parkin, *Chem. Soc. Rev.*, 1996, **25**, 199.
- 10 A. L. Hector and I. P. Parkin, *J. Mater. Chem.*, 1994, **4**, 279.
- 11 A. L. Hector and I. P. Parkin, *Z. Naturforsch., B: Chem. Sci.*, 1994, **49**, 477.
- 12 J. C. Fitzmaurice, A. Hector and I. P. Parkin, *J. Mater. Sci. Lett.*, 1994, **13**, 1.
- 13 A. L. Hector and I. P. Parkin, *Inorg. Chem.*, 1994, **33**, 1727.
- 14 C. J. Carmalt, D. E. Morrison and I. P. Parkin, *Polyhedron*, 2000, **19**, 829.
- 15 G. A. Shaw and I. P. Parkin, *Inorg. Chem.*, 2001, **40**, 6940.
- 16 X. M. Zhang, C. Wang, X. F. Qian, Y. Xie and Y. T. Qian, *J. Solid State Chem.*, 1999, **144**, 237.

- 17 C. Wang, X. F. Qian, X. M. Zhang, Y. D. Li, Y. Xie and Y. T. Qian, *Mater. Res. Bull.*, 1999, **34**, 1129.
- 18 J. Lu, Y. Xie, X. C. Jiang, W. He and G. A. Du, *J. Mater. Chem.*, 2001, **11**, 3281.
- 19 Y. Xie, J. Lu, P. Yan, X. C. Jiang and Y. T. Qian, *Chem. Lett.*, 2000, 114.
- 20 J. Gopalakrishnan, S. Pandey and K. K. Rangan, *Chem. Mater.*, 1997, **9**, 2113.
- 21 T. E. Albrecht-Schmitt, P. M. Almond, A. J. Illies, C. C. Raymond and C. E. Talley, *J. Cryst. Growth*, 2000, **217**, 250.
- 22 G. H. Singhal, L. D. Brown and D. F. Ryan, *J. Solid State Chem.*, 1994, **109**, 219.
- 23 K. L. Stamm, J. C. Gamo, G. Y. Liu and S. L. Brock, *J. Am. Chem. Soc.*, 2003, **125**, 4038.
- 24 K. Senevirathne, R. Tackett, P. R. Kharel, G. Lawes, K. Somaskandan and S. L. Brock, *ACS Nano*, 2009, **3**, 1129.
- 25 R. Podloucky, *J. Phys. F: Met. Phys.*, 1984, **14**, L145.
- 26 K. Bachmayer, H. N. Nowotny and A. Kohl, *Monatsh. Chem.*, 1955, **86**, 39.
- 27 K. Selte, A. Kjekshus and A. F. Andresen, *Acta Chem. Scand.*, 1972, **26**, 4057.
- 28 K. Selte, A. Kjekshus, W. E. Jamison, A. F. Andresen and J. E. Engebretsen, *Acta Chem. Scand.*, 1971, **25**, 1703.
- 29 R. H. Wilson and J. S. Kasper, *Acta Crystallogr.*, 1964, **17**, 95.
- 30 K. Selte and A. Kjekshus, *Acta Chem. Scand.*, 1969, **23**, 2047.
- 31 K. Selte and A. Kjekshus, *Acta Chem. Scand.*, 1971, **25**, 3277.
- 32 J. G. Thompson, A. D. Rae, R. L. Withers, T. R. Welberry and A. C. Willis, *J. Phys. C: Solid State Phys.*, 1988, **21**, 4007.
- 33 P. O. Snell, *Acta Chem. Scand.*, 1967, **21**, 1773.
- 34 S. Rundqvist, *Acta Chem. Scand.*, 1962, **16**, 287.
- 35 K. Motizuki, H. Ido, T. Itoh and M. Morifuji, Electronic structure and magnetism of 3d-transition metal pnictides, R. Hull, C. Jagadish, R. M. Osgood, J. Parisi, Z. Wang and H. Warlimont, Springer, Berlin, 2009.
- 36 S. Hilpert and T. Dieckmann, *Trans. Faraday Soc.*, 1912, **8**, 207.
- 37 K. Selte and A. Kjekshus, *Acta Chem. Scand.*, 1973, **27**, 3195.

- 38 M. P. Bichat, F. Gillot, L. Monconduit, F. Favier, M. Morcrette, F. Lemoigno
and M. Doublet, *Chem. Mater.*, 2004, **16**, 1002.
- 39 G. P. Meisner, H. C. Ku and H. Barz, *Materials Research Bulletin*, 1983, **18**, 983.
- 40 Y. Kamihara, T. Watanabe, M. Hirano and H. Hosono, *J. Am. Chem. Soc.*, 2008,
130, 3296.
- 41 A. L. Ivanovskii *Journal of Structural Chemistry*, 2009, **50**, 539.
- 42 D. G. Hinks *Nature Physics*, 2009, **5**, 386.
- 43 N. H. Long, M. Ogura and H. Akai, *J. Phys.: Condens. Matter*, 2009, **21**, 064241.
- 44 R. M. Lum, J. K. Klingert and M. G. Lamont, *Appl. Phys. Lett.*, 1987, **50**, 284.
- 45 C. H. Chen, C. A. Larsen and G. B. Stringfellow, *Appl. Phys. Lett.*, 1987, **50**, 218.
- 46 M. H. Zimmer, R. Hovel, W. Brysch, A. Brauers and P. Balk, *J. Cryst. Growth*,
1991, **107**, 348.
- 47 S. Goto, C. Jelen, Y. Nomura, Y. Morshita and Y. Katayama, *J. Cryst. Growth*,
1995, **150**, 568.
- 48 R. Nomura, Y. Seki and H. Matsuda, *J. Mater. Chem.*, 1992, **2**, 765.
- 49 A. C. Jones, A. K. Holliday, D. J. Colehamilton, M. M. Ahmad and N. D.
Gerrard, *J. Cryst. Growth*, 1984, **68**, 1.
- 50 H. S. Park, S. Schulz, H. Wessel and H. W. Roesky, *Chem. Vap. Deposition*, 1999,
5, 179.
- 51 F. Matsukura, H. Ohno, A. Shen and Y. Sugawara, *Phys. Rev. B: Condens. Matter*,
1998, **57**, R2037.
- 52 D. D. Awschalom and R. K. Kawakami, *Nature*, 2000, **408**, 923.
- 53 K. Ando, *Science*, 2006, **312**, 1883.
- 54 A. J. Blattner and B. W. Wessels, *Appl. Surf. Sci.*, 2004, **221**, 155.
- 55 CVD of nonmetals, W. S. Rees, 1996
- 56 A. C. Jones, *Chem. Soc. Rev.*, 1997, **26**, 101.
- 57 P. W. Lee, T. R. Omstead, D. R. McKenna and K. F. Jensen, *J. Cryst. Growth*,
1988, **93**, 134.
- 58 C. A. Larsen, N. I. Buchan, S. H. Li and G. B. Stringfellow, *J. Cryst. Growth*,
1989, **94**, 663.

- 59 M. Brynda, *Coord. Chem. Rev.*, 2005, **249**, 2013.
- 60 D. F. Foster, C. Glidewell, G. R. Woolley and D. J. Colehamilton, *Journal of Electronic Materials*, 1995, **24**, 1731.
- 61 X. H. Hou and K. L. Choy, *Chem. Vap. Deposition*, 2006, **12**, 583.
- 62 K. L. Choy, *Prog. Mater. Sci.*, 2003, **48**, 57.
- 63 J. P. Dekker, P. J. Vanderput, H. J. Veringa and J. Schoonman, *J. Electrochem. Soc.*, 1994, **141**, 787.
- 64 S. R. Kurtz and R. G. Gordon, *Thin Solid Films*, 1986, **140**, 277.
- 65 K. Sugiyama, S. Pac, Y. Takahashi and S. Motojima, *J. Electrochem. Soc.*, 1975, **122**, 1545.
- 66 R. M. Fix, R. G. Gordon and D. M. Hoffman, *J. Am. Chem. Soc.*, 1990, **112**, 7833.
- 67 R. Fix, R. G. Gordon and D. M. Hoffman, *Chem. Mater.*, 1991, **3**, 1138.
- 68 J. A. Prybyla, C. M. Chiang and L. H. Dubois, *J. Electrochem. Soc.*, 1993, **140**, 2695.
- 69 B. H. Weiller *J. Am. Chem. Soc.*, 1996, **118**, 4975.
- 70 P. Hasan, S. E. Potts, C. J. Carmalt, R. G. Palgrave and H. O. Davies, *Polyhedron*, 2008, **27**, 1041.
- 71 M. Juppo, M. Ritala and M. Leskela, *J. Electrochem. Soc.*, 2000, **147**, 3377.
- 72 H. A. Jehn, J. H. Kim and S. Hofmann, *Surf. Coat. Technol.*, 1988, **36**, 715.
- 73 Y. Gotoh, M. Nagao, T. Ura, H. Tsuji and J. Ishikawa, *Nucl. Instrum. Methods Phys. Res., Sect. B*, 1999, **148**, 925.
- 74 Y. Gotoh, H. Tsuji and J. Ishikawa, *Rev. Sci. Instrum.*, 2000, **71**, 1002.
- 75 R. M. Fix, R. G. Gordon and D. M. Hoffman, *Chem. Mater.*, 1990, **2**, 235.
- 76 A. Newport, C. J. Carmalt, I. P. Parkin and S. A. O'Neill, *J. Mater. Chem.*, 2002, **12**, 1906.
- 77 C. J. Carmalt, A. C. Newport, I. P. Parkin, A. J. P. White and D. J. Williams, *J. Chem. Soc., Dalton Trans.*, 2002, 4055.
- 78 C. J. Carmalt, A. Newport, I. P. Parkin, P. Mountford, A. J. Sealey and S. R. Dubberley, *J. Mater. Chem.*, 2003, **13**, 84.

- 79 C. J. Carmalt, A. H. Cowley, R. D. Culp, R. A. Jones, Y. M. Sun, B. Fitts, S. Whaley and H. W. Roesky, *Inorg. Chem.*, 1997, **36**, 3108.
- 80 C. J. Carmalt, S. R. Whaley, P. S. Lall, A. H. Cowley, R. A. Jones, B. G. McBurnett and J. G. Ekerdt, *J. Chem. Soc., Dalton Trans.*, 1998, 553.
- 81 W. Schintlmeister, O. Pacher, K. Pfaffinger and T. Raine, *J. Electrochem. Soc.*, 1976, **123**, 924.
- 82 J. Takadoum, H. H. Bennani and M. Allouard, *Surf. Coat. Technol.*, 1997, **88**, 232.
- 83 S. Motojima, T. Wakamatsu and K. Sugiyama, *J. Less-Common Met.*, 1981, **82**, 379.
- 84 C. H. Chen, C. A. Larsen, G. B. Stringfellow, D. W. Brown and A. J. Robertson, *J. Cryst. Growth*, 1986, **77**, 11.
- 85 M. E. Gross and J. Lewis, *J. Vac. Sci. Technol., B: Microelectron. Process. Phenom.*, 1988, **6**, 1553.
- 86 Y. Senzaki and W. L. Gladfelter, *Polyhedron*, 1994, **13**, 1159.
- 87 A. N. Gleizes, *Chem. Vap. Deposition*, 2000, **6**, 155.
- 88 T. S. Lewkebandara, J. W. Proscia and C. H. Winter, *Chem. Mater.*, 1995, **7**, 1053.
- 89 T. S. Lewkebandara and C. H. Winter, *Chem. Vap. Deposition*, 1996, **2**, 75.
- 90 C. S. Blackman, C. J. Carmalt, I. P. Parkin, L. Apostolico, K. C. Molloy, A. J. P. White and D. J. Williams, *J. Chem. Soc., Dalton Trans.*, 2002, 2702.
- 91 L. Apostolico, M. F. Mahon, K. C. Molloy, R. Binions, C. S. Blackman, C. J. Carmalt and I. P. Parkin, *Dalton Trans.*, 2004, 470.
- 92 C. Blackman, C. J. Carmalt, S. A. O'Neill, I. P. Parkin, L. Apostilco and K. C. Molloy, *J. Mater. Chem.*, 2001, **11**, 2408.
- 93 C. Blackman, C. J. Carmalt, I. P. Parkin, S. O'Neill, L. Apostolico, K. C. Molloy and S. Rushworth, *Chem. Mater.*, 2002, **14**, 3167.
- 94 C. S. Blackman, C. J. Carmalt, T. D. Manning, I. P. Parkin, L. Apostolico and K. C. Molloy, *Appl. Surf. Sci.*, 2004, **233**, 24.
- 95 R. Binions, C. J. Carmalt and I. P. Parkin, *Polyhedron*, 2003, **22**, 1683.
- 96 C. S. Blackman, C. J. Carmalt, S. A. O'Neill, I. P. Parkin, K. C. Molloy and L. Apostolico, *J. Mater. Chem.*, 2003, **13**, 1930.

- 97 C. S. Blackman, C. J. Carmalt, I. P. Parkin, S. A. O'Neill, K. C. Molloy and L. Apostolico, *Mater. Lett.*, 2003, **57**, 2634.
- 98 C. S. Blackman, C. J. Carmalt, T. D. Manning, S. A. O'Neill, I. P. Parkin, L. Apostolico and K. C. Molloy, *Chem. Vap. Deposition*, 2003, **9**, 10.
- 99 R. Binions, C. S. Blackman, C. J. Carmalt, S. A. O'Neill, I. P. Parkin, K. Molloy and L. Apostilco, *Polyhedron*, 2002, **21**, 1943.
- 100 C. S. Blackman, C. J. Carmalt, S. A. O'Neill, I. P. Parkin, L. Apostolico and K. C. Moloy, *Appl. Surf. Sci.*, 2003, **211**, 2.
- 101 C. S. Blackman, C. J. Carmalt, S. A. O'Neill, I. P. Parkin, K. C. Molloy and L. Apostolico, *Chem. Vap. Deposition*, 2004, **10**, 253.
- 102 C. S. Blackman, C. J. Carmalt, S. A. O'Neill, I. P. Parkin, L. Apostolico and K. C. Molloy, *Chem. Mater.*, 2004, **16**, 1120.
- 103 T. S. Moss *Proc. Phys. Soc. London, Sect. B*, 1950, **63**, 167.
- 104 D. M. Speckman and J. P. Wendt, *Appl. Phys. Lett.*, 1987, **50**, 676.
- 105 G. A. Gover, *Sov. Phys. Solid State*, 1986, **28**, 18.
- 106 R. Street, *Nature*, 1955, **175**, 518.
- 107 P. A. Lane, B. Cockayne, P. J. Wright, P. E. Oliver, M. E. G. Tilsley, N. A. Smith and I. R. Harris, *J. Cryst. Growth*, 1994, **143**, 237.
- 108 M. E. G. Tilsley, N. A. Smith, B. Cockayne, I. R. Harris, P. A. Lane, P. E. Oliver and P. J. Wright, *J. Alloys Compd.*, 1997, **248**, 125.
- 109 M. Bolzan, I. Bergenti, G. Rossetto, P. Zanella, V. Dediu and M. Natali, *J. Magn. Magn. Mater.*, 2007, **316**, 221.
- 110 P. A. Lane, P. J. Wright, B. Cockayne, P. E. Oliver, M. E. G. Tilsley, N. A. Smith and I. R. Harris, *J. Cryst. Growth*, 1995, **153**, 25.
- 111 H. Ido *J. Appl. Phys.*, 1985, **57**, 3247.
- 112 R. D. Heyding and L. D. Calvert, *Can. J. Chem.*, 1957, **35**, 449.
- 113 S. Haneda, S. Koshihara and H. Munekata, *Physica E*, 2001, **10**, 437.
- 114 Z. A. Ren and Z. X. Zhao, *Adv. Mater.*, 2009, **21**, 4584.
- 115 E. P. Loewen, G. N. Bisanz and K. L. Gilbert, *Thin Solid Films*, 2004, **457**, 313.
- 116 T. Siegrist and F. Hulliger, *J. Solid State Chem.*, 1986, **63**, 23.

-
- 117 C. C. Hsu, G. L. Jin, J. Ho and W. D. Chen, *J. Vac. Sci. Technol., A*, 1992, **10**,
1020.
- 118 F. R. Klingan, A. Miehr, R. A. Fischer and W. A. Herrmann, *Appl. Phys. Lett.*,
1995, **67**, 822.
- 119 S. E. Hiscocks and C. T. Elliott, *J. Mater. Sci.*, 1969, **4**, 784.
- 120 L. Zdanowicz, S. Miotkowska and M. Niedzwiedz, *Thin Solid Films*, 1976, **34**, 41.
- 121 J. J. Dubowski and D. F. Williams, *Thin Solid Films*, 1984, **117**, 289.
- 122 J. Jurusik and L. Zdanowicz, *Thin Solid Films*, 1986, **144**, 241.
- 123 M. F. Mahon, N. L. Moldovan, K. C. Molloy, A. Muresan, I. Silaghi-Dumitrescu
and L. Silaghi-Dumitrescu, *Dalton Trans.*, 2004, 4017.

Chapter 2

The Synthesis and Characterisation of Titanium(IV) Arsine Complexes

As previously mentioned (Section 1.3.2), single-source precursors circumvent problems associated with precursor volatility when used in conjunction with AACVD, and in addition, enable high levels of stoichiometric control. Few single-source precursors for the deposition of transition metal arsenides exist, with examples limited to CoAs, which has successfully been deposited *via* the MOCVD of $[\text{Co}(\text{CO})_2\{\text{As}(\text{tBu})_2\text{H}\}(\text{NO})]$,¹ and $[\text{Co}(\text{CO})_4\{\text{AsN}(\text{tBu})\text{CH}_2\text{CH}_2\text{N}(\text{tBu})\}]$.² This chapter describes the synthesis and characterisation of titanium arsine adducts synthesised from the reaction of TiCl_4 with n equivalents of AsPh_3 ($n = 1, 2$), $\text{Ph}_2\text{AsCH}_2\text{AsPh}_2$, tBuAsH_2 and $\text{As}(\text{NMe}_2)_3$, in an attempt to synthesise single-source precursors for the deposition of titanium arsenide.

2.1 Experimental

2.1.1 General Procedures and Instrumentation

All manipulations and reactions were conducted under a dry, oxygen-free dinitrogen atmosphere, using standard Schlenk techniques or an MBraun Unilab glovebox; nitrogen (99.9%, BOC) was used as supplied. All solvents employed were stored in alumina columns and dried using anhydrous engineering equipment, such that the water concentration was 5 – 10 ppm. AsPh_3 , $\text{Ph}_2\text{AsCH}_2\text{AsPh}_2$ and AsCl_3 were purchased

from Sigma Aldrich and $\text{As}(\text{NMe}_2)_3$, ${}^t\text{BuAsH}_2$ and $\text{Ti}(\text{NMe}_2)_4$ were kindly supplied by SAFC Hitech Ltd.; all reagents were used without further purification.

2.1.2 Physical Measurements

Microanalytical data were obtained at University College London (UCL) using an EA-440 horizontal load analyser supplied by Exeter analytical. ${}^1\text{H}$ and ${}^{13}\text{C}\{{}^1\text{H}\}$ NMR spectra were recorded using a Brüker AMX400 spectrometer and referenced to C_6D_6 (distilled over Na-benzophenone ketyl), with chemical shifts reported relative to SiMe_4 ($\delta = 0.00$). Cl^+ mass spectra were recorded using a Micromass ZABSE instrument. Single crystals were mounted on a glass fibre with silicon grease from Fomblin® vacuum oil with datasets collected on a Brüker SMART APEX CCD diffractometer using graphite-monochromated Mo- $\text{K}\alpha$ radiation ($\lambda_1 = 0.71073 \text{ \AA}$) at 150(2) K. Data reduction and integration was carried out with SAINT+,³ and absorption corrections applied using SADABS.⁴ All solutions and refinements were performed using PLATON,⁵ the WinGX package and all software packages within.⁶ All non-hydrogen atoms were refined using anisotropic thermal parameters and hydrogens were added using a riding model.

2.1.3 Synthesis of Titanium(IV) Arsine Complexes

2.1.3.1 Synthesis of $[\text{TiCl}_4(\text{AsPh}_3)]$ (2.1)

AsPh_3 (0.83 g, 2.7 mmol) was dissolved in toluene (20 cm^3) to give a clear colourless solution, which was added with stirring to a 1 M orange-red solution of TiCl_4 in toluene (2.7 cm^3 , 2.7 mmol). Upon the immediate introduction of the AsPh_3 solution, a permanent dark red solution developed. After the complete addition of the AsPh_3 solution, the reaction mixture was allowed to stir for approximately 30 minutes, prior to solvent removal under vacuum yielding a purple-pink solid **(2.1)** (yield 85%). Crystals of **(2.1)** with a suitable quality to conduct single crystal X-ray diffraction were grown *via* dichloromethane/hexane layering recrystallisation. **Analysis found (calc. for $\text{C}_{18}\text{H}_{15}\text{AsCl}_4\text{Ti}$):** C 41.78% (43.60); H 3.24% (3.05). **${}^1\text{H}$ NMR:** δ/ppm (C_6D_6 , 400.1

MHz) 7.6 (m, 6H, *m*-C₆H₅), 7.1 (m, 9H, *o*-C₆H₅ and *p*-C₆H₅). **¹³C{¹H} NMR:** δ/ppm (C₆D₆, 100.6 MHz) 137.0 (*i*-C), 133.99 (*o*-CH), 129.6 (*m*-CH), 129.23 (*p*-CH). **Mass Spec:** *m/z* (CI⁺, methane) 152 [AsPh]H⁺, 229 [AsPh₂]H⁺, 306 [AsPh₃]H⁺, 330, 353 [TiAsPh₃]H⁺, 360, 424 [TiCl₂AsPh₃]H⁺, 430, 458 [AsPh₂][AsPh₂]H⁺, 493 [TiCl₄AsPh₃]H⁺, 535 [AsPh₂][AsPh₃]H⁺, 612 [AsPh₃][AsPh₃]H⁺, 687. **Melting point:** 126 °C.

2.1.3.2 Synthesis of [TiCl₄(AsPh₃)₂] (2.2)

A 1M orange-red solution of TiCl₄ in toluene (1.3 cm³, 1.3 mmol) was added to a colourless solution of AsPh₃ (0.80 g, 2.61 mmol) in toluene (20 cm³) with stirring. The solution turned dark red immediately upon addition of the TiCl₄ solution. The reaction mixture was allowed to stir for approximately 30 minutes, prior to refluxing under nitrogen for 24 hours. After cooling to room temperature, the solvent was removed under vacuum to yield a purple-pink solid (**2.2**) (yield 85%). Crystals of (**2.2**) with a suitable quality to conduct single crystal X-ray diffraction were grown *via* dichloromethane/hexane layering recrystallisation. **Analysis found (calc. for C₃₆H₃₀As₂Cl₄Ti):** C 50.60% (53.90); H 3.78% (3.77). **¹H NMR:** δ/ppm (C₆D₆, 400.1 MHz) 7.4 (m, 12H, *m*-C₆H₅), 7.0 (m, 18H, *o*-C₆H₅ and *p*-C₆H₅). **¹³C{¹H} NMR:** δ/ppm (C₆D₆, 100.6 MHz) 138.3 (*i*-C), 134.0 (*o*-CH), 129.3 (*m*-CH), 129.1 (*p*-CH). **Mass Spec:** *m/z* (CI⁺, methane) 152 [AsPh]H⁺, 229 [AsPh₂]H⁺, 306 [AsPh₃]H⁺, 335, 458, 535. **Melting point:** 88 – 90 °C.

2.1.3.3 Reaction of TiCl₄ and Ph₂AsCH₂AsPh₂ (2.3)

A pale-yellow solution of Ph₂AsCH₂AsPh₂ (1.28 g, 2.7 mmol) in toluene (20 cm³) was added with stirring to a red-orange 1M solution of TiCl₄ in toluene (2.7 cm³, 2.7 mmol). A dark red-orange suspension formed immediately on addition of the Ph₂AsCH₂AsPh₂ solution. The reaction mixture was allowed to stir for approximately 30 minutes, prior to the removal of solvent under vacuum, yielding a bright orange solid (**2.3**) (yield 86%). **Analysis found (calc. for C₂₅H₂₂As₂Cl₄Ti):** C 45.08% (45.36); H 3.30% (3.35). Compound (**2.3**) was found to be insoluble in a variety of solvents (*e.g.*

dichloromethane, hexane, and toluene) and no satisfactory ^1H or $^{13}\text{C}\{^1\text{H}\}$ NMR spectra could be obtained. **Mass Spec:** m/z (Cl^+ , methane) 105, 155, 167 $[\text{AsPhCH}_2]\text{H}^+$, 191 $[\text{TiCl}_4]\text{H}^+$, 229 $[\text{AsPh}_2]\text{H}^+$, 245, 260, 306 $[\text{AsPh}_3]\text{H}^+$, 313 $[\text{TiClAsPh}_2]\text{H}^+$, 330, 395 $[\text{Ph}_2\text{AsCH}_2\text{AsPh}]\text{H}^+$, 472 $[\text{Ph}_2\text{AsCH}_2\text{AsPh}_2]\text{H}^+$, 501 $[\text{TiCl}_2\text{As}_2\text{Ph}_3]\text{H}^+$, 563, 639, 701, 869. **Melting point:** 116 – 118 °C.

2.1.3.4 Reaction of TiCl_4 and $^t\text{BuAsH}_2$ (2.4)

$^t\text{BuAsH}_2$ (0.36 cm³, 0.36 g, 2.69 mmol) was added to an orange-red 1M solution of TiCl_4 in toluene (2.7 cm³, 2.7 mmol) which was cooled to -78 °C. The solution turned bright red immediately upon the addition of the $^t\text{BuAsH}_2$ solution. The reaction mixture was allowed to stir whilst warming to room temperature, during which the deep red colour intensified. Once the reaction mixture had reached room temperature, it was cooled to -70 °C for approximately four weeks, after which time a dark brown solid was obtained. Excess reagents and solvents were carefully removed under vacuum, a small quantity of brown solid remained (**2.4**) (yield 16%). **^1H NMR:** δ/ppm (C_6D_6 , 400.1 MHz) 3.0 (broad s, 2H, AsH_2), 1.3 (s, 9H, $^t\text{BuAs}$). Due to difficulty in product manipulation and isolation, mass spectrometry analysis and melting point analysis were not possible for (**2.4**).

2.1.3.5 Synthesis of $[\text{TiCl}_3(\text{NMe}_2)(\mu\text{-NMe}_2)_2\text{AsCl}]$ (2.5)

A colourless solution of $\text{As}(\text{NMe}_2)_3$ (0.5 cm³, 0.62 g, 3 mmol) in toluene (10 cm³) was added *via* cannula to a red-orange 1M solution of TiCl_4 in toluene (2.7 cm³, 2.7 mmol). The solution turned dark green immediately upon addition of the $\text{As}(\text{NMe}_2)_3$ solution. After the addition, the reaction mixture was allowed to stir for approximately 30 minutes, prior to the removal of solvent under vacuum, yielding a dark-green solid (**2.5**) (yield 98%). Crystals of (**2.5**) with a suitable quality to conduct single crystal X-ray diffraction were grown *via* dichloromethane/hexane layering recrystallisation. **Analysis found (calc. for $\text{C}_6\text{H}_{18}\text{AsCl}_4\text{N}_3\text{Ti}$):** C 18.50% (18.16); H 4.81% (4.57); N 10.70% (10.59). **^1H NMR:** δ/ppm (C_6D_6 , 400.1 MHz) 3.7 (s, 6H, terminal NMe_2), 2.7 (s, 12H, $\mu\text{-NMe}_2$). **$^{13}\text{C}\{^1\text{H}\}$ NMR:** δ/ppm (C_6D_6 , 100.6 MHz) 53.7 (terminal NMe_2), 46.5 ($\mu\text{-NMe}_2$).

NMe₂). **Mass Spec:** m/z (CI⁺, methane) 84 [TiCl]H⁺, 105 [AsN₂]H⁺, 110 [TiClNC]H⁺, 120 [AsNMe₂]H⁺, 136 [AsNNMe₂]H⁺, 145 [TiCl₂NC]H⁺, 154 [TiCl₃]H⁺, 163 [TiCl₂NMe₂]H⁺, 170, 190 [TiCl₄]H⁺, 199 [TiCl₃NMe₂]H⁺, 208 [As(NMe₂)₃]H⁺, 216, 227, 75 254, 264, 300, 352, 365, 371, 406. **Melting point:** 95 – 97 °C.

2.1.3.6 Reaction of TiCl₄ with 2 As(NMe₂)₃ (2.6)

TiCl₄ (0.2 ml, 1.82 mmol) was dissolved in toluene (50 ml) to yield a clear orange solution. The TiCl₄ solution was added with stirring to As(NMe₂)₃ (0.6 ml, 3.61 mmol), resulting in the immediate formation of a bright red reaction solution upon its introduction. After the addition, the reaction mixture was allowed to stir for approximately 48 hours, during which time the dark red colour of the reaction solution intensified. After this time, the solvent was removed under vacuum to yield a dark-green solid (**2.6**) (yield 60%). **Analysis found (calc. for C₁₂H₃₆As₂Cl₄N₆Ti):** C 23.98% (23.86); H 5.99% (6.01), N 13.36% (13.91). **¹H NMR:** δ/ppm (C₆D₆, 400.1 MHz) 2.9 (s, 12H, terminal NMe₂), 2.5 (s, 24H, μ-NMe₂).

2.1.3.7 Reaction of [Ti(NMe₂)₄] with AsCl₃ (2.7)

A colourless solution of AsCl₃ (0.2 ml, 0.43 g, 2.37 mmol) in diethyl ether (20 ml) was added dropwise with stirring to a yellow solution of [Ti(NMe₂)₄] (0.6 ml, 0.57 g, 2.53 mmol) in diethyl ether (20 ml), resulting in the immediate formation of an orange solution, developing into a red solution upon its complete addition. After the addition, the reaction mixture was allowed to stir for approximately 48 hours, after which the solvent was removed under vacuum to yield a dark-green solid (**2.7**) (yield 93%). Crystals of (**2.7**) with a suitable quality to conduct single crystal X-ray diffraction were grown *via* dichloromethane/hexane layering recrystallisation. **Analysis found (calc. for C₈H₂₄AsCl₃N₄Ti):** C 19.41% (23.76%); H 5.03% (5.99%); N 10.51% (13.87%). **¹H NMR:** δ/ppm (C₆D₆, 400.1 MHz) 2.5 (s), 2.2 (s).

2.2 Results and Discussion

2.2.1 Reactions of TiCl_4 with AsPh_3

Due to the limited commercial availability of arsines, AsPh_3 was investigated as a potential arsenic source within a single-source precursor to titanium arsenide. Previous studies involving the single-source precursors $[\text{TiCl}_4(\text{L})_2]$ ($\text{L} = \text{PhPH}_2$, Ph_2PH and PPh_3) have proven unsuccessful in the deposition of titanium phosphide *via* LPCVD,⁷ however, the arsenide equivalents have never been investigated. In order to determine the suitability of AsPh_3 as the arsenic source within a single-source precursor to titanium arsenide, and to determine whether the titanium to arsenic ratio has any effect on the resultant film deposition, the complexes $[\text{TiCl}_4(\text{AsPh}_3)]$ (**2.1**) and $[\text{TiCl}_4(\text{AsPh}_3)_2]$ (**2.2**) were synthesised.

Reactions between metal halides and organometallic arsenic compounds were reported as early as 1924, where $[\text{TiCl}_4(\text{AsPh}_3)]$ was synthesised *via* the reaction of TiCl_4 with AsPh_3 . In this study, Pritchard reported the observation of heat evolution upon the reaction, and the precipitation of a red additive product identified as $[\text{TiCl}_4(\text{AsPh}_3)]$.⁸ In addition, $[\text{TiCl}_4(\text{AsPh}_3)_2]$ has also been reported in the literature,⁹ however, crystal structures for both the 1:1 and 1:2 titanium arsenide adducts have never been reported.

Following Pritchard's method, compounds (**2.1**) and (**2.2**) were synthesised in high yields (>85%). The ^1H NMR spectrum of (**2.1**) demonstrated two proton environments, with a multiplet at 7.6 ppm integrating to six protons assigned to *m*- C_6H_5 , and another multiplet observed at 7.1 ppm integrating to nine protons assigned to *o*- C_6H_5 and *p*- C_6H_5 . Coordination of the arsine to the titanium metal was apparent, due to the observed colour change during the reaction (*i.e.* the formation of a pink-purple precipitate) consistent with that previously reported,^{10,11} and additionally, due to the observed proton peak shifts in the ^1H NMR spectrum of (**2.1**) relative to that of the unbound arsine. The $^{13}\text{C}\{^1\text{H}\}$ NMR spectrum of (**2.1**) showed four carbon environments at 137.0 ppm, 134.0 ppm, 129.6 ppm and 129.2 ppm which can be assigned to *i*-C, *o*-CH, *m*-CH and *p*-CH, respectively.

Similarly to **(2.1)**, the ^1H NMR spectrum of **(2.2)** also demonstrated two proton environments, a multiplet at 7.4 ppm integrating to 12 protons and assigned to *m*-C₆H₅, and another multiplet at 7.0 ppm integrating to 18 protons and assigned to *o*-C₆H₅ and *p*-C₆H₅. The $^{13}\text{C}\{^1\text{H}\}$ NMR spectrum of **(2.2)** showed four carbon environments at 138.3 ppm, 134.0 ppm, 129.3 ppm and 129.1 ppm which can be assigned to *i*-C, *o*-CH, *m*-CH and *p*-CH, respectively.

The microanalytical data for compounds **(2.1)** and **(2.2)** showed a satisfactory hydrogen analysis for the formation of a 1:1 and a 1:2 adduct, however the carbon analyses were low. Due to the associated thermal decomposition during the microanalysis procedure, it is likely that the observed carbon was lower than expected due to the formation of metal carbide during the analysis; this observation has been previously reported for related TiCl₄ phosphorus compounds.⁷

The ^1H and $^{13}\text{C}\{^1\text{H}\}$ NMR spectra and microanalytical data for compounds **(2.1)** and **(2.2)** indicated the formation of the monomeric species [TiCl₄(AsPh₃)_{*n*}] where *n* = 1 or 2. To probe this further, and to investigate whether the *cis* or *trans* isomer of **(2.2)** had formed, the X-ray crystal structures of **(2.1)** and **(2.2)** were determined.

Compound **(2.1)** was found to crystallise into the monoclinic space group *P*2₁/*c*, with the titanium atom adopting a five-coordinate distorted trigonal bipyramidal geometry (**Figure 2.1**). It is monomeric in the solid state (as suggested by ^1H , $^{13}\text{C}\{^1\text{H}\}$ NMR spectroscopy and microanalysis), with the As atom of the AsPh₃ group and a chlorine atom occupying axial positions, and three chlorine atoms located in equatorial positions. A Ti-As bond length of 2.7465(13) Å was observed (**Table 2.1**), which is approximately equal to the sum of the independent atomic radii of titanium and arsenic (1.47 and 1.25 Å respectively) indicative of a weak Ti-As dative bond.

Compound **(2.2)** crystallised into the triclinic space group *P*-1, and was found to lie on an inversion centre in the unit cell, adopting a centrosymmetric, octahedral *trans*-[(Ph₃As)₂TiCl₄] geometry (**Figure 2.2**) which has previously been observed for the OsBr₄,¹² and SnCl₄ analogues.¹³ Compound **(2.2)** was found to exhibit a Ti-As bond length of 2.7238(7) Å, which was similar to that reported for **(2.1)**. All other bond

distances and angles of **(2.2)** were found to be similar to related complexes (**Table 2.2**), with the octahedral coordination geometry exhibited by **(2.2)** expected.

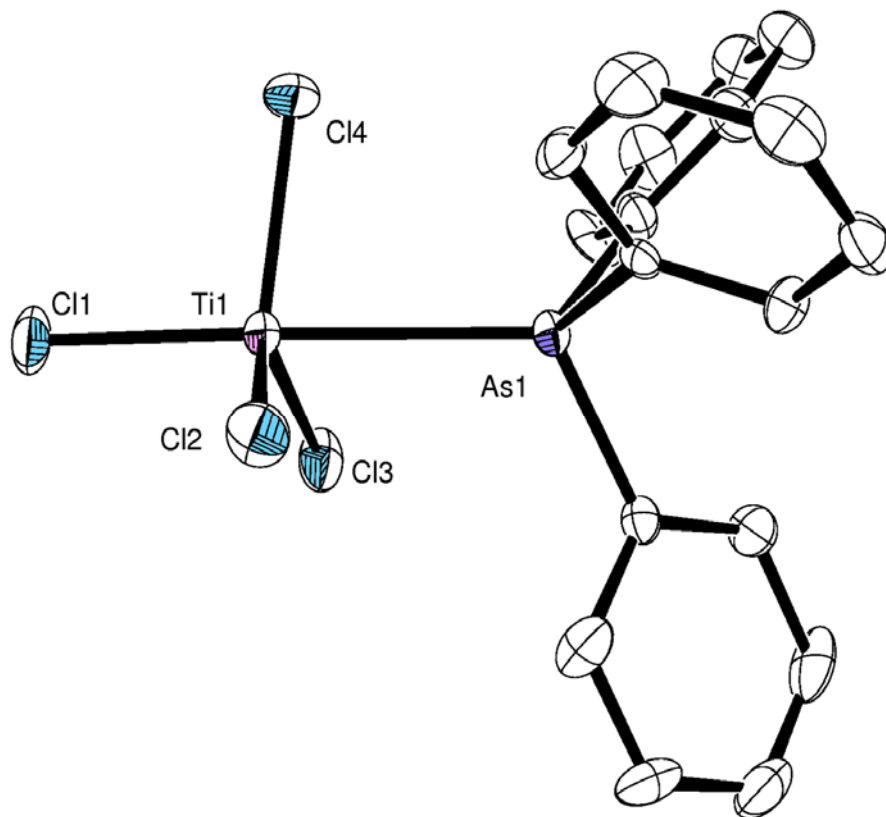


Figure 2.1 ORTEP representation of $[\text{TiCl}_4(\text{AsPh}_3)]$ (**2.1**) with thermal ellipsoids at the 50% probability level. Hydrogen atoms are omitted for clarity.

Table 2.1 Selected bond lengths (Å) and angles (°) for $[\text{TiCl}_4(\text{AsPh}_3)]$ (**2.1**).

Bond lengths (Å)		Bond angles (°)	
Ti(1)-As(1)	2.7465(13)	Cl(1)-Ti(1)-As(1)	175.41(8)
Ti(1)-Cl(1)	2.244(2)	Cl(2)-Ti(1)-As(1)	83.95(6)
Ti(1)-Cl(2)	2.185(2)	Cl(3)-Ti(1)-As(1)	81.02(6)
Ti(1)-Cl(3)	2.220(2)	Cl(4)-Ti(1)-As(1)	82.86(6)
Ti(1)-Cl(4)	2.193(2)		

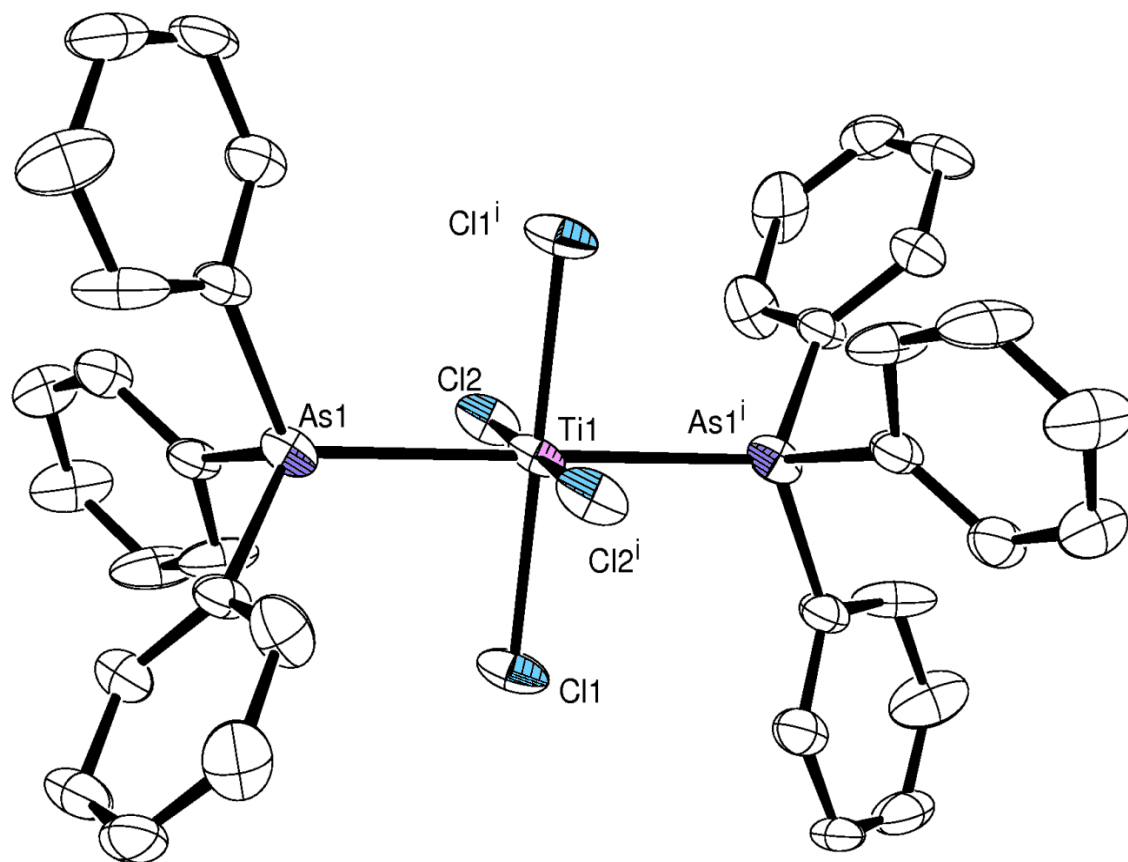


Figure 2.2 ORTEP representation of $[\text{TiCl}_4(\text{AsPh}_3)_2]$ (**2.2**) showing one of the two orientations of the disordered AsPh_3 group. Thermal ellipsoids are at the 50% probability level, with hydrogen atoms omitted for clarity. Symmetry transformations used to generate equivalent atoms: $1^i -x + 1, -y + 2, -z + 2$.

Table 2.2 Selected bond lengths (Å) and angles (°) for $[\text{TiCl}_4(\text{AsPh}_3)]$ (**2.2**).

Bond lengths (Å)		Bond angles (°)	
Ti(1)-As(1)	2.7238(7)	Cl(1)-Ti(1)-As(1)	86.68(4)
Ti(1)-Cl(1)	2.2713(11)	Cl(1)-Ti(1)-As(1 ⁱ)	93.32(4)
Ti(1)-Cl(2)	2.2719(11)	As(1)-Ti(1)-As(1 ⁱ)	180.0
		Cl(2)-Ti(1)-As(1)	90.36(4)
		Cl(2)-Ti(1)-As(1 ⁱ)	89.64(4)

2.2.2 The Reaction of TiCl_4 with $\text{Ph}_2\text{AsCH}_2\text{AsPh}_2$ (**2.3**)

The adduct $[\text{TiCl}_4(\text{Ph}_2\text{PCH}_2\text{PPh}_2)]$ has previously been reported as a successful single-source precursor to titanium phosphide *via* LPCVD,⁷ and it was hoped that similar success would be observed for the arsenide equivalent. As such, the reaction between TiCl_4 and $\text{Ph}_2\text{AsCH}_2\text{AsPh}_2$ was conducted, with $[\text{TiCl}_4(\text{Ph}_2\text{AsCH}_2\text{AsPh}_2)]$ (**2.3**) synthesised in high yield (>85%).

^1H NMR spectroscopy was not conducted on (**2.3**) due to insolubility issues (*e.g.* in dichloromethane, hexane and toluene), however, the microanalytical data for (**2.3**) was indicative of the formation of a 1:1 adduct, with satisfactory hydrogen and carbon analyses. Although a crystal structure for (**2.3**) could not be obtained, and the geometry of (**2.3**) could not be determined by IR spectroscopy due to partial decomposition during analysis, it is believed that a *cis*-octahedral geometry, similar to that observed for the phosphine analogue $[\text{TiCl}_4(\text{Ph}_2\text{PCH}_2\text{PPh}_2)]$, would be adopted (**Figure 2.3**); this additionally was also reported as an orange-red compound synthesised in high yield.¹⁴

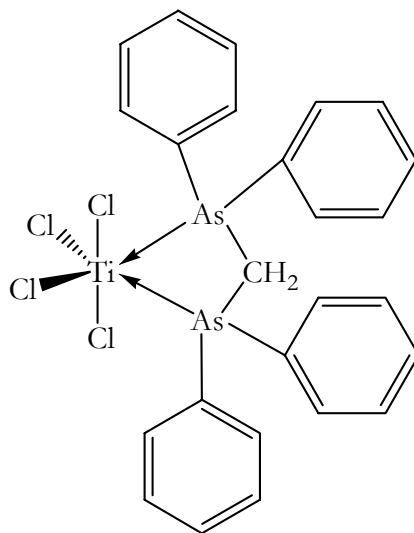


Figure 2.3 Proposed structure of (**2.3**) synthesised *via* the 1:1 reaction of TiCl_4 and $\text{Ph}_2\text{AsCH}_2\text{AsPh}_2$.

2.2.3 The Reaction of TiCl_4 with ${}^t\text{BuAsH}_2$ (2.4)

As previously mentioned, ${}^t\text{BuAsH}_2$ has proven to be a successful alternative to the traditionally used group V hydrides within film deposition, and has been used in the deposition of GaAs.^{15,16} Unlike compounds (2.1) – (2.3) which possess phenyl groups which could lead to high levels of carbon incorporation upon decomposition, use of the primary arsine ${}^t\text{BuAsH}_2$ with its potentially more efficient decomposition route¹⁷⁻¹⁹ should lead to lower levels of carbon incorporation within deposited films. Consequently, its use with TiCl_4 as a potential single-source precursor to titanium arsenide has been investigated.

${}^t\text{BuAsH}_2$ was reacted with one equivalent of TiCl_4 in toluene to yield a dark red solution, thought to be formation of the adduct $[\text{TiCl}_4({}^t\text{BuAsH}_2)_n]$ (2.4). Due to the high volatility exhibited by (2.4), isolation attempts *via* solvent removal in *vacuo* resulted in the loss of the compound to the vacuum trap. In order to facilitate product isolation, the reaction solution was kept at $-70\text{ }^\circ\text{C}$ for a few days, after which time a dark brown product was isolated (2.4). The ${}^1\text{H}$ NMR spectrum of (2.4) contained two proton environments at 1.3 and 3.0 ppm in a 9:2 ratio, corresponding to the ${}^t\text{Bu}$ and AsH_2 protons respectively. It was apparent from the ${}^1\text{H}$ NMR spectrum of (2.4) that an adduct had formed due to the upfield peak shift observed upon comparison to that of the free arsine. Due to the high volatility and air sensitive nature of (2.4), further characterisation was not possible, however the adduct $[\text{TiCl}_4({}^t\text{BuAsH}_2)_n]$ was believed to have formed (Figure 2.4).

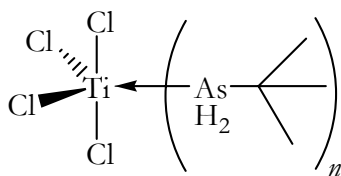


Figure 2.4 Proposed structure of (2.4) synthesised from the reaction of TiCl_4 with ${}^t\text{BuAsH}_2$.

2.2.4 Synthesis of $[\text{TiCl}_3(\text{NMe}_2)(\mu\text{-NMe}_2)_2\text{AsCl}]$ (2.5) and Investigation Into the Observed $\text{NMe}_2\text{-Cl}$ Exchange *via* the Synthesis of (2.6) and (2.7).

Similarly to ${}^t\text{BuAsH}_2$, $\text{As}(\text{NMe}_2)_3$ has also proven to be a successful alternative to the group V hydrides, with deposited films exhibiting low levels of carbon incorporation, due to its decomposition *via* β -hydride elimination.²⁰ Unlike the synthesis of complexes (2.1) – (2.4), the addition of $\text{As}(\text{NMe}_2)_3$ to the TiCl_4 solution resulted in the immediate formation of a dark green reaction solution. A simple 1:1 adduct was expected from the reaction, and its formation was suggested upon conduction of microanalysis. However the ${}^1\text{H}$ NMR spectrum of (2.5) displayed two proton environments at 2.7 and 3.7 ppm in a 2:1 ratio, indicative of the presence of both bridging and terminal NMe_2 groups. In order to determine the true structure of (2.5) its crystal structure was determined (Figure 2.5).

Compound (2.5) was found to crystallise into the monomeric space group $\text{P2}_1/n$, adopting a distorted octahedral titanium centre, consisting of three terminal Cl atoms, one terminally bound NMe_2 group, and two bridging dimethylamido groups. The crystal structure of (2.5) indicated that an exchange between one of the chlorine atoms from the TiCl_4 , and an NMe_2 group from $\text{As}(\text{NMe}_2)_3$ had occurred, with bonding occurring *via* the two nitrogen atoms, consequently resulting in the formation of the adduct $[\text{TiCl}_3(\text{NMe}_2)(\mu\text{-NMe}_2)_2\text{AsCl}]$ (2.5). Upon comparing the Ti-N bond lengths observed in (2.5) (Table 2.3) with that of a similar complex, both the terminal and bridging NMe_2 Ti-N bond lengths (1.864(2) Å and approximately 2.3 Å respectively) were found to be consistent with those reported for the complex $[\text{TiCl}_2(\text{NMe}_2)_2(\text{HNMe}_2)]$ (approximately 1.85 Å ($\text{C}_2\text{H}_6\text{N}$) and 2.25 Å ($\text{C}_2\text{H}_7\text{N}$)).²¹ This is the first time that an exchange of this type has been reported for arsenic, however similar observations have previously been reported during solvolysis reactions between TiCl_4 and aliphatic primary and secondary amines.²²

Although (2.5) lacks any titanium-arsenic bonds, thus making it an unsuitable single-source precursor to titanium arsenide, further investigations were carried out in

the hope of determining the reasoning behind this observed group exchange, with two further reactions being conducted; the reaction of TiCl_4 with two equivalents of $\text{As}(\text{NMe}_2)_3$ (**2.6**) and that of $[\text{Ti}(\text{NMe}_2)_4]$ with AsCl_3 (**2.7**).

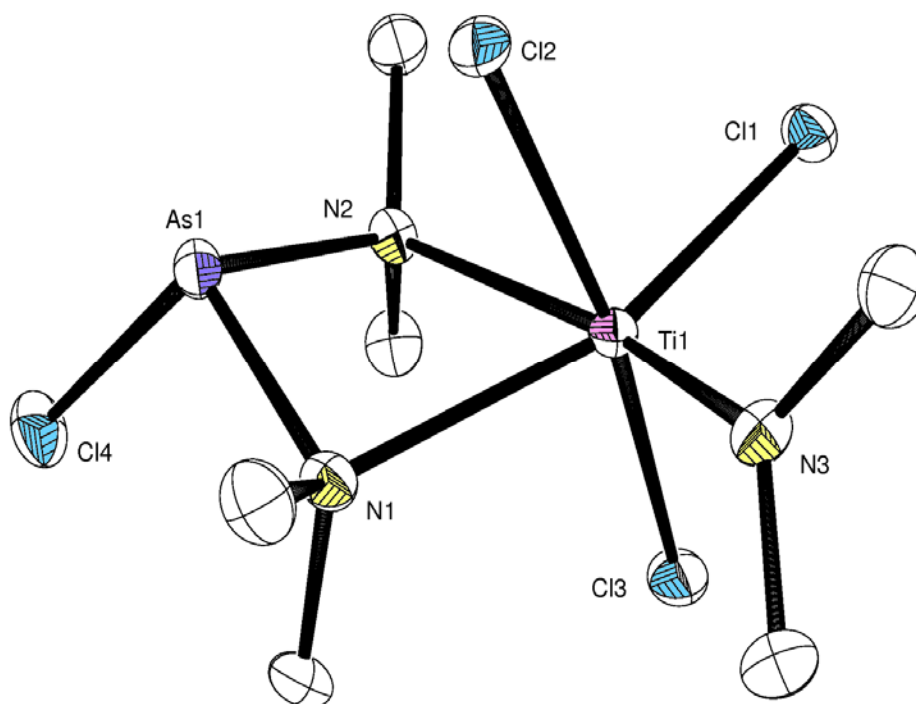


Figure 2.5 ORTEP representation of $[\text{TiCl}_3(\text{NMe}_2)(\mu\text{-NMe}_2)_2\text{AsCl}]$ (**2.5**) with thermal ellipsoids at the 50% probability level. Hydrogen atoms have been omitted for clarity.

Table 2.3 Selected bond lengths (Å) and angles (°) for $[\text{TiCl}_3(\text{NMe}_2)(\mu\text{-NMe}_2)_2\text{AsCl}]$ (**2.5**).

Bond lengths (Å)		Bond angles (°)	
N(1)-Ti(1)	2.323(2)	As(1)-N(1)-Ti(1)	93.89(8)
N(2)-Ti(1)	2.417(2)	N(1)-Ti(1)-N(2)	69.62(7)
N(3)-Ti(1)	1.864(2)	N(2)-As(1)-N(1)	89.60(9)
Cl(1)-Ti(1)	2.311(8)	As(1)-N(2)-Ti(1)	91.90(8)
Cl(2)-Ti(1)	2.3814(8)	N(3)-Ti(1)-N(2)	165.86(9)
Cl(3)-Ti(1)	2.3004(8)	N(2)-As(1)-Cl(4)	99.97(7)
Cl(4)-As(1)	2.2075(7)		

2.2.4.1 The reaction of TiCl_4 and 2 $\text{As}(\text{NMe}_2)_3$ (**2.6**)

In order to determine whether a similar exchange observed in the formation of (**2.5**) (the 1:1 reaction product) would occur when two equivalents of $\text{As}(\text{NMe}_2)_3$ were reacted with TiCl_4 , the 1:2 reaction was conducted (**2.6**).

Similarly to (**2.5**), the microanalysis of (**2.6**) indicated the formation of a 1:2 complex, however again upon inspection of the ^1H NMR spectrum, two proton environments in a 2:1 ratio were observed, with peaks occurring at 2.5 and 2.9 ppm, once again indicating the presence of both bridging and terminal NMe_2 groups.

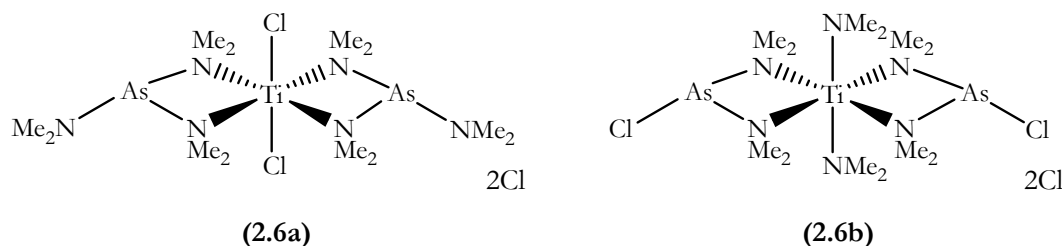


Figure 2.6 Schematic representing two potential structures adopted by (**2.6**).

It was unclear at this stage the exact structure adopted by (**2.6**), with a number of potential structures proposed (**Figure 2.6**). However, (**2.6b**) was believed to be the most likely structure due to the proton shifts observed in the ^1H NMR spectrum compared to that of free $\text{As}(\text{NMe}_2)_3$.

To investigate this further, (**2.6**) was reacted with an excess of NaBF_4 (a halide abstractor) which would cause proton shifts within the ^1H NMR of (**2.6**) if chlorine atoms were bound directly to the titanium centre. Upon treating (**2.6**) with an excess of NaBF_4 , the ^1H NMR spectrum was identical to that previously observed, with two proton environments at 2.4 and 2.9 ppm in an approximate 2:1 ratio. From this, it was deduced that (**2.6**) adopts the (**2.6b**) structure, whereby the titanium is coordinated to six dimethylamido groups, two terminal and four bridging, with two non-coordinating chloride ions surrounding the complex.

2.2.4.2 The reaction of $[\text{Ti}(\text{NMe}_2)_4]$ and AsCl_3 (**2.7**)

To assess the effect of swapping the substituents on the two reagents, and to determine whether a Cl, NMe₂ group exchange would still be observed, the reaction of $[\text{Ti}(\text{NMe}_2)_4]$ and AsCl_3 was conducted. Similarly to (**2.5**), a green solid was obtained suggesting similar titanium environments, although unlike both (**2.5**) and (**2.6**), a 1:1 complex was not confirmed by microanalysis. The ¹H NMR spectrum of (**2.7**) identified two singlet proton environments with peaks at 2.5 ppm, and 2.2 ppm in an approximate 2:1 ratio, which did not correspond to the presence of four dimethylamido groups. The recrystallisation of (**2.7**) produced a crystal structure exhibiting three proton environments (**Figure 2.7**), indicating that either the recrystallised product is a minor product from the reaction, or that its formation is as a result of the recrystallisation procedure itself (*i.e.* the formation of the coordinated amide). Although the exact products from the reaction of $[\text{Ti}(\text{NMe}_2)_4]$ and AsCl_3 were difficult to deduce, the crystal structure of (**2.7**) clearly shows chlorine bound to the titanium, indicative of a similar exchange to that observed in (**2.5**) having occurred.

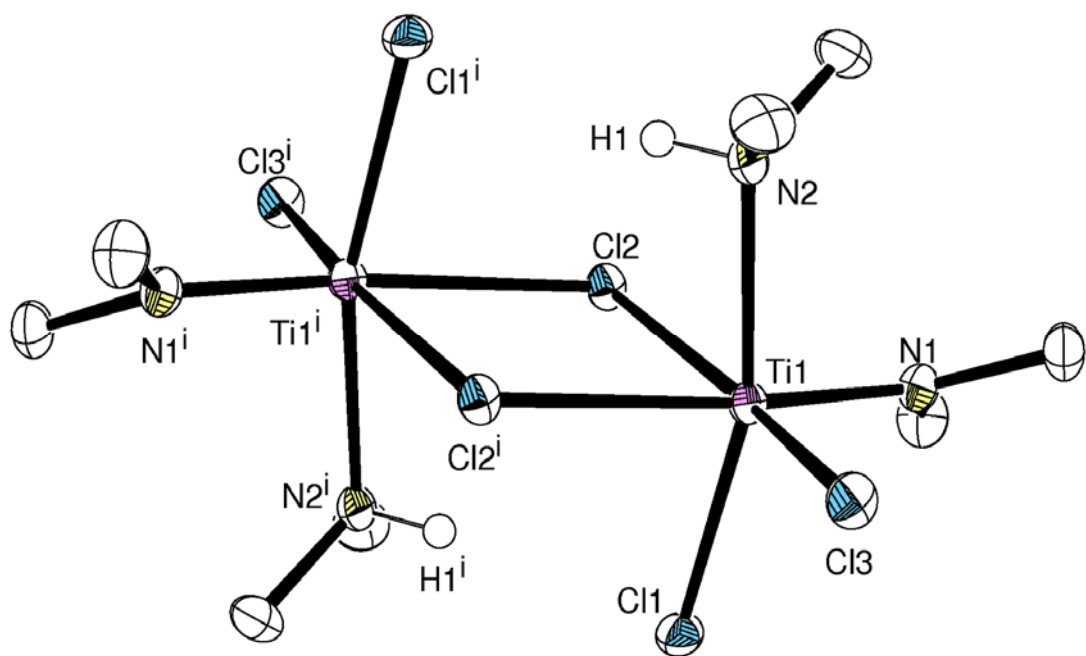


Figure 2.7 ORTEP representation of $[\text{TiCl}_2(\mu\text{-Cl})_2(\text{NMe}_2)(\text{NHMe}_2)]_2$ (**2.7**) with thermal ellipsoids at the 50% probability level. Hydrogen atoms (excluding the amine NH) have been omitted for clarity.

Table 2.4 Selected bond lengths (Å) and angles (°) for $[\text{TiCl}_2(\mu\text{-Cl})_2(\text{NMe}_2)(\text{NHMe}_2)]_2$ (**2.7**).

Bond lengths (Å)		Bond angles (°)	
Ti(1)-N(1)	1.8576(16)	N(1)-Ti(1)-N(2)	96.59(7)
Ti(1)-N(2)	2.2364(16)	Cl(1)-Ti(1)-N(1)	96.95(5)
Ti(1)-Cl(1)	2.3371(5)	Cl(1)-Ti(1)-Cl(2)	89.233(18)
Ti(1)-Cl(2)	2.4414(5)	Cl(2)-Ti(1)-Cl(3)	95.98(2)
Ti(1)-Cl(2 ⁱ)	2.6759(5)	Cl(2)-Ti(1)-Cl(2 ⁱ)	79.620(18)
Ti(1)-Cl(3)	2.2847(5)		

2.3 Conclusions

Four potential single-source precursors to titanium arsenide have been synthesised in typically high yields; $[\text{TiCl}_4(\text{AsPh}_3)]$ (**2.1**), $[\text{TiCl}_4(\text{AsPh}_3)_2]$ (**2.2**), $[\text{TiCl}_4(\text{Ph}_2\text{AsCH}_2\text{AsPh}_2)]$ (**2.3**) and $[\text{TiCl}_4(\text{tBuAsH}_2)_n]$ (**2.4**). Upon the reaction of TiCl_4 with $\text{As}(\text{NMe}_2)_3$ a group exchange was observed resulting in the formation of $[\text{TiCl}_3(\text{NMe}_2)(\mu\text{-NMe}_2)_2\text{AsCl}]$ (**2.5**). Although an unsuitable single-source precursor to titanium arsenide due to the lack of a direct titanium-arsenic bond, the group exchange observed within (**2.5**) is the first reported of its kind. Similar group exchanges were also observed within the reaction products of TiCl_4 and two equivalents of $\text{As}(\text{NMe}_2)_3$ and additionally $\text{Ti}(\text{NMe}_2)_4$ and AsCl_3 , however the reasoning behind the exchange is still not fully understood.

In order to determine the suitability of compounds (**2.1**) – (**2.4**) as potential single-source precursor routes to titanium arsenide, and additionally (**2.5**) as a single-source precursor to titanium nitride, decomposition studies, AACVD and LPCVD were conducted on the five compounds; this will be described in Chapter 3.

References

- 1 Y. Senzaki and W. L. Gladfelter, *Polyhedron*, 1994, 13, 1159.
- 2 F. R. Klingan, A. Miehr, R. A. Fischer and W. A. Herrmann, *Appl. Phys. Lett.*, 1995, 67, 822.
- 3 V. 6.45a BRUKER AXS Inc., 2003.
- 4 V. 2.03 BRUKER AXS Inc., 2001.
- 5 A. L. Spek, *J. Appl. Crystallogr.*, 2003, 36, 7.
- 6 L. J. Farrugia, *J. Appl. Cryst.*, 1999, 32, 83.
- 7 C. S. Blackman, C. J. Carmalt, I. P. Parkin, L. Apostolico, K. C. Molloy, A. J. P. White and D. J. Williams, *J. Chem. Soc., Dalton Trans.*, 2002, 2702.
- 8 F. Challenger and F. Pritchard, *J. Chem. Soc., Trans.*, 1924, 125, 864.
- 9 G. Booth, *Adv. Inorg. Chem.*, 1964, 6, 1.
- 10 G. W. A. Fowles and R. A. Walton, *J. Chem. Soc.*, 1964, 4330.
- 11 A. D. Westland and L. Westland, *Can. J. Chem.*, 1965, 43, 426.
- 12 C. C. Hinckley, M. Matusz and P. D. Robinson, *Acta Crystallogr., Sect. C: Cryst. Struct. Commun.*, 1988, 44, 371.
- 13 M. F. Mahon, N. L. Moldovan, K. C. Molloy, A. Muresan, I. Silaghi-Dumitrescu and L. Silaghi-Dumitrescu, *Dalton Trans.*, 2004, 4017.
- 14 R. Hart, W. Levason, B. Patel and G. Reid, *Eur. J. Inorg. Chem.*, 2001, 2927.
- 15 R. M. Lum, J. K. Klingert and M. G. Lamont, *Appl. Phys. Lett.*, 1987, 50, 284.
- 16 C. H. Chen, C. A. Larsen and G. B. Stringfellow, *Appl. Phys. Lett.*, 1987, 50, 218.
- 17 P. W. Lee, T. R. Omstead, D. R. McKenna and K. F. Jensen, *J. Cryst. Growth*, 1988, 93, 134.
- 18 C. A. Larsen, N. I. Buchan, S. H. Li and G. B. Stringfellow, *J. Cryst. Growth*, 1989, 94, 663.
- 19 M. Brynda, *Coord. Chem. Rev.*, 2005, 249, 2013.
- 20 A. C. Jones, *Chem. Soc. Rev.*, 1997, 26, 101.

- 21 K. Kirschbaum, O. Conrad and D. M. Giolando, *Acta Crystallogr., Sect. C: Cryst. Struct. Commun.*, 2000, 56, E541.
- 22 R. T. Cowdell and G. W. A. Fowles, *J. Chem. Soc.*, 1960, 2522.

Chapter 3

Single-source CVD Attempts to TiAs

Following the synthesis of five potential single-source precursors to titanium arsenide/nitride, their use within AACVD and LPCVD was investigated. This chapter describes decomposition studies of the potential single-source precursors $[\text{TiCl}_4(\text{AsPh}_3)]$ (**2.1**), $[\text{TiCl}_4(\text{AsPh}_3)_2]$ (**2.2**), $[\text{TiCl}_4(\text{Ph}_2\text{AsCH}_2\text{AsPh}_2)]$ (**2.3**), $[\text{TiCl}_4(\text{tBuAsH}_2)_n]$ (**2.4**), and $[\text{TiCl}_3(\text{NMe}_2)(\mu\text{-NMe}_2)\text{AsCl}]$ (**2.5**) (Figure 3.1), in addition to their use within AACVD and LPCVD.

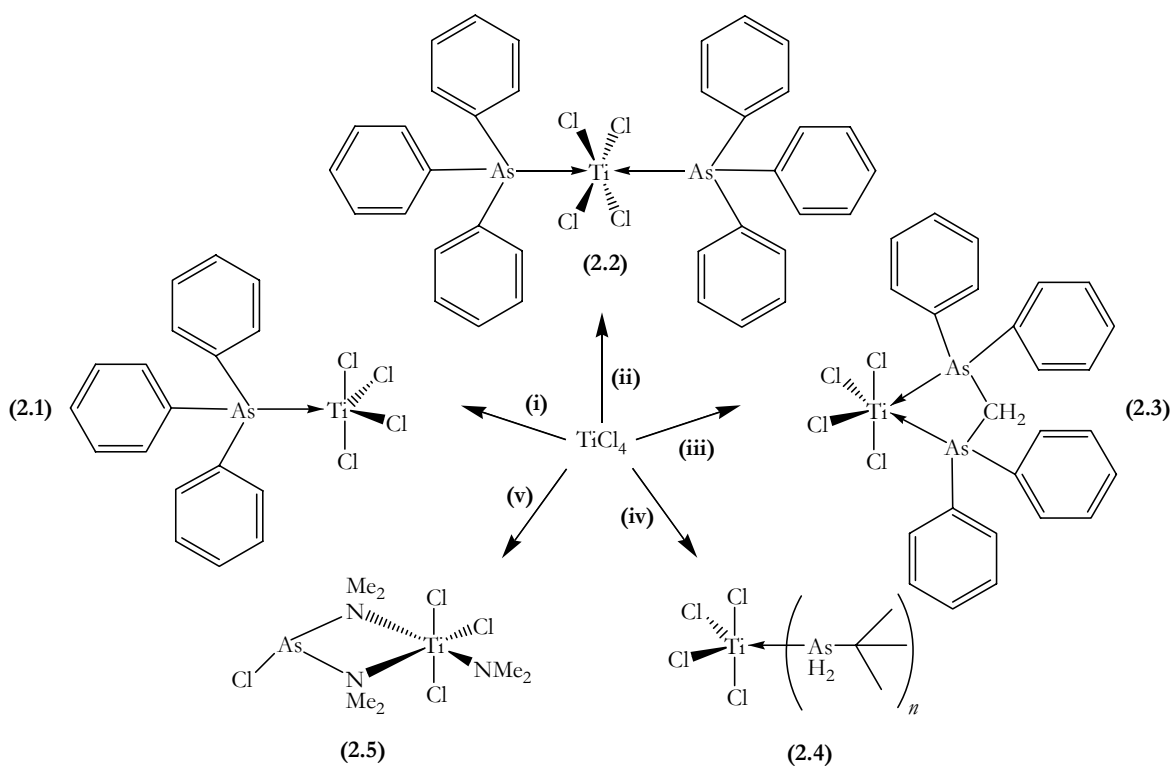


Figure 3.1 Schematic illustrating the synthesis of compounds **(2.1)** – **(2.5)** *via* the reaction of TiCl_4 with (i) AsPh_3 , (ii) 2AsPh_3 , (iii) $\text{Ph}_2\text{AsCH}_2\text{AsPh}_2$, (iv) tBuAsH_2 and (v) $\text{As}(\text{NMe}_2)_3$.

3.1 Experimental

3.1.1 General Procedures, Precursors and Substrate

All manipulations and reactions were conducted under a dry, oxygen-free dinitrogen atmosphere, using standard Schlenk techniques or an MBraun Unilab glovebox; nitrogen (99.9%, BOC) was used as supplied. All employed solvents were stored in alumina columns and dried using anhydrous engineering equipment, such that the water concentration was 5 – 10 ppm. Single-source precursors were synthesised as previously described (**Section 2.1.3**) and used either as isolated material (AACVD and LPCVD) or generated *in situ* (AACVD).

AACVD depositions were conducted on 90 mm x 45 mm x 4 mm float glass coated with a 50 nm thick SiCO barrier layer to stop diffusion of ions from the glass, as supplied by Pilkington. LPCVD was conducted on five and a half 75 mm x 12 mm x 1 mm borosilicate glass slides. All substrates were cleaned with petroleum ether (60 – 80 °C) and 2-propanol, and allowed to air dry at room temperature prior to use.

3.1.2 Physical Measurements

Thermogravimetric analysis (TGA) was conducted using a Netzsch STA 449C instrument, with samples sealed using aluminium sample pans. Due to the air sensitive nature of the samples, TGA was conducted under a flow of helium gas; heating rates of 10 °C min⁻¹ were used in all instances. X-ray powder diffraction patterns were obtained using a Brüker AXS D8 discover machine using monochromatic Cu-K α radiation. Wavelength dispersive X-ray analysis (WDX) was conducted using a Philips XL30ESEM machine. Scanning electron microscopy (SEM) was performed using a JSM-6301F scanning field emission machine.

3.1.3 CVD Equipment and Methods

3.1.3.1 Aerosol Assisted (AA)CVD

AACVD was conducted using a horizontal cold wall CVD reactor, with a bottom substrate mounted onto a graphite heating block containing a Whatman cartridge

heater, and a top substrate placed approximately 1 cm above. Temperature control was achieved using a Pt-Rh thermocouple, with the top substrate exhibiting temperatures typically 50 °C lower than the bottom substrate, due to its non-direct heating. A Vicks VE5520E humidifier was used to produce the aerosol mist within a flat-bottomed AACVD Schlenk flask. The compounds were either used as synthesised (**Section 2.1.3**) or generated *in situ* within the flask, and dissolved in a suitable solvent (see **Section 1.3.3.1** for solvent requirements) such that an aerosol mist could be formed. Prior to the conduction of AACVD, the equipment and substrates were allowed to heat to the required temperature under a flow of nitrogen (1 L min^{-1}), after which, redirection of the N_2 carrier gas through the bubbler resulted in aerosol delivery to the CVD reactor (**Figure 3.2**). After the conduction of AACVD, the substrates were allowed to cool under a flow of nitrogen before being removed and subsequently stored in air.

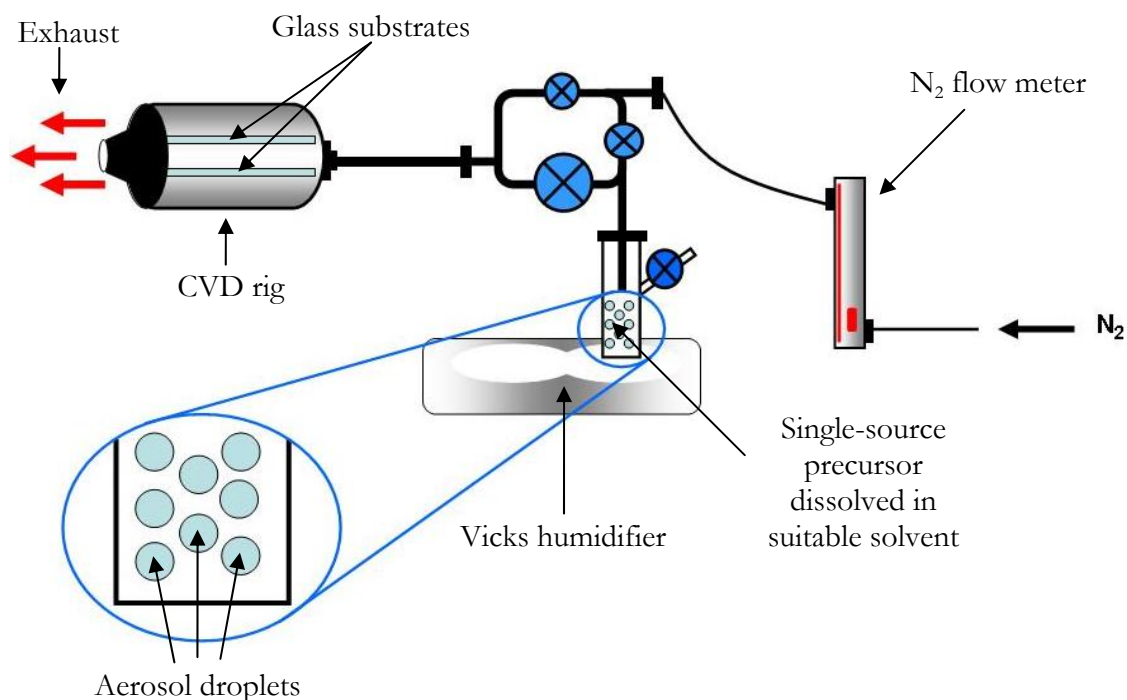


Figure 3.2 Schematic representing the equipment used within the AACVD of compounds (2.1), (2.2), (2.4) and (2.5).

3.1.3.2 Vapour Draw Low Pressure (LP)CVD

Within a glovebox, approximately 0.5 g of synthesised compound (**Section 2.1.3**) was placed within a sample vial and positioned at the end of a 60 cm quartz column. Once in position, five and a half glass microscope slides were inserted along the entire length of the column, ensuring that no overlap occurred, and that all substrates were positioned horizontally. Whilst remaining horizontal, the column was sealed using a Schlenk tap fitting, removed from the glovebox and placed inside a tube furnace. Once inside, the quartz column was placed under vacuum and the temperature increased to 600 °C to start the LPCVD. The LPCVD was conducted until all material had sublimed, after which the substrates were removed and subsequently stored under nitrogen.

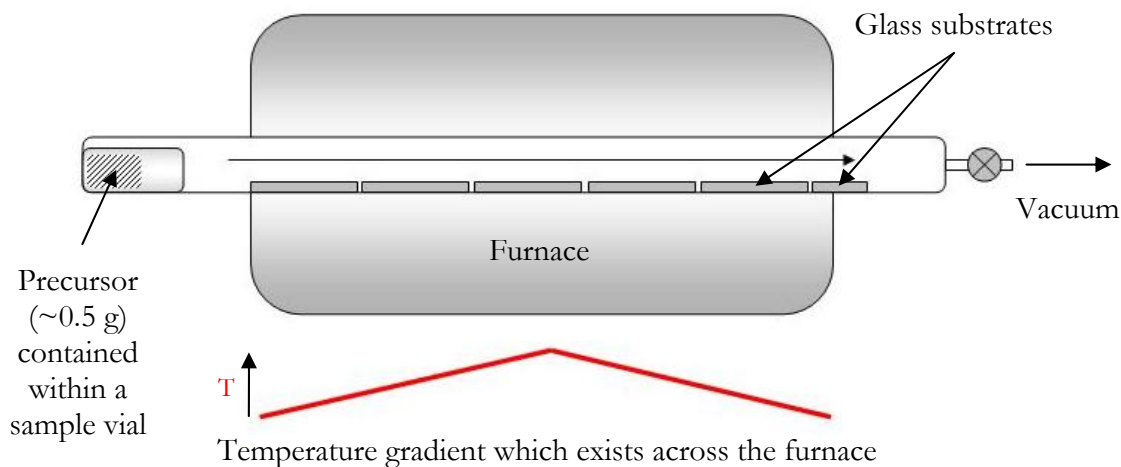


Figure 3.3 Schematic representing the equipment used within the vapour draw LPCVD of compounds **(2.1)**, **(2.2)**, **(2.3)** and **(2.5)** in an attempt to deposit TiAs.

3.1.4 AACVD Precursor Delivery

Typically all AACVD experiments were conducted using substrate temperatures between 400 – 600 °C and investigated using toluene and dichloromethane as the solvents. AACVD was conducted using three different precursor delivery routes: simultaneous delivery, isolated material delivery, and sequential delivery (as described overleaf):

- **Simultaneous delivery** – The two components (i.e. TiCl_4 and the arsine) were added to the AACVD reaction flask and allowed to mix for approximately two minutes prior to the conduction of AACVD.
- **Isolated material delivery** – Compounds were synthesised (**Section 2.1.3**) and isolated, prior to dissolving in a suitable solvent and conducting AACVD.
- **Sequential delivery** – The arsine was added to the solvent and allowed to pass through the rig for approximately 5 minutes prior to the addition of the TiCl_4 .

Table 3.1 Table summarising the experimental parameters investigated within the AACVD of compounds **(2.1)**, **(2.2)**, **(2.4)** and **(2.5)**. Compound **(2.3)** was not investigated using AACVD due to its insolubility within a range of tested solvents including toluene, dichloromethane (DCM) and hexane. Solvent volumes used, were the minimal solvent required to ensure complete compound solubility.

Compound	Precursor Delivery Method	Solvent (volume/cm ³)	Substrate Temperature/°C
(2.1)	Simultaneous	Toluene (20)	200 400 600
		DCM (40)	400
(2.2)	Isolated material	Toluene (20)	550
(2.4)	Simultaneous	Toluene (20)	400 600
	Sequential	Toluene (20)	400
(2.5)	Simultaneous	DCM (40)	400
	Sequential	Toluene (40)	400

3.2 Results and Discussion

3.2.1 Thermogravimetric Analysis

To acquire information as to how compounds **(2.1)** – **(2.5)** would decompose upon heating, and to determine their suitability as CVD precursors, thermogravimetric analysis (TGA) was conducted over the temperature range 100 – 500 °C (**Figure 3.4** and **Table 3.2**).

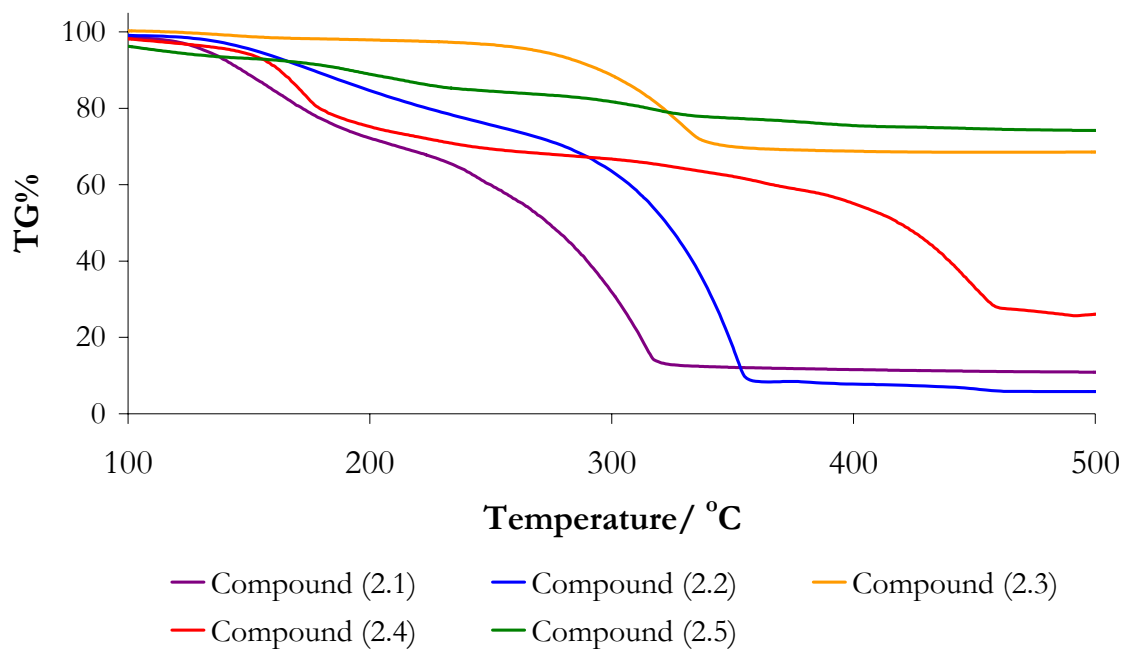


Figure 3.4 TGA plots for compounds **(2.1)** – **(2.5)** between 100 and 500 °C.

Table 3.2 Residual mass data from the TGA of compounds **(2.1)** – **(2.5)** compared to the calculated residual mass for decomposition to TiAs.

Compound	Observed residual mass (%)	Calculated residual mass for TiAs (%)
(2.1)	10.8	24.8
(2.2)	5.8	15.3
(2.3)	68.6	18.6
(2.4)	24.5	37.9
(2.5)	74.3	30.9

All compounds exhibited clean, multi-step mass loss decompositions, with decompositions starting after approximately 100 °C. Upon comparison of the observed residual masses with that expected for the decomposition to TiAs, all compounds exhibited masses inconsistent with the formation of TiAs, as discussed below.

3.2.1.1 [TiCl₄(AsPh₃)] (2.1) and [TiCl₄(AsPh₃)₂] (2.2)

The TGA of (2.1) resulted in a two-step decomposition profile with mass losses observed at approximately 120 °C (starting at around the melting point, 126 °C) and 220 °C, and mass loss completion achieved by 320 °C. The observed residual mass of (2.1) was not in agreement with that expected for the decomposition to TiAs (24.8%), but rather decomposition to titanium metal (expected residual mass of ~9.7%). Although the residual mass was not in agreement with that expected for TiAs, it should be noted that sublimation of the precursor may have occurred, which would have resulted in a higher than expected weight loss. Comparison of the TGA profile of (2.1) with that previously reported for the related tin complex [SnCl₄(AsPh₃)₂], shows that a similar TGA profile is observed. TGA of [SnCl₄(AsPh₃)₂] resulted in a two-step weight loss profile, with complete weight loss observed by 330 °C. The decomposition of [SnCl₄(AsPh₃)₂] was proposed to be by loss of AsPh₃Cl₂ and/or AsPh₃;¹ this is in agreement with the TGA of (2.1).

The TGA of (2.2) resulted in a two-step decomposition profile with mass losses observed at approximately 130 °C and 240 °C, and mass loss completion achieved by 240 °C. Similarly to (2.1), the residual mass of compound (2.2) was not in agreement with that expected for the decomposition to TiAs (15.3%), but again demonstrated an observed residual mass consistent with decomposition to titanium metal (expected residual mass of ~6%).

Although both (2.1) and (2.2) demonstrated potential as CVD precursors due to their clean decompositions and observed weight-losses, it is possible that the observed weight losses correspond to the dissociation of the arsine ligand before decomposition, due to the weak Ti-As bonds present within both compounds (**Section**

2.2.1), due to the hard Lewis acid (TiCl_4) soft Lewis base (AsPh_3) interaction. As such, **(2.1)** and **(2.2)** may prove unsuitable as single-source precursors to titanium arsenide.

3.2.1.2 $[\text{TiCl}_4(\text{Ph}_2\text{AsCH}_2\text{AsPh}_2)]$ **(2.3)**

The TGA of **(2.3)** resulted in a three-step decomposition profile, with weight losses occurring at approximately 40, 80 and 200 °C, The observed residual mass of **(2.3)** was not in agreement with that expected for its decomposition to TiAs, however it was consistent with that calculated for $\text{TiPh}_2\text{AsCH}_2\text{AsPh}$ (~67%). Due to the high residual mass exhibited by **(2.3)** it is likely that any film deposited using **(2.3)** may result in high levels of carbon incorporation due to its incomplete decomposition; an observation previously observed for the deposition of TiP using the analogous phosphorus single-source precursor $[\text{TiCl}_4(\text{Ph}_2\text{PCH}_2\text{PPh}_2)]$, which exhibited a similarly high residual mass.² However, solubility tests investigating suitable solvents for the use of **(2.3)** within AACVD, showed compound **(2.3)** to be insoluble in a range of solvents. Due to the observed insolubility of **(2.3)** it is likely that an oligomer had formed, which may contribute to the observation of a high residual mass upon its decomposition.

3.2.1.3 $[\text{TiCl}_4(\text{tBuAsH}_2)_n]$ **(2.4)**

The TGA of **(2.4)** resulted in a three-step decomposition profile, with weight losses occurring at approximately 80, 290 and 460 °C. A residual mass lower than that expected for decomposition to TiAs was observed (assuming that $n = 1$), however, this weight loss difference between the observed and expected values could be as a result of the difficult isolation and manipulation of **(2.4)** (**Section 2.2.3**). As previously mentioned (**Section 1.3.2.2**), the decomposition of tBuAsH_2 consists of many proposed decomposition routes, including β -hydride elimination and disproportionation reactions,³⁻⁵ and has proven itself as a successful arsenic precursor;^{6,7} as such, it was anticipated that compound **(2.4)** would prove successful in the deposition of TiAs.

3.2.1.4 [TiCl₃(NMe₂)(μ-NMe)₂AsCl] (2.5)

The TGA of (2.5) resulted in a five-step decomposition profile, with weight losses occurring at approximately 20, 150, 250, 350 and 420 °C. Although (2.5) was already deemed an unsuitable single-source precursor to TiAs due to its lack of pre-formed Ti-As bonds, it may prove suitable within the deposition of titanium nitride films. As expected, the residual mass of (2.5) was not in agreement with that expected for decomposition to TiAs, however, it was consistent with that expected for TiCl₄N₃As (expected residual mass of ~77%). This residual mass indicates that potential arsenic incorporation within deposited films may result from the decomposition of (2.5), even with its lack of Ti-As bonds.

3.2.2 Aerosol Assisted (AA)CVD

3.2.2.1 [TiCl₄(AsPh₃)] (2.1) and [TiCl₄(AsPh₃)₂] (2.2)

AACVD of (2.1) was conducted using toluene and dichloromethane at substrate temperatures ranging from 200 – 600 °C, using the simultaneous precursor delivery method. In all instances, a strongly adherent rainbow film was deposited on the bottom substrate, which was typically accompanied by the deposition of a white non-adhesive powder on the top substrate (which is approximately 50 °C lower in temperature than the bottom substrate), indicative of homogenous reactions within the gas phase.

In contrast to the *in situ* formation of compound (2.1), during AACVD compound (2.2) was synthesised (Section 2.1.3) and isolated prior to its use within AACVD. Similarly to compound (2.1), AACVD of compound (2.2) also produced a strongly adherent rainbow film (bottom substrate) accompanied by a white non-adhesive powder (top substrate). In order to determine the composition of the deposited rainbow films when using compounds (2.1) and (2.2), XRD and WDX analysis was conducted.

X-ray powder diffraction of the rainbow films deposited using both compound (2.1) and (2.2) produced diffractograms similar to that expected for the formation of TiO₂ anatase,⁸ with 2θ peaks observed at approximately 25.8, 37.9, 38.5,

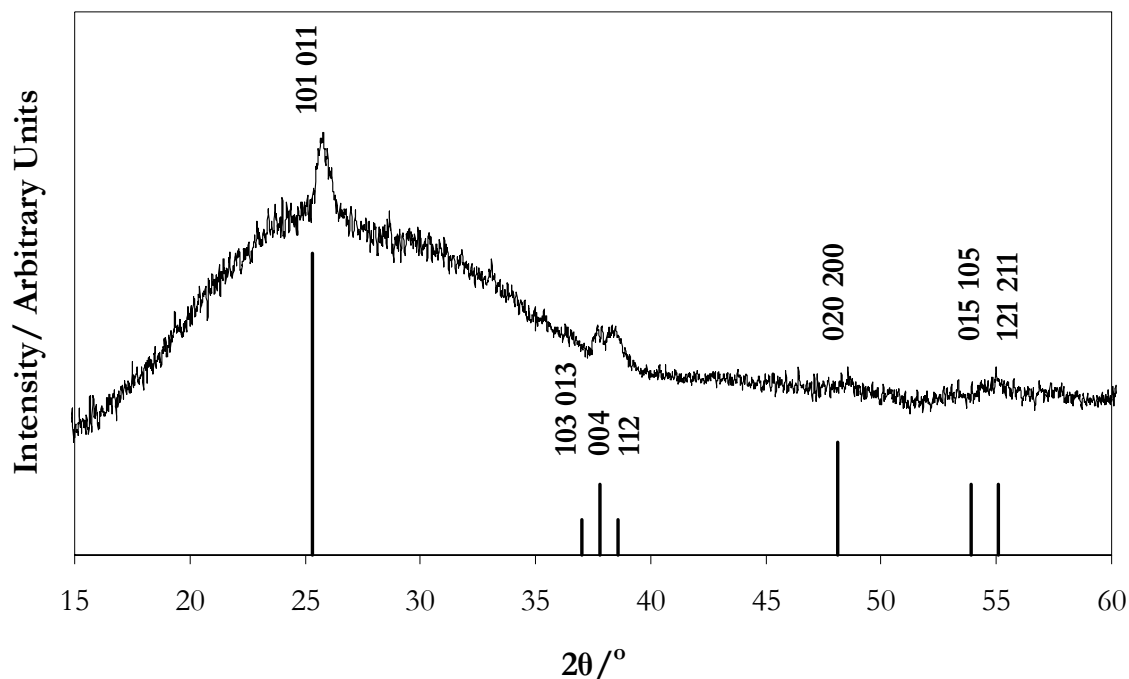


Figure 3.5 Typical X-ray powder diffraction pattern for the rainbow films deposited during the AACVD of $[\text{TiCl}_4(\text{AsPh}_3)]$ **(2.1)** and $[\text{TiCl}_4(\text{AsPh}_3)_2]$ **(2.2)** with comparison to a reference TiO_2 anatase powder diffractogram.⁸

48.8 and 55.2°. In addition to peaks associated with TiO_2 anatase, a broad peak was also observed at approximately 22° which can be attributed to the underlying glass substrate on which the CVD was conducted (**Figure 3.5**).

WDX analysis of the rainbow films deposited using both compounds produced results in agreement with that observed within XRD. Removal of approximate silicon and oxygen atomic percentages attributed to the underlying glass substrate, showed that films produced from both compounds **(2.1)** and **(2.2)** exhibited an approximate 1:2 ratio of titanium to oxygen. This is consistent with the formation of TiO_2 anatase deposition, as also indicated by XRD. Although both compounds resulted in negligible chlorine incorporation within the films deposited *via* AACVD, no arsenic incorporation was detected in either case (**Table 3.3**).

Both the XRD and WDX analysis of films deposited using compounds **(2.1)** and **(2.2)** were in agreement with the previously described TGA results (**Section 3.2.1**), in which residual masses consistent with titanium metal remaining upon decomposition

were observed. Additionally, the results are consistent with that previously reported for the AACVD of $[\text{SnCl}_4(\text{AsPh}_3)_2]$, where films of SnO_2 were deposited rather than tin arsenide.¹ The crystal structures of compounds **(2.1)** and **(2.2)** indicated that relatively long and weak Ti-As bonds were present (2.7465(13) and 2.7238(7) Å respectively), which appears to be the reason behind the dissociation of arsine and subsequent oxidation of titanium to form TiO_2 anatase. Although care was taken to eliminate oxygen from the CVD system, it is possible that leaks occurred, or that the SiO_2 substrate acted as an oxygen source. Consequently, compounds **(2.1)** and **(2.2)** were found to be unsuccessful single-source precursors to titanium arsenide *via* AACVD.

Element	Typical Atomic %	
	(2.1)	(2.2)
Ti	32.0	27.3
As	0.0	0.0
Cl	0.4	0.4
O	67.6	72.2

Table 3.3 Wavelength dispersive X-ray (WDX) analysis showing typical values for the rainbow films deposited *via* the AACVD of $[\text{TiCl}_4(\text{AsPh}_3)]$ **(2.1)** and $[\text{TiCl}_4(\text{AsPh}_3)_2]$ **(2.2)**.

3.2.2.2 $[\text{TiCl}_4(\text{tBuAsH}_2)_n]$ **(2.4)**

AACVD of **(2.4)** was conducted using a simultaneous precursor delivery method at substrate temperatures of 400 and 600 °C, and sequential precursor delivery method at 400 °C; all depositions were conducted using toluene. Similarly to that observed for compounds **(2.1)** and **(2.2)**, AACVD of **(2.4)** produced strongly adherent rainbow films in all instances. Interestingly, whilst films deposited using the simultaneous precursor delivery method produced powder XRD diffractograms consistent with TiO_2 anatase, films deposited using the sequential method were amorphous, with only a

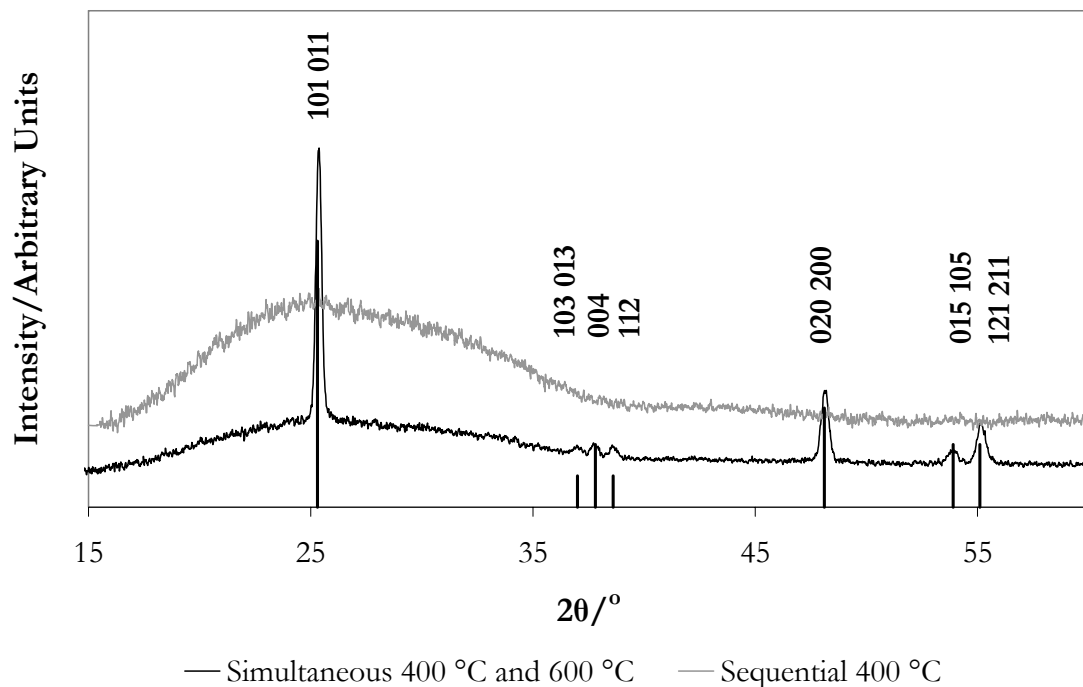


Figure 3.6 Typical X-ray powder diffractograms for rainbow films deposited *via* the AACVD of $[\text{TiCl}_4(\text{tBuAsH}_2)_n]$ (**2.4**) using a simultaneous method of precursor delivery at substrate temperatures of 400 and 600 °C, and a sequential precursor delivery method at 400 °C, with comparison to a reference TiO_2 anatase powder diffractogram.⁸

broad peak attributed to the underlying glass substrate at approximately 22° observed (**Figure 3.6**).

WDX analysis of the rainbow films indicated that whilst films deposited using the simultaneous method contained little to no arsenic, films deposited using the sequential method exhibited an approximate 4:1 ratio of titanium to arsenic. This observed incorporation of arsenic within the films *via* the sequential method may indicate the formation of TiAs, or the deposition of arsenic. However, high levels of oxidation of the film largely resulted in the formation of oxide, likely in this case to be amorphous TiO_2 (**Table 3.4**). The results obtained for the sequential deposition using TiCl_4 and tBuAsH_2 are consistent with the TGA results of (**2.4**), which indicated that arsenic may remain upon decomposition. It is however interesting to note that arsenic deposition was dependent on allowing the arsine to pass through the CVD system first, suggesting that excess arsine is required to keep some of the Ti-As interactions intact

during the CVD process, and to limit oxidation. This observation supports the previous comment that TiO₂ may be forming as a result of the SiO₂ substrate acting as an oxygen source, with passage of the arsine through the CVD system first in the sequential method resulting in arsine-substrate reactions, and hence minimising the amount of oxygen available for the formation of TiO₂.

Table 3.4 Wavelength dispersive X-ray (WDX) analysis showing typical values for the rainbow films deposited *via* the AACVD of [TiCl₄(^tBuAsH₂)_{*n*}] (**2.4**) using a simultaneous and sequential precursor delivery method at substrate temperatures of 400 and 600 °C.

Element	Typical Atomic %		
	Simultaneous 400 °C	Simultaneous 600 °C	Sequential 400 °C
Ti	30.0	28.2	23.0
As	0.0	0.4	6.4
Cl	1.9	1.5	9.1
O	68.1	69.9	61.5

Scanning electron microscopy analysis of the TiO₂ anatase films deposited *via* the AACVD of (**2.4**) using the simultaneous precursor delivery method was conducted to determine whether any visible difference in films deposited at different substrate

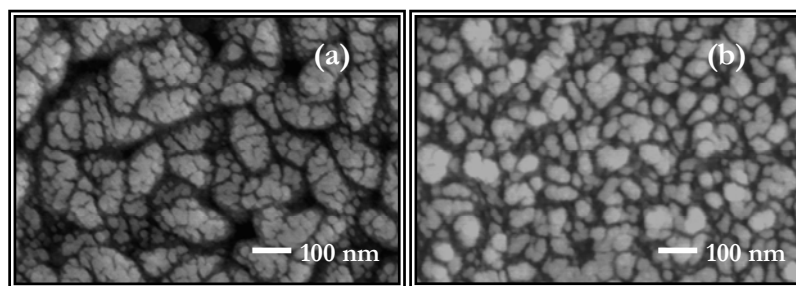


Figure 3.7 Scanning electron micrographs of TiO₂ anatase films deposited *via* the AACVD of [TiCl₄(^tBuAsH₂)_{*n*}] (**2.4**) using the simultaneous precursor delivery method, at substrate temperatures of 400 °C (a) and 600 °C (b) (x100,000 magnification).

temperatures could be observed. SEM analysis showed island growth agglomerates of TiO₂ for both films (i.e. those deposited at both 400 °C and 600 °C), with no visible difference between the two films observed (**Figure 3.7**).

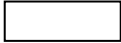


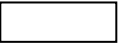


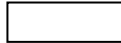
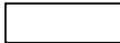

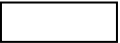


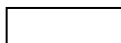









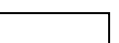

3.2.2.3 [TiCl₃(μ-NMe₂)₂(NMe₂)AsCl] (2.5)





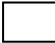
Although compound **(2.5)** was not considered to be a suitable single-source precursor to titanium arsenide due to the lack of a pre-formed Ti-As bond, the AACVD of **(2.5)** was conducted. The AACVD of **(2.5)** was conducted at 400 °C using both the simultaneous and sequential precursor delivery methods, and dichloromethane and toluene respectively. Whilst no films were deposited *via* the AACVD of **(2.5)** using the simultaneous delivery method, a very thin amorphous rainbow film was observed when using the sequential method, with only a broad peak at approximately 22° observed, attributed to the underlying glass substrate. WDX analysis of this film was not possible due to the minimal thickness of the film, however it is likely that this film consists of an amorphous titanium oxide species similar to that previously reported when using compound **(2.4)**.

3.2.3 Vapour Draw Low Pressure (LP)CVD

Vapour draw LPCVD was conducted on compounds **(2.1)**, **(2.2)**, **(2.3)** and **(2.5)** using methods previously described (**Section 3.1.3.2**). Vapour draw LPCVD was not conducted on compound **(2.4)** due to difficulties with product manipulation and limited material isolation. All LPCVD experiments were conducted at 600 °C with deposition considered complete once all material had sublimed. Upon the completion of LPCVD, the observed depositions within each region (i.e. individual glass microscope substrates) were recorded, with film deposition positions and colours noted (**Table 3.5**). In all instances, LPCVD resulted in the deposition of at least two visibly different films, with all compounds resulting in film deposition within the central part of the furnace (i.e. the hottest part).

Table 3.5 Schematic illustrating the different depositions observed within the LPCVD of compounds (2.1), (2.2), (2.3), and (2.5), where region 6 represents the substrate closest to the sample vial, and 1, the substrate closest to the vacuum.

Compound	LPCVD region and observed deposits					
	6	5	4	3	2	1
(2.1)						
(2.2)						
(2.3)						
(2.5)						

	Rainbow film		Black transparent film
	Predominantly orange rainbow film		Thick dark red/orange film
	No film deposited		

3.2.3.1 The LPCVD of $[\text{TiCl}_4(\text{AsPh}_3)]$ (2.1) and $[\text{TiCl}_4(\text{AsPh}_3)_2]$ (2.2)

For the LPCVD of compounds (2.1) and (2.2) two visibly different deposits were observed; one predominantly orange in colour and the other a rainbow film observed near the tube outlet. Powder X-ray diffraction of the region two films (i.e. the orange films) for both compounds showed the films to be crystalline, with a sharp peak observed at approximately $20^\circ 2\theta$. This peak was found to be inconsistent with that expected for TiO_2 anatase,⁸ rutile,⁹ or brookite phases,¹⁰ however the peak was consistent with that expected for Ti_4O_7 , which shows a sharp intense peak at approximately 20° .¹¹ Although other peaks associated with Ti_4O_7 formation were not present, these peaks may be lost due to the broad peak observed at approximately 22° attributed to the underlying glass substrate. All other deposited films were found to be

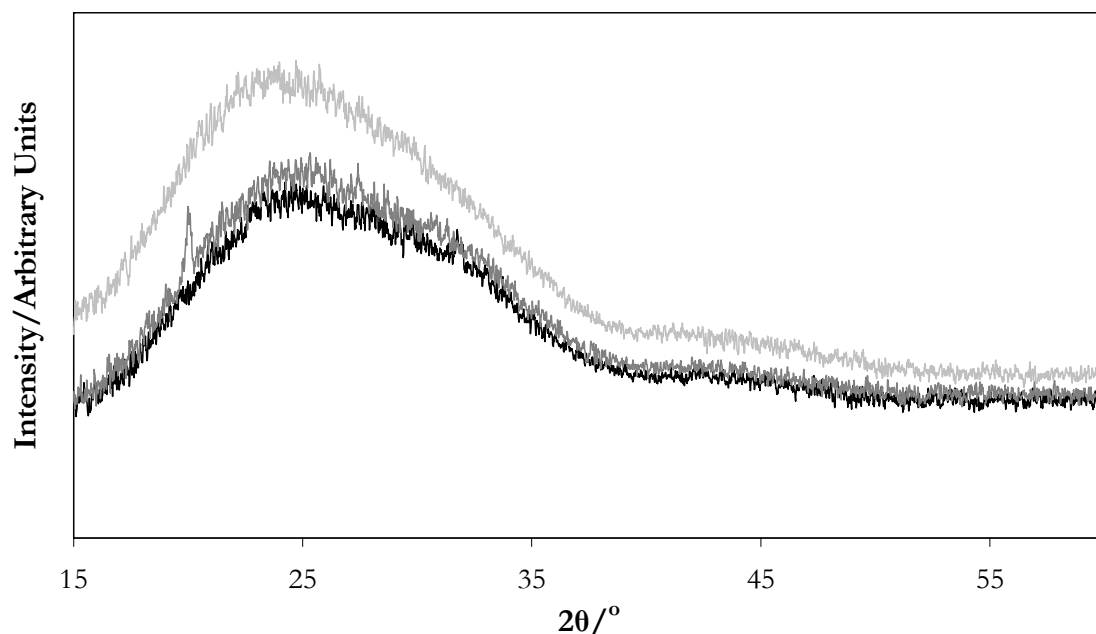


Figure 3.8 Typical X-ray powder diffractograms for films deposited *via* the LPCVD of $[\text{TiCl}_4(\text{AsPh}_3)]$ **(2.1)** [and $\text{TiCl}_4(\text{AsPh}_3)_2$] **(2.2)** at 600 °C within regions 1 (black), 2 (dark grey) and 4 (light grey).

amorphous with only a broad peak associated with the underlying glass substrate observed (**Figure 3.8**).

WDX analysis was conducted on the three films deposited *via* the LPCVD of **(2.1)** (regions 1, 2 and 4) and additionally on the two visibly different deposits from the LPCVD of **(2.2)** (regions 1 and 2). LPCVD of **(2.1)** resulted in the deposition of material exhibiting an approximate 3:1 ratio of titanium to arsenic within region 1 of the furnace, indicating that some of the Ti-As interaction remained intact during the decomposition. It is interesting to note that whilst this rainbow film exhibited some arsenic content, all other regions (i.e. regions 2 and 4) contained no arsenic. Relatively high levels of titanium were observed for regions 2 and 4, and additionally a high level of chlorine within the orange-rainbow film deposited within region 4.

In an attempt to deposit material with a higher arsenic content, the 1:2 adduct of TiCl_4 and AsPh_3 was used **(2.2)**. LPCVD of **(2.2)** resulted in the deposition of visually similar deposits to that observed within the LPCVD of **(2.1)**. WDX analysis of

the films deposited within regions 1 and 2 did however demonstrate differences between that observed for **(2.1)**, with a high level of titanium to arsenic (approximately 3:1) observed within region 2 of the furnace. In addition, higher atomic percentages of titanium were observed within both regions, indicating the deposition of a thicker film in comparison to films deposited *via* the LPCVD of **(2.1)**.

Table 3.6 Wavelength dispersive X-ray (WDX) analysis showing typical values for the films deposited *via* the LPCVD of $[\text{TiCl}_4(\text{AsPh}_3)]$ **(2.1)** at 600 °C within regions 1, 2 and 4 of the tube furnace.

Element	Typical Atomic %		
	Region 1	Region 2	Region 4
Ti	3.6	4.7	6.1
As	1.2	0.0	0.0
Cl	0.9	0.0	6.9
O	14.1	34.0	47.9

Table 3.7 Wavelength dispersive X-ray (WDX) analysis showing typical values for the films deposited *via* the LPCVD of $[\text{TiCl}_4(\text{AsPh}_3)_2]$ **(2.2)** at 600 °C within regions 1, and 2 of the tube furnace.

Element	Typical Atomic %	
	Region 1	Region 2
Ti	13.1	13.2
As	0.2	5.0
Cl	0.4	1.7
O	66.0	58.6

For both the LPCVD of **(2.1)** and **(2.2)**, it was expected that high carbon incorporation had occurred within the deposited films due to the phenyl groups, however due to carbon coating of the sample during WDX analysis, the atomic carbon percentage could not be determined.

3.2.3.2 The LPCVD of $[\text{TiCl}_4(\text{Ph}_2\text{AsCH}_2\text{AsPh}_2)]$ **(2.3)**

Previously, the LPCVD of the phosphorus equivalent of **(2.3)**, $[\text{TiCl}_4(\text{Ph}_2\text{PCH}_2\text{PPh}_2)]$, resulted in the deposition of an amorphous gold film, which was identified as a mixture of TiO_2 and TiP from XPS analysis. Similarly to **(2.3)**, the TGA of the phosphorus equivalent demonstrated a weight loss between 50-60%, possibly suggesting incomplete decomposition to TiP .² As such, **(2.3)** was hoped to exhibit similar success in the deposition of TiAs *via* LPCVD.

Unlike the phosphorus analogue, the LPCVD of **(2.3)** resulted in the deposition of two visibly different films, an orange deposit within regions 1 and 2, and a black transparent film between regions 3 and 4. XRD analysis of the deposited films showed that whilst the orange material deposited at the outlet of the furnace was crystalline and exhibited a peak at approximately $23^\circ 2\theta$, the black transparent material was amorphous.

To further probe the deposited material and to determine any elemental composition difference between the two visibly different deposits, WDX analysis was conducted. WDX analysis showed that whilst the orange films deposited at the outlet end of the furnace exhibited high levels of arsenic relative to titanium, the opposite was observed within the black transparent films deposited at the centre of the furnace. As high levels of titanium and arsenic were not observed together within any region of the substrates, it is indicative that the titanium-arsenic interaction is not being maintained during the decomposition, but rather the interaction is being lost and the two components are being deposited individually. Interestingly, high levels of oxygen were observed within region 3 of the furnace, indicating that the deposited titanium is being oxidised. Due to the samples requiring carbon coating for analysis, it was not possible

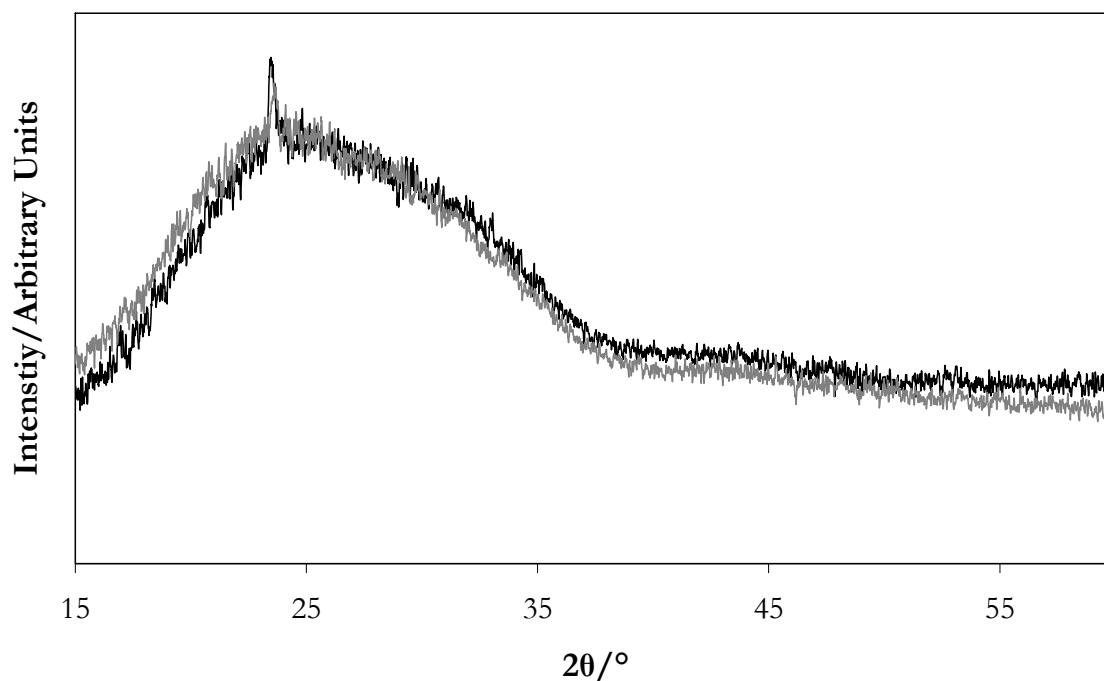


Figure 3.9 Typical X-ray powder diffractograms for films deposited *via* the LPCVD of $[\text{TiCl}_4(\text{Ph}_2\text{AsCH}_2\text{AsPh}_2)]$ (**2.3**) at 600 °C within regions 1 (black), 2 (dark grey).

for the carbon content of the films to be determined. However, from the TGA of (**2.3**), it is thought that carbon deposition would be high.

Table 3.8 Wavelength dispersive X-ray (WDX) analysis showing typical values for the films deposited *via* the LPCVD of $[\text{TiCl}_4(\text{Ph}_2\text{AsCH}_2\text{AsPh}_2)]$ (**2.3**) at 600 °C within regions 1, 2 and 3 of the tube furnace.

Element	Typical Atomic %		
	Region 1	Region 2	Region 3
Ti	1.1	0.3	7.2
As	6.1	8.3	0.0
Cl	0.6	0.5	0.3
O	15.8	12.9	50.5

3.2.3.3 The LPCVD of $[\text{TiCl}_3(\text{NMe}_2)(\mu\text{-NMe})_2\text{AsCl}]$ (2.5)

As previously mentioned, it is not thought that compound (2.5) would be a suitable single-source precursor to TiAs due to its lack of preformed Ti-As bonds, however the LPCVD of compound (2.5) was conducted to determine whether it may be a suitable single-source precursor to TiN.

The LPCVD of (2.5) resulted in the deposition of three visibly different deposits, a predominantly red-orange rainbow film within region 1, a black transparent film within regions 3, 4 and 5, and a rainbow film within region 6. XRD analysis of the three visibly different films showed that whilst the black and the rainbow films were amorphous, the red-orange rainbow film deposited towards the outlet end of the furnace was crystalline, exhibiting peaks at approximately 13 and $20^\circ 2\theta$ (Figure 3.10). The identity of this crystalline red-orange rainbow film could not be determined, however, due to its position within the tube furnace it is possible that it is an oxide.

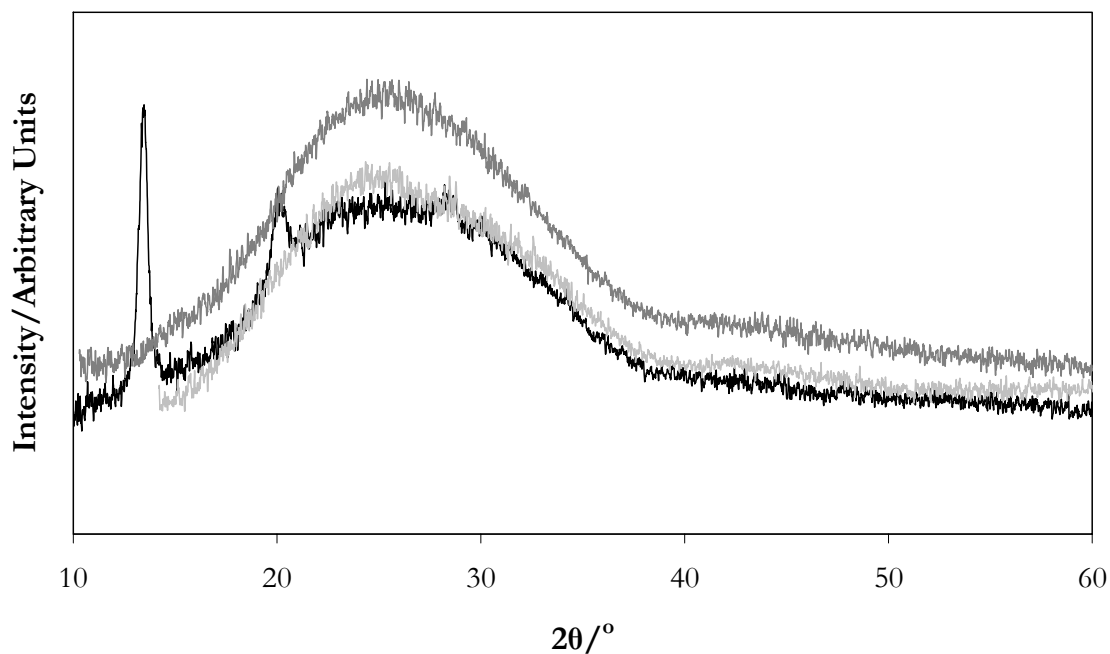


Figure 3.10 Typical X-ray powder diffractograms for films deposited *via* the LPCVD of $[\text{TiCl}_3(\text{NMe}_2)(\mu\text{-NMe})_2\text{AsCl}]$ (2.5) at 600°C within regions 1 (black), 4 (dark grey) and 5 (light grey).

WDX analysis of the films showed that although a direct titanium-arsenic interaction was not present within compound **(2.5)**, material deposited within region 1 (i.e. the red-orange rainbow film) demonstrated relatively high levels of titanium and arsenic. As expected, high levels of nitrogen were also observed within this region, which may be attributed to the dimethylamido group bridging between the titanium and the arsenic within the compound. All other regions within the furnace displayed relatively high levels of titanium, but demonstrated low levels of arsenic. Nitrogen content was high within all regions of deposited material, which is not surprising given the strength of the titanium-nitrogen bond; all regions demonstrated an approximate 1:1 ratio of titanium to nitrogen.

Table 3.9 Wavelength dispersive X-ray (WDX) analysis showing typical values for the films deposited *via* the LPCVD of $[\text{TiCl}_3(\text{NMe}_2)(\mu\text{-NMe}_2)\text{AsCl}]$ **(2.5)** at 600 °C within regions 1, 4 and 5 of the tube furnace.

Element	Typical Atomic %		
	Region 1	Region 4	Region 5
Ti	3.2	11.8	13.5
As	5.2	0.3	0.4
Cl	6.5	1.8	2.4
O	9.2	35.9	35.9
N	4.1	9.8	11.4

3.2.4 Conclusions

Following the synthesis of compounds $[\text{TiCl}_4(\text{AsPh}_3)]$ **(2.1)**, $[\text{TiCl}_4(\text{AsPh}_3)_2]$ **(2.2)**, $[\text{TiCl}_4(\text{Ph}_2\text{AsCH}_2\text{AsPh}_2)]$ **(2.3)**, $[\text{TiCl}_3(\text{NMe}_2)(\mu\text{-NMe}_2)\text{AsCl}]$ **(2.5)** and $[\text{TiCl}_4(\text{tBuAsH}_2)_n]$ **(2.4)**, TGA was conducted in an attempt to determine the suitability of the compounds as single-source precursors to TiAs and TiN (compound **(2.5)**).

TGA indicated that compounds **(2.3)** and **(2.4)** showed potential for decomposition to TiAs due to their observed residual masses following decomposition. However, compounds **(2.1)** and **(2.2)** demonstrated residual masses consistent with titanium remaining upon decomposition, a result in agreement with the previously observed long and weak Ti-As interactions within the compounds. The TGA of **(2.5)** produced a residual mass consistent with $\text{TiCl}_4\text{N}_3\text{As}$, indicating that this compound may be a suitable single-source precursor to TiN films.

As expected, the AACVD of **(2.1)** and **(2.2)** using a variety of conditions, resulted in the deposition of TiO_2 anatase, a result of the long and weak Ti-As interactions and the oxophilic nature of titanium. Whilst the AACVD of **(2.3)** was not possible due to compound insolubility, the AACVD of **(2.4)** proved more successful in the deposition of TiAs, since an increased arsenic content within deposited films on introduction of the precursors sequentially was observed. It is not fully understood why this method alteration resulted in the deposition of arsenic, however one possible reason is that the arsine acts as an oxygen scavenger, reducing the oxygen content within the CVD reaction chamber and thus reducing oxidation of the titanium centre, allowing some Ti-As bonds to remain intact during decomposition. The AACVD of compound **(2.5)** resulted in the deposition of thin, amorphous, rainbow films upon introduction of the precursors sequentially, however due to the films being extremely thin, compositional analysis was not possible.

The LPCVD of compounds **(2.1)**, **(2.2)**, **(2.3)** and **(2.5)** were also investigated, and in all cases resulted in visibly different deposits along the length of the tube furnace. Unlike within the AACVD of the compounds (excluding **(2.3)** which was not used within AACVD), all compounds produced regions of deposit containing both titanium and arsenic, with regions demonstrating approximate ratios of 1:3, 1:3, 1:6 and 1:2 of titanium to arsenic for compounds **(2.1)**, **(2.2)**, **(2.3)** and **(2.5)**, respectively. Additionally, compound **(2.5)** demonstrated regions of relatively high nitrogen content, indicating its potential as a TiN single-source precursor.

From both the AA and LPCVD results, it can be concluded that in all cases, the titanium-arsenic interaction is not strong enough to fully withstand the

temperatures involved in the decomposition process, typically resulting in TiO₂ anatase deposition. It is possible that the oxygen source for the formation of TiO₂ is the SiO₂ substrate, and as such, it would be interesting to investigate this further *via* the use of substrates that do not contain oxygen. In addition, it is believed that with milder conditions, and with strengthening of the Ti-As interaction, these compounds may prove successful in the deposition of TiAs and TiN films (compound **(2.5)**) *via* CVD.

References

- 1 M. F. Mahon, N. L. Moldovan, K. C. Molloy, A. Muresan, I. Silaghi-Dumitrescu and L. Silaghi-Dumitrescu, *Dalton Trans.*, 2004, 4017.
- 2 C. S. Blackman, C. J. Carmalt, I. P. Parkin, L. Apostolico, K. C. Molloy, A. J. P. White and D. J. Williams, *J. Chem. Soc., Dalton Trans.*, 2002, 2702.
- 3 P. W. Lee, T. R. Omstead, D. R. McKenna and K. F. Jensen, *J. Cryst. Growth*, 1988, 93, 134.
- 4 C. A. Larsen, N. I. Buchan, S. H. Li and G. B. Stringfellow, *J. Cryst. Growth*, 1989, 94, 663.
- 5 M. Brynda, *Coord. Chem. Rev.*, 2005, 249, 2013.
- 6 R. M. Lum, J. K. Klingert and M. G. Lamont, *Appl. Phys. Lett.*, 1987, 50, 284.
- 7 C. H. Chen, C. A. Larsen and G. B. Stringfellow, *Appl. Phys. Lett.*, 1987, 50, 218.
- 8 R. L. Parker, *Z. Kristallogr. Kristallgeom. Kristallphys. Kristallchem.*, 1924, 59, 1.
- 9 L. Vegard, *Philos. Mag.*, 1916, 32, 505.
- 10 L. Pauling and J. H. Sturdivant, *Z. Kristallogr. Kristallgeom. Kristallphys. Kristallchem.*, 1928, 68, 239.
- 11 S. Andersson and L. Jahnberg, *Ark. Kemi*, 1963, 21, 413.

Chapter 4

The APCVD of TiAs Thin Films

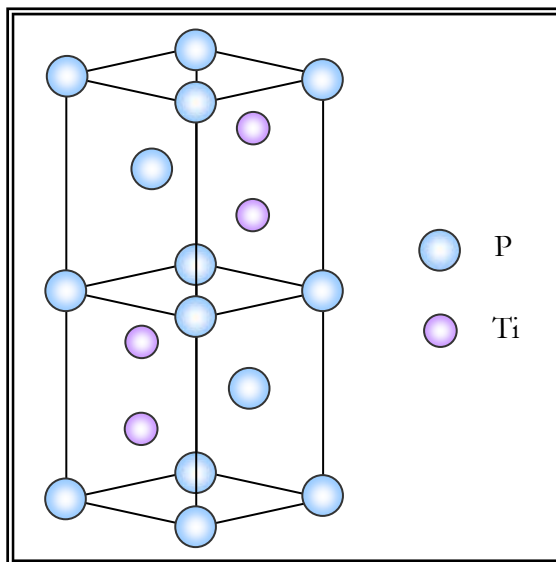


Figure 4.1 The crystal structure of TiP which TiAs is known to adopt.¹

4.1 Introduction

In an attempt to deposit TiAs thin films, the APCVD reactions of TiCl_4 and $[\text{Ti}(\text{NMe}_2)_4]$ with ${}^t\text{BuAsH}_2$ have been studied. Both TiCl_4 and $[\text{Ti}(\text{NMe}_2)_4]$ have previously proven successful in the deposition of titanium nitride and phosphide thin films,²⁻⁵ and additionally, ${}^t\text{BuPH}_2$ has previously proved to be an excellent phosphorus precursor;⁶ it was hoped that similar success would be observed for the arsenide reaction equivalents. Within this chapter the APCVD reactions of TiCl_4 and $[\text{Ti}(\text{NMe}_2)_4]$ with ${}^t\text{BuAsH}_2$ are described, in addition to discussions regarding the analysis of the deposited films.

4.2 Experimental

4.2.1 Precursors and Substrate

Nitrogen (99.9%, BOC) was used as a carrier gas in all APCVD experiments. Titanium (IV) chloride (99.9%, Sigma Aldrich), $[\text{Ti}(\text{NMe}_2)_4]$ and ${}^t\text{BuAsH}_2$ (both SAFC Hitech Ltd.), were all utilised in APCVD *via* containment within stainless steel bubblers. The TiCl_4 and $[\text{Ti}(\text{NMe}_2)_4]$ bubblers were fitted with heating jackets set to 60 °C and 125 °C in all instances, resulting in vapour pressures of approximately 62 Torr and 28 Torr, respectively. Due to the high volatility of ${}^t\text{BuAsH}_2$ a heating jacket was not required, with ${}^t\text{BuAsH}_2$ being used in all instances at room temperature, resulting in an approximate vapour pressure of 181 Torr. Nitrogen, TiCl_4 , $[\text{Ti}(\text{NMe}_2)_4]$ and ${}^t\text{BuAsH}_2$ were all used as supplied, without further purification.

APCVD depositions were conducted on 90 mm x 45 mm x 4 mm SiCO float-glass as supplied by Pilkington. Substrates were cleaned with petroleum ether (60 – 80 °C) and 2-propanol, and allowed to air dry at room temperature prior to use.

4.2.2 APCVD Equipment and Methods

APCVD experiments were conducted using a horizontal-bed cold-wall quartz reactor, comprising a graphite heating block containing a Watlow cartridge heater, with heating control achieved using Pt-Rh thermocouples. The CVD chamber, inclusive of glass, was allowed to heat to the desired temperature under a flow of nitrogen prior to deposition.

Three nitrogen gas lines were used in all experiments with gas line temperatures monitored using Pt-Rh thermocouples, and controlled *via* Eurotherm heat controllers. In all instances the gas was heated within two metres of curled stainless steel tubing contained within a tube furnace set to approximately 120 °C prior to introduction. All delivery lines were heated at 100 °C under a flow of nitrogen before deposition. All gas handling lines, flow valves and regulators were constructed from stainless steel. Internal flow diameters were ¼ in. throughout, with the exceptions of the inlet to the mixing chamber and exhaust line with internal flow diameters of ½ in.

In all experiments precursors were delivered into the system *via* two-way valves fitted to the stainless steel bubblers, which could be directly incorporated into the CVD system. The two-way valves were used to direct hot nitrogen flow either into or away from the bubblers. The bubblers were allowed to heat to the required temperature (60 °C for TiCl_4 and 125 °C for $[\text{Ti}(\text{NMe}_2)_4]$) *via* heating jackets, prior to conduction of deposition. For all reagents, precursor introductory lines were temperature controlled using Pt-Rh thermocouples. Both precursor lines were set to 100 °C with nitrogen flow maintained throughout the lines during both heating and cooling, to prevent precursor deposition and build-up.

After all components had reached their desired temperatures, and delivery lines had been heated at approximately 100 °C for 30 minutes, redirection of hot nitrogen carrier gas into the precursor bubblers using the two-way valves resulted in the introduction of the two components into the delivery system (**Figure 4.2**). After sufficient precursor build-up within the delivery lines (approximately 15 seconds), three-way valves were used to redirect the two precursor lines from the exhaust into the mixing chamber, where the two components were directly introduced.

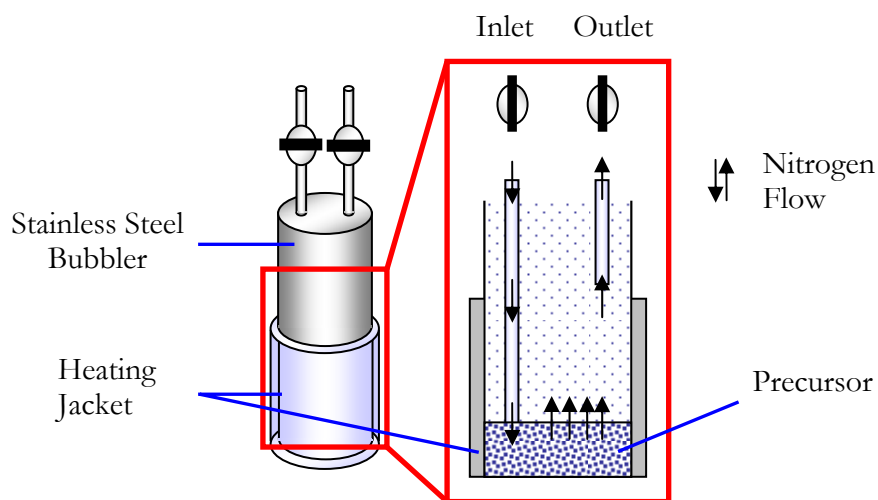


Figure 4.2 Schematic representing the inside of the stainless steel bubblers used in APCVD, and how the redirection of hot N_2 gas into the bubbler causes movement of precursors out of the bubbler, ultimately resulting in precursor delivery to the mixing chamber.

Upon the introduction of the two components into the mixing chamber, hot nitrogen carrier gas from the third gas line caused movement of material directly into the CVD reactor. The exhaust from the reactor was attached to a bleach bubbler which vented to the back of a fume cupboard. Deposition times were measured using a stopwatch, with deposition times varied between 30 to 120 seconds. Exact flows, temperatures and deposition times used during experiments are described (**Table 4.1** using the titanium precursor TiCl_4 and **Table 4.4** [$\text{Ti}(\text{NMe}_2)_4$]).

Upon completion of deposition the precursor delivery into the mixing chamber was redirected to the exhaust, with bubblers closed to redirect nitrogen through delivery lines only. The CVD chamber and substrate were then allowed to cool to room temperature under a flow of nitrogen, before extraction of the substrate plus deposit and subsequent storage in air.

4.2.3 Physical Measurements of Deposited Films

Scanning electron microscopy (SEM) was conducted using a JSM-6301F scanning field emission machine. X-ray powder diffraction patterns were obtained using a Brüker AXS D8 discover machine using monochromatic $\text{Cu-K}\alpha$ radiation. Wavelength dispersive X-ray (WDX) analysis was performed using a Philips XL30ESEM machine. High resolution X-ray photoemission spectroscopy (XPS) was performed using a Kratos Axis Ultra DLD spectrometer at the University of Nottingham, using a monochromated $\text{Al K}\alpha$ ($h\nu = 1486.6 \text{ eV}$) X-ray source. A standard wide scan with high resolution large areas ($\sim 300 \times 700$ microns) with pass energy 80 and 20 were used respectively. The photoelectrons were detected using a hemispherical analyzer with channelplates and Delay line detector. The etch was performed using 4 KeV Argon ions, using a Kratos minibeam III, rastered over an approximate area of 0.7 cm, at an approximate etch rate of 6 \AA min^{-1} . The binding energies were referenced to an adventitious C 1s peak at 284.9 eV. Raman spectra were acquired using a Renishaw Raman system 1000, using a helium-neon laser of wavelength 632.8 nm. The Raman system being calibrated against emission lines of neon. Atomic force microscopy

(AFM) was conducted using a Dimension 3100 AFM under ambient conditions. Reflectance and transmittance spectra were recorded between 300 and 1200 nm using a Perkin Elmer lambda 950 photospectrometer. Measurements were standardised relative to a spectralab standard mirror (reflectance) and air (transmittance). Water contact angle measurements were conducted by measuring the spread of an 8/10 μl drop of distilled water, and applying an appropriate calculation.

4.3 The APCVD of TiCl_4 and ${}^t\text{BuAsH}_2$

4.3.1 Introduction

APCVD has been used to deposit TiAs thin films from the reaction of TiCl_4 and ${}^t\text{BuAsH}_2$ onto glass substrates at 450 – 550 °C. The effect of substrate temperature and deposition time length on the resultant TiAs deposits has been investigated, with substrate temperatures of 450, 500 and 550 °C and deposition time lengths of 30, 60 and 120 seconds used. Typically, all APCVD experiments were conducted using TiCl_4 and ${}^t\text{BuAsH}_2$ in a 1:2 ratio, however the ${}^t\text{BuAsH}_2$ was increased in one experiment to give an approximate 1:4 ratio, in order to determine the effect of increasing the amount of arsine on the deposited film composition. The experimental parameters for the films deposited *via* the APCVD of TiCl_4 and ${}^t\text{BuAsH}_2$ are described (**Table 4.1**).

Table 4.1 Experimental conditions for TiAs films deposited from the APCVD of TiCl_4 and ${}^t\text{BuAsH}_2$.

Substrate Temp, °C	N_2 flow rate through TiCl_4 bubbler, L/min; (mol/min)	N_2 flow rate through ${}^t\text{BuAsH}_2$ bubbler, L/min; (mol/min)	Plain line flow, L/min; Mixing chamber temp, °C	Deposition time, secs
450	0.18; (0.00066)	0.1; (0.00128)	4; 130	120
500	0.18; (0.00066)	0.1; (0.00128)	4; 140	30
500	0.18; (0.00066)	0.1; (0.00128)	4; 130	60
500	0.18; (0.00066)	0.1; (0.00128)	4; 135	120
550	0.18; (0.00066)	0.1; (0.00128)	4; 130	120
500	0.18; (0.00066)	0.2; (0.00257)	4; 140	60

4.3.2 TiAs Deposition and Visual Appearance

Below 450 °C no deposit was observed, however between substrate temperatures of 450 – 550 °C thin films of TiAs were deposited. At the lower substrate temperatures of 450 °C and 500 °C a silver TiAs film was deposited. Upon increasing the substrate temperature to 550 °C the deposited TiAs films appeared predominantly blue in colour with a gold appearance on the leading edge (**Figure 4.3**).



Figure 4.3 Digital photographs illustrating the difference in visual appearance of the TiAs films deposited *via* the APCVD of TiCl_4 and ${}^t\text{BuAsH}_2$ at deposition temperatures of 450 °C and 500 °C (left), and 550 °C (right).

Upon conduction of compositional analysis on the blue-gold TiAs film deposited at 550 °C, the film demonstrated consistent material composition irrespective of analysed film colour (an approximate composition of $\text{TiAs}_{0.8}\text{Cl}_{0.1}$, **Section 4.3.3.2**). The difference in observed deposit colour from blue to gold can therefore be attributed to a variation in film thickness, rather than a difference in film composition. The blue-gold film observed for the TiAs film deposited at a substrate temperature of 550 °C was consistent in visual appearance to TiP films deposited *via* the APCVD of TiCl_4 and ${}^t\text{BuPH}_2$.³ All TiAs films, particularly those deposited at 450 °C and 500 °C, were highly reflective and did not show any visible change in appearance after approximately twelve months storage in air. Given that depositions only occurred with substrate temperatures exceeding 450 °C, it is possible that this is the temperature required for the two precursors to react completely, thus depositing TiAs. Previous studies have indicated that ${}^t\text{BuAsH}_2$ decomposes *via* the loss of H_2 to produce ${}^t\text{BuAs}$, which can further decompose *via* β -hydride elimination to form 2-methylpropane and AsH ,⁷ one potential decomposition pathway for the APCVD reaction of TiCl_4 and ${}^t\text{BuAsH}_2$. However, as previously discussed (Chapter 2), it has been noted that the reaction of

TiCl₄ with organoarsines results in the formation of adducts, therefore, the APCVD reaction may proceed *via* the formation of a gas phase adduct, such as [TiCl₄(^tBuAsH₂)₂].

All deposited films demonstrated good substrate coverage, with deposition thickness controllable *via* alteration of deposition time length (see **Table 4.1** for experimental details). In order to determine an approximate deposition rate for the TiAs films, side-on SEM analysis was used to measure approximate film thicknesses. Film thicknesses were found to increase from 190 nm at 450 °C to 270 nm at 550 °C for films deposited using a deposition time length of 120 seconds. Due to difficulties in imaging the TiAs film deposited at 500 °C for 120 seconds, the film thickness for TiAs deposited at 500 °C for 60 seconds was measured and found to be 110 nm. Based upon the assumption that a linear relationship exists between deposition time length and the observed film thickness, a film thickness of 220 nm is expected for TiAs deposited at 500 °C for 120 seconds. Upon comparing the TiAs deposition rates with substrate temperature, an approximately linear relationship was observed; this temperature-growth relationship for TiAs was expected (**Figure 4.4**).

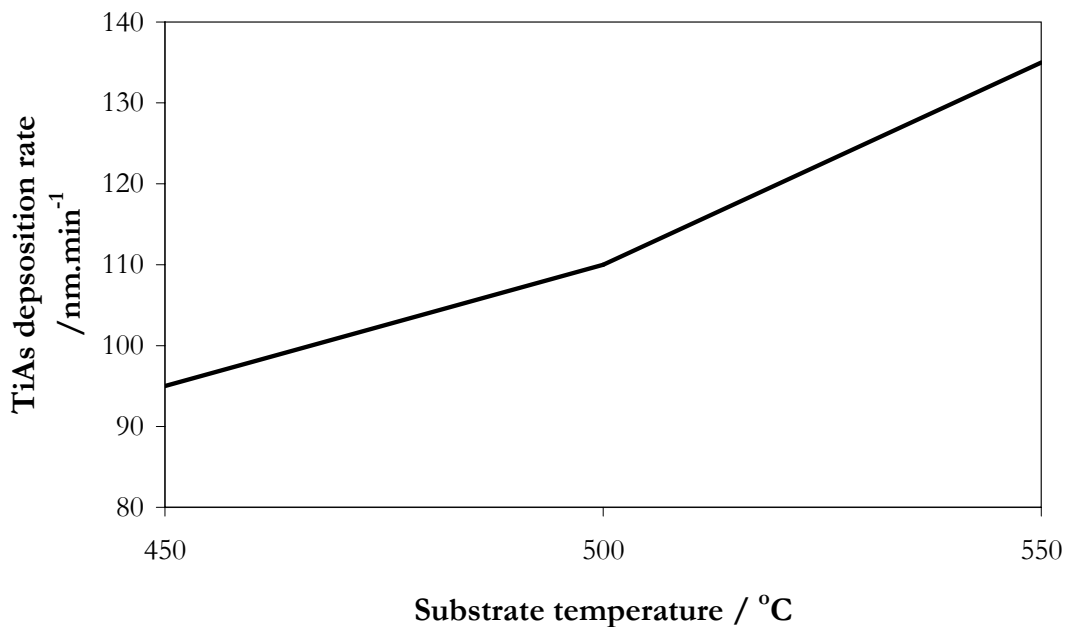


Figure 4.4 The effect of substrate temperature on the deposition rate of TiAs from the APCVD of TiCl₄ and ^tBuAsH₂.

4.3.3 TiAs Characterisation

4.3.3.1 Powder X-ray Diffraction Analysis (XRD)

X-ray powder diffraction of both the silver and blue TiAs films obtained from the reaction of $t\text{-BuAsH}_2$ and TiCl_4 produced diffractograms consistent with the formation of crystalline TiAs,⁸ with peaks observed at approximately 29.6, 32.0, 37.0, 41.3, 47.5, 50.2, 54.0 and 58.9 $2\theta/^\circ$. All films produced powder X-ray diffractograms consistent with that shown for TiAs deposited at 550 $^\circ\text{C}$ (**Figure 4.5**). Strong peaks were observed along the (102) and (110) planes indicative of preferred orientation, with the weakly diffracting (103) planes near perpendicular to the scattering vector. In addition to peaks associated with TiAs formation, a broad peak was also observed at approximately 22° , which can be attributed to the underlying glass substrate on which the TiAs films were deposited. Line broadening studies utilising the Scherer equation gave an approximate TiAs crystallite size of 90 nm.

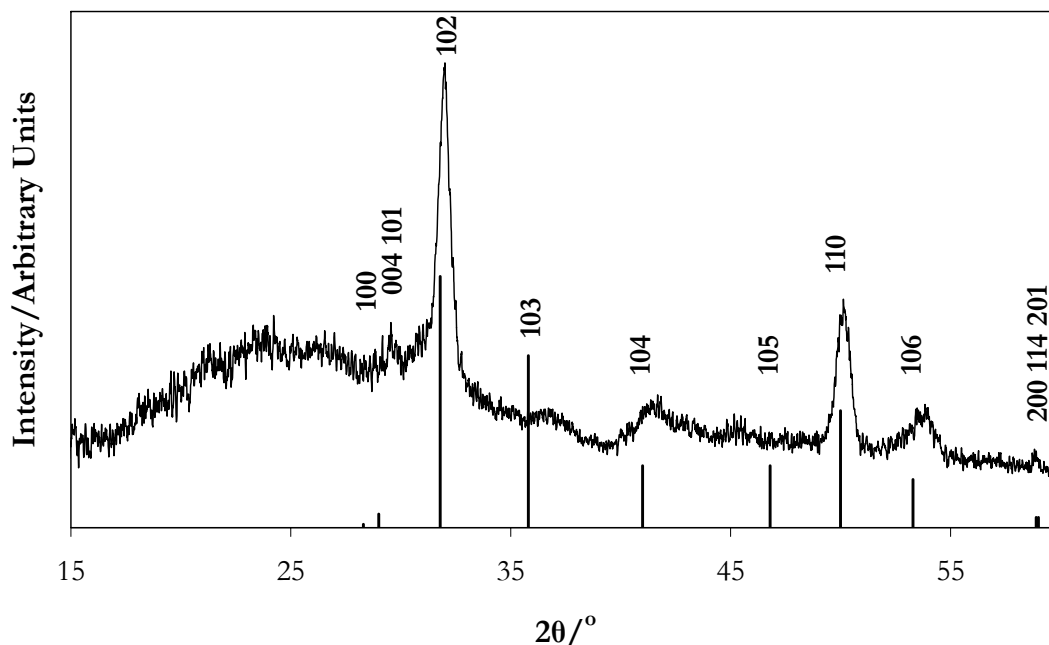


Figure 4.5 Typical X-ray powder diffraction pattern for TiAs films deposited *via* the APCVD of TiCl_4 and $t\text{-BuAsH}_2$ between the substrate temperatures 450 $^\circ\text{C}$ – 550 $^\circ\text{C}$, with comparison to a reference TiAs powder diffractogram of bulk material.⁸

4.3.3.2 Wavelength Dispersive X-ray (WDX) Analysis

Wavelength dispersive X-ray (WDX) analysis showed variable titanium to arsenic ratios within the deposited TiAs films, with films deposited at the substrate temperature of 500 °C and using deposition time lengths of 60 and 120 seconds demonstrating approximate 1:1 ratios of titanium to arsenic. Several of the TiAs films were found to be arsenic deficient, an indication that surface oxidation had occurred. For films deposited using an approximate 1:2 ratio of TiCl₄ to tBuAsH₂ resultant films exhibited an approximate 5 at.% chlorine incorporation, an impurity resulting from the use of the titanium precursor TiCl₄. The observed chlorine incorporation for TiAs deposition was found to be higher than that previously reported for the analogous TiP deposition, for which chlorine incorporation was considered negligible; however, within these TiP depositions, TiCl₄ and tBuPH₂ were used in an approximate 1:4 ratio.³ To investigate the effect of increasing the amount of arsine within the deposition of TiAs, an experiment using a 1:4 ratio of TiCl₄ and tBuAsH₂ was conducted. With this increase in tBuAsH₂, chlorine incorporation was found to reduce to 1 at.% or less, however due to safety concerns regarding abatement of unreacted arsenic species at these high molar flow levels, further experiments were not conducted (**Table 4.2**).

Table 4.2 Wavelength dispersive X-ray (WDX) analysis of TiAs films deposited *via* the APCVD of TiCl₄ and tBuAsH₂ using a range of substrate temperatures, TiCl₄ to tBuAsH₂ ratios and deposition times.

Substrate Temp, °C	Approximate TiCl ₄ :tBuAsH ₂	Deposition time, secs	Atomic percentage based on a TiAsCl species			Ti:As:Cl
			Ti	As	Cl	
450	1:2	120	53.7	39.9	6.4	TiAs _{0.74} Cl _{0.12}
500	1:2	30	39.8	52.3	7.9	TiAs _{1.31} Cl _{0.20}
500	1:2	60	47.5	45.7	6.8	TiAs _{0.96} Cl _{0.14}
500	1:2	120	42.1	46.1	11.8	TiAs _{1.10} Cl _{0.28}
550	1:2	120	55.2	40.0	4.8	TiAs _{0.72} Cl _{0.09}
500	1:4	60	57.3	41.0	1.7	TiAs _{0.72} Cl _{0.03}

Due to the oxyphilic nature of titanium and previous reports of a TiO₂ overlayer within the analogous deposition of TiP,³ a similar TiO₂ overlayer was expected for TiAs. X-ray photoelectron spectroscopy (XPS) confirmed the presence of this layer (**Section 4.3.3.3**) which is believed to have occurred upon exposure of the films to atmospheric conditions following deposition. Upon comparing the oxygen content of a TiAs film deposited at 500 °C for 120 seconds shortly after deposition and after approximately one year of storage in air, the oxygen content was found to be consistent, this indicates that the surface oxidation occurs immediately following deposition and is not due to room temperature oxidation.

4.3.3.3 X-ray Photoelectron Spectroscopy (XPS)

X-ray photoelectron spectroscopy (XPS) analysis was conducted on a TiAs film deposited at a substrate temperature of 500 °C to determine the chemical states of the elements present. The Ti 2p_{3/2} ionisation displayed three surface peaks, with a principal peak detected at 458.5 eV, and two minor peaks at 456.5 eV and 454.0 eV. The Ti 2p_{3/2} peak at 458.5 eV is consistent with that exhibited for TiO₂, with the presence of TiO₂ due to oxidation of the film surface after deposition upon exposure to atmospheric conditions. The Ti 2p_{3/2} peak at 454.0 eV is comparable to that observed for TiP,⁹ and as such, is assigned to TiAs. The As 3d_{5/2} ionisations demonstrated two peaks at 40.0 eV and 40.9 eV, with the peak at 40.0 eV being consistent with that of other metal arsenides,¹⁰ and additionally, demonstrating an approximate 1:1 ratio of normalised peak areas to the Ti 2p_{3/2} peak positioned at 454.0 eV. The O 2p ionisation had two major peaks at 532.3 eV and 530.0 eV, suggesting the presence of SiO₂ and TiO₂ respectively; with the SiO₂ occurring either due to the presence of pin-holes within the film, or a silicon-oxygen polymer found on the surface (i.e. grease). An unassigned Cl 2p_{3/2} peak at 203.7 eV was observed, which supports the observation of chlorine incorporation within the films as determined by WDX. The remaining unassigned peaks were the Ti 2p_{3/2} ionisation observed at 456.5 eV, the As 3d_{5/2} ionisation observed at 40.9 eV and a O 2p_{3/2} ionisation at 534.4 eV; these peaks may correspond to a titanium arsenate species such as Ti₃(AsO₄)₄, however due to difficulties in

comparing normalised peak areas and limited data within the literature, the true identity of this species could not be determined.

In order to probe how the composition of the film changed with depth, and to determine the extent of the observed surface oxidation, depth-profile XPS was conducted. All elements as previously investigated for the XPS on the non-etched sample were included within this analysis, with the addition of carbon analysis also conducted. A C 2p_{3/2} ionisation resulted in a peak at 285.1 eV, with all other peaks as previously reported for the ionisations of the Ti 2p_{3/2}, As 3d_{5/2}, O 2p_{3/2}, Si 2p_{3/2}, and Cl 2p_{3/2} within the XPS of the non-etched sample also observed. Upon comparing how the molar percentages of the titanium species (TiO₂, TiAs and the titanium arsenate species) altered with film depth, it was found that with probing, the molar contribution of the TiO₂ decreased with sample depth, with TiO₂ contributing to approximately 70% of the titanium species at the surface, which was observed to reduce to approximately 20% contribution within the bulk. This result is indicative of the

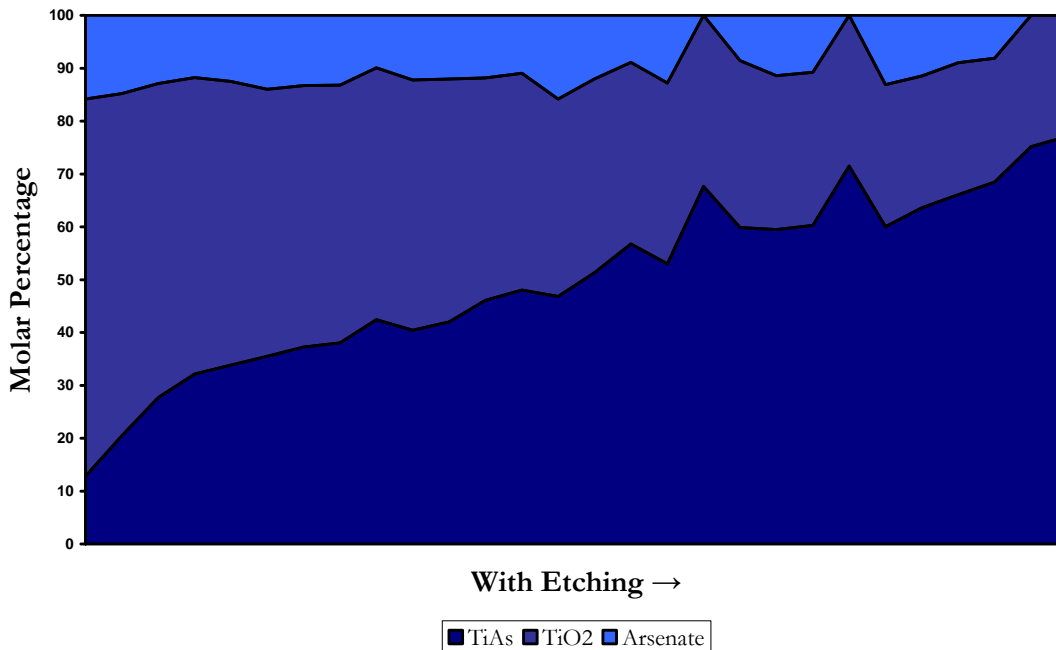


Figure 4.6 Schematic representing how the molar percentage of the titanium species TiAs, TiO₂ and the titanium arsenate species vary with depth within a TiAs film deposited from the APCVD of TiCl₄ and ^tBuAsH₂ at a substrate temperature of 500 °C (total etch time of 27,000 seconds).

presence of a TiO_2 overlayer, which is consistent with that previously observed for TiP .³ In addition, the molar percentage of the titanium arsenate species was also found to decrease upon moving into the bulk of the material, with this also thought to be as a result of surface oxidation. As expected, the TiAs amount was found to increase upon moving from the surface into the bulk of the material, with the titanium species within the bulk found to consist of over 70% TiAs (**Figure 4.6**).

To enable comparison between all species found within the film, and in particular how the carbon, chlorine and silicon content change with sample depth, the atomic percentage composition of the film was considered (**Figure 4.7**). Upon etching, the carbon was observed to rapidly decrease below the detection limit of the instrument, suggesting that the carbon content is surface limited. It should however be noted that with etching, changes within the topography and composition can occur due to preferred sputtering of lighter elements, which could be causing this observation of reduced carbon detection with depth. The chlorine content was found to increase upon etching, with the chlorine increasing in line with TiAs, indicating that the chlorine

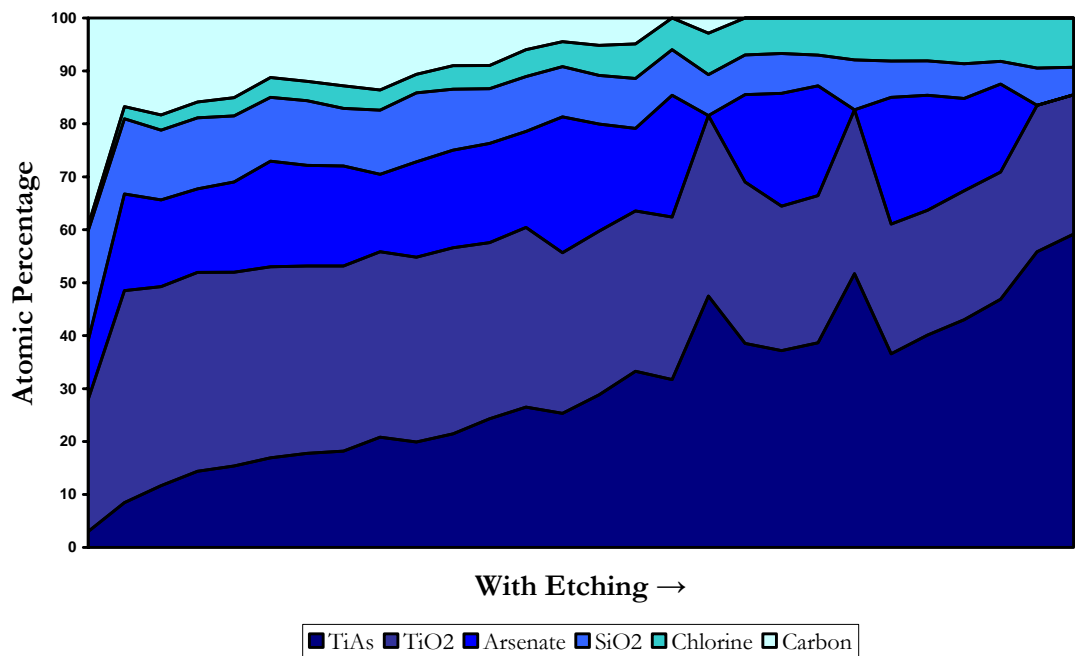


Figure 4.7 Schematic representing how the atomic percentage composition varies with depth within a TiAs film deposited from the APCVD of TiCl_4 and BuAsH_2 at a substrate temperature of $500\text{ }^\circ\text{C}$ (total etch time of 27,000 seconds).

incorporation is a feature of the bulk TiAs material. The silicon was also observed to decrease upon moving into the bulk, suggesting that the higher level of silicon observed at the surface is due to the presence of both surface silicon (e.g. grease) and SiO₂ from the underlying substrate.

4.3.3.4 Raman Microscopy Analysis

Raman microscopy was conducted on all TiAs films deposited using a 1:2 ratio of TiCl₄ to tBuAsH₂. All Raman patterns were found to be consistent between different regions of the same deposit, in addition to films deposited using different conditions (**Figure 4.8**). Typically, Raman patterns demonstrated two relatively intense sharp peaks at 193 and 244 cm⁻¹, and two weak broad peaks at 420 and 600 cm⁻¹. Although no Raman patterns have been previously reported for titanium arsenide, the obtained Raman patterns exhibited similar peaks to that previously reported for TiP, which demonstrates two peaks at the higher energies of 320 and 248 cm⁻¹, with the observed peak shift expected upon substitution for a heavier atom.³

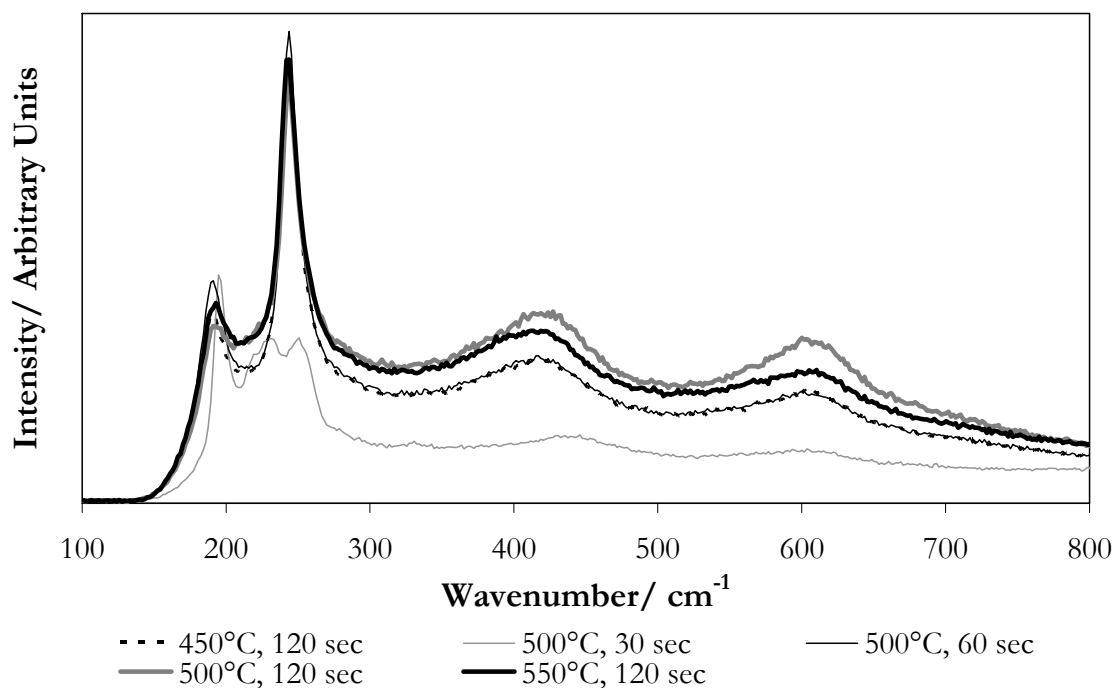


Figure 4.8 Raman spectra for TiAs films deposited *via* the APCVD of TiCl₄ and tBuAsH₂ at substrate temperatures 450 – 550 °C and deposition time lengths of 30, 60 and 120 seconds.

4.3.4 TiAs Morphology

4.3.4.1 Scanning Electron Microscopy Analysis (SEM)

To investigate the mechanism of TiAs deposition and to determine how alteration of both deposition time and substrate temperature affected the deposited films, comparative scanning electron microscopy (SEM) analysis was conducted. SEM images were obtained for films deposited at 500 °C using deposition times of 30, 60 and 120 seconds (**Figure 4.9**), in an attempt to capture how the films deposit over time. Upon comparison of the images, an island growth mechanism was elegantly demonstrated, with nucleation and growth of discrete islands clearly evident, and the formation of agglomerates and a more continuous film observed with an increase in deposition time length. The observed TiAs agglomerates were found to be roughly spherical, with approximate sizes of 150, 200 and 400 nm at deposition time lengths of 30, 60 and 120 seconds, respectively. As expected, these agglomerate sizes are larger than the previously reported crystallite size of 90 nm obtained from line broadening studies (**Section 4.3.3.1**), with the island growth mechanism of deposition consistent with that previously reported for TiP.³

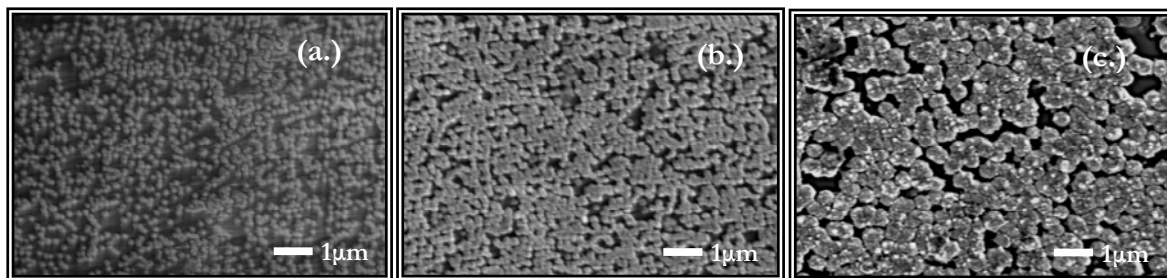


Figure 4.9 Scanning electron micrographs of TiAs film deposited *via* the APCVD of TiCl_4 and BuAsH_2 at 500 °C using deposition times of 30 (a), 60 (b) and 120 seconds (c) (x10,000 magnification).

In addition to investigating how the TiAs films altered with an increase in deposition time length, comparative SEM analysis was also conducted on three TiAs films deposited at 450 °C, 500 °C and 550 °C using a deposition time of 120 seconds, to determine how alteration of substrate temperature affected the TiAs films deposited (**Figure 4.10**). As expected, an increase in substrate temperature resulted in the

observation of a more continuous material, the result of an increase in nucleation and growth with the increase in substrate temperature.

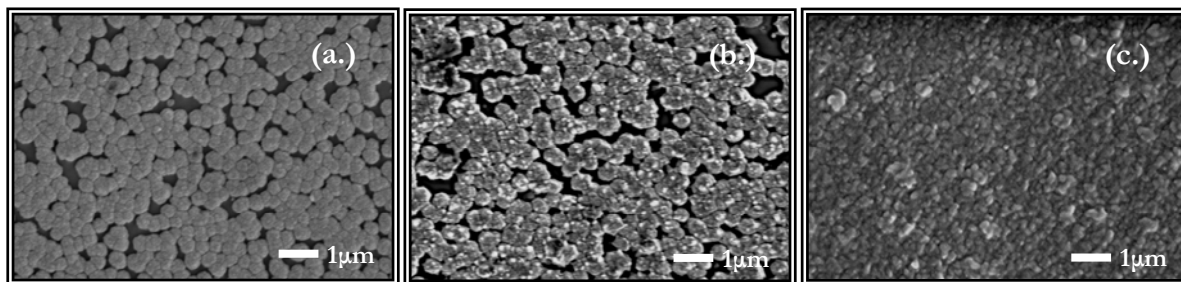


Figure 4.10 Scanning electron micrographs of TiAs films deposited *via* the APCVD of TiCl_4 and ${}^t\text{BuAsH}_2$ using a deposition time of 120 seconds and substrate temperatures of 450 (a), 500 (b) and 550 °C (c) (x10,000 magnification).

Although the TiAs films typically demonstrated a continuous material deposit, regions where material had failed to nucleate and grow were observed for all films, thought to be as a result of large particles which have formed in the gas phase (**Figure 4.11**).

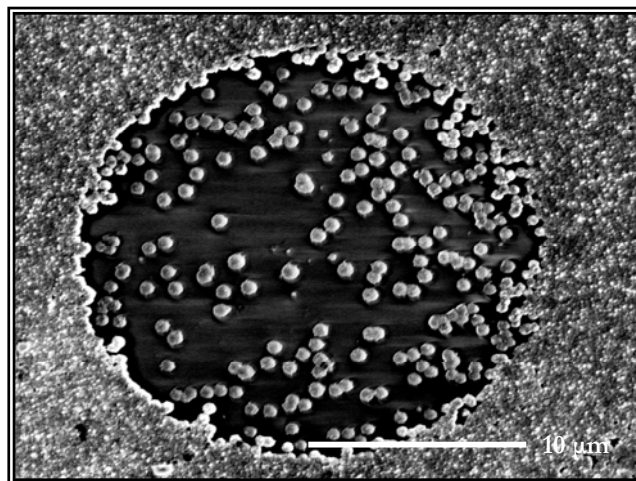


Figure 4.11 Scanning electron micrograph of an un-nucleated area within a TiAs film deposited *via* the APCVD of TiCl_4 and ${}^t\text{BuAsH}_2$ at 500 °C for 120 seconds (x3,700 magnification).

4.3.4.2 Atomic Force Microscopy (AFM) Analysis

As a continuation from the comparative SEM image analysis, and to gain further insight into the surface of the TiAs thin films, atomic force microscopy (AFM)

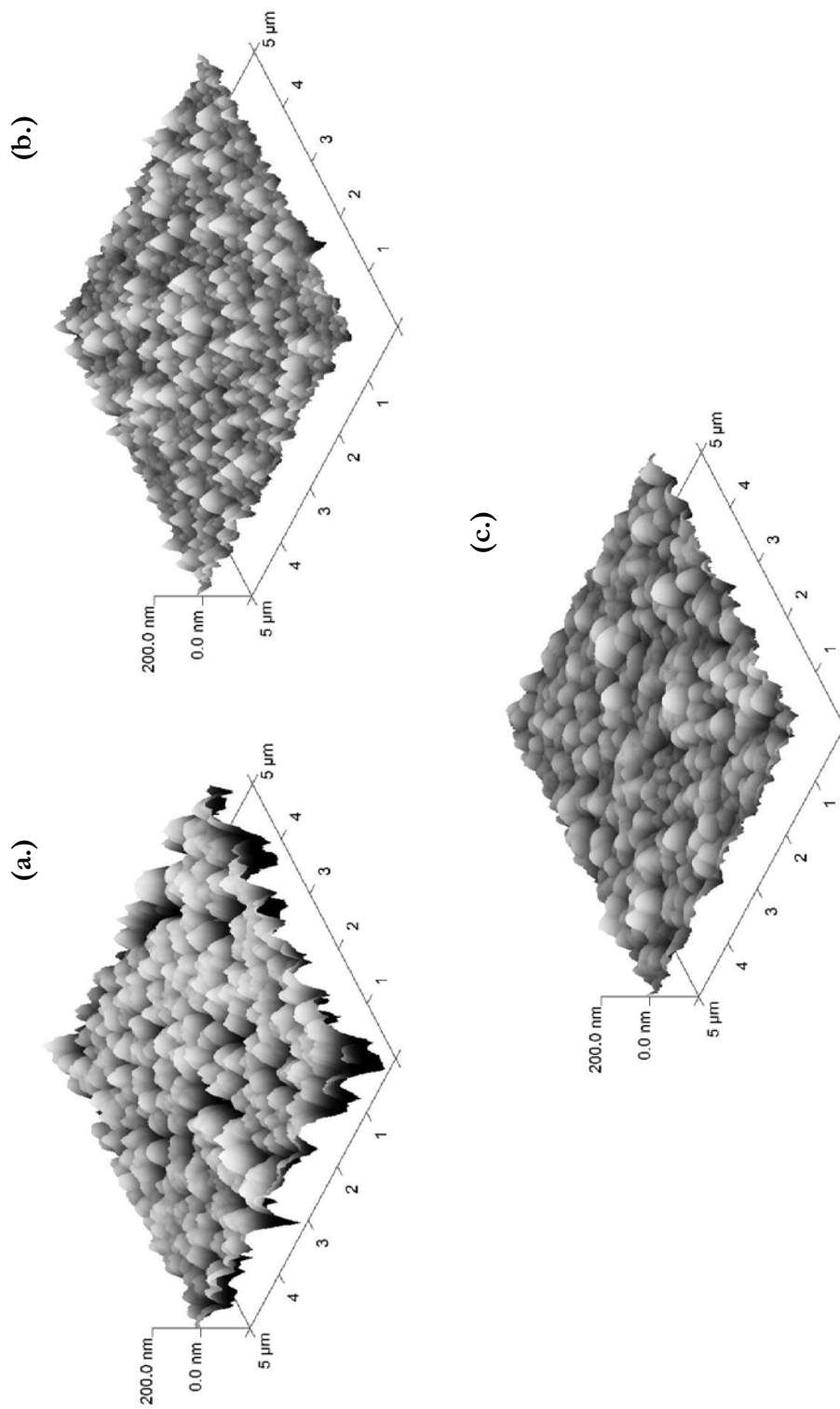


Figure 4.12 Atomic force micrographs representing a $5\ \mu\text{m} \times 5\ \mu\text{m}$ region of TiAs deposited using a deposition time of 120 seconds and substrate temperatures of $450\ ^\circ\text{C}$ (a), $500\ ^\circ\text{C}$ (b) and $550\ ^\circ\text{C}$ (c).

analysis was conducted. AFM micrographs representing 5 μm x 5 μm regions were obtained for TiAs films deposited using a deposition time of 120 seconds at substrate temperatures of 450 °C, 500 °C and 550 °C (**Figure 4.12**).

The TiAs films demonstrated a decrease in surface roughness upon an increase in substrate temperature, with RMS values of 44.9 nm, 21.3 nm and 20.2 nm found at substrate temperatures of 450 °C, 500 °C and 550 °C respectively. This decrease in surface roughness is in agreement with that observed during the SEM analysis, whereby an increase in substrate temperature resulted in a more continuous film due to a decrease in discrete islands of material.

4.3.5 TiAs Film Properties

4.3.5.1 Adherence, Hardness and Resistivity

Upon investigation into film adherence, excluding that for the TiAs film deposited at 500 °C for 120 seconds which exhibited regions of delamination, all films passed the Scotch tape test. The TiAs film deposited at 550 °C for 120 seconds was the only film to pass the steel stylus test, exhibiting comparable hardness to that of previously reported TiP films. Additionally, all TiAs films demonstrated resistivities in the range of 10 – 50 $\text{m}\Omega\text{ cm}$, indicative of borderline metallic- or semiconductor-like conductivity, with resistivities also consistent with that previously reported for TiP.³

4.3.5.2 Optical Properties

Reflectance measurements of the TiAs films showed them to display less reflectivity within the IR region, contradictory to that observed for TiP which exhibits increased reflectivity within this region (**Figure 4.13**).³

The thickest TiAs films demonstrated 0% transmission over all wavelengths, whereas the thinnest film (i.e. that deposited for 30 seconds), demonstrated an approximate 40% transmittance over the analysed wavelength range, which may be as a result of pin-holes within the films and non-continuous coverage (**Figure 4.14**).

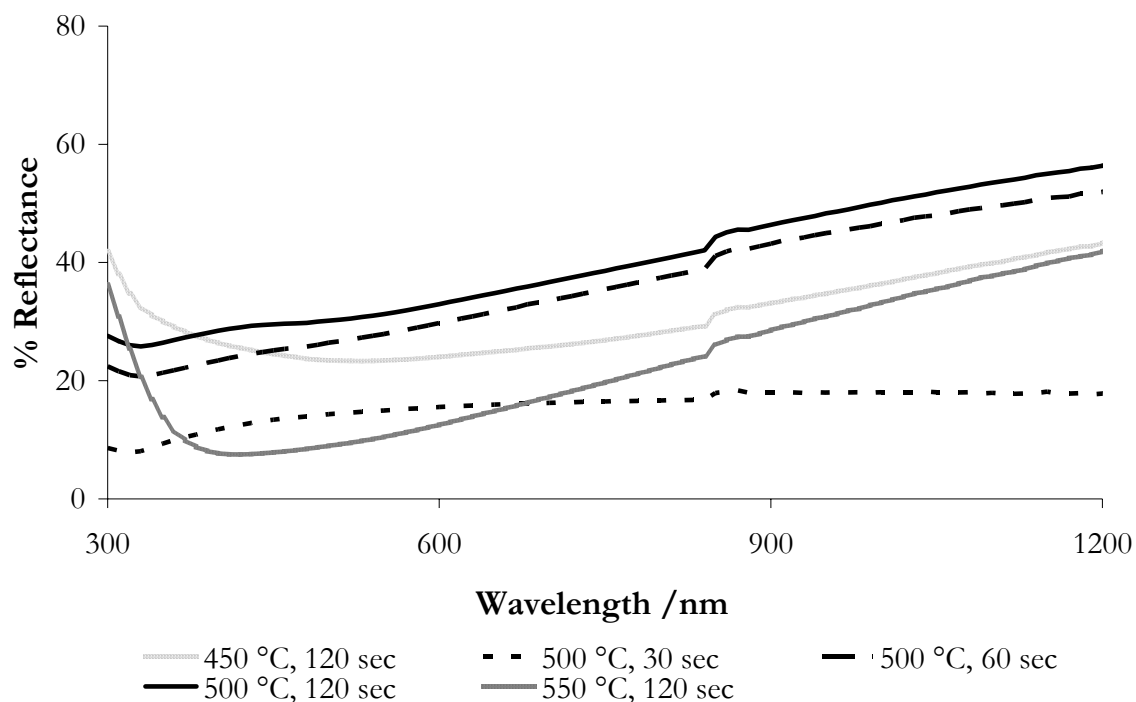


Figure 4.13 Percentage reflectance data for TiAs films deposited *via* the APCVD of TiCl_4 and tBuAsH_2 using a range of substrate temperatures and deposition times.

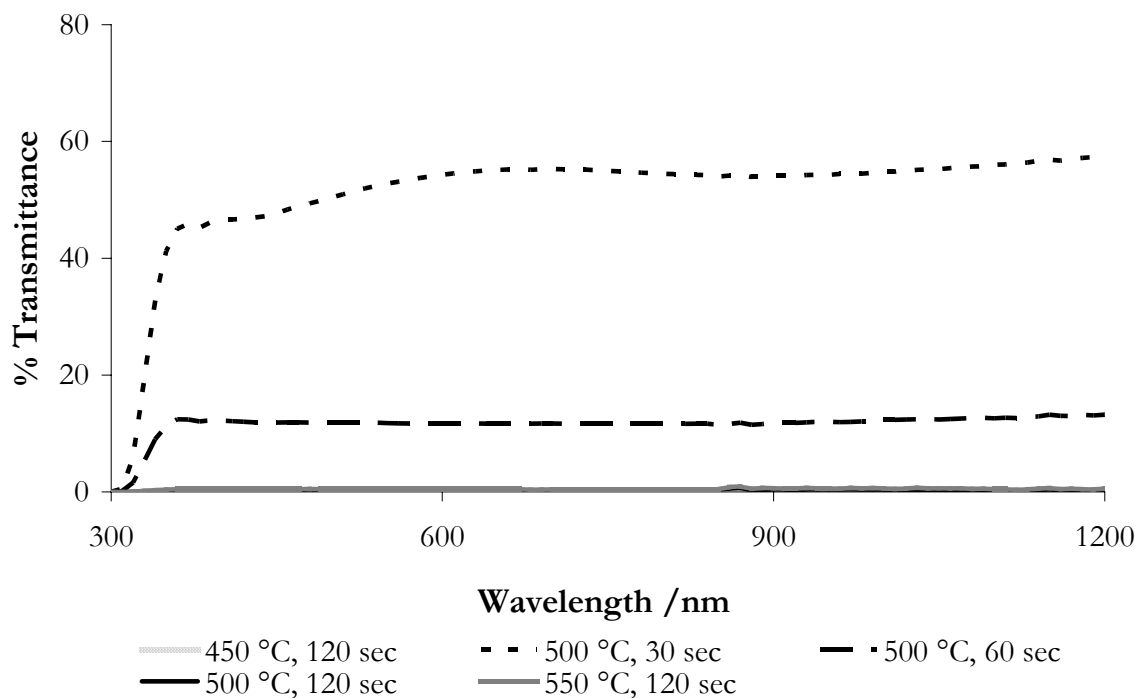


Figure 4.14 Percentage transmittance measurements for TiAs films deposited *via* the APCVD of TiCl_4 and tBuAsH_2 using a range of substrate temperatures and deposition times.

4.3.5.3 Water Contact Angle Measurements

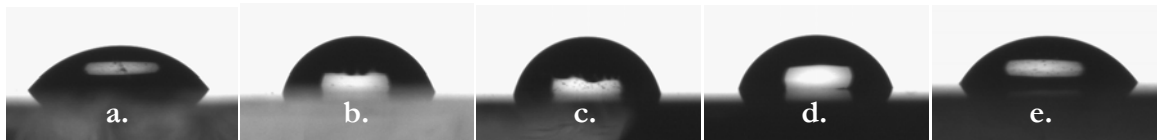


Figure 4.15 Photographs of a 10 μl water droplet on the surface of TiAs deposited *via* the APCVD of TiCl_4 and tBuAsH_2 .

Water contact angle measurements of a 10 μl water droplet were conducted on TiAs films deposited using different substrate temperatures and deposition times (**Figure 4.15 and Table 4.3**). The TiAs films deposited at 450 $^{\circ}\text{C}$ and 550 $^{\circ}\text{C}$ demonstrated water contact angles in the region of 45 $^{\circ}$ – 65 $^{\circ}$, with an increase in water contact angles to 70 $^{\circ}$ – 100 $^{\circ}$ for films deposited using a substrate temperature of 500 $^{\circ}\text{C}$. These values are typical for that of a hydrophobic material, and consistent with that previously reported for TiP.³ It should however be noted that due to the TiO_2 overlayer, these water contact angles may not be a true measurement of the bulk material, and may indeed represent the TiO_2 overlayer only.

Table 4.3 Water contact angle measurements ($^{\circ}$) of TiAs films deposited *via* the APCVD of TiCl_4 and tBuAsH_2 .

Image	Substrate Temp, $^{\circ}\text{C}$	Deposition time, secs	Water contact angles ($^{\circ}$) on three areas			Approximate $^{\circ}$ Range
			1	2	3	
a	450	120	56	66	46	45 - 65
b	500	30	77	75	99	75 - 100
c	500	60	76	76	96	75 - 100
d	500	120	72	75	73	70 - 75
e	550	120	56	54	56	50 - 55

4.3.6 Conclusions

Crystalline TiAs films have been successfully deposited from the APCVD of TiCl_4 and tBuAsH_2 between substrate temperatures $450\text{ }^\circ\text{C} - 550\text{ }^\circ\text{C}$. The TiAs films were found to be typically silver in appearance, demonstrate high reflectivity and hardness, and exhibit borderline metallic-semiconductor resistivities. The films exhibited an approximate 1:1 ratio of Ti:As, in addition to a 5 at.% chlorine incorporation when TiCl_4 and tBuAsH_2 were used in a 1:2 ratio. The films were hydrophobic, transparent when sufficiently thin and found to deposit *via* an island growth mechanism.

4.4 The APCVD of [Ti(NMe₂)₄] and ^tBuAsH₂

4.4.1 Introduction

Following the successful deposition of TiAs films *via* the APCVD of TiCl₄ and ^tBuAsH₂, investigation into an alternative titanium precursor to TiCl₄ was conducted. An alternative precursor would not only enable deposition of the TiAs films at different CVD conditions, and hence potentially alter the expressed properties of the films, but due to the problems associated with chlorine incorporation when using TiCl₄, could serve as a route to prevent this; as such [Ti(NMe₂)₄] was investigated.

It was expected that upon the substitution of TiCl₄ with the organometallic titanium precursor [Ti(NMe₂)₄], TiAs deposition would occur at a lower substrate temperature. This was indeed the case, with TiAs successfully deposited *via* the APCVD of [Ti(NMe₂)₄] and ^tBuAsH₂ over substrate temperatures 350 – 550 °C. Similarly to that of the APCVD using TiCl₄ and ^tBuAsH₂, both the effect of substrate temperature and deposition time length on the resultant TiAs deposits were investigated, with substrate temperatures of 350 °C, 400 °C, 450 °C, 500 °C and 550 °C and deposition time lengths of 60 and 120 seconds used. In this instance, all APCVD experiments were conducted with [Ti(NMe₂)₄] and ^tBuAsH₂ used in an approximate 1:2 ratio (**Table 4.4**).

Table 4.4 Experimental conditions for TiAs films deposited from the APCVD of [Ti(NMe₂)₄] and ^tBuAsH₂.

Substrate Temp, °C	N ₂ flow rate through [Ti(NMe ₂) ₄] bubbler, L/min; (mol/min)	N ₂ flow rate through ^t BuAsH ₂ bubbler, L/min; (mol/min)	Plain line flow, L/min; Mixing chamber temp, °C	Deposition time, secs
350	0.4; (0.00062)	0.1; (0.00128)	1.8; 150	60
400	0.4; (0.00062)	0.1; (0.00128)	1.8; 160	60
450	0.4; (0.00062)	0.1; (0.00128)	1.8; 160	60
500	0.4; (0.00062)	0.1; (0.00128)	1.8; 150	60
500	0.4; (0.00062)	0.1; (0.00128)	1.8; 160	120
550	0.4; (0.00062)	0.1; (0.00128)	1.8; 150	60

4.4.2 TiAs Deposition and Visual Appearance

Below 350 °C no deposit was observed, however between the substrate temperatures of 350 – 550 °C thin films of TiAs were deposited from the CVD reaction of $[\text{Ti}(\text{NMe}_2)_4]$ and ${}^t\text{BuAsH}_2$. Unlike the APCVD of TiAs using TiCl_4 and ${}^t\text{BuAsH}_2$, all depositions using the titanium precursor $[\text{Ti}(\text{NMe}_2)_4]$ produced films which were visually consistent, with all films being predominately silver in colour with a gold appearance on the leading edge (**Figure 4.16**).



Figure 4.16 Digital photographs illustrating the high reflectivity (left) and gold appearance on the leading edge (right) of TiAs films deposited *via* the APCVD of $[\text{Ti}(\text{NMe}_2)_4]$ and ${}^t\text{BuAsH}_2$.

All deposited films demonstrated good substrate coverage at all investigated deposition temperatures. Side-on SEM analysis was used to determine a film thickness of 309 nm for a TiAs film deposited at 500 °C for 120 seconds, corresponding to a deposition rate of $\sim 154 \text{ nm min}^{-1}$. This rate was consistent with that previously reported when using TiCl_4 as a titanium precursor, although it was found to be significantly different to that reported for TiP films deposited using $[\text{Ti}(\text{NMe}_2)_4]$ at 500 °C ($\sim 235 \text{ nm min}^{-1}$). It should however be noted that a different phosphine precursor was used in this instance ($\text{Cy}^{\text{Hex}}\text{PH}_2$), in addition to the higher $[\text{Ti}(\text{NMe}_2)_4]$ to phosphine ratio of 1:5.⁵

4.4.3 TiAs Characterisation

4.4.3.1 X-ray Powder Diffraction (XRD) Analysis

X-ray powder diffraction was conducted on all TiAs films, with all films irrespective of the region of deposition, or specific deposition conditions used, producing diffractograms consistent with the formation of crystalline TiAs,⁸ with peaks observed at approximately 29.6, 31.7, 36.0, 41.3, 47.3, 49.8, 54.1 and 58.8 2 θ /° (**Figure 4.17**). Unlike the powder diffractogram for TiAs films deposited using TiCl₄, a much stronger peak along the (103) plane was observed, and indeed all other peaks appeared more intense. Again, a broad peak was observed at approximately 22°, which can be attributed to the underlying glass substrate.

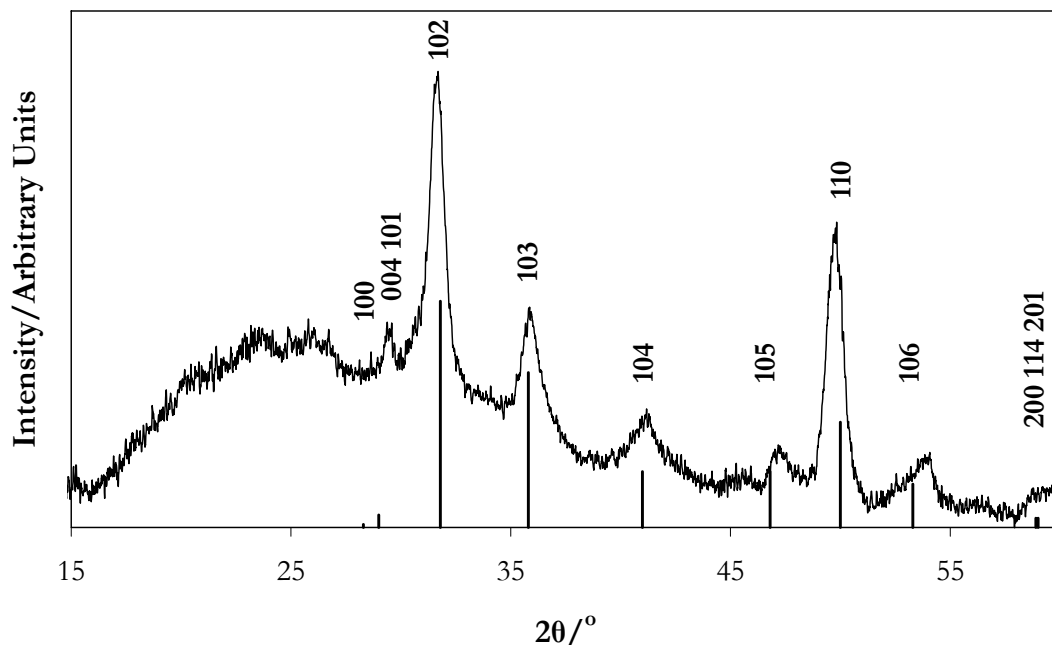


Figure 4.17 Typical X-ray powder diffraction pattern for TiAs films deposited *via* the APCVD of [Ti(NMe₂)₄] and ^tBuAsH₂ between the substrate temperatures 350 °C – 500 °C, with comparison to a reference TiAs diffractogram of bulk material.⁸

On comparing diffractograms of TiAs films deposited *via* the APCVD of [Ti(NMe₂)₄] and ^tBuAsH₂, under the same conditions but at different substrate temperatures, a slight increase in crystallinity was observed for films deposited at 500 °C compared to those deposited at 450 °C (**Figure 4.18**); in particular, a large increase

in peak intensity was observed for the 110 plane, suggesting that preferred orientation was occurring.

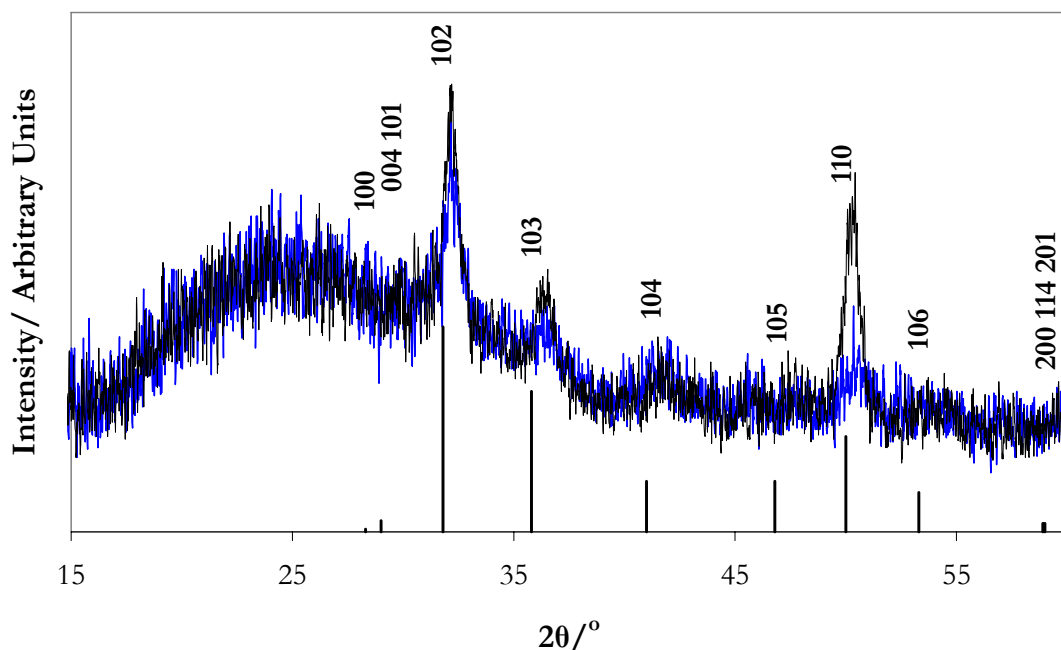


Figure 4.18 X-ray powder diffraction patterns for TiAs films deposited *via* the APCVD of $[\text{Ti}(\text{NMe}_2)_4]$ and ${}^1\text{BuAsH}_2$ in a 1:2 ratio, using a deposition time length of 60 seconds, at substrate temperatures of 450 °C (blue), and 500 °C (black), with comparison to a reference TiAs diffractogram of bulk material.⁸

4.4.3.2 Wavelength Dispersive X-ray (WDX) Analysis

Similarly to when using TiCl_4 , WDX analysis showed variable titanium to arsenic ratios when using $[\text{Ti}(\text{NMe}_2)_4]$ as the titanium precursor. For films deposited at 500 °C and 550 °C using a deposition time of 60 seconds, approximately 1:1 ratios of titanium to arsenic were observed, with all other films close to this ratio (**Table 4.5**). Unlike when using TiCl_4 , the film deposited at 350 °C was the only film found to be arsenic deficient, with the majority of TiAs films typically exhibiting a high arsenic content. Due to the titanium line being close to the nitrogen line within WDX analysis, the nitrogen content could not be determined using this method.

Table 4.5 Wavelength dispersive X-ray analysis of TiAs films deposited *via* the APCVD of $[\text{Ti}(\text{NMe}_2)_4]$ and BuAsH_2 in a 1:2 ratio, using a range of substrate temperatures and deposition times.

Substrate Temp, °C	Deposition time, secs	Atomic percentage based on a TiAs species		Ti:As
		Ti	As	
350	60	56.6	43.4	TiAs _{0.77}
400	60	39.1	60.9	TiAs _{1.56}
450	60	40.8	59.2	TiAs _{1.45}
500	60	46.7	53.3	TiAs _{1.14}
500	120	39.9	60.1	TiAs _{1.51}
550	60	49.6	50.4	TiAs _{1.02}

4.4.3.3 X-ray Photoelectron Spectroscopy (XPS)

XPS analysis was conducted on a TiAs film deposited at a substrate temperature of 500 °C for 120 seconds. Similarly to that observed when using the titanium precursor TiCl_4 , the Ti $2p_{3/2}$ ionisation displayed three peaks detected at 458.7 eV, 457.0 eV and 455.4 eV, with the peaks at 458.7 and 455.4 eV thought to be TiO_2 and TiAs respectively. The As $3d_{5/2}$ ionisation displayed two peaks at 41.0 and 40.1 eV, with the peak at 40.1 eV being consistent with that previously reported when using TiCl_4 , and demonstrating an approximate 1:1 ratio for normalised peak areas to the Ti $2p_{3/2}$ peak at 455.4 eV. The O $2p$ ionisation had two major peaks at 532.2 eV and 530.4 eV which were assigned to SiO_2 and TiO_2 respectively. Similarly to that previously reported when using TiCl_4 , unassigned Ti $2p_{3/2}$ and As $3d_{5/2}$ peaks at 457.0 eV and 41.0 eV were observed, which may again indicate the presence of a titanium arsenate species. A nitrogen 1s peak at 396 eV, or corresponding Ti $2p$ peaks at 460 eV and 455 eV for TiN were not observed, unlike that previously reported for TiP films deposited *via* the APCVD of $\text{Ti}(\text{NMe}_2)_4$ and $\text{Cy}^{\text{Hex}}\text{PH}_2$, which were found to consist of less than 3 at.% of TiN.⁵ Although depth-profile XPS was not conducted on this film, it is believed that a TiO_2 overlayer, similar to that reported when using TiCl_4 , is present.

4.4.3.4 Raman Microscopy

Raman microscopy was conducted on all TiAs films deposited *via* the APCVD of $[\text{Ti}(\text{NMe}_2)_4]$ and ${}^t\text{BuAsH}_2$. Although the peaks at approximately 193, 420 and 600 cm^{-1} were found to be consistent with the peaks observed when using the titanium precursor TiCl_4 , the peak previously observed at 244 cm^{-1} shifted to approximately 220 cm^{-1} (**Figure 4.19**). Shifts in Raman peaks have been previously observed for metal-rich TiP films,³ which is likely to be the source of the shift here, and is consistent with that reported by WDX analysis (**Section 4.4.3.2**).

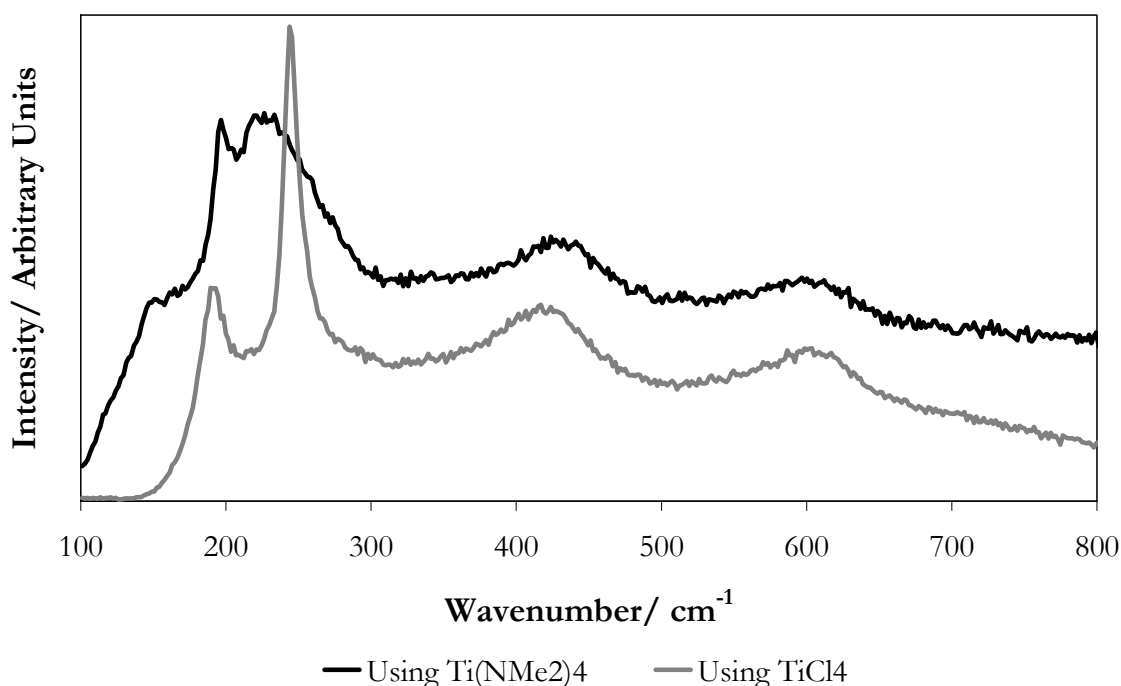


Figure 4.19 Comparison of typical Raman spectra for TiAs films deposited *via* the APCVD of $[\text{Ti}(\text{NMe}_2)_4]$ and ${}^t\text{BuAsH}_2$, and TiCl_4 and ${}^t\text{BuAsH}_2$.

4.4.4 TiAs Morphology

SEM analysis was conducted on all TiAs films to determine how alteration of both deposition time and substrate temperature affected the deposited films. SEM images were obtained for TiAs films deposited at 500 $^\circ\text{C}$ using deposition times of 60 and 120 seconds to illustrate how the TiAs films grew over time (**Figure 4.20**). Upon comparison of the images, roughly spherical agglomerates of approximate sizes 75 nm

and 150 nm were observed for films deposited for 60 and 120 seconds, respectively. Upon comparing these images to the analogous films deposited using TiCl_4 , more continuous films with slightly smaller agglomerate sizes were observed.

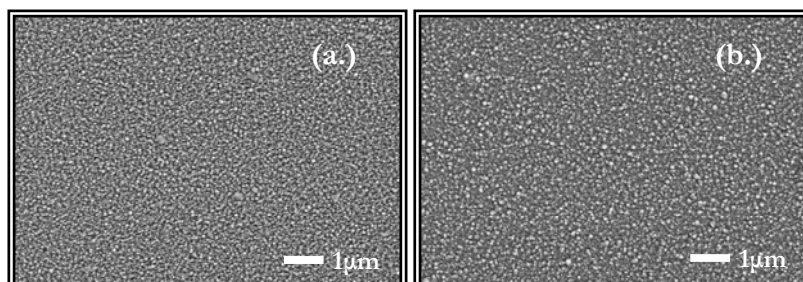


Figure 4.20 Scanning electron micrographs of TiAs films deposited *via* the APCVD of $[\text{Ti}(\text{NMe}_2)_4]$ and ${}^t\text{BuAsH}_2$ using a substrate temperature of 500 °C and deposition times of 60 (left) and 120 (right) seconds (x10,000 magnification).

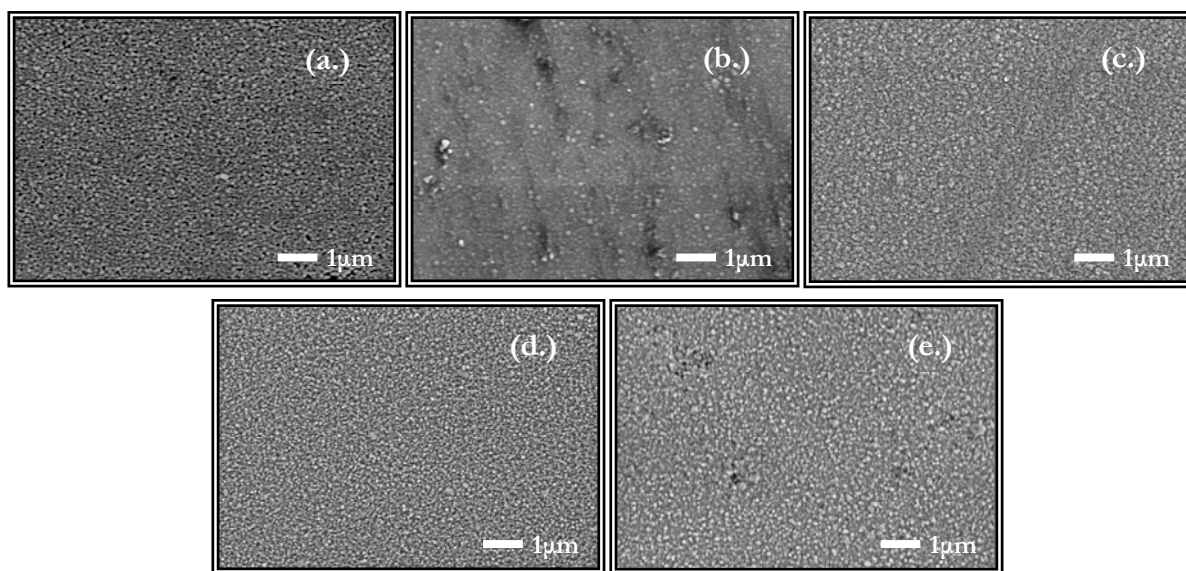


Figure 4.21 Scanning electron micrographs of TiAs films deposited *via* the APCVD of $[\text{Ti}(\text{NMe}_2)_4]$ and ${}^t\text{BuAsH}_2$ using a deposition time of 60 seconds and substrate temperatures of 350 °C (a.), 400 °C (b.), 450 °C (c.), 500 °C (d.) and 550 °C (e.) (x10,000 magnification).

Unlike when using TiCl_4 , no regions where material had failed to nucleate and deposit were observed. Discrete islands were evident at higher magnifications,

indicative of an island growth mechanism, consistent with that previously reported for the deposition of TiAs using TiCl_4 (**Figure 4.22**).

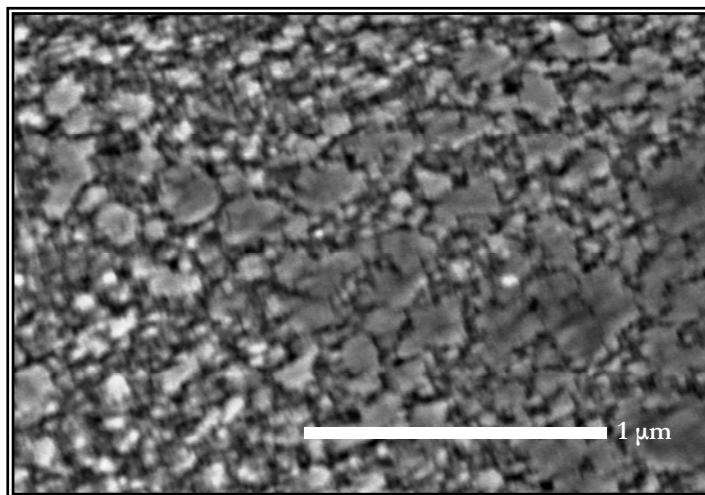


Figure 4.22 Scanning electron micrograph representing a typical image of the TiAs films deposited *via* the APCVD of $[\text{Ti}(\text{NMe}_2)_4]$ and BuAsH_2 showing islands of deposit (x40,000 magnification).

4.4.5 TiAs Film Properties

4.4.5.1 Adherence, Hardness and Resistivity

All films passed the Scotch tape test, however partial delamination was observed for the TiAs film deposited at 400 °C for 60 seconds. Although this film exhibited partial delamination, it was however the only film to pass the steel stylus test, thus demonstrating a similar hardness to previously reported TiP films.³ Similarly to TiAs films deposited using TiCl_4 , the films exhibited resistivities indicative of borderline metallic- or semiconductor-like conductivity.

4.4.5.2 Optical Properties

Similarly to that reported for TiAs films deposited using TiCl_4 , reflectance measurements of the TiAs films deposited using $[\text{Ti}(\text{NMe}_2)_4]$ indicated less reflectivity within the IR region. Upon comparison of TiAs films deposited at 500 °C for 60 and

120 second deposition time lengths, films deposited using $[\text{Ti}(\text{NMe}_2)_4]$ were less reflective than those using TiCl_4 (**Figure 4.23**).

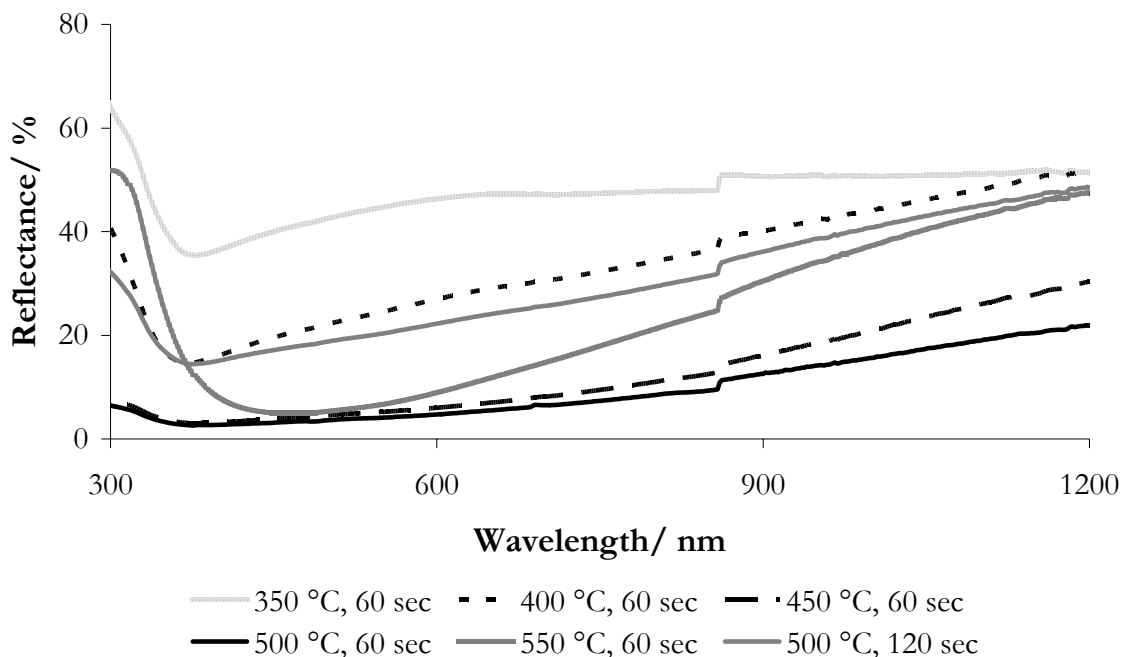


Figure 4.23 Percentage reflectance data for TiAs films deposited *via* the APCVD of $[\text{Ti}(\text{NMe}_2)_4]$ and ${}^t\text{BuAsH}_2$ using a range of substrate temperatures and deposition times.

Although thickness measurements for all films were not conducted, transmittance measurements can be used as an approximation of film thickness. From the results, it is likely that the film deposited at 350 °C is the thinnest, as it shows the highest percentage transmittance (approximately 25%) compared to all other films. Typically, regardless of specific film deposition conditions, all TiAs films deposited *via* the APCVD of $[\text{Ti}(\text{NMe}_2)_4]$ and ${}^t\text{BuAsH}_2$ demonstrated an equal transmittance over all analysed wavelengths (**Figure 4.24**). Upon comparing TiAs films deposited at 500 °C for 60 and 120 second deposition time lengths, both films using $[\text{Ti}(\text{NMe}_2)_4]$ exhibited approximately 0% transmittance, whilst that of the TiCl_4 deposited film exhibited approximately 10% transmittance when deposited for 60 seconds.

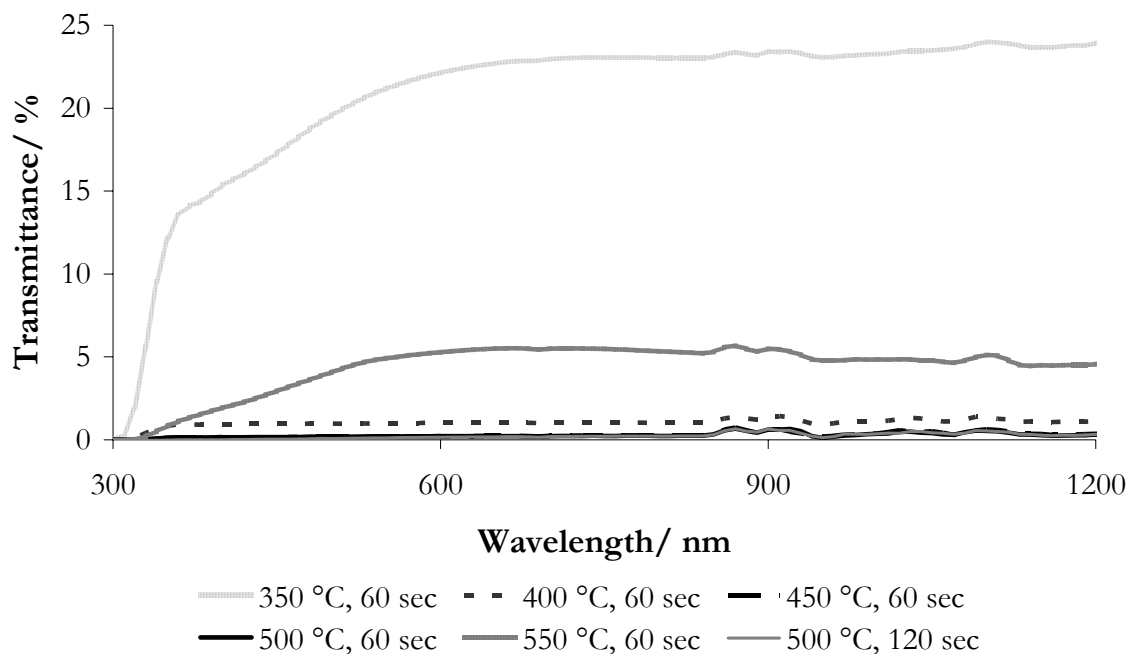


Figure 4.24 Percentage transmittance data for TiAs films deposited *via* the APCVD of $[\text{Ti}(\text{NMe}_2)_4]$ and ${}^t\text{BuAsH}_2$ using a range of substrate temperatures and deposition times.

4.4.5.3 Water Contact Angle Measurements

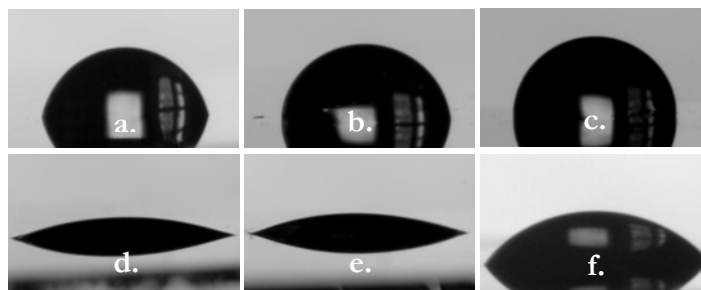


Figure 4.25 Photographs of an 8 μl water droplet on the surface of TiAs deposited *via* the APCVD of $[\text{Ti}(\text{NMe}_2)_4]$ and ${}^t\text{BuAsH}_2$.

Water contact angle measurements of an 8 μl water droplet were conducted on TiAs films deposited using different substrate temperatures and deposition times (**Figure 4.25 and Table 4.6**). Unlike the TiAs films deposited using TiCl_4 , some TiAs films deposited using $[\text{Ti}(\text{NMe}_2)_4]$ exhibited mild hydrophilicity when deposited at 450 and 500 °C, with contact angles as low as 12° reported. Excluding these films, all other

TiAs films exhibited contact angles in the region $50 - 90^\circ$, typical for that of hydrophobic material and consistent with that previously reported using the titanium precursor TiCl_4 . However, similar to that previously reported, it should be noted that these water contact angles may be as a result of the TiO_2 overlayer, rather than the bulk TiAs material.

Table 4.6 Water contact angle measurements ($^\circ$) of TiAs films deposited *via* the APCVD of $[\text{Ti}(\text{NMe}_2)_4]$ and ${}^t\text{BuAsH}_2$.

Image	Substrate Temp, $^\circ\text{C}$	Deposition time, secs	Water contact angles ($^\circ$) on three areas			Approximate $^\circ$ Range
			1	2	3	
a	350	60	74	71	54	55 – 75
b	400	60	84	84	70	70 – 85
c	450	60	26	91	86	25 – 85
d	500	60	12	17	26	10 – 25
e	500	120	19	50	50	20 – 50
f	550	60	49	55	57	50 – 60

4.4.6 Conclusions

Crystalline TiAs films have been successfully deposited from the APCVD of $[\text{Ti}(\text{NMe}_2)_4]$ and ${}^t\text{BuAsH}_2$ between substrate temperatures $350\text{ }^\circ\text{C} - 550\text{ }^\circ\text{C}$. The TiAs films were silver in appearance with a gold leading edge, demonstrated very high visible reflectivity and hardness, and exhibited borderline metallic-semiconductor resistivities. As expected, TiAs films deposited using $[\text{Ti}(\text{NMe}_2)_4]$ were found to deposit at lower deposition temperatures compared to TiCl_4 , with both precursors exhibiting similar deposition rates at a substrate temperature of $500\text{ }^\circ\text{C}$ (ca. 110 and 154 nm min^{-1}). TiAs films deposited using $[\text{Ti}(\text{NMe}_2)_4]$ at $500\text{ }^\circ\text{C}$ for 60 and 120 seconds were found to be less reflective and exhibit a lower percentage transmittance over the wavelength range $300 - 1200\text{ cm}^{-1}$ upon comparison to comparable films deposited using TiCl_4 . Additionally, films deposited at $450\text{ }^\circ\text{C}$ and $500\text{ }^\circ\text{C}$ using $[\text{Ti}(\text{NMe}_2)_4]$ exhibited

hydrophilicity, however, all other physical properties were found to be consistent between the two deposition methods.

References

- ¹ P. O. Snell, *Acta Chem. Scand.*, 1967, 21, 1773.
- ² J. P. Dekker, P. J. Vanderput, H. J. Veringa and J. Schoonman, *J. Electrochem. Soc.*, 1994, 141, 787.
- ³ C. Blackman, C. J. Carmalt, I. P. Parkin, S. O'Neill, L. Apostolico, K. C. Molloy and S. Rushworth, *Chem. Mater.*, 2002, 14, 3167.
- ⁴ K. Sugiyama, S. Pac, Y. Takahashi and S. Motojima, *J. Electrochem. Soc.*, 1975, 122, 1545.
- ⁵ C. S. Blackman, C. J. Carmalt, S. A. O'Neill, I. P. Parkin, L. Apostolico and K. C. Molloy, *Chem. Mater.*, 2004, 16, 1120.
- ⁶ C. Blackman, C. J. Carmalt, S. A. O'Neill, I. P. Parkin, L. Apostilco and K. C. Molloy, *J. Mater. Chem.*, 2001, 11, 2408.
- ⁷ D. F. Foster, C. Glidewell, G. R. Woolley and D. J. Colehamilton, *Journal of Electronic Materials*, 1995, 24, 1731.
- ⁸ K. Bachmayer, H. N. Nowotny and A. Kohl, *Monatsh. Chem.*, 1955, 86, 39.
- ⁹ C. E. Myers, H. F. Franzen and J. W. Anderegg, *Inorg. Chem.*, 1985, 24, 1822.
- ¹⁰ M. K. Bahl, R. O. Woodall, R. L. Watson and K. J. Irgolic, *J. Chem. Phys.*, 1976, 64, 1210.

Chapter 5

The APCVD of VAs Thin Films

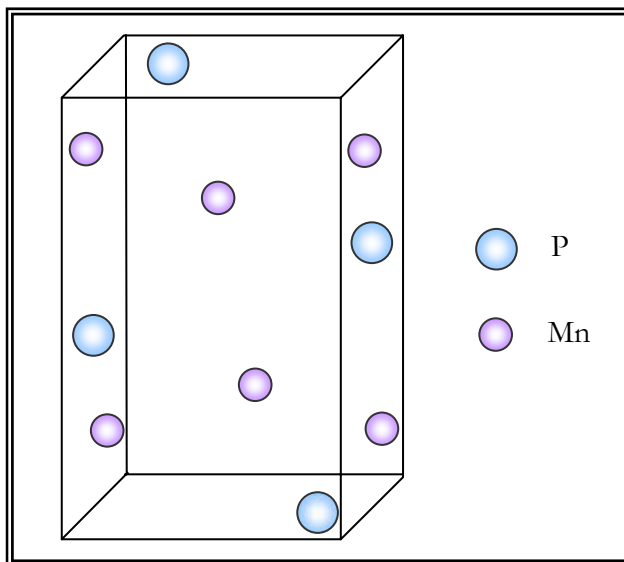


Figure 5.1 The crystal structure of MnP which VAs is known to adopt.¹

5.1 Introduction

Unlike titanium arsenide, vanadium arsenide (VAs) is known to adopt the orthorhombic MnP type crystal structure (**Figure 5.1**), and exhibits a reported average V-As bond length of 2.543 Å.² In an attempt to determine how the film properties change on moving from TiAs to VAs, and following the successful deposition of TiAs films *via* the APCVD reactions of TiCl₄ and [Ti(NMe₂)₄] with ^tBuAsH₂, investigations into VAs film deposition were conducted.

Within the deposition of VP films it was noted that although some APCVD reactions proved successful for the deposition of TiP, they were unsuccessful in the deposition of VP, with both the APCVD of VCl₄ with Cy^{Hex}₂PH and P(SiMe₃)₃

resulting in no film deposition.³ VP films have however been successfully deposited *via* the APCVD of VCl_4 , VOCl_3 and $[\text{V}(\text{NMe}_2)_4]$ with $\text{Cy}^{\text{Hex}}\text{PH}_2$ at 600 °C, and it was hoped that similar results would be observed for the deposition of VAs. Following the success of the arsenic precursor ${}^t\text{BuAsH}_2$ within the deposition of TiAs, and the vanadium precursors VCl_4 and VOCl_3 within the deposition of VP, the APCVD reactions of VCl_4 and VOCl_3 with ${}^t\text{BuAsH}_2$ have been investigated. This chapter describes these APCVD reactions, in addition to discussions regarding the analysis of the deposited films, and comparison of properties to previously deposited VP and TiAs films.

5.2 Experimental

5.2.1 Precursors and Substrate

Nitrogen (99.9%, BOC) was used as a carrier gas in all APCVD experiments. Vanadium (IV) chloride (99.9%, Acros Organic), VOCl_3 (99.9%, Alfa Aesar), and ${}^t\text{BuAsH}_2$ (SAFC Hitech Ltd.), were all utilised in APCVD *via* containment within stainless steel bubblers. Both the VCl_4 and VOCl_3 bubblers were fitted with heating jackets set to 100 °C and 55 °C in all instances, resulting in vapour pressures of approximately 100 Torr and 69 Torr, respectively. Due to the high volatility of ${}^t\text{BuAsH}_2$ a heating jacket was not required, with ${}^t\text{BuAsH}_2$ being used in all instances at room temperature, resulting in an approximate vapour pressure of 181 Torr. Nitrogen, VCl_4 , VOCl_3 and ${}^t\text{BuAsH}_2$ were all used as supplied, without further purification.

APCVD depositions were conducted on 90 mm x 45 mm x 4 mm SiCO float-glass as supplied by Pilkington. Substrates were cleaned with petroleum ether (60 – 80 °C) and 2-propanol and allowed to air dry at room temperature prior to use.

5.2.2 APCVD Equipment and Methods

APCVD was conducted using the methods as described in **Section 4.2**. Exact flows temperatures and deposition times used during experiments are described (**Table 5.1 and Table 5.5**).

5.2.3 Physical Measurements of Deposited Films

Scanning electron microscopy (SEM) was conducted using a JSM-6301F scanning field emission machine. X-ray powder diffraction patterns were obtained using a Brüker AXS D8 discover machine using monochromatic Cu-K α radiation. Wavelength dispersive X-ray (WDX) analysis was performed using a Philips XL30ESEM machine. High resolution X-ray photoemission spectroscopy (XPS) was performed using a Kratos Axis Ultra DLD spectrometer at the University of Nottingham, using a monochromated Al K α ($h\nu = 1486.6$ eV) X-ray source. A standard wide scan with high resolution large areas ($\sim 300 \times 700$ microns) with pass energy 80 and 20 were used respectively. The photoelectrons were detected using a hemispherical analyzer with channelplates and Delay line detector. The etch was performed using 4KeV Argon ions, using a Kratos minibeam III, rastered over an approximate area of 0.7 cm, at an approximate etch rate of 6 Å min⁻¹. The binding energies were referenced to an adventitious C 1s peak at 284.9 eV. Raman spectra were acquired using a Renishaw Raman system 1000, using a helium-neon laser of wavelength 632.8 nm. The Raman system being calibrated against emission lines of neon. Reflectance and transmittance spectra were recorded between 300 and 1200 nm using a Perkin Elmer lambda 950 photospectrometer. Measurements were standardised relative to a spectralab standard mirror (reflectance) and air (transmittance). Water contact angle measurements were conducted by measuring the spread of an 8 μ l drop of water, and applying an appropriate calculation.

5.3 APCVD of VCl₄ and ^tBuAsH₂

5.3.1 Introduction

The APCVD reaction of VCl₄ and ^tBuAsH₂ was used to deposit VAs films between substrate temperatures 550 – 600 °C. All depositions were conducted using VCl₄ and ^tBuAsH₂ in a 1:2 ratio, with deposition times of 60 and 120 seconds investigated. The experimental parameters for the films deposited *via* the APCVD of VCl₄ and ^tBuAsH₂ are described (**Table 5.1**).

Table 5.1 Experimental conditions used to deposit VAs films from the APCVD of VCl_4 and ${}^t\text{BuAsH}_2$.

Substrate temp, °C	N_2 flow rate through VCl_4 bubbler, L/min; (mol/min)	N_2 flow rate through ${}^t\text{BuAsH}_2$ bubbler, L/min; (mol/min)	Plain line flow, L/min; Mixing chamber temp, °C	Deposition time, secs
550	0.1; (0.000621)	0.1; (0.00128)	4; 130	60
550	0.1; (0.000621)	0.1; (0.00128)	4; 130	120
600	0.1; (0.000621)	0.1; (0.00128)	4; 130	60
600	0.1; (0.000621)	0.1; (0.00128)	4; 135	120

5.3.2 VAs Deposition and Visual Appearance

Below 550 °C no deposit was observed, however between the substrate temperatures of 550 – 600 °C thin films of VAs were deposited. All films were black-gold in appearance, exhibited limited coverage (~1 – 2 cm) and were restricted to the hottest part of the substrate (central), believed to be approximately 25 °C hotter than at the substrate edges. Due to the softening of the glass substrates above 600 °C, investigation into depositions at higher substrate temperatures could not be conducted. The exhibited appearance and limited depositions of the VAs films were found to be consistent with that previously reported for VP films deposited *via* the APCVD of VCl_4 and VOCl_3 with $\text{Cy}^{\text{Hex}}\text{PH}_2$, and additionally *via* the APCVD of VOCl_3 with $\text{P}(\text{SiMe}_3)_3$.³ Although the black-gold deposit did not show any change in visual appearance upon storage in air, the area surrounding the black-gold deposit was found to turn green after approximately two weeks, indicative of post deposition oxidation and formation of vanadium oxide.

Although the deposited VAs films were thin, side-on SEM analysis was used to give an approximate deposition rate of $<100 \text{ nm min}^{-1}$ at a substrate temperature of 600 °C. This rate is significantly lower than the reported rate of 550 nm min^{-1} for the deposition of VP *via* the APCVD of VCl_4 and $\text{Cy}^{\text{Hex}}\text{PH}_2$ at 600 °C, however it should be noted that within this deposition of VP, a VCl_4 to $\text{Cy}^{\text{Hex}}\text{PH}_2$ ratio of 1:5 was used.³

5.3.3 VAs Characterisation

5.3.3.1 Powder X-ray Diffraction (XRD) Analysis

In contrast to the previously reported deposition of amorphous black-gold VP films,³ XRD of the black-gold VAs films produced diffractograms consistent with the formation of crystalline VAs.⁴ All films produced diffractograms consistent with that shown for a VAs film deposited at 600 °C for 120 seconds (**Figure 5.2**), with peaks observed at approximately 32.6, 34.2, 41.2, 42.5, 46.0, 49.1, 50.2, 51.6, 55.0, 56.7 2 θ /°. In addition to the peaks associated with VAs, a broad peak at approximately 22 2 θ /° and a peak at 38.8° were also observed. The peak at 22° can be attributed to the underlying glass substrate, however, although the peak at 38.8° may relate to the formation of either a vanadium or arsenic oxide, or another vanadium arsenide phase, due to the lack of other associated peaks, a peak assignment could not be made.

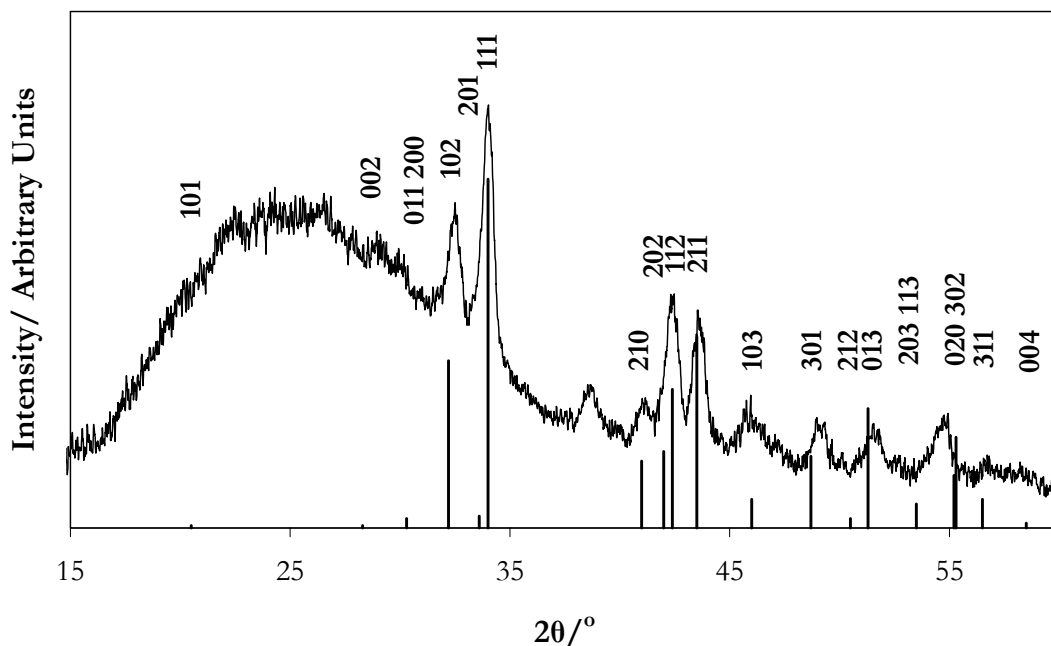


Figure 5.2 Typical X-ray powder diffraction pattern for VAs films deposited *via* the APCVD of VCl_4 and tBuAsH_2 between the substrate temperatures 550 °C – 600 °C, with comparison to a reference VAs diffractogram of bulk material.⁴

On comparing diffractograms of VAs films deposited under the same conditions but at different substrate temperatures, no increase in crystallinity was observed with an increase in deposition temperature (**Figure 5.3**). However, it is likely that an increase in film crystallinity would be observed with an increase in substrate temperature, if comparing VAs films deposited at vastly different substrate temperatures (*i.e.* >50 °C difference).

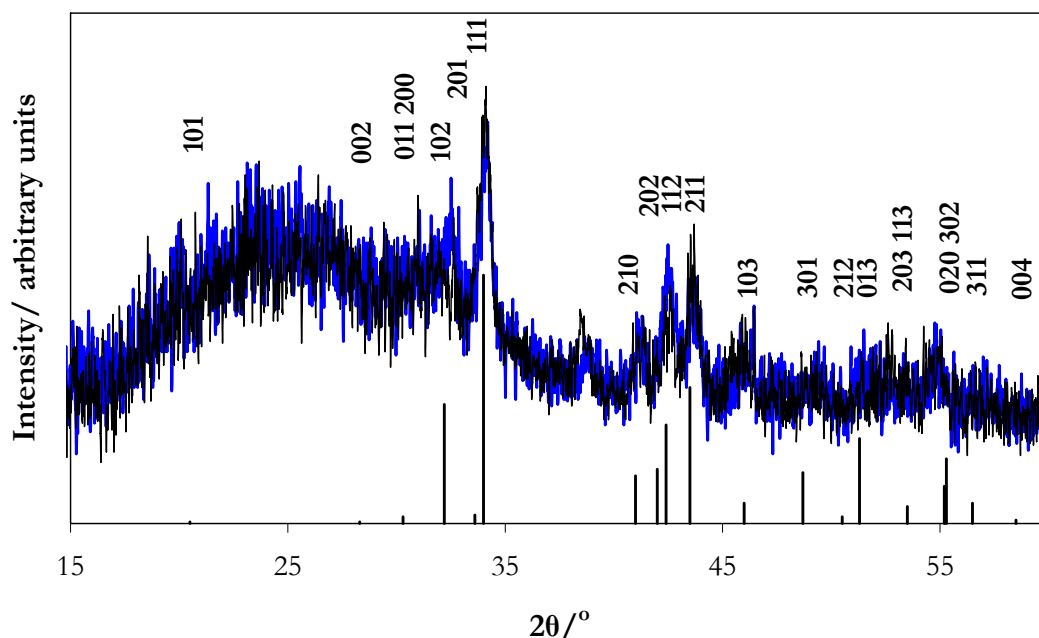


Figure 5.3 X-ray powder diffraction patterns for VAs films deposited *via* the APCVD of VCl_4 and ${}^t\text{BuAsH}_2$ in a 1:2 ratio, using a deposition time length of 120 seconds, at substrate temperatures of 550 °C (blue), and 600 °C (black), with comparison to a reference VAs diffractogram of bulk material.⁴

5.3.3.2 Wavelength Dispersive X-ray (WDX) Analysis

Similarly to that reported for the deposition of TiAs, WDX showed variable vanadium to arsenic ratios within the VAs films. All films were found to be metal rich, and upon comparing the vanadium to arsenic ratios of films deposited at the same substrate temperature, large differences were observed between films deposited for 60 and 120 seconds. If the variable ratios were due to the presence of a mixture of phases it would be expected that these ratios would be similar, regardless of deposition time. As such,

the variable ratios observed within the films are attributed to varying levels of film oxidation.

Table 5.2 WDX analysis for VAs films deposited *via* the APCVD of VCl_4 and ${}^t\text{BuAsH}_2$ using substrate temperatures of 550 and 600 °C, and deposition time lengths of 60 and 120 seconds.

Substrate Temp, °C	Deposition time, secs	Atomic percentage based on a VAsCl species			V:As:Cl
		V	As	Cl	
550	60	64.0	24.6	11.4	$\text{V}_{2.6}\text{AsCl}_{0.46}$
550	120	73.8	19.6	6.6	$\text{V}_{3.8}\text{AsCl}_{0.34}$
600	60	67.5	27.7	4.8	$\text{V}_{2.4}\text{AsCl}_{0.17}$
600	120	56.1	33.8	10.1	$\text{V}_{1.7}\text{AsCl}_{0.30}$

The VAs film deposited at 600 °C for 120 seconds exhibited a stoichiometry of $\text{V}_{1.7}\text{As}$, identical to that reported for VP films deposited at 600 °C *via* the APCVD of VCl_4 and $\text{Cy}^{\text{Hex}}\text{PH}_2$ in a 1:5 ratio.³ Unlike this VP film for which chlorine contamination was considered negligible (<1 at.%), the VAs film exhibited an approximate 10 at.% incorporation of chlorine. Indeed, all VAs films exhibited high levels of chlorine incorporation ranging from approximately 5 – 11 at.%, significantly higher than that reported for VP, however consistent with that previously reported for the deposition of TiAs *via* the APCVD of TiCl_4 and ${}^t\text{BuAsH}_2$ using a 1:2 ratio of precursors. During the deposition of TiAs, it was noted that upon increasing the TiCl_4 to ${}^t\text{BuAsH}_2$ ratio to 1:4, a significant reduction in the film chlorine incorporation was observed. It was hoped that this effect could also be investigated within the deposition of VAs, however, upon conduction of experiments using a 1:4 ratio of VCl_4 to ${}^t\text{BuAsH}_2$, no film was deposited.

5.3.3.3 X-ray Photoelectron Spectroscopy (XPS)

XPS analysis was conducted on a VAs film deposited at a substrate temperature of 600 °C for 120 seconds. After etching through the surface layer, the V 2p_{3/2} ionisation displayed three peaks at 516.5 eV, 515.3 eV and 513.9 eV, with the peaks at 516.5 eV and 515.3 eV being consistent with the literature values of V₂O₅ (~517 eV),⁵ and V₂O₃ (~515 eV),⁶ respectively. The V 2p_{3/2} peak at 513.9 eV is comparable to that observed for VP,^{3,7} and as such, was assigned as VAs. Due to the overlap of the As 3d ionisation peaks with that of the V 3d peaks, assignment of a corresponding As 3d_{3/2} VAs peak was not possible. The O 2p ionisation had two major peaks at 530.3 eV and 532.1 eV, with the peak at 530.3 eV being consistent with that expected for both V₂O₅ and V₂O₃, and the peak at 532.1 eV to SiO₂. A very small Cl 1s ionisation at 199.72 eV was observed, supporting WDX results which indicated an approximately 6 at.% incorporation of chlorine (**Section 5.3.3.2**).

To enable comparison between all species found within the VAs films, and to determine how the levels of these species change with film depth, depth-profile XPS analysis was conducted. All elements as previously investigated for the XPS on the non-etched sample were included within this analysis. The atomic percentage composition of the film was considered and calculated based on the presence of VAs, vanadium oxide (assuming V₂O₃ and V₂O₅ in equal quantities), SiO₂, chlorine and carbon (**Figure 5.4**).

Upon etching, the carbon content was found to decrease, from approximately 50 at.% at the surface, to a consistent 20 at.% within the bulk. Although the vanadium oxide species exhibited a slight reduction upon etching, the species were found to contribute significantly to the bulk material, which is consistent with that previously observed within XPS analysis conducted on VP films deposited *via* the APCVD of VCl₄ and Cy^{Hex}PH₂.³ The VAs contribution to the film composition was low, indicative of a thin film. Upon etching, the VAs was found to increase slightly on moving into the bulk, where VAs maintained a consistent 10 at.% contribution. As expected, the chlorine content was similarly low, and demonstrated consistent levels with VAs. High

levels of SiO₂ were observed throughout the material, indicative of pin-holes within the material, and consequent probing of the underlying SiO₂ substrate.

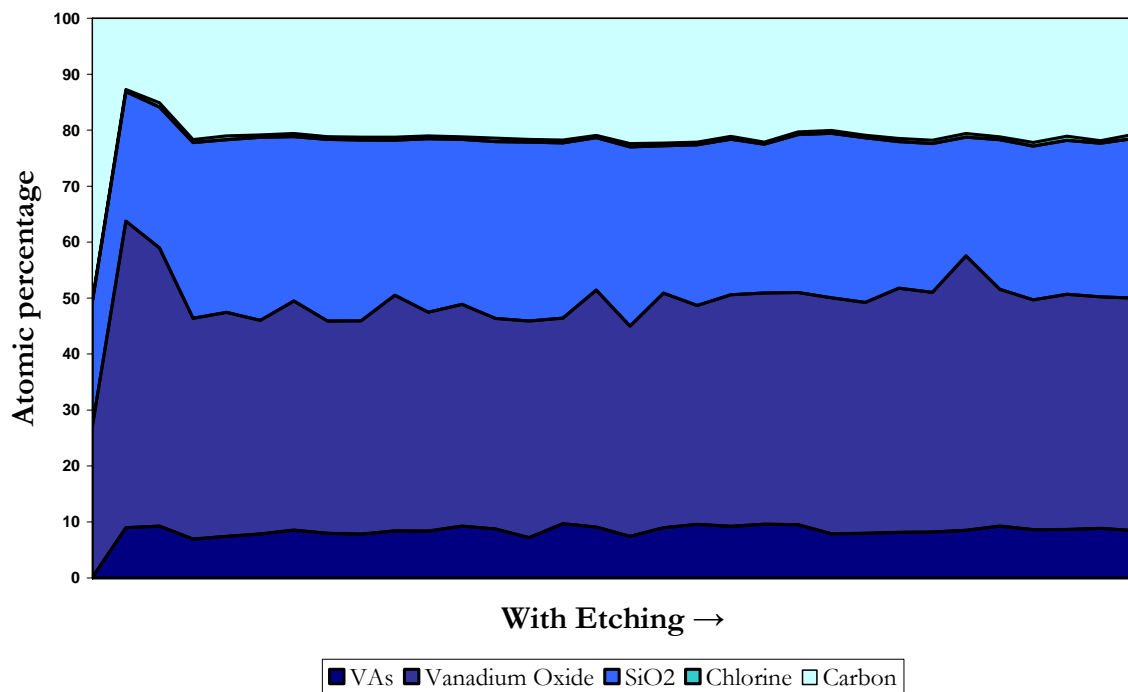


Figure 5.4 Schematic representing how the atomic percentage composition varies with depth within a VAs film deposited from the APCVD of VCl₄ and ^tBuAsH₂ at a substrate temperature of 600 °C (total etch time of 1860 seconds).

Table 5.3 Comparison of at.% contribution within a VAs film deposited *via* the APCVD of VCl₄ and ^tBuAsH₂ at 600 °C and a TiAs film deposited *via* the APCVD of TiCl₄ and ^tBuAsH₂ at 500 °C after etching for 1800 seconds.

Species	VAs At.%	TiAs At.%
Metal Arsenide	8	18
Total Oxide	42	54
SiO ₂	28	12
Chlorine	1	4
Carbon	21	12

It should be noted that whilst the TiAs film deposited *via* the APCVD of TiCl_4 and ${}^t\text{BuAsH}_2$ was etched for 27000 seconds, the VAs film here was only etched for 1860 seconds, and as such, a shallower film depth for VAs was probed. Upon comparing similar depth levels of the two materials, similar at.% contribution from the species are observed (**Table 5.3**), with the lower at.% contribution of metal arsenide and higher at.% of SiO_2 attributed to a thinner films and the presence of pin holes within VAs.

5.3.3.4 Raman Microscopy Analysis

Raman microscopy was conducted on all deposited VAs films formed from the APCVD of VCl_4 and ${}^t\text{BuAsH}_2$, with two distinct Raman patterns observed. Films deposited for 120 second deposition times exhibited intense sharp peaks at approximately 140, 190, 280, 403, and 992 cm^{-1} , and intense broad peaks at approximately 499 and 680 cm^{-1} , consistent with the formation of V_2O_5 (**Figure 5.5**).⁸ This observation of V_2O_5 is consistent with WDX and XPS results which indicated a

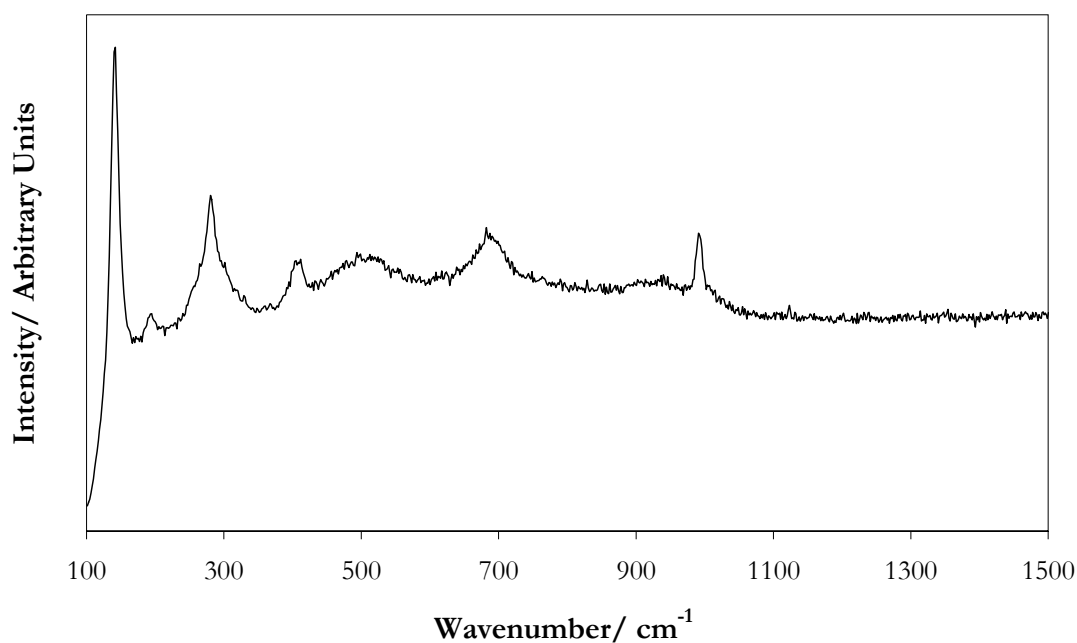


Figure 5.5 Typical Raman spectrum for VAs films deposited *via* the APCVD of VCl_4 and ${}^t\text{BuAsH}_2$ for a deposition time length of 120 seconds.

significant degree of oxidation had occurred. Films deposited for 60 seconds at both 550 and 600 °C however did not show these characteristic vanadium oxide peaks, with the film deposited at 600 °C exhibiting a broad peak at approximately 226 cm^{-1} , and two broad peaks at approximately 933 and 988 cm^{-1} (**Figure 5.6**). Although no Raman data is available for VAs or VP bulk material for comparison, these peaks are attributed to the formation of VAs.

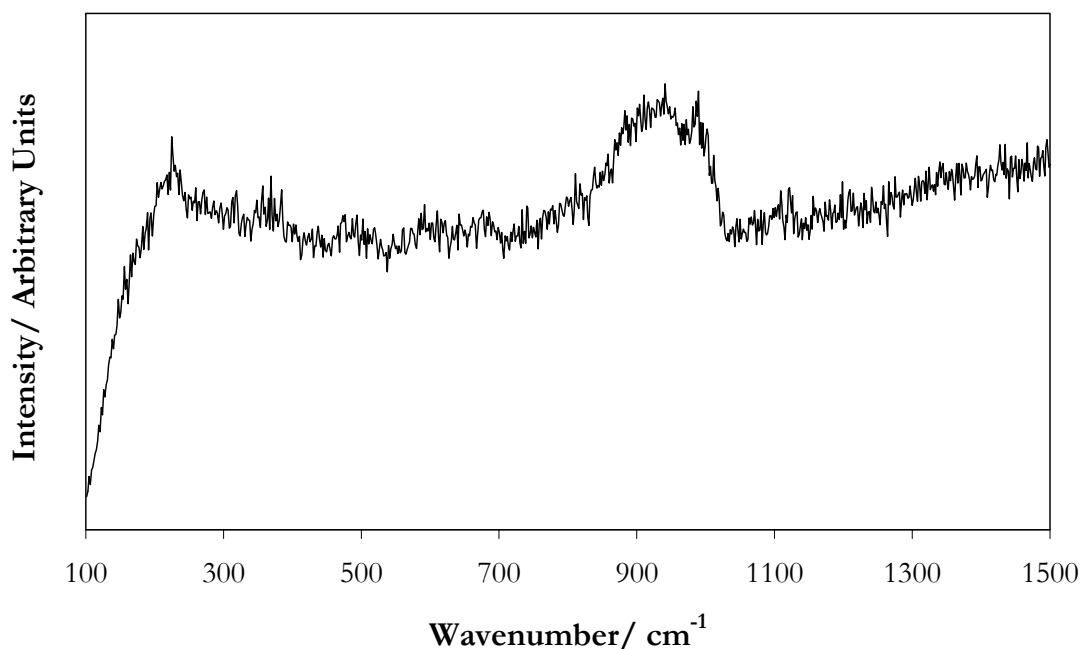


Figure 5.6 Raman spectrum for a VAs film deposited *via* the APCVD of VCl_4 and ${}^t\text{BuAsH}_2$ at a substrate temperature of 600 °C for a deposition time length of 60 seconds.

5.3.4 VAs Morphology Analysis

Due to the VAs films being extremely thin with limited surface coverage, and difficulties incurred during SEM imaging, SEM analysis was only possible on the two VAs films deposited at 600 °C. Unlike that previously reported for the deposition of TiAs films *via* the APCVD of TiCl_4 and ${}^t\text{BuAsH}_2$, an island growth mechanism was not apparent upon comparison of images obtained from films deposited at 600 °C for 60 and 120 seconds (**Figure 5.7**). The VAs film deposited at 600 °C for 120 seconds was found to show a fractured surface, which may explain why Raman microscopy of films deposited for longer deposition time lengths exhibited Raman patterns consistent with

V_2O_5 , due to an increase in film surface area and hence observed oxidation. Although individual agglomerates were difficult to observe within the film deposited for 120 seconds, roughly spherical agglomerates of approximate size 100 nm were evident within the film deposited for 60 seconds.

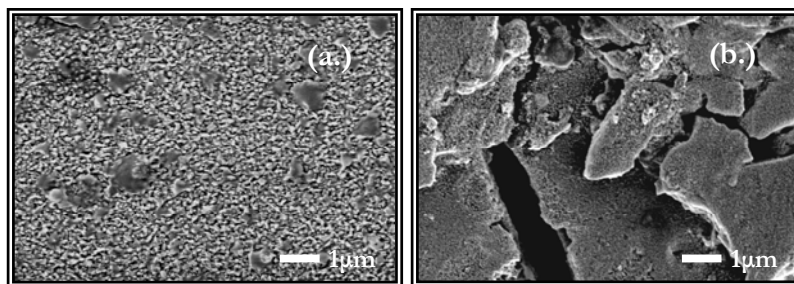


Figure 5.7 Scanning electron micrographs of VAs films deposited *via* the APCVD of VCl_4 and $tBuAsH_2$ at 600 °C using deposition times of 60 (a.) and 120 (b.) seconds (x10,000 magnification).

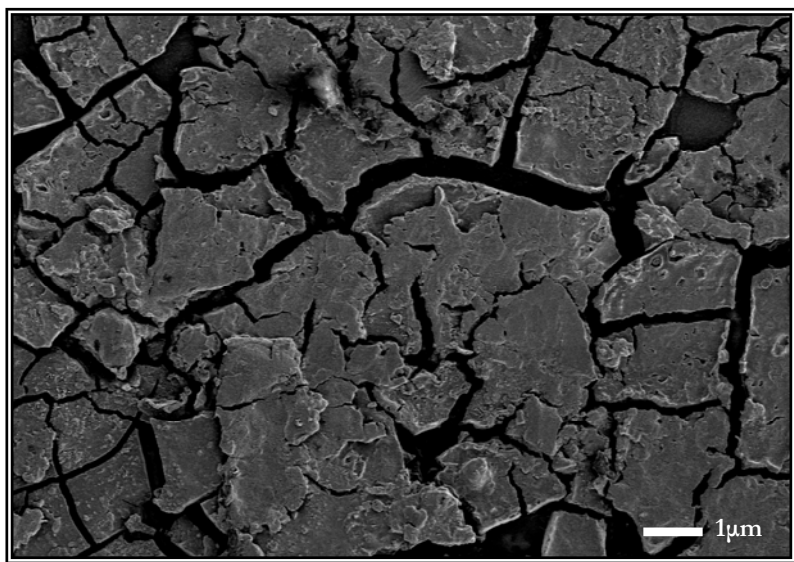


Figure 5.8 Scanning electron micrograph of a VAs film deposited *via* the APCVD of VCl_4 and $tBuAsH_2$ at 600 °C using a deposition time of 120 seconds showing the fractured surface (x1,000 magnification).

5.3.5 VAs Properties

5.3.5.1 Adherence, Hardness and Resistivity

All films passed the Scotch tape test and were scratched using a steel stylus, indicating similar adherence and hardness properties to that of VP films deposited *via* the APCVD of VCl_4 and $Cy^{Hex}PH_2$.³ Due to the area required for probing by the four-point probe, resistivity measurements were only possible on the VAs films deposited at 600 °C, due to limited deposition for the other two films. Both analysed films exhibited resistivities of approximately 8 m Ω cm, indicative of borderline metallic- or semiconductor-like conductivities, with resistivities similar to that previously reported for TiAs films, and VP films deposited *via* the APCVD of $[V(NMe_2)_4]$ and $Cy^{Hex}PH_2$ (300 – 800 $\mu\Omega$ cm).⁷ It was observed that resistivity measurements were only possible on select areas of the VAs film deposited at 600 °C for 120 seconds, which is likely to be due to the fractured surface as previously reported during SEM analysis.

5.3.5.2 Optical Properties

Reflectance and transmittance analysis was only possible on the VAs film deposited at 600 °C for 60 seconds, due to limited substrate coverage exhibited by all other films. Upon analysis, the VAs film exhibited less reflectivity within the IR region, with an increase in reflectance observed at the UV region (\sim 400 nm). Similarly to its reflectance profile, the VAs film also exhibited less transmittance within the IR region, exhibiting similar transmittance and reflectance properties to that previously reported for TiAs (Figure 5.9).

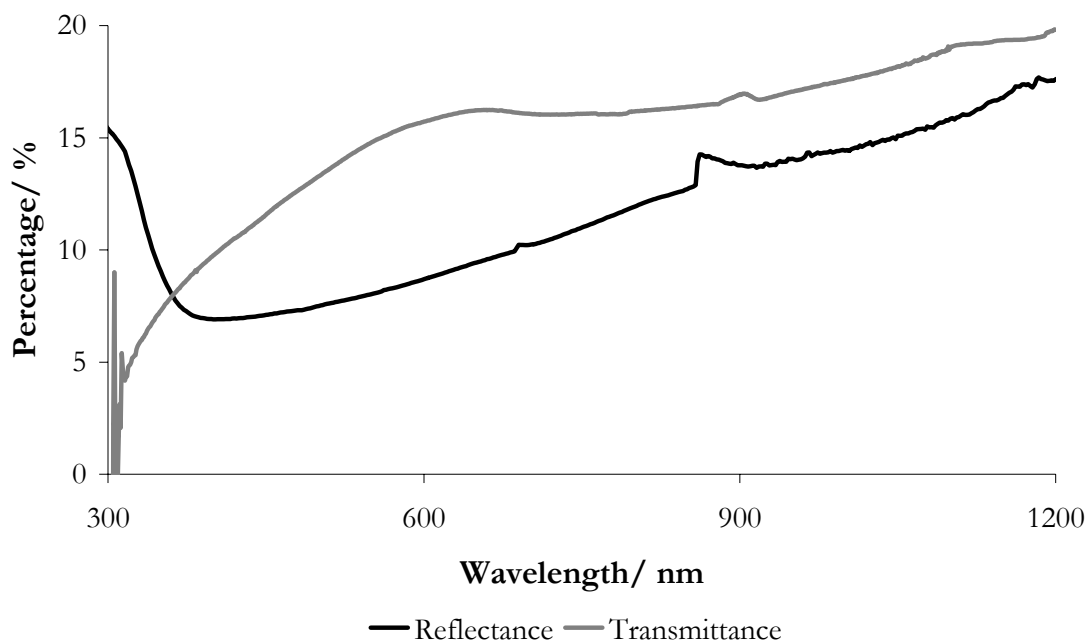


Figure 5.9 Reflectance and transmittance data for a VAs film deposited *via* the APCVD of VCl_4 and $tBuAsH_2$ at a substrate temperature of 600 °C and for a deposition time of 60 seconds.

5.3.5.3 Water Contact Angle Measurements

Water contact angle measurements using an 8 μ l water droplet were conducted on all VAs films. Water contact angles between 30 – 45° were observed for VAs films deposited at 550 °C, with the low contact angles thought to be due to high levels of film oxidation and thus formation of surface vanadium oxide which is known to be hydrophilic (V_2O_5 and V_2O_3).⁸ Upon comparing VAs films deposited at 600 °C, this effect was also evident, with the film deposited for 120 seconds, previously found to exhibit Raman patterns consistent with V_2O_5 , demonstrating smaller contact angles than the equivalent film deposited for 60 seconds. The VAs film deposited at 600 °C for 60 seconds demonstrated water contact angles between 85 – 95°, consistent with that previously reported for the mildly hydrophobic TiAs films (**Figure 5.10 and Table 5.4**).

Figure 5.10 Photographs of an 8 μ l water droplet on the surface of VAs deposited *via* the APCVD of VCl_4 and ${}^t\text{BuAsH}_2$.

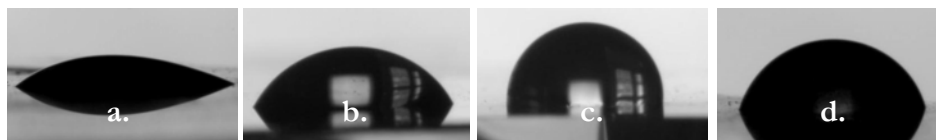


Table 5.4 Water contact angle measurements ($^\circ$) of VAs films deposited *via* the APCVD of VCl_4 and ${}^t\text{BuAsH}_2$.

Image	Substrate Temp, $^\circ\text{C}$	Deposition time, secs	Water contact angles ($^\circ$) on three areas			Approximate $^\circ$ Range
			1	2	3	
a	550	60	44	34	41	30 – 45
b	550	120	37	43	41	35 – 45
c	600	60	92	94	87	85 – 95
d	600	120	73	27	53	25 - 75

5.3.6 Conclusions

Crystalline VAs films were successfully deposited *via* the APCVD of VCl_4 and ${}^t\text{BuAsH}_2$ in a 1:2 ratio at substrate temperatures of 550 and 600 $^\circ\text{C}$. The films were black-gold in appearance, and demonstrated similar adherence, hardness and conductivity properties to previously reported VP films.^{3,7} All VAs films were found to be metal rich, exhibit approximately 5 – 11 at.% chlorine incorporation, and demonstrate high levels of oxidation (particularly evident in films deposited for longer deposition times). Reflectance, transmittance and water contact angle measurements of a VAs with the lowest level of oxidation, were found to be consistent with that previously reported for TiAs.

5.4 APCVD of VOCl₃ and ^tBuAsH₂

5.4.1 Introduction

Following the successful deposition of VAs films *via* the APCVD of VCl₄ and ^tBuAsH₂, investigations into an alternative vanadium precursor to VCl₄ were conducted. VOCl₃ has already proven successful in the deposition of VP films, with films exhibiting low chlorine and oxygen content,³ and as such, use of the vanadium precursor VOCl₃ within the deposition of VAs was investigated.

The APCVD of VOCl₃ and ^tBuAsH₂ successfully deposited films over the substrate temperatures of 450 °C – 600 °C, with deposition time lengths of 60 and 120 seconds used. In an attempt to investigate the effect of the VOCl₃ to ^tBuAsH₂ ratio on the resultant films, precursor ratios of 1:2, 1:4 and 1:6 were used. **Table 5.5** describes the experimental conditions which resulted in film deposition, however VAs films deposited using substrate temperatures of 450 °C, 500 °C and 550 °C, VOCl₃ to ^tBuAsH₂ ratios of 1:2, and deposition times of 60 seconds did not produce good quality films; as such, analysis was only conducted on the best quality films (*i.e.* only those which demonstrated good surface coverage; highlighted in grey in **Table 5.5**).

Table 5.5 Experimental conditions for VAs films deposited *via* the APCVD of VCl₄ and ^tBuAsH₂. Those highlighted in grey represent the VAs films on which analysis was conducted.

Substrate Temp, °C	N ₂ flow rate through VOCl ₃ bubbler, L/min; (mol/min)	N ₂ flow rate through ^t BuAsH ₂ bubbler, L/min; (mol/min)	Plain line flow, L/min; Mixing chamber temp, °C	Deposition time, secs
450	0.15; (0.000614)	0.1; (0.00128)	4; 125	60
500	0.15; (0.000614)	0.1; (0.00128)	4; 125	60
550	0.15; (0.000614)	0.1; (0.00128)	4; 125	60
550	0.15; (0.000614)	0.2; (0.00257)	4; 125	60
550	0.15; (0.000614)	0.3; (0.00385)	4; 130	60
550	0.15; (0.000614)	0.1; (0.00128)	4; 125	120
550	0.15; (0.000614)	0.2; (0.00257)	4; 130	120
600	0.15; (0.000614)	0.2; (0.00257)	4; 130	60

5.4.2 VAs Deposition and Visual Appearance

Similarly to that previously reported for the deposition of VAs films using the vanadium precursor VCl_4 , below $550\text{ }^\circ\text{C}$ no deposit was observed, however between the substrate temperatures of $550 - 600\text{ }^\circ\text{C}$ thin films of VAs were deposited. Unlike those deposited using VCl_4 , the films were silver in appearance, highly reflective, and with a gold leading edge (**Figure 5.11**), consistent in appearance to VP films deposited *via* the APCVD of $[\text{V}(\text{NMe}_2)_4]$ and $\text{Cy}^{\text{Hex}}\text{PH}_2$.⁷ Although these silver VP films exhibited total substrate coverage, VAs coverage was limited to $\sim 2 - 3\text{ cm}$ strips spanning the width of the substrate (approximately 4.5 cm); however, these films exhibited a larger substrate coverage than that previously reported for VP films deposited *via* the APCVD of VOCl_3 and $\text{Cy}^{\text{Hex}}\text{PH}_2$.³ Similarly to the VAs films deposited using VCl_4 , regions surrounding the film turned green after approximately two weeks storage in air, again indicative of post deposition oxidation and formation of vanadium oxide.

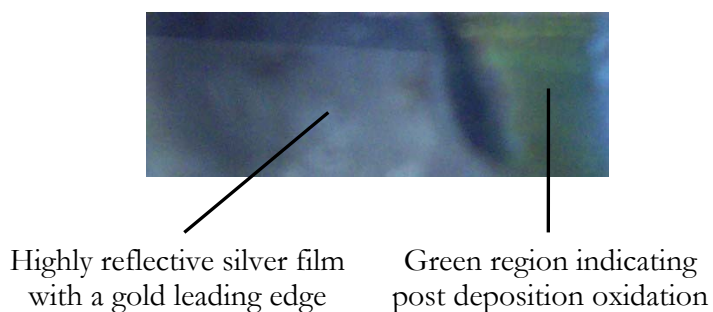


Figure 5.11 Digital photograph illustrating the typical appearance of VAs films deposited *via* the APCVD of VOCl_3 and ${}^t\text{BuAsH}_2$.

Side-on SEM analysis was used to determine the thickness, this gave an approximate deposition rate of $\sim 50\text{ nm min}^{-1}$ for a VAs film deposited at $550\text{ }^\circ\text{C}$ using a VOCl_3 to ${}^t\text{BuAsH}_2$ ratio of 1:2. Although this film was deposited at $550\text{ }^\circ\text{C}$, this rate is lower than that previously reported for VAs films deposited using the vanadium precursor VCl_4 at $600\text{ }^\circ\text{C}$ ($< 100\text{ nm min}^{-1}$). This decrease in deposition rate upon alteration of the vanadium precursor is consistent with that reported for the deposition of VP using $\text{Cy}^{\text{Hex}}\text{PH}_2$, which showed a decrease in deposition rate from 550 nm min^{-1}

to $\sim 375 \text{ nm min}^{-1}$ on an exchange of VCl_4 to VOCl_3 at $600 \text{ }^\circ\text{C}$.³ Additionally, it should also be noted that different ratios of vanadium to phosphine were used within these experiments (1:5 using VCl_4 and 1:8 using VOCl_3), and a larger decrease in deposition rate would be expected if $\text{Cy}^{\text{Hex}}\text{PH}_2$ and VOCl_3 had also been used in a 1:5 ratio.

5.4.3 VAs Characterisation

5.4.3.1 X-ray Powder Diffraction (XRD) Analysis

Similar to that previously reported for VAs films deposited using VCl_4 , XRD of the VAs films deposited using VOCl_3 produced diffractograms consistent with the formation of crystalline VAs.⁴ All films produced diffractograms consistent with that shown for a VAs film deposited at $550 \text{ }^\circ\text{C}$ for 120 seconds, using a VOCl_3 to ${}^t\text{BuAsH}_2$ ratio of 1:2 (**Figure 5.12**), with peaks observed at approximately $32.6, 34.2, 41.2, 42.5, 43.7, 46.2, 49.3, 51.7, 53.1, 54.9$ and $56.8 \text{ } 2\theta/^\circ$. Additional peaks to VAs at approximately 22 and $38.8 \text{ } 2\theta/^\circ$ were again observed, and although the broad peak at

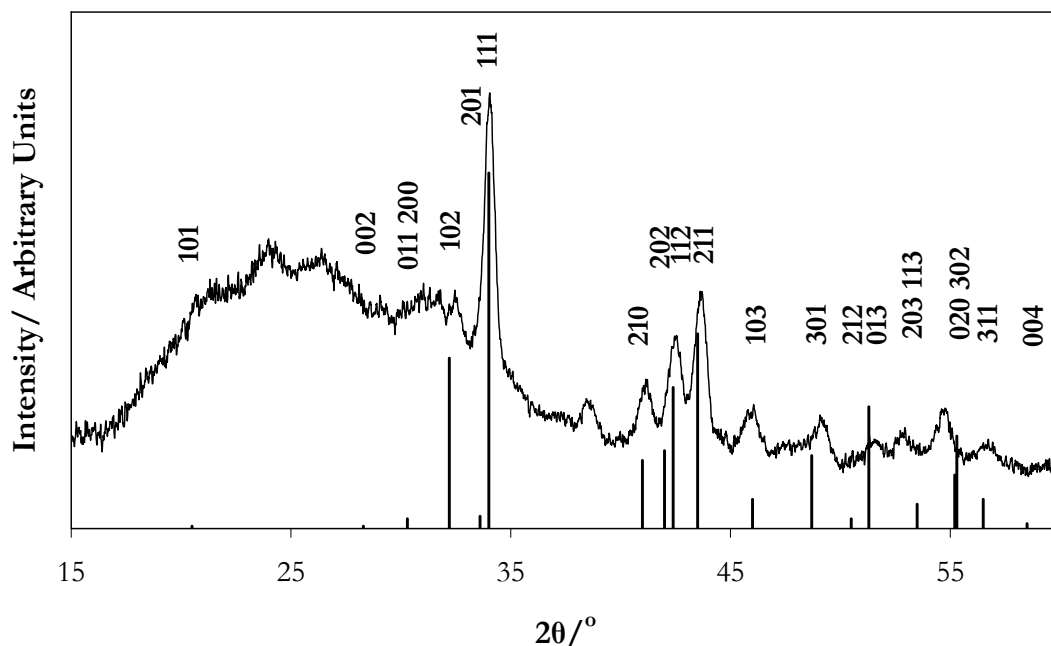


Figure 5.12 Typical X-ray powder diffraction pattern for VAs films deposited *via* the APCVD of VOCl_3 and ${}^t\text{BuAsH}_2$ between the substrate temperatures $550 \text{ }^\circ\text{C} - 600 \text{ }^\circ\text{C}$, with comparison to a reference VAs diffractogram of bulk material.⁴

22° could be attributed to the glass substrate, assignment of the peak at 38.8° was again not possible due to lack of other associated peaks.

Similarly to that observed for the VAs films deposited *via* the APCVD of VCl_4 and ${}^t\text{BuAsH}_2$, upon comparison of VAs films deposited *via* the APCVD of VOCl_3 and ${}^t\text{BuAsH}_2$, no increase in crystallinity was observed between films deposited using the same conditions but different substrate temperatures (**Figure 5.13**).

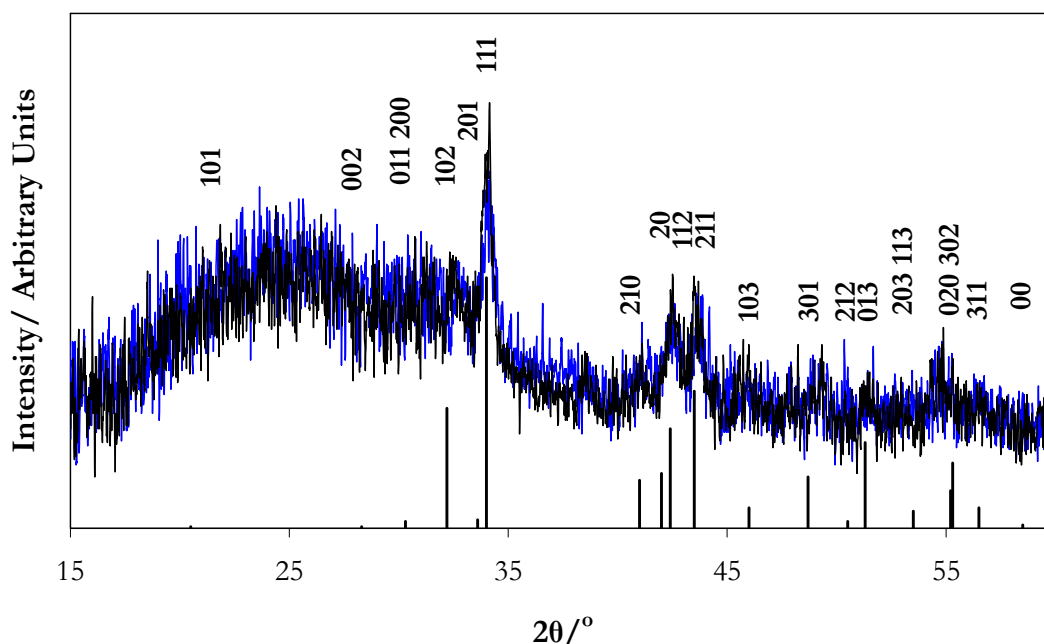


Figure 5.13 X-ray powder diffraction patterns for VAs films deposited *via* the APCVD of VOCl_3 and ${}^t\text{BuAsH}_2$ in a 1:4 ratio, using a deposition time length of 60 seconds, at substrate temperatures of 550°C (blue), and 600°C (black), with comparison to a reference VAs diffractogram of bulk material.⁴

5.4.3.2 Wavelength Dispersive X-ray (WDX) Analysis

Similarly to that reported for VAs films deposited using VCl_4 , WDX showed films deposited *via* the reaction of VOCl_3 and ${}^t\text{BuAsH}_2$ to exhibit variable vanadium to arsenic ratios. However, unlike when using VCl_4 , all films deposited using the vanadium precursor VOCl_3 were found to be arsenic rich. Less oxygen contamination has been previously reported for VP films deposited *via* the APCVD of VOCl_3 and $\text{C}_y^{\text{Hex}}\text{PH}_2$ compared to those deposited using the vanadium precursor VCl_4 .³ This is in agreement with that observed for VAs film deposition, with the arsenic rich VAs films deposited

using VOCl_3 being indicative of low levels of oxidation. All VAs films exhibited vanadium to arsenic ratios close to 1:1, with films deposited at 550 °C for 60 seconds using VOCl_3 to ${}^t\text{BuAsH}_2$ ratios of 1:4 and 1:6 exhibiting approximate 1:1 ratios.

Table 5.6 WDX analysis for VAs films deposited *via* the APCVD of VOCl_3 and ${}^t\text{BuAsH}_2$ using a range of substrate temperatures, deposition time lengths and VOCl_3 to ${}^t\text{BuAsH}_2$ ratios.

Substrate Temp, °C	Approximate $\text{VOCl}_3: {}^t\text{BuAsH}_2$	Deposition time, secs	Atomic percentage based on a VAsCl species			V:As
			V	As	Cl	
550	1:4	60	49.1	50.6	0.3	$\text{VAs}_{1.03}$
550	1:6	60	47.7	52.2	0.1	$\text{VAs}_{1.09}$
550	1:2	120	42.5	56.9	0.6	$\text{VAs}_{1.34}$
550	1:4	120	41.2	58.4	0.4	$\text{VAs}_{1.42}$
600	1:4	60	45.2	53.4	1.4	$\text{VAs}_{1.18}$

Similarly to VP films deposited *via* the APCVD of VCl_4 and $\text{Cy}^{\text{Hex}}\text{PH}_2$ (1:5 ratio) and VOCl_3 and $\text{Cy}^{\text{Hex}}\text{PH}_2$ (1:8 ratio),³ all deposited VAs films exhibited negligible chlorine incorporation. It was noted that upon increasing the VOCl_3 to ${}^t\text{BuAsH}_2$ ratio from 1:2 to 1:4, and 1:4 to 1:6, the chlorine incorporation was reduced by approximately 0.2 at.% and the arsenic incorporation increased by approximately 2 at.%, for VAs films deposited using identical conditions.

5.4.3.3 X-ray Photoelectron Spectroscopy (XPS) Analysis

X-ray photoelectron spectroscopy (XPS) analysis was conducted on a VAs film deposited at a substrate temperature of 550 °C for 120 seconds using a VOCl_3 to ${}^t\text{BuAsH}_2$ ratio of 1:2. Although high levels of carbon were observed at the surface, upon etching the carbon levels were found to significantly reduce. After etching through the surface layer, the V $2p_{3/2}$ ionisation displayed three peaks at 516.5 eV, 515.2 eV and 513.7 eV, with the peaks at 516.5 eV and 515.2 eV being consistent with literature values of V_2O_5 (~517 eV),⁵ and V_2O_3 (~515 eV),⁶ respectively. The V $2p_{3/2}$

peak at 513.7 eV is comparable to that observed for VP,^{3,7} and additionally that assigned to VAs within the deposition of VAs films using the vanadium precursor VCl_4 , and as such, can be assigned to VAs. Due to the overlap of the As 3d ionisation peaks with that of the V 3d peaks, assignment of a corresponding As $3d_{3/2}$ VAs peak was not possible. The O 2p ionisation had two major peaks at 530.2 eV and 532.0 eV, with the peak at 530.2 eV being consistent with that expected for both V_2O_5 and V_2O_3 , and the peak at 532.0 eV to SiO_2 . A barely detectable Cl 1s peak at approximately 230 eV was observed, supporting the WDX results that chlorine incorporation was negligible.

5.4.3.4 Raman Microscopy Analysis

Raman microscopy was conducted on all deposited VAs films, with all films producing consistent diffractograms, exhibiting relatively intense broad peaks observed at approximately 220 and 930 cm^{-1} . Unlike that previously reported for VAs films deposited *via* the APCVD of VCl_4 and ${}^t\text{BuAsH}_2$, no films produced patterns

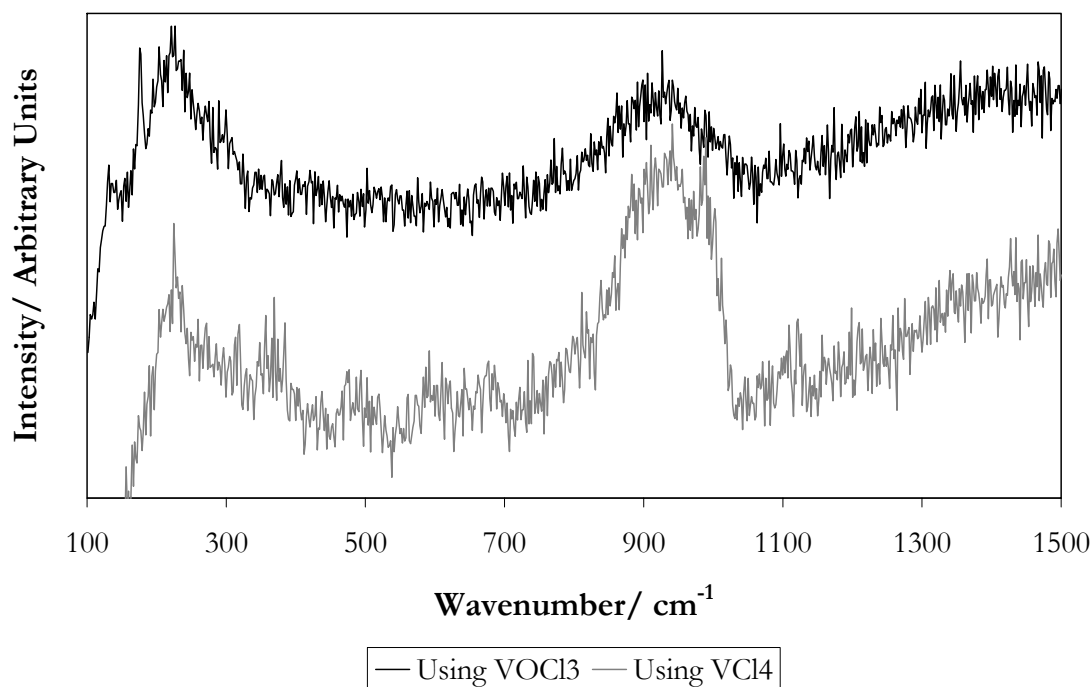


Figure 5.14 Comparison of typical Raman spectra for VAs films deposited *via* the APCVD of VOCl_3 and ${}^t\text{BuAsH}_2$ and VCl_4 and ${}^t\text{BuAsH}_2$.

consistent with the formation of V_2O_5 . Upon comparison of a typical Raman pattern observed for VAs films deposited using $VOCl_3$ with that previously attributed to the formation of VAs when using VCl_4 , peak consistency was observed (**Figure 5.12**).

5.4.4 VAs Morphology

To investigate the mechanism of VAs deposition and to determine how alteration of deposition time, temperature, and $VOCl_3$ to $tBuAsH_2$ ratios affected the deposited films, comparative SEM analysis was conducted. Upon comparing films deposited at 500 °C and using a $VOCl_3$ to $tBuAsH_2$ ratio of 1:4, a higher degree of surface agglomerates were observed within the film deposited for 120 seconds, compared to the film deposited for 60 seconds (**Figure 5.15**); with both films exhibiting roughly spherical agglomerates approximately 100 nm in size. Comparison of the films deposited using different deposition temperatures (550 °C and 600 °C) (**Figure 5.16**) and $VOCl_3$ to $tBuAsH_2$ ratios (1:2 and 1:4) (**Figure 5.17**) no significant differences were observed. Unlike VAs films deposited using VCl_4 , all films, regardless of deposition conditions, exhibited a continuous material deposit with excellent substrate coverage. All films consisted of roughly spherical agglomerates all approximately 100 nm in diameter, consistent with that previously reported when using VCl_4 (**Figure 5.18**).

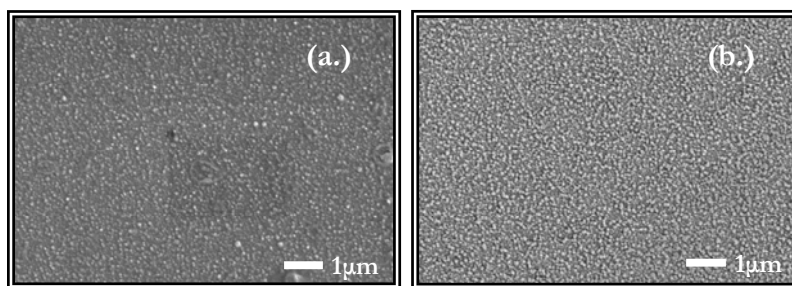


Figure 5.15 Scanning electron micrographs of VAs films deposited *via* the APCVD of $VOCl_3$ and $tBuAsH_2$ at 550 °C using a $VOCl_3$ to $tBuAsH_2$ ratio of 1:4 and deposition times of 60 (a) and 120 seconds (b) (x10,000 magnification).

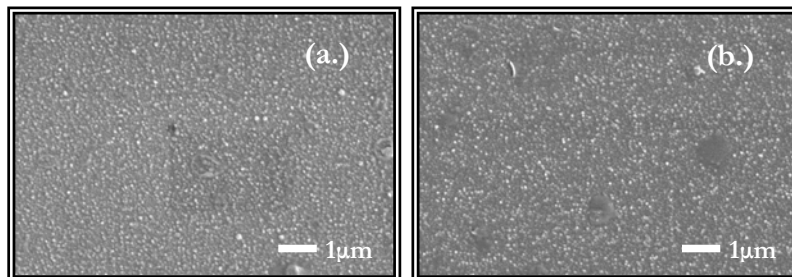


Figure 5.16 Scanning electron micrographs of VAs films deposited *via* the APCVD of VOCl_3 and ${}^t\text{BuAsH}_2$ using a VOCl_3 to ${}^t\text{BuAsH}_2$ ratio of 1:4, a deposition time of 60 seconds, and substrate temperatures of 550 °C (a) and 600 °C (b) (x10,000 magnification).

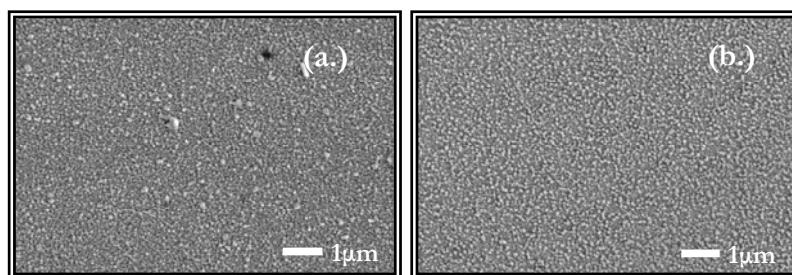


Figure 5.17 Scanning electron micrographs of VAs films deposited *via* the APCVD of VOCl_3 and ${}^t\text{BuAsH}_2$ at 550 °C and deposition times of 2 minutes, using VOCl_3 to ${}^t\text{BuAsH}_2$ ratios of (a) 1:2 and (b) 1:4 (x10,000 magnification).

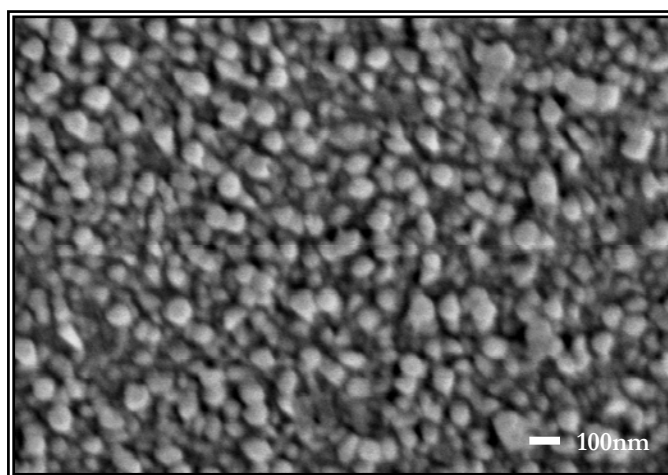


Figure 5.18 Typical scanning electron micrograph of VAs films deposited *via* the APCVD of VOCl_3 and ${}^t\text{BuAsH}_2$. Specific image is of a VAs film deposited at 550 °C for 2 minutes using a VOCl_3 to ${}^t\text{BuAsH}_2$ ratio of 1:4 (x40,000 magnification).

5.4.5 VAs Film Properties

5.4.5.1 Adherence, Hardness and Resistivity

Similarly to that of the APCVD of VCl_4 and ${}^t\text{BuAsH}_2$, all films demonstrated good substrate adherence, with all films passing the Scotch tape test. The VAs film deposited at $600\text{ }^\circ\text{C}$ for 60 seconds using a VOCl_3 to ${}^t\text{BuAsH}_2$ ratio of approximately 1:2, was the only film to pass the steel stylus test, indicating a film hardness greater than that reported for VP,³ however similar to that previously reported for TiAs. VAs films exhibited resistivities in the range $200 - 400\ \mu\Omega\ \text{cm}$, indicative of borderline metallic-semiconductor-like conductivities, and additionally exhibiting resistivities similar to that previously reported for VAs films deposited using VCl_4 , VP films deposited *via* the APCVD of $[\text{V}(\text{NMe}_2)_4]$ and $\text{Cy}^{\text{Hex}}\text{PH}_2$,⁷ and TiAs films.

5.4.5.2 Optical Properties

Similarly to that reported for the VAs film deposited *via* the APCVD of VCl_4 and ${}^t\text{BuAsH}_2$, all films exhibited decreased reflectivity within the IR region with a slight increase in reflectivity within the UV (**Figure 5.19**). No difference in reflectance properties were observed for VAs films deposited using the same conditions but different VOCl_3 to ${}^t\text{BuAsH}_2$ ratios, however upon comparing the reflectance profiles for VAs films deposited at $550\text{ }^\circ\text{C}$ using a VOCl_3 to ${}^t\text{BuAsH}_2$ ratio of 1:4, an increase in reflectivity was observed for the VAs film deposited for 60 seconds compared to 120 seconds. WDX results indicated the film deposited for 60 seconds had a vanadium to arsenic ratio closer to 1:1, and as such, the higher reflectance is considered to be a truer property of the VAs films.

All VAs films exhibited consistently low transmittance over the range $1200 - 300\ \text{nm}$, with typical transmittance values lower than that reported when using VCl_4 , indicative of the thicker films deposited when using VOCl_3 (**Figure 5.20**).

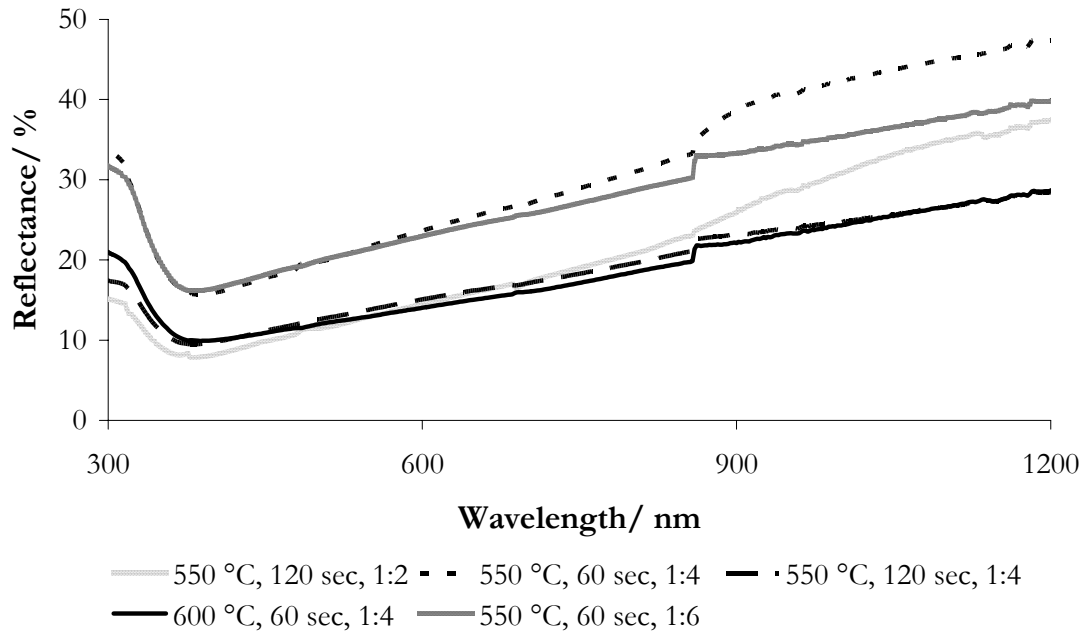


Figure 5.19 Percentage reflectance data for VAs films deposited *via* the APCVD of VOCl_3 and $t\text{BuAsH}_2$ using a range of substrate temperatures, deposition times, and VOCl_3 to $t\text{BuAsH}_2$ ratios.

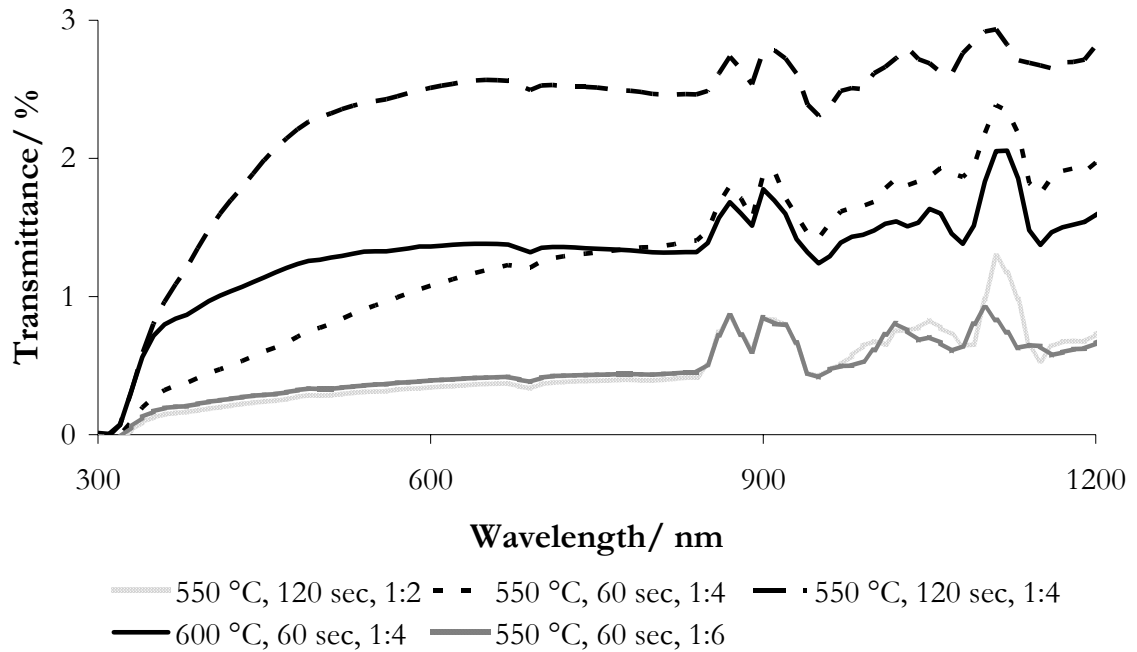


Figure 5.20 Percentage transmittance data for VAs films deposited *via* the APCVD of VOCl_3 and $t\text{BuAsH}_2$ using a range of substrate temperatures, deposition times, and VOCl_3 to $t\text{BuAsH}_2$ ratios.

5.4.5.3 Water Contact Angle Measurements

Water contact angle measurements using an 8 μl water droplet were conducted on all VAs films. Water contact angles were fairly consistent between films deposited using different conditions, with all films demonstrating water contact angles between 40 – 75°. These water contact angles are typically higher than that previously reported for VAs films deposited using VCl_4 , which is attributed to lower levels of film oxidation when using VOCl_3 . All films demonstrated water contact angles consistent with that previously reported for the VAs film deposited at 600 °C for 60 seconds using VCl_4 , and previously reported mildly hydrophobic TiAs films.

Figure 5.21 Photographs of an 8 μl water droplet on the surface of VAs deposited *via* the APCVD of VOCl_3 and ${}^t\text{BuAsH}_2$.

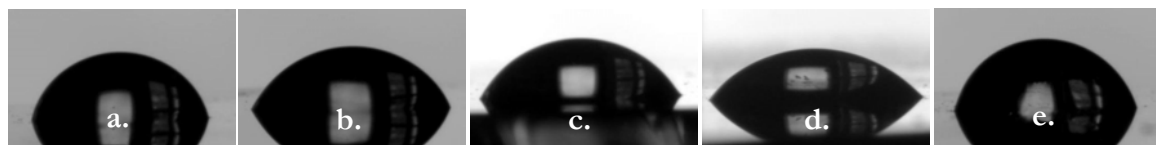


Table 5.7 Water contact angle measurements (°) of VAs films deposited *via* the APCVD of VOCl_3 and ${}^t\text{BuAsH}_2$.

Image	Substrate Temp, °C	Ratio, VOCl_3 to ${}^t\text{BuAsH}_2$	Deposition time, secs	Water contact angles (°) on three areas			Approximate ° Range
				1	2	3	
a	550	1:4	60	71	59	59	55 – 75
b	550	1:6	60	63	60	66	60 – 70
c	550	1:2	120	59	58	58	55 – 60
d	550	1:4	120	43	42	59	40 – 60
e	600	1:4	60	73	64	43	40 – 75

5.4.6 Conclusions

Crystalline VAs films were successfully deposited *via* the APCVD of VOCl_3 and ${}^t\text{BuAsH}_2$ using substrate temperatures of 550 and 600 °C and variable VOCl_3 to ${}^t\text{BuAsH}_2$ ratios (1:2, 1:4 and 1:6). The films were silver in appearance with a gold leading edge, exhibited high reflectivity, and exhibited similar adherence and hardness properties to previously reported TiAs films. The film resistivities were similar to that previously reported for VAs films deposited using VCl_4 , VP films deposited *via* the APCVD of $[\text{V}(\text{NMe}_2)_4]$ and $\text{C}_y^{\text{Hex}}\text{PH}_2$, and previously discussed TiAs films. Unlike the VAs films deposited using VCl_4 , the films exhibited vanadium to arsenic ratios close to 1:1, with negligible chlorine incorporation. All films produced Raman patterns consistent with that previously assigned to VAs (**Section 5.3.3.4**), with no films exhibiting patterns consistent with V_2O_5 . All films were observed to consist of roughly spherical agglomerates approximately 100 nm in diameter, with agglomerate sizes consistent with that reported when using VCl_4 . Reflectance, transmittance and water contact angle measurements of all films were consistent with that previously reported for TiAs (see Chapter 4).

References

- 1 S. Rundqvist, *Acta Chem. Scand.*, 1962, 16, 287.
- 2 K. Selte, A. Kjekshus and A. F. Andresen, *Acta Chem. Scand.*, 1972, 26, 4057.
- 3 C. S. Blackman, C. J. Carmalt, S. A. O'Neill, I. P. Parkin, K. C. Molloy and L. Apostolico, *J. Mater. Chem.*, 2003, 13, 1930.
- 4 K. Bachmayer and H. N. Nowotny, *Monatsh. Chem.*, 1955, 86, 741.
- 5 J. Soria, J. C. Conesa, M. L. Granados, R. Mariscal, J. L. G. Fierro, J. F. G. Delabanda and H. Heinemann, *J. Catal.*, 1989, 120, 457.
- 6 B. Horvath, J. Strutz, J. Geyerlippmann and E. G. Horvath, *Z. Anorg. Allg. Chem.*, 1981, 483, 181.
- 7 C. S. Blackman, C. J. Carmalt, S. A. O'Neill, I. P. Parkin, K. C. Molloy and L. Apostolico, *Chem. Vap. Deposition*, 2004, 10, 253.
- 8 C. Piccirillo, R. Binions and I. P. Parkin, *Chem. Vap. Deposition*, 2007, 13, 145.

Chapter 6

Conclusions

6.1 The Synthesis of Potential Single-Source Precursors to TiAs

The complexes $[\text{TiCl}_4(\text{AsPh}_3)]$ (**2.1**), $[\text{TiCl}_4(\text{AsPh}_3)_2]$ (**2.2**), $[\text{TiCl}_4(\text{Ph}_2\text{AsCH}_2\text{AsPh}_2)]$ (**2.3**) and $[\text{TiCl}_4(\text{tBuAsH}_2)_n]$ (**2.4**) were synthesised from the reaction of TiCl_4 with the corresponding arsine. Whilst complexes (**2.1**), (**2.2**) and (**2.3**) were easily isolated as solids, the manipulation and isolation of compound (**2.4**) was more difficult owing to its high volatility; however, with storage at $-70\text{ }^\circ\text{C}$ for four weeks, a red/brown solid was obtained. In all instances an orange/red product was obtained, with products characterised using a variety of analysis techniques. X-ray quality crystals of (**2.1**) and (**2.2**) were grown *via* dichloromethane/hexane layering, with crystal structures consistent with the formation of a 1:1 and 1:2 adduct, with Ti-As bond lengths of 2.7465(13) and 2.7238(7) Å, respectively. All complexes exhibited analyses similar with the formation of a titanium-arsine complex, indicating potential for their use as single-source precursors to titanium arsenide.

Unlike the syntheses of compounds (**2.1**) – (**2.4**), the reaction of TiCl_4 with $\text{As}(\text{NMe}_2)_3$ resulted in the formation of a dark-green solid (**2.5**). Upon characterisation of compound (**2.5**), formation of a simple 1:1 adduct was indicated, however, upon single crystal XRD analysis of crystals of (**2.5**) grown *via* dichloromethane/hexane layering, an interesting Cl, NMe_2 group exchange was observed, with the complex adopting the structure $[\text{TiCl}_3(\text{NMe}_2)(\mu\text{-NMe}_2)_2\text{AsCl}]$. This was the first time an exchange of this type had been observed for arsenic, however, similar observations have been previously reported during solvolysis reactions between TiCl_4 and aliphatic primary and secondary amines.¹ Although compound (**2.5**) lacked titanium-arsenic bonds, thereby making it an unsuitable single-source precursor to titanium arsenide, it

did possess three titanium-nitrogen bonds, and as such, was investigated as a potential single-source precursor to titanium nitride.

To further investigate the Cl, NMe₂ group exchange observed in compound **(2.5)**, the reactions of TiCl₄ with two equivalents of As(NMe₂)₃, and [Ti(NMe₂)₄] with AsCl₃ were conducted. The reaction of TiCl₄ with two equivalents of As(NMe₂)₃ resulted in the formation of a dark green compound **(2.6)**, and similarly to compound **(2.5)**, elemental analysis indicated the formation of a 1:2 adduct. Unfortunately X-ray quality crystals of **(2.6)** could not be grown, however, upon conduction of ¹H NMR after the treatment of compound **(2.6)** with an excess of NaBF₄ (a halide abstractor), it was deduced that a similar Cl, NMe₂ group exchange to that observed in **(2.5)** had occurred, with the formation of the complex [Ti(NMe₂)₂((μ-NMe₂)₂AsCl)₂].

Similarly to compounds **(2.5)** and **(2.6)**, the reaction of [Ti(NMe₂)₄] with AsCl₃ resulted in the formation of a dark-green solid **(2.7)**, however, a 1:1 complex was not confirmed by microanalysis. Although ¹H NMR and single-crystal X-ray analyses were conducted on **(2.6)**, the products from the reaction were difficult to deduce. However, crystals obtained from the recrystallisation of **(2.7)** ([TiCl₂(μ-Cl)₂(NMe₂)(NHMe₂)₂]₂) showed that a chlorine was bound to the titanium, indicating that a similar exchange as observed within compounds **(2.5)** and **(2.6)** had occurred.

6.2 Single-source CVD Attempts to TiAs

Following the synthesis of compounds **(2.1)**, **(2.2)**, **(2.3)**, **(2.4)** and **(2.5)**, their potential use as single-source precursors to titanium arsenide, and titanium nitride for compound **(2.5)**, was investigated. All compounds exhibited clean, multi-step mass losses, as determined by TGA, highlighting their potential use as precursors. Although the TGA of compounds **(2.1)** and **(2.2)** exhibited mass losses consistent with titanium metal remaining after decomposition, the residual masses of compounds **(2.3)** and **(2.4)** indicated potential for decomposition to TiAs. Compound **(2.5)** demonstrated a residual mass consistent with that expected for TiCl₄N₃As, indicating the possibility for its use as a single source precursor to titanium nitride.

AACVD was conducted using compounds **(2.1)**, **(2.2)**, **(2.4)** and **(2.5)**. The AACVD of compounds **(2.1)** and **(2.2)** resulted in the deposition of TiO₂ anatase, with WDX analysis confirming zero arsenic content. These results were consistent with that previously reported for the AACVD of [SnCl₄(AsPh₃)₂],² and also with that expected from the TGA results. The lack of success of compounds **(2.1)** and **(2.2)** as single-source precursors to TiAs was attributed to the long, weak Ti-As bonds exhibited in the compounds, combined with the oxophilic nature of titanium. The AACVD of compound **(2.4)** did however prove more successful, with the deposition of films containing both titanium and arsenic (in an approximate 1:4 ratio) observed upon the sequential delivery of the precursors to the CVD system. It is postulated that passage of the ^tBuAsH₂ through the CVD prior to conduction of the deposition, reduced the oxygen content within the system (thought to arise from the SiO₂ substrate); thereby reducing the oxidation of compound **(2.4)** and thus the cleavage of the Ti-As bond. Unfortunately, the films deposited *via* the AACVD of compound **(2.5)** were too thin to analyse, however amorphous rainbow films were observed upon the sequential introduction of the precursors.

LPCVD was conducted using compounds **(2.1)**, **(2.2)**, **(2.3)** and **(2.5)**, with all compounds resulting in the deposition of visibly different deposits along the length of the furnace. All compounds resulted in the deposition of at least one region of deposit which exhibited both titanium and arsenic content; with compounds **(2.1)**, **(2.2)**, **(2.3)** and **(2.5)** demonstrating regions exhibiting titanium to arsenic ratios of approximately 1:3, 1:3, 1:6, and 1:2 respectively. In addition to this, the LPCVD of compound **(2.5)** resulted in the deposition of material expressing a relatively high level of nitrogen content, indicating its potential for use as a single-source TiN precursor.

6.3 The APCVD of TiAs Thin Films

The deposition of titanium arsenide thin films *via* the dual-source APCVD reactions of TiCl₄ and [Ti(NMe₂)₄] with ^tBuAsH₂ have been investigated. Crystalline TiAs films were successfully deposited *via* the APCVD of TiCl₄ and ^tBuAsH₂ at substrate

temperatures of 450 – 550 °C. Typically the deposited TiAs films were silver in appearance, however, at the higher substrate temperature of 550 °C, a blue film with a gold leading edge was deposited. All films produced X-ray diffractograms consistent with that of bulk TiAs,³ with line broadening studies indicating a crystallite particle size of 90 nm. WDX analysis showed that films deposited using a 1:2 ratio of TiCl₄ to tBuAsH₂ demonstrated an approximate 1:1 ratio of titanium to arsenic, however, an approximate 5 at.% of chlorine was detected. To investigate whether this chlorine incorporation could be reduced upon increasing the amount of arsine within the system, as has been previously demonstrated within the equivalent phosphorus reaction,⁴ a film deposited using a 1:4 ratio of TiCl₄ to tBuAsH₂ was analysed and exhibited a reduced chlorine incorporation of approximately 1 at.%; however, due to safety concerns regarding the levels of arsine used, further experiments were not conducted. XPS and Raman analysis of the films confirmed the presence of TiAs, with films exhibiting analyses consistent with that previously reported for TiP.⁴ The films were found to deposit *via* an island growth mechanism, with regions where material had failed to nucleate and grow observed. The films exhibited borderline metallic- or semiconducting-like conductivity, were optically transparent when sufficiently thin, and demonstrated hydrophobicity.

The APCVD of [Ti(NMe₂)₄] and tBuAsH₂ resulted in the successful deposition of crystalline TiAs thin films at substrate temperatures of 350 – 550 °C. Unlike the deposition of TiAs using the titanium precursor TiCl₄, all films exhibited visual consistency, with all deposited films being silver in appearance with a gold leading edge. WDX analysis of the films typically showed titanium to arsenic ratios close to 1:1, with the deposition of TiAs confirmed by both XPS and Raman microscopy. Similarly to that observed for TiAs films deposited using TiCl₄, the films were found to deposit *via* an island growth mechanism and exhibited borderline metallic- or semiconductor-like conductivities. Compared to films deposited using TiCl₄, the films demonstrated less reflectivity and exhibited a lower percentage transmittance over the wavelength range of 300 – 1200 cm⁻¹. Additionally, whilst

hydrophobicity was observed in all films deposited using TiCl_4 , some films deposited using $[\text{Ti}(\text{NMe}_2)_4]$ demonstrated hydrophilicity.

6.4 The APCVD of VAs Thin Films

The deposition of vanadium arsenide thin films *via* the dual-source APCVD reactions of VCl_4 and VOCl_3 with ${}^t\text{BuAsH}_2$ have been investigated. Crystalline VAs films were successfully deposited *via* the APCVD of VCl_4 and ${}^t\text{BuAsH}_2$ at substrate temperatures of 550 – 600 °C. All deposited films were typically black-gold in appearance, exhibited limited substrate coverage, with depositions restricted to the hottest part of the substrate (*i.e.* the middle); with film deposition consistent with that previously reported for VP films.⁵ Upon storage of the films in air, the films were observed to turn green on their leading edges, indicating the oxidation of the films post-CVD. All films produced diffractograms consistent with that of bulk VAs,⁶ with extra peaks observed thought to be due to a vanadium oxide species. WDX analysis of the films showed that all films were metal rich, with films deposited under identical conditions but for different deposition time lengths exhibiting great variety in the V:As ratios. As this difference was observed during identical CVD reaction conditions, the variable elemental ratios were attributed to varying degrees of oxidation, rather than the presence of different material phases. All films exhibited high levels of chlorine incorporation, ranging from 5 – 11 at.%, with the chlorine content inconsistent with that previously reported for VP film deposition.⁵ VAs deposition and vanadium oxide formation were confirmed *via* XPS and Raman microscopy. Unlike the TiAs films, the VAs films demonstrated a fractured surface upon investigation using SEM, with roughly spherical agglomerates approximately 100 nm in size observed. The VAs films demonstrated borderline metallic- semiconductor-like conductivities, with reflectance, transmittance and water contact properties similar to that previously reported for deposited TiAs films.

The APCVD of VOCl_3 and ${}^t\text{BuAsH}_2$ resulted in the successful deposition of VAs films at substrate temperatures between 450 – 600 °C. Unlike the VAs films

deposited using the vanadium precursor VCl_4 , films deposited using $VOCl_3$ were silver in appearance, highly reflective and demonstrated a gold leading edge, with their appearance consistent with VP films deposited from the APCVD of $[V(NMe_2)_4]$ and $Cy^{Hex}PH_2$.⁷ Additionally, unlike when using VCl_4 , the films exhibited good substrate coverage, however, similarly to when using VCl_4 , regions of the films turned green upon storage in air post-CVD. All films produced diffractograms consistent with bulk VAs,⁶ again with unassigned peaks thought to be due to the presence of vanadium oxide observed. Unlike when using VCl_4 , WDX analysis showed that all films were arsenic rich, exhibited V:As ratios close to 1:1, and contained negligible chlorine incorporation. VAs deposition was confirmed by XPS and Raman microscopy, with films demonstrating borderline metallic- semiconductor-like conductivities. SEM analysis of the films showed them to consist of roughly spherical agglomerates, approximately 100 nm in size; consistent with that observed for VAs films deposited using VCl_4 . Reflectance, transmittance and water contact properties of the films were found to be consistent with that reported for films deposited using VCl_4 , in addition to TiAs films deposited from the reactions of $TiCl_4$ and $[Ti(NMe_2)_4]$ with $tBuAsH_2$.

6.5 Summary

A range of titanium arsine complexes have been synthesised and used within AACVD and LPCVD for investigation into their potential use as single-source precursors to titanium arsenide. The dual-source APCVD reactions of $TiCl_4$ and $[Ti(NMe_2)_4]$ with $tBuAsH_2$, and VCl_4 and $VOCl_3$ with $tBuAsH_2$ have been used to deposit TiAs and VAs thin films, respectively.

References

- 1 R. T. Cowdell and G. W. A. Fowles, *J. Chem. Soc.*, 1960, 2522.
- 2 M. F. Mahon, N. L. Moldovan, K. C. Molloy, A. Muresan, I. Silaghi-Dumitrescu and L. Silaghi-Dumitrescu, *Dalton Trans.*, 2004, 4017.

-
- ³ K. Bachmayer, H. N. Nowotny and A. Kohl, *Monatsh. Chem.*, 1955, 86, 39.
 - ⁴ C. Blackman, C. J. Carmalt, I. P. Parkin, S. O'Neill, L. Apostolico, K. C. Molloy and S. Rushworth, *Chem. Mater.*, 2002, 14, 3167.
 - ⁵ C. S. Blackman, C. J. Carmalt, S. A. O'Neill, I. P. Parkin, K. C. Molloy and L. Apostolico, *J. Mater. Chem.*, 2003, 13, 1930.
 - ⁶ K. Bachmayer and H. N. Nowotny, *Monatsh. Chem.*, 1955, 86, 741.
 - ⁷ C. S. Blackman, C. J. Carmalt, S. A. O'Neill, I. P. Parkin, K. C. Molloy and L. Apostolico, *Chem. Vap. Deposition*, 2004, 10, 253.

Appendices

A1 Publications

Synthesis, X-ray structures and CVD of titanium(IV) arsine complexes

T. Thomas, D. Pugh, I. P. Parkin and C. J. Carmalt, *Dalton Trans.*, 2010, **39**, 5325-5331.

Atmospheric pressure chemical vapour deposition of TiCl_4 and ${}^t\text{BuAsH}_2$ to form titanium arsenide thin films

T. Thomas, C. S. Blackman, I. P. Parkin and C. J. Carmalt, *Eur. J. Inorg. Chem.*, 2010, 5629-5634.

Novel ion pairs obtained from the reaction of titanium(IV) halides with simple arsine ligands

T. Thomas, D. Pugh, I. P. Parkin and C. J. Carmalt, *Acta. Cryst. C*, 2011, **67**, m96-m99.

Ligand exchange in titanium arsane complexes

T. Thomas, D. Pugh, I. P. Parkin and C. J. Carmalt, *Acta. Cryst. C*, 2011, submitted

Titanium arsenide films from the atmospheric pressure chemical vapour deposition of tetrakisdimethylamidotitanium and tert-butylarsine

T. Thomas, C. S. Blackman, I. P. Parkin and C. J. Carmalt, in preparation.

The deposition of vanadium arsenide thin films *via* the atmospheric pressure chemical vapour deposition reactions of VCl_4 and VOCl_3 with ${}^t\text{BuAsH}_2$

T. Thomas, C. S. Blackman, I. P. Parkin and C. J. Carmalt, in preparation.

A2 Crystal Data for [TiCl₄(AsPh₃)] (2.1)

Empirical formula	C ₁₈ H ₁₅ As Cl ₄ Ti
Formula weight	495.92
Temperature	150(2) K
Wavelength	0.71073 Å
Crystal system	Monoclinic
Space group	P21/c
Unit cell dimensions	a = 9.5026(19) Å α = 90°. b = 11.324(2) Å β = 92.501(4)°. c = 18.683(4) Å γ = 90°.
Volume	2008.5(7) Å ³
Z	4
Density (calculated)	1.640 Mg/m ³
Absorption coefficient	2.591 mm ⁻¹
F(000)	984
Crystal size	0.30 x 0.30 x 0.02 mm ³
Theta range for data collection	2.15 to 28.31°.
Index ranges	-12 ≤ h ≤ 12, -14 ≤ k ≤ 14, -24 ≤ l ≤ 24
Reflections collected	16527
Independent reflections	4787 [R(int) = 0.0609]
Completeness to theta = 28.31°	95.7 %
Absorption correction	Semi-empirical from equivalents
Max. and min. transmission	0.9500 and 0.5104
Refinement method	Full-matrix least-squares on F ²
Data / restraints / parameters	4787 / 0 / 217
Goodness-of-fit on F ²	1.182
Final R indices [I > 2σ(I)]	R1 = 0.0809, wR2 = 0.1380
R indices (all data)	R1 = 0.1013, wR2 = 0.1496
Largest diff. peak and hole	1.093 and -1.321 e.Å ⁻³

Atomic coordinates ($\times 10^4$) and equivalent isotropic displacement parameters ($\text{\AA}^2 \times 10^3$) for compound **(2.1)**. U(eq) is defined as one third of the trace of the orthogonalized U^{ij} tensor.

	x	y	z	U(eq)
C(1)	1211(6)	7379(5)	-341(3)	15(1)
C(2)	1965(7)	6721(6)	-817(4)	22(1)
C(3)	1527(8)	6679(7)	-1536(4)	30(2)
C(4)	345(8)	7287(7)	-1776(4)	30(2)
C(5)	-413(8)	7946(6)	-1299(4)	26(2)
C(6)	16(7)	7987(6)	-577(3)	18(1)
C(7)	96(7)	7714(6)	1144(3)	18(1)
C(8)	-360(8)	8817(6)	1310(4)	24(2)
C(9)	-1656(9)	8952(8)	1651(4)	36(2)
C(10)	-2450(8)	7987(8)	1806(4)	37(2)
C(11)	-1972(7)	6875(8)	1629(4)	32(2)
C(12)	-712(7)	6723(7)	1299(4)	30(2)
C(13)	2755(7)	8997(6)	726(4)	20(1)
C(14)	2810(8)	9738(6)	142(4)	26(2)
C(15)	3486(8)	10821(6)	197(4)	30(2)
C(16)	4157(8)	11155(7)	834(5)	33(2)
C(17)	4126(9)	10422(7)	1424(4)	35(2)
C(18)	3416(9)	9325(7)	1398(4)	33(2)
Cl(1)	4839(2)	4199(2)	1671(1)	33(1)
Cl(2)	1917(2)	4531(2)	594(1)	33(1)
Cl(3)	3001(2)	6459(2)	2207(1)	32(1)
Cl(4)	5056(2)	6431(2)	499(1)	26(1)
Ti(1)	3484(1)	5625(1)	1171(1)	17(1)
As(1)	1845(1)	7464(1)	661(1)	15(1)

Bond lengths [Å] and angles [°] for compound **(2.1)**.

C(1)-C(6)	1.384(8)	C(11)-C(12)	1.381(10)
C(1)-C(2)	1.384(9)	C(11)-H(11)	0.9500
C(1)-As(1)	1.945(6)	C(12)-H(12)	0.9500
C(2)-C(3)	1.389(9)	C(13)-C(14)	1.379(9)
C(2)-H(2)	0.9500	C(13)-C(18)	1.427(9)
C(3)-C(4)	1.376(11)	C(13)-As(1)	1.941(7)
C(3)-H(3)	0.9500	C(14)-C(15)	1.386(10)
C(4)-C(5)	1.387(10)	C(14)-H(14)	0.9500
C(4)-H(4)	0.9500	C(15)-C(16)	1.379(11)
C(5)-C(6)	1.393(9)	C(15)-H(15)	0.9500
C(5)-H(5)	0.9500	C(16)-C(17)	1.381(11)
C(6)-H(6)	0.9500	C(16)-H(16)	0.9500
C(7)-C(8)	1.363(9)	C(17)-C(18)	1.414(11)
C(7)-C(12)	1.397(10)	C(17)-H(17)	0.9500
C(7)-As(1)	1.945(6)	C(18)-H(18)	0.9500
C(8)-C(9)	1.419(10)	Cl(1)-Ti(1)	2.244(2)
C(8)-H(8)	0.9500	Cl(2)-Ti(1)	2.185(2)
C(9)-C(10)	1.367(12)	Cl(3)-Ti(1)	2.220(2)
C(9)-H(9)	0.9500	Cl(4)-Ti(1)	2.193(2)
C(10)-C(11)	1.383(11)	Ti(1)-As(1)	2.7465(13)
C(10)-H(10)	0.9500		
C(6)-C(1)-C(2)	120.2(6)	C(4)-C(5)-C(6)	120.1(7)
C(6)-C(1)-As(1)	119.9(5)	C(4)-C(5)-H(5)	120.0
C(2)-C(1)-As(1)	119.9(5)	C(6)-C(5)-H(5)	120.0
C(1)-C(2)-C(3)	119.9(6)	C(1)-C(6)-C(5)	119.6(6)
C(1)-C(2)-H(2)	120.1	C(1)-C(6)-H(6)	120.2
C(3)-C(2)-H(2)	120.1	C(5)-C(6)-H(6)	120.2
C(4)-C(3)-C(2)	120.2(7)	C(8)-C(7)-C(12)	120.4(6)
C(4)-C(3)-H(3)	119.9	C(8)-C(7)-As(1)	121.7(5)
C(2)-C(3)-H(3)	119.9	C(12)-C(7)-As(1)	117.9(5)
C(3)-C(4)-C(5)	120.0(7)	C(7)-C(8)-C(9)	119.4(7)
C(3)-C(4)-H(4)	120.0	C(7)-C(8)-H(8)	120.3
C(5)-C(4)-H(4)	120.0	C(9)-C(8)-H(8)	120.3

C(10)-C(9)-C(8)	120.5(7)	C(17)-C(16)-H(16)	120.1
C(10)-C(9)-H(9)	119.8	C(16)-C(17)-C(18)	121.9(7)
C(8)-C(9)-H(9)	119.8	C(16)-C(17)-H(17)	119.1
C(9)-C(10)-C(11)	119.2(7)	C(18)-C(17)-H(17)	119.1
C(9)-C(10)-H(10)	120.4	C(17)-C(18)-C(13)	116.7(7)
C(11)-C(10)-H(10)	120.4	C(17)-C(18)-H(18)	121.6
C(12)-C(11)-C(10)	121.4(8)	C(13)-C(18)-H(18)	121.6
C(12)-C(11)-H(11)	119.3	Cl(2)-Ti(1)-Cl(4)	114.84(9)
C(10)-C(11)-H(11)	119.3	Cl(2)-Ti(1)-Cl(3)	120.60(9)
C(11)-C(12)-C(7)	119.2(7)	Cl(4)-Ti(1)-Cl(3)	119.63(9)
C(11)-C(12)-H(12)	120.4	Cl(2)-Ti(1)-Cl(1)	99.45(9)
C(7)-C(12)-H(12)	120.4	Cl(4)-Ti(1)-Cl(1)	98.40(8)
C(14)-C(13)-C(18)	120.5(6)	Cl(3)-Ti(1)-Cl(1)	94.56(8)
C(14)-C(13)-As(1)	121.7(5)	Cl(2)-Ti(1)-As(1)	83.95(6)
C(18)-C(13)-As(1)	117.7(5)	Cl(4)-Ti(1)-As(1)	82.86(6)
C(13)-C(14)-C(15)	120.8(7)	Cl(3)-Ti(1)-As(1)	81.02(6)
C(13)-C(14)-H(14)	119.6	Cl(1)-Ti(1)-As(1)	175.41(8)
C(15)-C(14)-H(14)	119.6	C(13)-As(1)-C(1)	102.9(3)
C(16)-C(15)-C(14)	120.2(7)	C(13)-As(1)-C(7)	103.2(3)
C(16)-C(15)-H(15)	119.9	C(1)-As(1)-C(7)	102.6(3)
C(14)-C(15)-H(15)	119.9	C(13)-As(1)-Ti(1)	114.34(19)
C(15)-C(16)-C(17)	119.9(7)	C(1)-As(1)-Ti(1)	116.32(18)
C(15)-C(16)-H(16)	120.1	C(7)-As(1)-Ti(1)	115.63(19)

Anisotropic displacement parameters ($\text{\AA}^2 \times 10^3$) for compound **(2.1)**. The anisotropic displacement factor exponent takes the form: $-2\pi^2 [h^2 a^{*2} U^{11} + \dots + 2 h k a^* b^* U^{12}]$.

	U ¹¹	U ²²	U ³³	U ²³	U ¹³	U ¹²
C(1)	15(3)	12(3)	18(3)	4(2)	1(2)	-3(2)
C(2)	19(3)	27(4)	20(3)	0(3)	4(3)	6(3)
C(3)	35(4)	42(5)	14(3)	-7(3)	2(3)	2(4)
C(4)	41(4)	32(4)	18(3)	-3(3)	-1(3)	-5(3)
C(5)	27(4)	27(4)	24(4)	9(3)	-5(3)	-3(3)
C(6)	16(3)	20(3)	18(3)	-4(3)	-4(2)	2(2)
C(7)	21(3)	17(3)	16(3)	1(2)	-1(2)	3(2)
C(8)	28(4)	22(3)	24(4)	-3(3)	5(3)	3(3)
C(9)	42(5)	43(5)	25(4)	-8(3)	3(3)	28(4)
C(10)	19(4)	56(5)	35(4)	2(4)	2(3)	10(4)
C(11)	16(3)	46(5)	34(4)	-2(4)	5(3)	-4(3)
C(12)	20(4)	32(4)	38(4)	-8(3)	0(3)	3(3)
C(13)	22(3)	16(3)	22(3)	4(3)	0(3)	0(3)
C(14)	29(4)	24(4)	25(4)	0(3)	0(3)	-2(3)
C(15)	38(4)	19(3)	33(4)	-2(3)	1(3)	-8(3)
C(16)	29(4)	21(4)	49(5)	-1(3)	0(4)	-8(3)
C(17)	43(5)	26(4)	35(4)	-6(3)	-9(4)	-9(3)
C(18)	54(5)	36(4)	8(3)	9(3)	0(3)	1(4)
Cl(1)	38(1)	27(1)	34(1)	6(1)	1(1)	18(1)
Cl(2)	30(1)	23(1)	47(1)	-3(1)	-1(1)	-8(1)
Cl(3)	45(1)	32(1)	18(1)	2(1)	3(1)	17(1)
Cl(4)	22(1)	27(1)	31(1)	3(1)	6(1)	-5(1)
Ti(1)	17(1)	14(1)	19(1)	1(1)	1(1)	2(1)
As(1)	18(1)	13(1)	15(1)	0(1)	-1(1)	1(1)

A3 Crystal Data for [TiCl₄(AsPh₃)₂] (2.2)

Empirical formula	C ₃₆ H ₃₀ As ₂ Cl ₄ Ti	
Formula weight	802.14	
Temperature	150(2) K	
Wavelength	0.71073 Å	
Crystal system	Triclinic	
Space group	P-1	
Unit cell dimensions	a = 9.686(3) Å	α = 108.824(5)°.
	b = 9.789(3) Å	β = 111.489(5)°.
	c = 10.237(3) Å	γ = 92.081(5)°.
Volume	841.7(5) Å ³	
Z	1	
Density (calculated)	1.582 Mg/m ³	
Absorption coefficient	2.548 mm ⁻¹	
F(000)	402	
Crystal size	0.35 x 0.25 x 0.02 mm ³	
Theta range for data collection	2.91 to 28.40°.	
Index ranges	-12 ≤ h ≤ 12, -12 ≤ k ≤ 13, -13 ≤ l ≤ 13	
Reflections collected	6969	
Independent reflections	3757 [R(int) = 0.0280]	
Completeness to theta = 25.00°	95.6 %	
Absorption correction	Semi-empirical from equivalents	
Max. and min. transmission	0.9528 and 0.4672	
Refinement method	Full-matrix least-squares on F ²	
Data / restraints / parameters	3757 / 4 / 305	
Goodness-of-fit on F ²	1.053	
Final R indices [I > 2σ(I)]	R1 = 0.0461, wR2 = 0.1092	
R indices (all data)	R1 = 0.0692, wR2 = 0.1188	
Largest diff. peak and hole	1.230 and -1.291 e.Å ⁻³	

Atomic coordinates ($\times 10^4$) and equivalent isotropic displacement parameters ($\text{\AA}^2 \times 10^3$) for compound **(2.2)**. U(eq) is defined as one third of the trace of the orthogonalized U^{ij} tensor.

	x	y	z	U(eq)
Ti(1)	5000	10000	10000	26(1)
Cl(1)	3344(1)	11453(1)	9247(1)	39(1)
Cl(2)	3936(1)	9777(1)	11581(1)	37(1)
As(1)	2934(1)	7697(1)	7704(1)	28(1)
C(1A)	1270(7)	7174(8)	8199(8)	29(1)
C(2A)	500(8)	8282(9)	8642(9)	45(2)
C(3A)	-741(11)	7958(12)	8933(12)	56(3)
C(4A)	-1189(13)	6564(13)	8802(14)	52(3)
C(5A)	-433(8)	5477(8)	8373(8)	41(2)
C(6A)	797(7)	5756(8)	8045(7)	35(1)
C(7A)	1975(7)	7952(9)	5831(7)	29(1)
C(8A)	418(7)	7767(7)	5169(7)	33(1)
C(9A)	-267(8)	8069(8)	3880(7)	41(2)
C(10A)	583(10)	8584(8)	3278(8)	47(2)
C(11A)	2100(30)	8803(15)	3960(20)	52(4)
C(12A)	2863(9)	8452(11)	5235(8)	42(2)
C(13A)	3649(8)	5824(7)	7201(10)	29(1)
C(14A)	3182(9)	4907(9)	5652(9)	50(2)
C(15A)	3652(10)	3564(9)	5266(11)	57(2)
C(16A)	4515(9)	3092(11)	6352(14)	54(3)
C(17A)	4963(10)	3943(12)	7853(14)	62(3)
C(18A)	4492(7)	5289(8)	8243(8)	35(1)
C(1B)	927(13)	7619(15)	7783(15)	29(1)
C(2B)	854(14)	7315(14)	8998(13)	28(3)
C(3B)	-545(18)	7190(20)	9077(16)	29(3)
C(4B)	-1821(17)	7372(16)	8014(18)	40(3)
C(5B)	-1713(14)	7685(15)	6832(15)	37(3)
C(6B)	-336(13)	7821(15)	6727(15)	35(1)
C(7B)	2405(14)	7911(18)	5733(12)	29(1)

C(8B)	1849(14)	6649(14)	4385(13)	31(3)
C(9B)	1393(14)	6750(15)	2976(14)	36(3)
C(10B)	1447(14)	8068(15)	2816(15)	33(3)
C(11B)	2070(60)	9300(40)	4030(50)	52(4)
C(12B)	2468(16)	9224(16)	5482(15)	31(3)
C(13B)	3295(16)	5722(11)	7250(20)	29(1)
C(14B)	2392(13)	4737(13)	7301(13)	28(3)
C(15B)	2829(15)	3345(14)	7124(14)	35(3)
C(16B)	4220(20)	3163(19)	7070(20)	41(4)
C(17B)	5137(16)	4254(18)	7129(17)	40(3)
C(18B)	4718(14)	5626(16)	7289(15)	35(1)

Bond lengths [Å] and angles [°] for compound **(2.2)**. Symmetry transformations used to generate equivalent atoms: #1 -x+1,-y+2,-z+2.

Ti(1)-Cl(1)#1	2.2713(11)	C(12A)-H(12A)	0.9500
Ti(1)-Cl(1)	2.2713(11)	C(13A)-C(18A)	1.354(10)
Ti(1)-Cl(2)	2.2719(11)	C(13A)-C(14A)	1.432(11)
Ti(1)-Cl(2)#1	2.2719(11)	C(14A)-C(15A)	1.391(10)
Ti(1)-As(1)	2.7238(7)	C(14A)-H(14A)	0.9500
Ti(1)-As(1)#1	2.7238(7)	C(15A)-C(16A)	1.352(12)
As(1)-C(7A)	1.903(6)	C(15A)-H(15A)	0.9500
As(1)-C(13B)	1.914(9)	C(16A)-C(17A)	1.379(17)
As(1)-C(1A)	1.955(6)	C(16A)-H(16A)	0.9500
As(1)-C(13A)	1.963(6)	C(17A)-C(18A)	1.394(12)
As(1)-C(1B)	1.975(12)	C(17A)-H(17A)	0.9500
As(1)-C(7B)	1.975(9)	C(18A)-H(18A)	0.9500
C(1A)-C(6A)	1.386(9)	C(1B)-C(6B)	1.375(17)
C(1A)-C(2A)	1.388(9)	C(1B)-C(2B)	1.393(17)
C(2A)-C(3A)	1.389(10)	C(2B)-C(3B)	1.39(2)
C(2A)-H(2A)	0.9500	C(2B)-H(2B)	0.9500
C(3A)-C(4A)	1.365(14)	C(3B)-C(4B)	1.38(2)
C(3A)-H(3A)	0.9500	C(3B)-H(3B)	0.9500
C(4A)-C(5A)	1.361(12)	C(4B)-C(5B)	1.38(2)
C(4A)-H(4A)	0.9500	C(4B)-H(4B)	0.9500
C(5A)-C(6A)	1.392(9)	C(5B)-C(6B)	1.381(17)
C(5A)-H(5A)	0.9500	C(5B)-H(5B)	0.9500
C(6A)-H(6A)	0.9500	C(6B)-H(6B)	0.9500
C(7A)-C(12A)	1.378(10)	C(7B)-C(12B)	1.39(2)
C(7A)-C(8A)	1.385(8)	C(7B)-C(8B)	1.424(19)
C(8A)-C(9A)	1.376(8)	C(8B)-C(9B)	1.383(17)
C(8A)-H(8A)	0.9500	C(8B)-H(8B)	0.9500
C(9A)-C(10A)	1.361(11)	C(9B)-C(10B)	1.353(18)
C(9A)-H(9A)	0.9500	C(9B)-H(9B)	0.9500
C(10A)-C(11A)	1.35(2)	C(10B)-C(11B)	1.34(5)
C(10A)-H(10A)	0.9500	C(10B)-H(10B)	0.9500
C(11A)-C(12A)	1.403(19)	C(11B)-C(12B)	1.43(4)
C(11A)-H(11A)	0.9500	C(11B)-H(11B)	0.9500

C(12B)-H(12B)	0.9500	C(15B)-H(15B)	0.9500
C(13B)-C(14B)	1.302(17)	C(16B)-C(17B)	1.33(3)
C(13B)-C(18B)	1.373(16)	C(16B)-H(16B)	0.9500
C(14B)-C(15B)	1.417(17)	C(17B)-C(18B)	1.39(2)
C(14B)-H(14B)	0.9500	C(17B)-H(17B)	0.9500
C(15B)-C(16B)	1.39(2)	C(18B)-H(18B)	0.9500
Cl(1)#1-Ti(1)-Cl(1)	180.0	C(1A)-As(1)-Ti(1)	111.9(2)
Cl(1)#1-Ti(1)-Cl(2)	89.99(4)	C(13A)-As(1)-Ti(1)	115.9(2)
Cl(1)-Ti(1)-Cl(2)	90.01(4)	C(1B)-As(1)-Ti(1)	112.9(4)
Cl(1)#1-Ti(1)-Cl(2)#1	90.01(4)	C(7B)-As(1)-Ti(1)	112.3(5)
Cl(1)-Ti(1)-Cl(2)#1	89.99(4)	C(6A)-C(1A)-C(2A)	120.0(6)
Cl(2)-Ti(1)-Cl(2)#1	180.0	C(6A)-C(1A)-As(1)	122.9(5)
Cl(1)#1-Ti(1)-As(1)	93.32(4)	C(2A)-C(1A)-As(1)	117.0(5)
Cl(1)-Ti(1)-As(1)	86.68(4)	C(1A)-C(2A)-C(3A)	119.5(7)
Cl(2)-Ti(1)-As(1)	90.36(4)	C(1A)-C(2A)-H(2A)	120.2
Cl(2)#1-Ti(1)-As(1)	89.64(4)	C(3A)-C(2A)-H(2A)	120.2
Cl(1)#1-Ti(1)-As(1)#1	86.68(4)	C(4A)-C(3A)-C(2A)	120.2(8)
Cl(1)-Ti(1)-As(1)#1	93.32(4)	C(4A)-C(3A)-H(3A)	119.9
Cl(2)-Ti(1)-As(1)#1	89.64(4)	C(2A)-C(3A)-H(3A)	119.9
Cl(2)#1-Ti(1)-As(1)#1	90.36(4)	C(5A)-C(4A)-C(3A)	120.4(8)
As(1)-Ti(1)-As(1)#1	180.0	C(5A)-C(4A)-H(4A)	119.8
C(7A)-As(1)-C(13B)	106.9(6)	C(3A)-C(4A)-H(4A)	119.8
C(7A)-As(1)-C(1A)	104.3(3)	C(4A)-C(5A)-C(6A)	120.9(8)
C(13B)-As(1)-C(1A)	90.2(4)	C(4A)-C(5A)-H(5A)	119.6
C(7A)-As(1)-C(13A)	104.9(3)	C(6A)-C(5A)-H(5A)	119.6
C(1A)-As(1)-C(13A)	101.3(3)	C(1A)-C(6A)-C(5A)	118.9(6)
C(7A)-As(1)-C(1B)	86.1(4)	C(1A)-C(6A)-H(6A)	120.6
C(13B)-As(1)-C(1B)	105.4(5)	C(5A)-C(6A)-H(6A)	120.6
C(13A)-As(1)-C(1B)	116.5(4)	C(12A)-C(7A)-C(8A)	121.3(6)
C(13B)-As(1)-C(7B)	101.4(7)	C(12A)-C(7A)-As(1)	118.5(5)
C(1A)-As(1)-C(7B)	117.2(4)	C(8A)-C(7A)-As(1)	119.9(5)
C(13A)-As(1)-C(7B)	97.2(5)	C(9A)-C(8A)-C(7A)	119.8(6)
C(1B)-As(1)-C(7B)	99.5(5)	C(9A)-C(8A)-H(8A)	120.1
C(7A)-As(1)-Ti(1)	116.8(2)	C(7A)-C(8A)-H(8A)	120.1
C(13B)-As(1)-Ti(1)	122.4(5)	C(10A)-C(9A)-C(8A)	120.1(6)

C(10A)-C(9A)-H(9A)	119.9	C(4B)-C(3B)-H(3B)	118.9
C(8A)-C(9A)-H(9A)	119.9	C(2B)-C(3B)-H(3B)	118.9
C(11A)-C(10A)-C(9A)	119.6(9)	C(3B)-C(4B)-C(5B)	119.1(14)
C(11A)-C(10A)-H(10A)	120.2	C(3B)-C(4B)-H(4B)	120.4
C(9A)-C(10A)-H(10A)	120.2	C(5B)-C(4B)-H(4B)	120.4
C(10A)-C(11A)-C(12A)	122.8(14)	C(4B)-C(5B)-C(6B)	120.1(12)
C(10A)-C(11A)-H(11A)	118.6	C(4B)-C(5B)-H(5B)	120.0
C(12A)-C(11A)-H(11A)	118.6	C(6B)-C(5B)-H(5B)	120.0
C(7A)-C(12A)-C(11A)	116.3(11)	C(1B)-C(6B)-C(5B)	120.3(12)
C(7A)-C(12A)-H(12A)	121.9	C(1B)-C(6B)-H(6B)	119.8
C(11A)-C(12A)-H(12A)	121.9	C(5B)-C(6B)-H(6B)	119.8
C(18A)-C(13A)-C(14A)	117.0(6)	C(12B)-C(7B)-C(8B)	113.4(10)
C(18A)-C(13A)-As(1)	123.6(6)	C(12B)-C(7B)-As(1)	126.4(11)
C(14A)-C(13A)-As(1)	119.2(5)	C(8B)-C(7B)-As(1)	120.2(10)
C(15A)-C(14A)-C(13A)	120.3(7)	C(9B)-C(8B)-C(7B)	122.2(12)
C(15A)-C(14A)-H(14A)	119.8	C(9B)-C(8B)-H(8B)	118.9
C(13A)-C(14A)-H(14A)	119.8	C(7B)-C(8B)-H(8B)	118.9
C(16A)-C(15A)-C(14A)	120.2(9)	C(10B)-C(9B)-C(8B)	121.1(12)
C(16A)-C(15A)-H(15A)	119.9	C(10B)-C(9B)-H(9B)	119.5
C(14A)-C(15A)-H(15A)	119.9	C(8B)-C(9B)-H(9B)	119.5
C(15A)-C(16A)-C(17A)	120.7(8)	C(11B)-C(10B)-C(9B)	120.4(19)
C(15A)-C(16A)-H(16A)	119.7	C(11B)-C(10B)-H(10B)	119.8
C(17A)-C(16A)-H(16A)	119.7	C(9B)-C(10B)-H(10B)	119.8
C(16A)-C(17A)-C(18A)	119.3(8)	C(10B)-C(11B)-C(12B)	119(2)
C(16A)-C(17A)-H(17A)	120.4	C(10B)-C(11B)-H(11B)	120.6
C(18A)-C(17A)-H(17A)	120.4	C(12B)-C(11B)-H(11B)	120.6
C(13A)-C(18A)-C(17A)	122.4(8)	C(7B)-C(12B)-C(11B)	123.5(19)
C(13A)-C(18A)-H(18A)	118.8	C(7B)-C(12B)-H(12B)	118.3
C(17A)-C(18A)-H(18A)	118.8	C(11B)-C(12B)-H(12B)	118.3
C(6B)-C(1B)-C(2B)	120.9(11)	C(14B)-C(13B)-C(18B)	126.7(11)
C(6B)-C(1B)-As(1)	124.1(10)	C(14B)-C(13B)-As(1)	119.3(9)
C(2B)-C(1B)-As(1)	115.1(9)	C(18B)-C(13B)-As(1)	111.9(9)
C(3B)-C(2B)-C(1B)	117.5(12)	C(13B)-C(14B)-C(15B)	115.9(11)
C(3B)-C(2B)-H(2B)	121.3	C(13B)-C(14B)-H(14B)	122.1
C(1B)-C(2B)-H(2B)	121.3	C(15B)-C(14B)-H(14B)	122.1
C(4B)-C(3B)-C(2B)	122.1(16)	C(16B)-C(15B)-C(14B)	119.1(12)

C(16B)-C(15B)-H(15B)	120.4	C(16B)-C(17B)-H(17B)	120.0
C(14B)-C(15B)-H(15B)	120.4	C(18B)-C(17B)-H(17B)	120.0
C(17B)-C(16B)-C(15B)	121.5(13)	C(13B)-C(18B)-C(17B)	115.9(12)
C(17B)-C(16B)-H(16B)	119.2	C(13B)-C(18B)-H(18B)	122.0
C(15B)-C(16B)-H(16B)	119.2	C(17B)-C(18B)-H(18B)	122.0
C(16B)-C(17B)-C(18B)	120.0(13)		

Anisotropic displacement parameters ($\text{\AA}^2 \times 10^3$ for compound **(2.2)**). The anisotropic displacement factor exponent takes the form: $-2\pi^2 [h^2 a^{*2} U^{11} + \dots + 2 h k a^* b^* U^{12}]$.

	U11	U22	U33	U23	U13	U12
Ti(1)	23(1)	41(1)	19(1)	14(1)	10(1)	18(1)
Cl(1)	40(1)	55(1)	33(1)	22(1)	18(1)	33(1)
Cl(2)	34(1)	60(1)	28(1)	23(1)	18(1)	22(1)
As(1)	24(1)	43(1)	24(1)	15(1)	14(1)	13(1)
C(1A)	21(2)	38(2)	37(2)	23(1)	12(2)	12(1)
C(2A)	54(4)	51(5)	78(5)	50(4)	52(4)	39(4)
C(3A)	63(6)	68(6)	98(8)	63(7)	67(6)	53(6)
C(4A)	65(7)	64(7)	78(7)	51(6)	58(6)	38(5)
C(5A)	50(4)	39(4)	52(4)	24(3)	33(4)	18(3)
C(6A)	29(2)	45(3)	40(2)	26(2)	14(2)	11(2)
C(7A)	21(2)	38(2)	37(2)	23(1)	12(2)	12(1)
C(8A)	30(3)	41(4)	26(3)	12(3)	9(3)	14(3)
C(9A)	39(4)	50(4)	29(3)	16(3)	7(3)	23(3)
C(10A)	65(5)	36(4)	27(4)	16(3)	1(4)	16(4)
C(11A)	62(4)	66(12)	35(4)	33(9)	16(3)	-9(9)
C(12A)	38(4)	62(6)	29(4)	21(4)	12(3)	3(4)
C(13A)	21(2)	38(2)	37(2)	23(1)	12(2)	12(1)
C(14A)	73(5)	63(5)	54(5)	44(4)	45(4)	53(4)
C(15A)	82(6)	51(5)	77(6)	36(5)	63(5)	39(4)
C(16A)	42(4)	46(6)	102(8)	51(6)	37(5)	24(4)
C(17A)	29(4)	54(6)	107(9)	62(7)	2(5)	9(4)
C(18A)	29(2)	45(3)	40(2)	26(2)	14(2)	11(2)
C(1B)	21(2)	38(2)	37(2)	23(1)	12(2)	12(1)
C(2B)	36(6)	39(7)	20(6)	14(5)	19(5)	13(5)
C(3B)	34(9)	39(11)	20(6)	16(7)	13(6)	20(7)
C(4B)	32(7)	42(8)	52(9)	6(7)	33(7)	16(6)
C(5B)	29(6)	40(8)	43(8)	16(6)	14(6)	18(6)
C(6B)	29(2)	45(3)	40(2)	26(2)	14(2)	11(2)
C(7B)	21(2)	38(2)	37(2)	23(1)	12(2)	12(1)
C(8B)	38(7)	29(7)	25(6)	4(5)	19(5)	-7(5)
C(9B)	34(7)	39(8)	30(7)	5(6)	15(6)	-7(6)

C(10B)	28(6)	44(8)	30(7)	22(6)	8(6)	-1(6)
C(11B)	62(4)	66(12)	35(4)	33(9)	16(3)	-9(9)
C(12B)	39(7)	23(7)	22(6)	12(6)	-1(6)	-2(6)
C(13B)	21(2)	38(2)	37(2)	23(1)	12(2)	12(1)
C(14B)	32(6)	31(7)	33(6)	23(5)	15(5)	11(5)
C(15B)	42(7)	23(6)	38(7)	20(6)	4(6)	3(5)
C(16B)	56(11)	28(8)	35(9)	12(7)	12(8)	21(8)
C(17B)	32(7)	44(10)	30(7)	4(7)	5(6)	20(7)
C(18B)	29(2)	45(3)	40(2)	26(2)	14(2)	11(2)

A4 Crystal Data for [TiCl₃(NMe₂)(μ -NMe₂)₂AsCl] (2.5)

Empirical formula	C ₆ H ₁₈ As Cl ₄ N ₃ Ti	
Formula weight	396.85	
Temperature	150(2) K	
Wavelength	0.71073 Å	
Crystal system	Monoclinic	
Space group	P2 ₁ /n	
Unit cell dimensions	a = 9.5866(16) Å	$\alpha = 90^\circ$.
	b = 15.623(3) Å	$\beta = 92.562(3)^\circ$.
	c = 9.8386(16) Å	$\gamma = 90^\circ$.
Volume	1472.1(4) Å ³	
Z	4	
Density (calculated)	1.791 Mg/m ³	
Absorption coefficient	3.514 mm ⁻¹	
F(000)	792	
Crystal size	0.30 x 0.30 x 0.10 mm ³	
Theta range for data collection	2.49 to 28.31°.	
Index ranges	-12 ≤ h ≤ 12, -20 ≤ k ≤ 20, -12 ≤ l ≤ 12	
Reflections collected	12201	
Independent reflections	3496 [R(int) = 0.0258]	
Completeness to theta = 28.31°	95.4 %	
Absorption correction	Semi-empirical from equivalents	
Max. and min. transmission	0.7002 and 0.3787	
Refinement method	Full-matrix least-squares on F ²	
Data / restraints / parameters	3496 / 0 / 142	
Goodness-of-fit on F ²	1.126	
Final R indices [I > 2σ(I)]	R1 = 0.0322, wR2 = 0.0658	
R indices (all data)	R1 = 0.0347, wR2 = 0.0672	
Largest diff. peak and hole	0.585 and -0.548 e.Å ⁻³	

Atomic coordinates ($\times 10^4$) and equivalent isotropic displacement parameters ($\text{\AA}^2 \times 10^3$) for compound **(2.5)**. U(eq) is defined as one third of the trace of the orthogonalized U^{ij} tensor.

	x	y	z	U(eq)
C(1)	9046(3)	579(2)	6605(3)	25(1)
C(2)	7099(3)	-181(2)	7458(3)	23(1)
C(3)	5566(3)	1177(2)	10005(3)	23(1)
C(4)	6915(3)	2467(2)	10200(3)	23(1)
C(5)	7001(3)	2607(2)	4322(3)	22(1)
C(6)	6353(3)	1116(2)	4163(3)	27(1)
N(1)	7795(2)	676(1)	7450(2)	17(1)
N(2)	6689(2)	1672(1)	9379(2)	17(1)
N(3)	6572(2)	1847(1)	5066(2)	19(1)
Cl(1)	5149(1)	3103(1)	7255(1)	20(1)
Cl(2)	8546(1)	2592(1)	7345(1)	19(1)
Cl(3)	4431(1)	1006(1)	6891(1)	23(1)
Cl(4)	8136(1)	-10(1)	10518(1)	27(1)
Ti(1)	6392(1)	1856(1)	6945(1)	14(1)
As(1)	8439(1)	1117(1)	9210(1)	16(1)

Bond lengths [Å] and angles [°] for compound **(2.5)**.

C(1)-N(1)	1.497(3)	C(5)-H(5A)	0.9800
C(1)-H(1A)	0.9800	C(5)-H(5B)	0.9800
C(1)-H(1B)	0.9800	C(5)-H(5C)	0.9800
C(1)-H(1C)	0.9800	C(6)-N(3)	1.456(3)
C(2)-N(1)	1.496(3)	C(6)-H(6A)	0.9800
C(2)-H(2A)	0.9800	C(6)-H(6B)	0.9800
C(2)-H(2B)	0.9800	C(6)-H(6C)	0.9800
C(2)-H(2C)	0.9800	N(1)-As(1)	1.939(2)
C(3)-N(2)	1.482(3)	N(1)-Ti(1)	2.323(2)
C(3)-H(3A)	0.9800	N(2)-As(1)	1.903(2)
C(3)-H(3B)	0.9800	N(2)-Ti(1)	2.417(2)
C(3)-H(3C)	0.9800	N(3)-Ti(1)	1.864(2)
C(4)-N(2)	1.493(3)	Cl(1)-Ti(1)	2.3110(8)
C(4)-H(4A)	0.9800	Cl(2)-Ti(1)	2.3814(8)
C(4)-H(4B)	0.9800	Cl(3)-Ti(1)	2.3004(8)
C(4)-H(4C)	0.9800	Cl(4)-As(1)	2.2075(7)
C(5)-N(3)	1.464(3)	Ti(1)-As(1)	3.1249(6)
N(1)-C(1)-H(1A)	109.5	H(3B)-C(3)-H(3C)	109.5
N(1)-C(1)-H(1B)	109.5	N(2)-C(4)-H(4A)	109.5
H(1A)-C(1)-H(1B)	109.5	N(2)-C(4)-H(4B)	109.5
N(1)-C(1)-H(1C)	109.5	H(4A)-C(4)-H(4B)	109.5
H(1A)-C(1)-H(1C)	109.5	N(2)-C(4)-H(4C)	109.5
H(1B)-C(1)-H(1C)	109.5	H(4A)-C(4)-H(4C)	109.5
N(1)-C(2)-H(2A)	109.5	H(4B)-C(4)-H(4C)	109.5
N(1)-C(2)-H(2B)	109.5	N(3)-C(5)-H(5A)	109.5
H(2A)-C(2)-H(2B)	109.5	N(3)-C(5)-H(5B)	109.5
N(1)-C(2)-H(2C)	109.5	H(5A)-C(5)-H(5B)	109.5
H(2A)-C(2)-H(2C)	109.5	N(3)-C(5)-H(5C)	109.5
H(2B)-C(2)-H(2C)	109.5	H(5A)-C(5)-H(5C)	109.5
N(2)-C(3)-H(3A)	109.5	H(5B)-C(5)-H(5C)	109.5
N(2)-C(3)-H(3B)	109.5	N(3)-C(6)-H(6A)	109.5
H(3A)-C(3)-H(3B)	109.5	N(3)-C(6)-H(6B)	109.5
N(2)-C(3)-H(3C)	109.5	H(6A)-C(6)-H(6B)	109.5
H(3A)-C(3)-H(3C)	109.5	N(3)-C(6)-H(6C)	109.5

H(6A)-C(6)-H(6C)	109.5	Cl(1)-Ti(1)-N(1)	159.67(6)
H(6B)-C(6)-H(6C)	109.5	N(3)-Ti(1)-Cl(2)	92.83(7)
C(2)-N(1)-C(1)	106.3(2)	Cl(3)-Ti(1)-Cl(2)	169.89(3)
C(2)-N(1)-As(1)	115.93(16)	Cl(1)-Ti(1)-Cl(2)	91.11(3)
C(1)-N(1)-As(1)	107.55(16)	N(1)-Ti(1)-Cl(2)	81.84(6)
C(2)-N(1)-Ti(1)	117.18(15)	N(3)-Ti(1)-N(2)	165.86(9)
C(1)-N(1)-Ti(1)	115.59(16)	Cl(3)-Ti(1)-N(2)	90.81(5)
As(1)-N(1)-Ti(1)	93.89(8)	Cl(1)-Ti(1)-N(2)	90.46(5)
C(3)-N(2)-C(4)	107.5(2)	N(1)-Ti(1)-N(2)	69.62(7)
C(3)-N(2)-As(1)	117.26(16)	Cl(2)-Ti(1)-N(2)	80.25(5)
C(4)-N(2)-As(1)	108.62(16)	N(3)-Ti(1)-As(1)	128.40(7)
C(3)-N(2)-Ti(1)	114.72(16)	Cl(3)-Ti(1)-As(1)	106.83(2)
C(4)-N(2)-Ti(1)	116.44(15)	Cl(1)-Ti(1)-As(1)	121.89(2)
As(1)-N(2)-Ti(1)	91.90(8)	N(1)-Ti(1)-As(1)	38.24(5)
C(6)-N(3)-C(5)	111.6(2)	Cl(2)-Ti(1)-As(1)	63.14(2)
C(6)-N(3)-Ti(1)	126.45(18)	N(2)-Ti(1)-As(1)	37.48(5)
C(5)-N(3)-Ti(1)	121.98(17)	N(2)-As(1)-N(1)	89.60(9)
N(3)-Ti(1)-Cl(3)	94.85(7)	N(2)-As(1)-Cl(4)	99.97(7)
N(3)-Ti(1)-Cl(1)	102.07(7)	N(1)-As(1)-Cl(4)	101.09(7)
Cl(3)-Ti(1)-Cl(1)	93.69(3)	N(2)-As(1)-Ti(1)	50.62(6)
N(3)-Ti(1)-N(1)	97.32(9)	N(1)-As(1)-Ti(1)	47.87(6)
Cl(3)-Ti(1)-N(1)	90.67(6)	Cl(4)-As(1)-Ti(1)	128.00(2)

Anisotropic displacement parameters ($\text{\AA}^2 \times 10^3$) for compound **(2.5)**. The anisotropic displacement factor exponent takes the form: $-2\pi^2 [h^2 a^{*2} U^{11} + \dots + 2 h k a^* b^* U^{12}]$.

	U ¹¹	U ²²	U ³³	U ²³	U ¹³	U ¹²
C(1)	24(1)	26(1)	26(1)	-2(1)	7(1)	6(1)
C(2)	27(1)	13(1)	31(2)	-2(1)	-1(1)	1(1)
C(3)	18(1)	28(1)	24(1)	4(1)	6(1)	0(1)
C(4)	29(1)	23(1)	17(1)	-5(1)	-1(1)	3(1)
C(5)	21(1)	26(1)	19(1)	1(1)	1(1)	0(1)
C(6)	34(2)	24(1)	22(1)	-6(1)	-4(1)	0(1)
N(1)	17(1)	16(1)	19(1)	0(1)	2(1)	1(1)
N(2)	17(1)	16(1)	18(1)	1(1)	1(1)	2(1)
N(3)	19(1)	21(1)	15(1)	-1(1)	-1(1)	-1(1)
Cl(1)	19(1)	16(1)	25(1)	-1(1)	0(1)	2(1)
Cl(2)	16(1)	18(1)	22(1)	2(1)	-1(1)	-5(1)
Cl(3)	18(1)	18(1)	32(1)	1(1)	-2(1)	-5(1)
Cl(4)	29(1)	23(1)	29(1)	11(1)	0(1)	3(1)
Ti(1)	14(1)	12(1)	16(1)	0(1)	-1(1)	-1(1)
As(1)	15(1)	16(1)	17(1)	2(1)	0(1)	1(1)

A5 Crystal Data for [TiCl₂(μ -Cl)₂(NMe₂)(NHMe₂)]₂ (2.7)

Empirical formula	C ₈ H ₂₆ Cl ₆ N ₄ Ti ₂
Formula weight	486.77
Temperature	120(2) K
Wavelength	0.71073 Å
Crystal system	Monoclinic
Space group	P2 ₁ /n
Unit cell dimensions	a = 10.7088(4) Å $\alpha = 90^\circ$ b = 6.7143(3) Å $\beta = 104.753(2)^\circ$ c = 14.5281(5) Å $\gamma = 90^\circ$.
Volume	1010.16(7) Å ³
Z	2
Density (calculated)	1.600 Mg/m ³
Absorption coefficient	1.579 mm ⁻¹
F(000)	496
Crystal size	0.16 x 0.10 x 0.08 mm ³
Theta range for data collection	3.62 to 27.50°.
Index ranges	-13 ≤ h ≤ 13, -8 ≤ k ≤ 8, -18 ≤ l ≤ 18
Reflections collected	9954
Independent reflections	2317 [R(int) = 0.0386]
Completeness to theta = 27.50°	99.6 %
Absorption correction	Semi-empirical from equivalents
Max. and min. transmission	0.8841 and 0.7863
Refinement method	Full-matrix least-squares on F ²
Data / restraints / parameters	2317 / 0 / 99
Goodness-of-fit on F ²	1.118
Final R indices [I > 2σ(I)]	R1 = 0.0274, wR2 = 0.0585
R indices (all data)	R1 = 0.0326, wR2 = 0.0618
Largest diff. peak and hole	0.306 and -0.343 e.Å ⁻³

Atomic coordinates ($\times 10^4$) and equivalent isotropic displacement parameters ($\text{\AA}^2 \times 10^3$) for compound **(2.7)**. $U(\text{eq})$ is defined as one third of the trace of the orthogonalized U^{ij} tensor.

	x	y	z	$U(\text{eq})$
C(1)	8621(2)	2452(3)	8983(2)	23(1)
C(2)	6484(2)	3384(3)	8068(2)	26(1)
C(3)	7778(2)	3364(3)	10999(2)	26(1)
C(4)	8244(2)	5(3)	11595(1)	26(1)
N(1)	7235(2)	2093(2)	8822(1)	17(1)
N(2)	7315(2)	1275(2)	10913(1)	17(1)
Cl(1)	5131(1)	-1214(1)	8059(1)	21(1)
Cl(2)	4685(1)	2277(1)	9598(1)	16(1)
Cl(3)	8080(1)	-2140(1)	9606(1)	21(1)
Ti(1)	6477(1)	182(1)	9430(1)	14(1)

Bond lengths [Å] and angles [°] for compound **(2.7)**. Symmetry transformations used to generate equivalent atoms: #1 -x+1,-y,-z+2.

C(1)-N(1)	1.463(2)	C(4)-N(2)	1.482(2)
C(1)-H(1A)	0.9800	C(4)-H(4A)	0.9800
C(1)-H(1B)	0.9800	C(4)-H(4B)	0.9800
C(1)-H(1C)	0.9800	C(4)-H(4C)	0.9800
C(2)-N(1)	1.466(2)	N(1)-Ti(1)	1.8576(16)
C(2)-H(2A)	0.9800	N(2)-Ti(1)	2.2364(16)
C(2)-H(2B)	0.9800	N(2)-H(1)	0.86(3)
C(2)-H(2C)	0.9800	Cl(1)-Ti(1)	2.3371(5)
C(3)-N(2)	1.482(3)	Cl(2)-Ti(1)	2.4414(5)
C(3)-H(3A)	0.9800	Cl(2)-Ti(1)#1	2.6759(5)
C(3)-H(3B)	0.9800	Cl(3)-Ti(1)	2.2847(5)
C(3)-H(3C)	0.9800	Ti(1)-Cl(2)#1	2.6759(5)
N(1)-C(1)-H(1A)	109.5	H(4A)-C(4)-H(4B)	109.5
N(1)-C(1)-H(1B)	109.5	N(2)-C(4)-H(4C)	109.5
H(1A)-C(1)-H(1B)	109.5	H(4A)-C(4)-H(4C)	109.5
N(1)-C(1)-H(1C)	109.5	H(4B)-C(4)-H(4C)	109.5
H(1A)-C(1)-H(1C)	109.5	C(1)-N(1)-C(2)	111.27(15)
H(1B)-C(1)-H(1C)	109.5	C(1)-N(1)-Ti(1)	125.90(13)
N(1)-C(2)-H(2A)	109.5	C(2)-N(1)-Ti(1)	122.77(13)
N(1)-C(2)-H(2B)	109.5	C(3)-N(2)-C(4)	109.54(15)
H(2A)-C(2)-H(2B)	109.5	C(3)-N(2)-Ti(1)	115.81(12)
N(1)-C(2)-H(2C)	109.5	C(4)-N(2)-Ti(1)	119.46(12)
H(2A)-C(2)-H(2C)	109.5	C(3)-N(2)-H(1)	106.6(18)
H(2B)-C(2)-H(2C)	109.5	C(4)-N(2)-H(1)	105.7(17)
N(2)-C(3)-H(3A)	109.5	Ti(1)-N(2)-H(1)	97.7(17)
N(2)-C(3)-H(3B)	109.5	Ti(1)-Cl(2)-Ti(1)#1	100.380(18)
H(3A)-C(3)-H(3B)	109.5	N(1)-Ti(1)-N(2)	96.59(7)
N(2)-C(3)-H(3C)	109.5	N(1)-Ti(1)-Cl(3)	96.76(5)
H(3A)-C(3)-H(3C)	109.5	N(2)-Ti(1)-Cl(3)	90.61(4)
H(3B)-C(3)-H(3C)	109.5	N(1)-Ti(1)-Cl(1)	96.95(5)
N(2)-C(4)-H(4A)	109.5	N(2)-Ti(1)-Cl(1)	164.13(4)
N(2)-C(4)-H(4B)	109.5	Cl(3)-Ti(1)-Cl(1)	95.98(2)

N(1)-Ti(1)-Cl(2)	95.71(5)	N(2)-Ti(1)-Cl(2)#1	79.67(4)
N(2)-Ti(1)-Cl(2)	81.21(4)	Cl(3)-Ti(1)-Cl(2)#1	87.536(19)
Cl(3)-Ti(1)-Cl(2)	165.80(2)	Cl(1)-Ti(1)-Cl(2)#1	86.182(18)
Cl(1)-Ti(1)-Cl(2)	89.233(18)	Cl(2)-Ti(1)-Cl(2)#1	79.620(18)
N(1)-Ti(1)-Cl(2)#1	174.37(5)		

Anisotropic displacement parameters ($\text{\AA}^2 \times 10^3$) for compound **(2.7)**. The anisotropic displacement factor exponent takes the form: $-2\pi^2 [h^2 a^{*2} U_{11} + \dots + 2 h k a^* b^* U_{12}]$.

	U ₁₁	U ₂₂	U ₃₃	U ₂₃	U ₁₃	U ₁₂
C(1)	18(1)	24(1)	30(1)	1(1)	10(1)	-2(1)
C(2)	26(1)	27(1)	26(1)	7(1)	6(1)	3(1)
C(3)	30(1)	23(1)	25(1)	-6(1)	6(1)	-8(1)
C(4)	20(1)	33(1)	19(1)	1(1)	-4(1)	5(1)
N(1)	15(1)	19(1)	18(1)	1(1)	6(1)	2(1)
N(2)	12(1)	20(1)	18(1)	-1(1)	4(1)	-1(1)
Cl(1)	17(1)	28(1)	17(1)	-6(1)	3(1)	-1(1)
Cl(2)	13(1)	15(1)	21(1)	1(1)	4(1)	2(1)
Cl(3)	16(1)	19(1)	27(1)	0(1)	6(1)	5(1)
Ti(1)	11(1)	15(1)	15(1)	0(1)	2(1)	1(1)